**Università degli Studi di Siena**
Dipartimento di Chimica

Dottorato di Ricerca in Scienze Chimiche XVII° Ciclo
Coordinatore Prof. Enzo Tiezzi
TESI

# Biological Photoreceptors as Models for the Computer Design of Light Driven Molecular Rotors

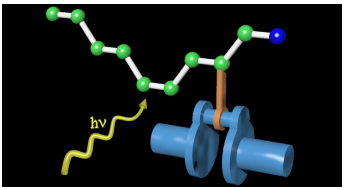


Dottorando
Luca De Vico

Supervisore
Prof. Massimo Olivucci

Dicembre 2004

*Ai miei Genitori, Antonella e Lucio*

*Grazie!!*

Stampato in Siena per i tipi di Top Copy nel mese di Dicembre 2004
Printed in Italy

# Table of Contents

# Acknowledgments

First and foremost I want to express my gratitude to my supervisor Prof. Massimo Olivucci, for all his help and encouragement. During all these years he drove my scientific education and gave me the opportunity to present the results of my work at conferences and meetings, at home and abroad.

I would also like to thank Prof. Roland Lindh at the University of Lund for the great opportunity and experience to work in his laboratory and for being always ready to help me.

I'd like to acknowledge Prof. Peter Hamm and his co-workers, especially Dr. Jan Helbing, at the University of Zürich for their fundamental contribution to this work.

Many thanks go to:

All the past and present members of the Computational Photochemistry Group for the pleasant and fruitful atmosphere at work:, Jacopo, Luis Manuel, Nicolás, Annapaola, Alessandra, Tadeusz, Pedro, Irena and Marco. Special mentions go to Chris, Diego, Elena and Adalgisa for their friendship and for their help. I'm honoured to call them friends.

All the nice people I met in Lund, for making my time there unforgettable: Juraj, Francesco, Alexander, Kasper, Valera, Olga, Houman, Ajitha, Lubomir, Takashi and Fabian. Tack så mycket!

Last but not least, I'd really like to thank all my family and my dear friends Marco, Riccardo, Ilaria, Tatiana, Nicola, Flavio and Janet for all their support and love. I'd never arrived here without them.

Generous funds for the work have been provided by the University of Siena (Progetto di Ateneo A.A. 02/04), HFSP (RG 0229/2000-M) and FIRB (RBAU01EPMR)

# Acronyms&Abbreviations

| | |
|---|---|
| AO | Atomic Orbital(s) |
| CASPT2 | Complete Active Space – Multireference Second Order Perturbation Theory |
| CASSCF | Complete Active Space - Self Consistent Field |
| CI | Conical Intersection(s) |
| ES | Excited State |
| FC | Frank-Condon |
| FS | Fluorescent State |
| GS | Ground State |
| HOMO | Highest Occupied Molecular Orbital |
| IC | Internal Conversion |
| IRC | Intrinsic Reaction Coordinate |
| IRD | Initial Relaxation Direction(s) |
| LUMO | Lowest Unoccupied Molecular Orbital |
| MD | Molecular Dynamics |
| MEP | Minimum Energy Path(s) |
| MO | Molecular Orbital(s) |
| PES | Potential Energy Surface(s) |
| PSB | Protonated Shiff Base |
| RP | Radical Pair |
| TS | Transition State(s) |

# List of Figures

# List of Tables

# Chapter 1. Introduction

## 1.1. Molecular Machinery: Smart Molecules

One of the guide lines of modern technological development is that of obtaining smaller and more efficient nanoscale tools. It is possible to date back to 1959 when the Nobel Prize winner *Richard Feynman*, in his famous talk to the annual meeting of the American Physical Society at the California Institute of Technology (Caltech) "There's Plenty of Room at the Bottom",[1] showed the advantages of a miniaturized technology. In the last years it has been possible to see how everything became smaller and more efficient, following the development of innovative technology. Nevertheless, the Feynman vision still shows the path to go beyond the actual limits. In fact, till today, the main approach to the design of new devices has been a *top-down* one, which means miniaturize what already exists (e.g. computer processors), creating new devices in a smaller scale. However, the bigger challenge is represented by the *bottom-up* development of new devices, which would be able to open new scenarios, which are only science fiction today. In the bottom-up vision, instead of starting from existing devices and then trying to miniaturize them, one starts from the fundamental components of matter, atoms, to build a molecular machinery able to perform a given task. Given

the dimensions of these smart molecules, the prefix nano[a] is used when describing anything related to them: nanodevices, nanostructures, nanotechnology.

The term '*NanoTechnology*' was created by Tokyo Science University professor *Norio Taniguchi* in 1974[2] to describe the precision manufacture of materials with nanometer tolerances. In the 1980s the term was reinvented and its definition expanded by *K. Eric Drexler*, particularly in his 1986 book "Engines of Creation: The Coming Era of Nanotechnology".[3] He explored this subject in much greater technical depth in his MIT doctoral dissertation, later expanded into "Nanosystems: Molecular Machinery, Manufacturing, and Computation".[4] Computational methods play a key role in the field today, because nanotechnologists can use them to design and simulate a wide range of molecular systems.[5]

One application of nanotechnology is the development of so-called *smart materials*. This term refers to any sort of material designed and engineered at the nanometre scale to perform a specific task, and encompasses a wide variety of possible applications. One example is represented by materials designed to respond differently to various molecules; such a capability could lead, for example, to artificial drugs which would recognize and render inert specific viruses. Another is the idea of self-healing structures, which would repair small tears in a surface naturally in the same way as self-sealing tires or human skin.

A nanosensor would resemble a smart material, involving a small component within a larger machine that would react to its environment and change in

[a] The prefix nano comes from Greek. A nanometer is one billionth of a meter, about the diameter of ten atoms placed side by side.

some fundamental, intentional way. As a very simple example: a photosensor could passively measure the incident light and discharge its absorbed energy as electricity when the light passes above or below a specified threshold, sending a signal to a larger machine. Such a sensor would cost less and use less power than a conventional sensor, and yet function usefully in all the same applications.

While smart materials and nanosensors both exemplify useful applications of nanotechnology, they pale in comparison with the complexity of the technology most popularly associated with the term: the nanobots, swarms of coordinated nanoscale robots working to build things. Today is still science fiction, but today's science fiction is tomorrow science fact.

## 1.2. Motors, Switches, Rotors

Most part of everyday life mechanical devices, generally, produces one of two kind of movement: linear or circular. Besides, there are many mechanism to transform one kind of movement in another. A classic example is the crankshaft mechanism of the old steam engines of train, which is able to transform the longitudinal movement of the piston into the circular movement of the train wheels. This kind of mechanism was already known to *Leonardo da Vinci* (Figure 1–1), and it has been used in infinite applications.

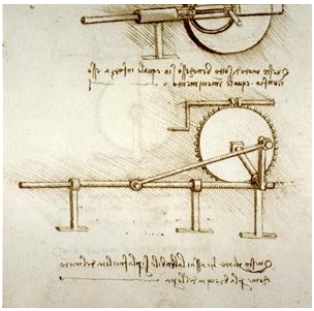

Figure 1–1: Leonardo da Vinci, Crankshaft driven by worm screw and toothed wheel, Madrid Ms. I (BNM), fol. 28v (detail). Institute and Museum of the History of Science, Florence.[6]

Nanotechnology tries to translate the main elements of the macroscopic world into the microscopic one. Obviously there are some substantial differences. For example, a typical element of any mechanism such as the wheel, unlikely would be reproduced in an atomic scale, maintaining the same functionality.[a] A big number of researches during last years tried to plan and realize devices capable of movement. Afterwards, next step will be to realize and assemble systems able to exploit and transform the generated movement.

It is important to be precise on terminology. An engine has to be able to produce an unidirectional movement, in a continuous way and without any external (i.e. human) input to modify its structure during the functioning,

[a] Maybe, the alien technology of " The War of the Worlds" by *H. G. Wells* will be our future technology:: "… nothing is more wonderful to a man than the curious fact that […in Martian technology…] the wheel is absent." (book 2, chapter 2).

apart from the supplied energy source. A rotor is an engine able to produce circular movement. A switch is a mechanism that can exist in (at least) two forms, and able to pass from one to another, and back, following an external stimulus.

## 1.3. Light as Energy Source

Nanodevices are subdue to external inputs of two different kinds: chemical and physical. Practically, the energy to carry out their function can be supplied to the devices as chemical energy (e.g. a pH change), redox energy at an electrode, or as an electromagnetic radiation. The first form of energy has the advantage of being easily controlled, and it is relatively easy to prepare chemical groups sensitive to a given chemical stimulus and, at the same time, that can work as promoters of the movement of the main molecular structure. On the other hand, for the process to be continuous, a incessant variation of the conditions (e.g. sudden changes of the pH) is needed, that in turn could obstruct the functionality of the mechanism in its whole. The same reasoning stands for the redox energy.

Otherwise, the usage of light as energy source could be more complicated, because, usually, big antenna complexes are needed to capture the light radiation. These complexes, in turn, are difficult to adjoin to the main molecular structure responsible for the movement. However, if the moving molecule would be, at the same time, the light harvesting one, everything would be more straightforward. That is the case of the molecules that will be studied in this thesis, as it will be explained later.

Light is the most logical choice as energy source of excellence (i.e. the fuel) for nanodevices. Given that it is available in big quantities, renewable and with zero emission, solar light respect all the needs for a good and lasting usage. Since one of the aim of nanotechnology, as for science in general, is that of making a better life for everybody, the usage of a "clean" energy source is imperative.

## 1.4. Fate of Light Energy at Molecular Level

In simple terms there are two events that may happen when the light energy is absorbed by a molecule. This energy is either wasted or exploited (Scheme 1–1). The control of these events can be considered as a basic requirement for the rational design of efficient photochemical reactions, artificial photosynthetic systems and for the rational design of novel materials, molecular devices and molecular level machines. In fact, technology often requires molecules where this energy is not wasted but exploited to achieve specific chemical, conformational and electronic changes. In contrast, other applications, as those in the field of photoprotection or in the field of photobiology, need molecules that are structurally unaffected by light absorption (e.g. through light emission and internal conversion).

In this respect, during the last few years, computational methods have been successfully applied to explore energy wastage processes such as the quenching of fluorescent probes[7,8] and the mechanism of fast internal conversion in the photostabilization of DNA basis.[9] Similarly, as an example of process where light is exploited to drive efficient and stereoselective photochemical reactions, one can recall the ultrafast pericyclic reactions.[10]

Most interestingly, the same types of processes are known in photobiology. For instance, there are fluorescent proteins, such as the Green Fluorescent

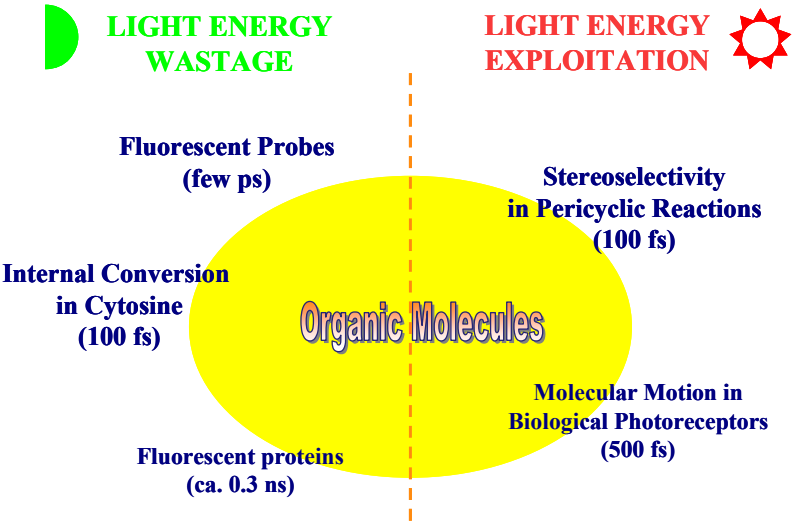


Scheme 1–1

Protein (GFP), where the energy of the photon can be wasted to produce fluorescence while there are other photoreceptors, such as the visual pigment Rhodopsin (Rh) (see later), where the energy of the photon is exploited to produce a change in the protein structure.

## 1.5. The Story So Far…

As an example, two models of molecular motors recently designed and realized will be now presented, one for linear and one for circular movement.

One of the most leading-edge research group, in Italy and in the world, in nanotechnology is the group of *Balzani* in Bologna. In the past years they realized many devices able to move a part along another, following a stimulus. Recently they developed the so-called molecular elevator, also know as Nanospider.[11] In this system, a platform shifts “up” and “down” over three supports, following the presence of an acid or a base in solution.(Scheme 1–2)

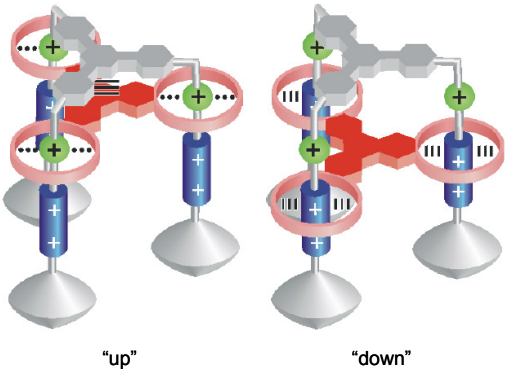


Scheme 1–2

An example of molecular motor able to produce circular movement is the molecule developed by the group of *Feringa*.[12] In this case, alternating light and thermal phases, it is possible to obtain a circular unidirectional movement. Scheme 1–3.

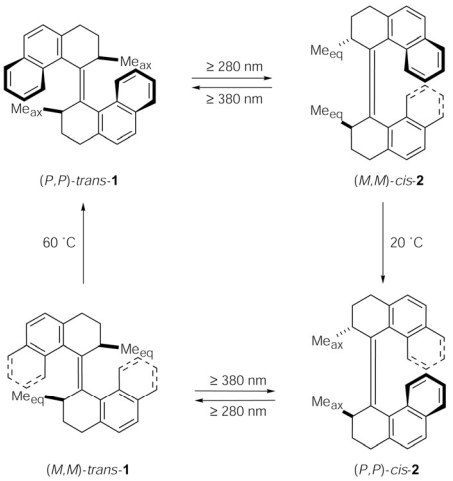


Scheme 1–3

The last factor, unidirectionality, is very important when designing a motor, because a movement non unidirectional, on average, is zero. Otherwise, it would be possible to obtain work directly from the Brownian movement of molecules, clearly breaking the second principle of thermodynamics. Nevertheless, recent studies on this argument showed that living cells exploit ratchets to use only a few components of the Brownian movement, blocking those not required.[13] This approach, in the future, could open new scenarios.

Back to the Feringa motor, as said its molecule perform its activity in four step. In the first and third, the molecule absorb a photon of light and changes its conformation around the central double bond. The second and forth step are re-arrangements of the molecular structure through a thermal reaction.

## 1.6. In Nature the Inspiration. Light Usage as Signal or Energy Source

As said, the Feringa motor is not totally driven by light only, but needs also some human tuning for the alternation of light and thermal steps. Some new ideas are needed to design a molecular motor driven only by light. Obviously, Nature is the primary inspiring source, when searching for systems able to perform a task when irradiated with light. Light is used by bioorganisms for two major purposes: sensory perception and energy conversion.[14] The former demands sensitivity and a wide range of photon energy detection, while the latter demands efficiency of photon energy conversion. Both qualities would be useful in a light driven molecular device. Indeed, photonic proteins are ubiquitous in the biological world. These include proteins involved in the transduction of light energy into chemical one, the detection of light for sensing purposes (bacterial phototaxis, plant phototropism and visual sensing), and the emission of light such as bioluminescence. In fact, many proteins evolved with the function of efficiently capturing the roughly $10^5$ Terawatts of solar power that impinges on the Earth's surface.

It is not uncommon that successful strategies in nature's repertoire are seen to repeat across the boundary between plants and animals, different phyla of organism, vision and photosynthesis. For example, the scotopic vision process (black and white vision) is performed by retina's rods. Their function is achieved by the rhodopsin protein, first ring in the chain that, in the end, generates a signal in the optical nerve. Other than the well known chlorophyll photosynthesis process, other systems are capable of transforming solar energy into chemical energy.[15] For example, the purple membrane of

*Halobacterium salinarum* performs this task by creating a proton gradient, used then to produce ATP. This function is done by bacteriorhodopsin protein. The *chromophores* residing inside both proteins, which are responsible for the absorption of a photon of light and trigger the entire process of the protein, are very similar. Indeed, both are retinals (derived from vitamin A), condensed to the protein chain via a protonated Schiff base linkage. Similar is also the response to the absorption of the photon: both undergoes a *cis-trans photoisomerization*. The chromophore of rhodopsin isomerise from 11-*cis*-retinal to all-*trans*-retinal (Scheme 1–4), while the bacteriorhodopsin one isomerise from all-*trans*-retinal to 13-*cis*-retinal (Scheme 1–5).

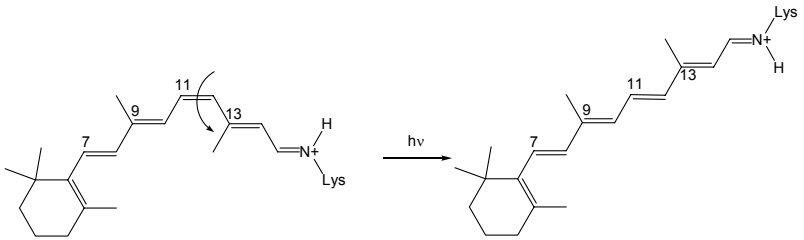


Scheme 1–4

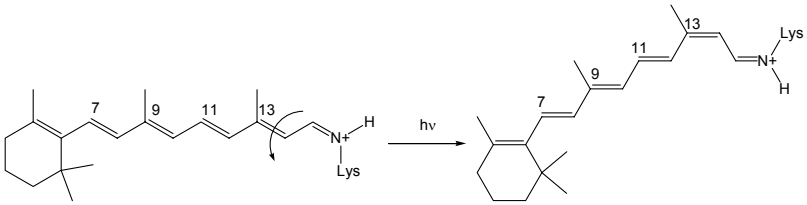


Scheme 1–5

These photoisomerizations are *ultrafast and stereospecific*. This means, retinal chromophores represent the ideal candidate as models for the modelling of light driven molecular rotors. An in depth view of both proteins will be given in Chapter 2, along with relative bibliography.

## 1.7. … and What Lies Ahead

The possibilities opened by the study and comprehension of the photoisomerization process of retinal chromophores are boundless. First of all, if the unidirectionality of the movement would be reproduced in an artificial devices, they would represent the perfect rotor: light driven, simple, and with the possibility of being linked into a protein chain. Other than as rotors, they could work also as switches, being the cis-trans conformations like the on-off states of an usual toggle. Actually, computers based on the bacteriorhodopsin molecule are only in science fiction books,[16] but they are not so far from being realized.[17]
A review of possible applications of retinal chromophores and, in general, photonics proteins can be found in ref. 18.

## 1.8. Aim of the Thesis

Inside this grand vision, this thesis represents a step towards the detailed comprehension of the photoisomerization processes and their exploitation. State-of-the-art *ab initio* quantum chemical calculations will be used to

achieve various objectives. When a molecule undergoes an excitation to an higher electronic energy level (see Chapter 5), one of the main features to study is the way followed by the molecule to relax back on the electronic fundamental state. This implies the computation of the molecular structures where radiationless deactivation is most probable: *conical intersections and singlet/triplet crossings*. Such crossings[19,20] provide effective channels for the radiationless deactivation to the ground state. During the last fifteen years the quantum chemical methods mentioned above have been successfully applied to the investigation of the mechanism of both the internal conversion and photochemical transformation of isolated molecules.[21]

### 1.8.1. First objective

First objective of this thesis is about retinal chromophores and the relationship between their structure and the ultrafastness and stereospecificity of the photoisomerization in the protein environment. As will be illustrated in Chapter 8, the behaviours of retinal chromophores inside the protein cavity and in solution are quite different. Comparison with time resolved spectroscopy data (the only experimental method capable to explore ultrafast reaction) will be useful to develop a theoretical model able to explain what is needed for an ultrafast photoisomerization. It is possible to make the hypothesis that if the photoisomerization is fast, it will be also very selective, if not specific. That's because if a molecule is rapidly pushed along one way, it doesn't "have the time" to take other possible routes of decay, and consequently the reaction gives only one product. The possible structural factors responsible for fastness of the reaction will be enquired by using

various models of retinal chromophore, resembling the natural occurring as well as artificial ones. This will develop a sort of "catalogue" of structural factors needed to achieve a fast photoisomerization.
Besides this line of research, the nature of first intermediates appearing as first photoproducts of the photoisomerization will be investigated, too. The definition of a mechanistic model of the photoisomerization process is of outermost importance for the exact interpretation of experimental spectroscopy data.

### 1.8.2. Second objective

The acquired experience will be used to investigate in Chapter 13 for possible applications of molecules that can undergo a cis-trans photoisomerization. In fact, the second objective of this thesis is the study of a chromophore, *N*-methylthioacetammide (NMTAA), model for a thio-substituted peptide bond. This molecule is capable of undergo a cis-trans photoisomerization through irradiation at a different wavelength other than the usual absorbance maximum of peptide bonds. Scheme 1–6

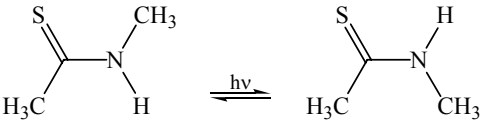


*trans*-NMTAA *cis*-NMTAA

Scheme 1–6

If working as hoped, after irradiation at its specific absorption maximum, this unit would be able to change the conformation of the protein into which it is inserted. The photoisomerization process will be fully explored and data obtained through a joint effort in computational and experimental photochemistry will constitute a mechanistic model. A possible application for such a device could be to study the conformational rearrangements (folding) of protein chains. Since irradiation of the NMTAA unit would be selective, one knows where the change in the protein structure would be. A systematic analysis through time resolved spectroscopy would let to build a data base, relating signals to protein folding movement (e.g. the signal for the beginning of formation of a $\alpha$–helices). The data base would then be used to analyse the signals of wild type proteins during the folding process. Obviously, with the progression of computational tools, it will also be possible to simulate the changes of thio-substituted proteins, relating them to the experimental data. This continuous exchange of data would lead to a better understanding of the protein folding event. Also, as previously said in Section 1.7, inclusion of an engineered unit into a peptide could produce new kinds of light-activated drugs.

### 1.8.3. Third objective

Both retinal chromophores and NMTAA photoisomerization processes involve a non radiative decay at a crossing between different electronic states (i.e. a non adiabatic process). See Chapter 5. From a computational point of view, the calculation of minimum energy structures, in the presence of an electronic degeneracy constraint, is always a demanding task, whether the

states share the same spin multiplicity (conical intersections), or different multiplicity (singlet-triplet crossing). The last part of the thesis (Chapter 14), and its third objective, is committed to the development of new tools for the geometry optimization of potential energy surfaces crossings, with high level *ab initio* computations. Mainly, it consists of a modified version of the method suggested by Anglada and Bofill[22] to use a Lagrange multiplier optimization scheme, in conjunction with internal coordinates space division into a constraint's subspace (of dimension m) and a subspace (of dimension 3n-6(5)-m) where the optimization is performed. The method will be tuned and exploited to calculate some intersystem crossing of the acrolein molecule.

## 1.9. Scheme of the Thesis

As stressed in Sections 1.6 and 1.7, retinal chromophores represent the starting material for a broad range of studies. Since also the part of the thesis related to the first objective is devoted to the study of this class of chromophores, in Chapter 2 an insight of the two classes of proteins will be given. Other experimental data will be provided at the beginning of Chapter 8.

As said in Section 1.8.1, the main experimental method employed in the investigation of ultrafast photoisomerization processes is time resolved spectroscopy. Since data obtained with this methodology will be presented throughout this thesis, Chapter 3 is devoted to the basis and key concepts of time resolved spectroscopy.

Following, in Chapter 4 - Chapter 7 I present the computational chemistry methods used in the rest of the thesis. These include the key concepts for the exploration of potential energy surfaces and the search for the photochemical funnel, that is the crossings between the surfaces. These chapters are also strictly related to the Appendix, which is devoted to the essential concepts of *ab initio* quantum chemistry.

The rest of the thesis can be seen as divided in three more parts, each one for every objectives. First, Chapter 8 - Chapter 11 will further introduce the retinal chromophores, along with the results of computations over a series of models. Afterwards, Chapter 12 - Chapter 13 are about NMTAA and its behaviour under photoexcitation. Finally Chapter 15 treats the definition of a new method to explore potential energy surfaces through constrained geometry optimizations.

At the end, some Conclusions are given, to summarise the obtained data and give some perspectives.

### 1.9.1. Roadmap

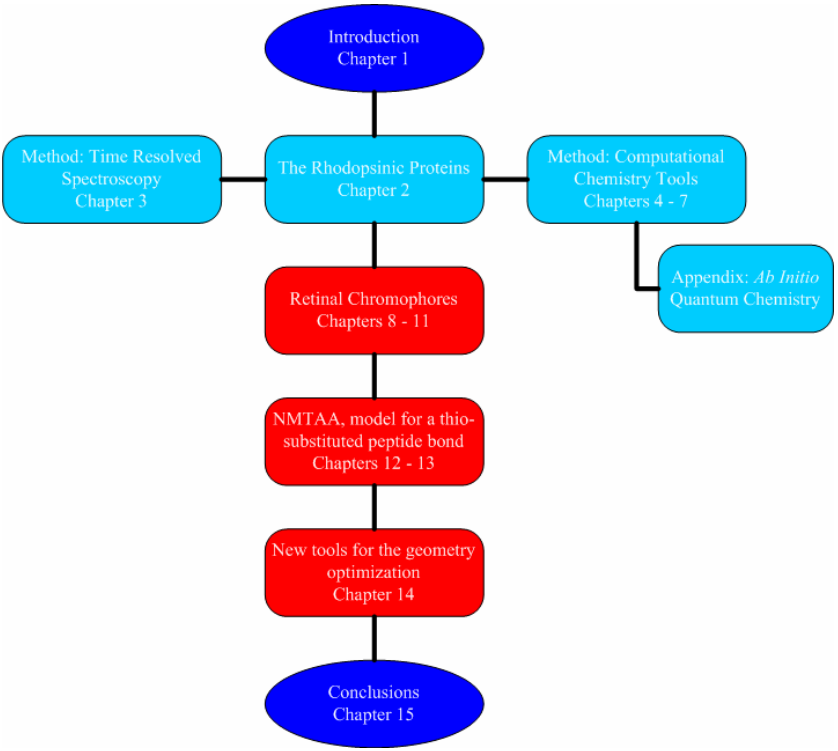
Introduction
Chapter 1
Method: Time Resolved
Spectroscopy
Chapter 3
The Rhodopsinic Proteins
Chapter 2
Method: Computational
Chemistry Tools
Chapters 4 - 7
Appendix: *Ab Initio*
Quantum Chemistry
Retinal Chromophores
Chapters 8 - 11
NMTAA, model for a thio-
substituted peptide bond
Chapters 12 - 13
New tools for the geometry
optimization
Chapter 14
Conclusions
Chapter 15

# Chapter 2. The Rhodopsinic Proteins

## 2.1. Introduction

In superior animals, the vision process begins with the light triggered isomerization of the retinal chromophore of the rhodopsin molecule, contained in rods and cones of the retina, from 11-*cis* into all-*trans* form.[23-26] Given the importance of vision on everyday life, this class of molecules have been extensively studied since decades ago. In 1967 *George Wald* received the Nobel prize for his studies on the recognition of cis-trans isomerization process as fundamental for vision,[27,28] but since 1942 the capabilities of rhodopsin molecule as even single photon detector were already stated.[29] Moreover, the first measurements of the energy at the visual threshold were made by *Samuel Langley* in 1889, using the bolometer he invented for such purpose.[30]

The importance of rhodopsinic proteins is not limited to the vision process. In fact, rhodopsinic proteins have been found in all domains of Life.[31] Actually, photoactive seven transmembrane helix proteins which use all-*trans*-retinal as their chromophore have been known and extensively studied in extreme halophiles (Archaea domain) for more than thirty years.[32] Recently, homologs have been discovered also in the Bacteria and Eucarya domains.[31] The main action of this kind of proteins is as ion-pumps or for light detection (phototropism and phototaxis). Even more recently, *Craig Venter* and co-

workers identified nearly eight hundred different rhodopsin-like photoreceptors.[33]

This fact means that rhodopsinic proteins are widely used in the natural world as photonic material, and can constitutes a very good starting point for the design of light-driven innovative molecules. In this Chapter some outlines of the two most studied proteins will be given.

## 2.2. Photochemical Aspects of Rhodopsin

The visual transduction process in rod photoreceptors cells for scotopic vision begins with absorption of a photon by a rhodopsin molecule, which is a seven-transmembrane α-helical protein having 11-*cis*-retinal as a chromophore. Figure 2–1. The chromophore is the protonated Schiff base of a 6 conjugated double bond retinal. The Schiff base is formed by condensation with the $NH_2$ ending of the side chain of a lysine residue of chain VII. As already stated, the double bonds chain is in the 11-*cis* conformation; along it there are two methyl groups and the double bond opposite to the nitrogen atom is embedded into a six-member ring (β-ionone ring).

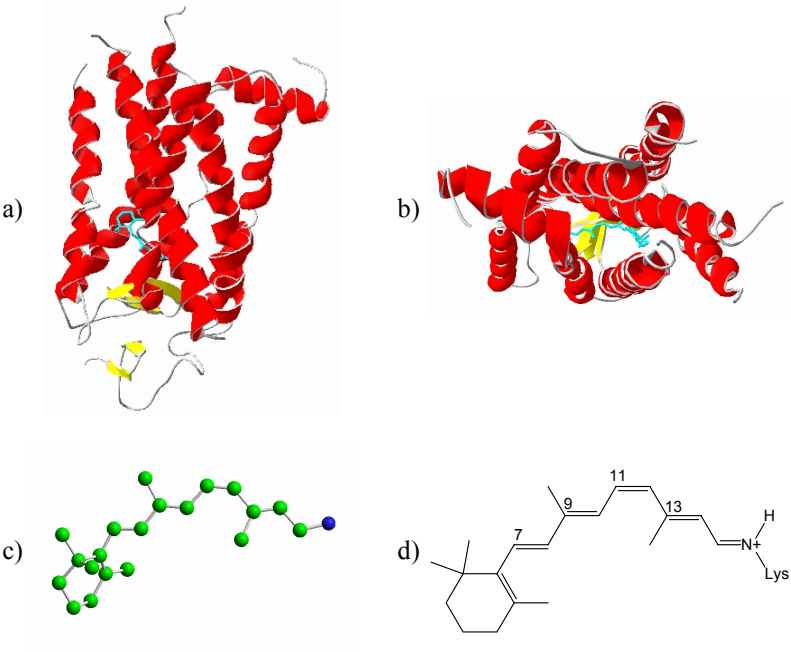


Figure 2–1: The rhodopsin molecule, side (a) and upper (b) view. In evidence the seven α-helices and the chromophore, in blue. (c) The chromophore of rhodopsin as resulting from x-ray crystallography and (d) a scheme of its structure.

Light isomerises the 11-*cis*-retinal into all-*trans* form (Scheme 2–1),[28] resulting in conformational changes of the protein moiety to form an enzymatically active intermediate, metarhodopsin II (meta II).[34,35] The meta II then activates the retinal G protein, transducin,[34] which in turn, activates the signal transduction cascade that eventually generates an electrical response of the receptor cells.[36]

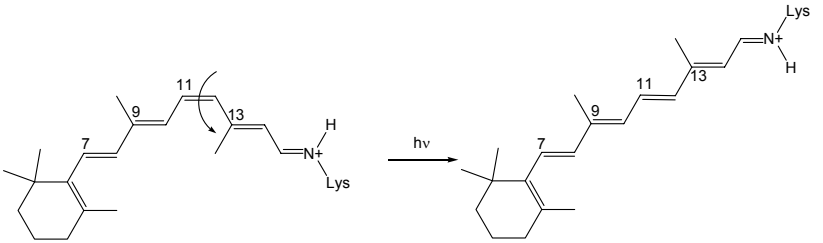


Scheme 2–1

Rhodopsin is one of the members of G protein-coupled receptor (GPCR) family, in the sense that it can activate the G protein transducin. However, it is unique because it can be activated not by a chemical stimulus but by light, a physical stimulus. Several lines of evidence indicated that rhodopsin exhibits an extremely high photosensitivity, an effective activation of G protein, and an inert character in the dark.[37,a] These properties yield a molecular mechanism in which a rod photoreceptor cell works as a single photon counter with an extremely low level of noise in the dark. Because the functional expression of the photoreceptor cell is totally different from those of the cells that are activated by hormones, neurotransmitters, and so on, the molecular mechanisms of G protein activation by rhodopsin was thought to be somewhat different from those by other ligand-binding GPCRs.[38] However, accumulated evidence reveals that the chromophore of rhodopsin acts as an inverse agonist, and light fulfils a role in converting the inverse agonist[39] into the agonist, all-*trans*-retinal, within the protein moiety, suggesting that the G protein activation mechanism is similar between rhodopsin and other GPCRs.

[a] This means that activation by accident in very unlikely.

### 2.2.1. Structures of retinal chromophore and its binding site in rhodopsin

Rhodopsin is a ~40 kDa membrane protein that consists of a single polypeptide opsin and a chromophore, 11-*cis*-retinal. Opsin contains seven transmembrane α-helices, the structural motif typical of the GPCRs.[40] Recently, a three-dimensional crystal of bovine rhodopsin was successfully synthesized,[41] and its atomic structure was analysed by x-ray crystallography.[42,43] This provides a comprehensive structural basis for giving insight into the functional roles of rhodopsin. Other recent studies started to develop the basis for the understanding of the interaction between the chromophore and its protein surrounding.[44]

Earlier studies indicated that 11-*cis*-retinal forms a protonated Schiff base with Lys-296 of opsin,[45] and the proton on the Schiff base is stabilized by a negatively charged glutamate at position 113 (Glu-113).[46] Crystal structure of rhodopsin confirmed that the retinal is really bound to Lys-296 and Glu-113 is located at 3.2 Å from the Schiff base nitrogen.[42,43] Recently, the spatial resolution of the diffraction of the rhodopsin crystal was improved to visualize water molecules in the rhodopsin molecule.[47] The results showed that a water molecule is located not in between the Schiff base and the counterion (as previously thought), but on the carboxyl and peptide carbonyl groups of the glutamate at position 113. These results suggest that the water molecule would have a role of stabilizing the proton on the Schiff base by reducing the negative charge of the carboxylate of the glutamate.

### 2.2.2. Cis-trans isomerization mechanism of chromophore in rhodopsin

On absorption of light, rhodopsin changes its absorption maximum from 500 to 380 nm, fading in colour from red to pale yellow. This photobleaching process of rhodopsin is composed of photoreactions (photochemical reaction) and subsequent thermal reactions. How efficiently the photoreaction occurs is closely connected with a trapping yield of light signal, that is, the absolute photosensitivity of rhodopsin, while subsequent thermal reactions are important for generating an active state that transduces a light signal to a retinal G protein. Because the chromophore acts as an intrinsic probe to monitor conformational changes of the protein during the thermal reactions of rhodopsin, each step of the change was confirmed by detection of an intermediate state having specific absorption spectrum. Historically, low-temperature spectroscopy was applied to detect the distinctive intermediate states, such as bathorhodopsin, lumirhodopsin, metarhodopsin I to III.[48] Subsequently, kinetic experiments using an ultrashort laser pulse identified photorhodopsin as the primary intermediate[49] and then observed the excited state of rhodopsin.[50] Recent kinetic experiments using laser photolysis at room temperature and time-resolved low-temperature spectroscopy showed that other intermediates exist between the originally identified intermediates.[51] Thus, the bleaching process of rhodopsin could be summarized in Scheme 2–2.[26,52]

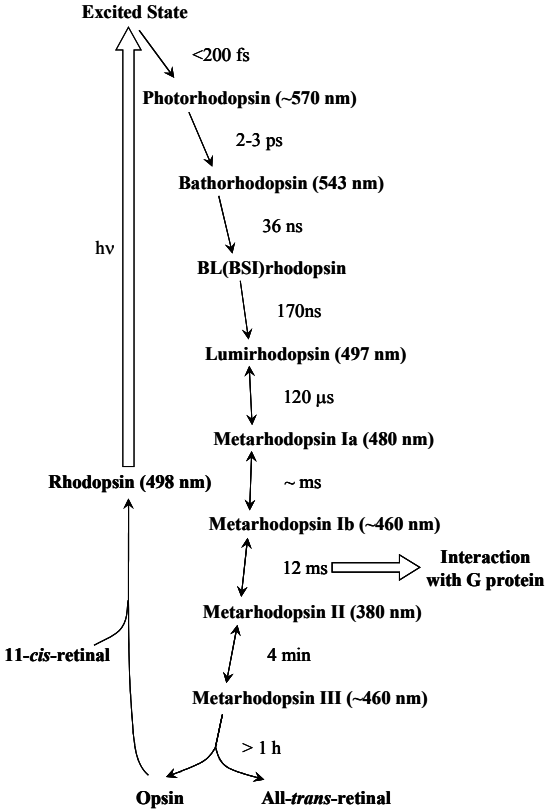


Scheme 2–2

Several experiments established that the chromophore of bathorhodopsin is already in a nearly all-*trans* conformation.[48,53] A more detailed description of the early events in the rhodopsin photocycle (Primary Event) is given in Section 8.1. The chromophore of lumirhodopsin is supposed to be already in the all-*trans* form. During the passage from bathorhodopsin to lumirhodopsin also the β-ionone ring change position inside the protein cavity (Figure 2–

2).[54,55] This fact is supposed to trigger a rearrangement of the α-helices, which, in turn, exposes different groups to the environment and, consequently, activates transducin. The protein reassembling is, likely, related also to the deprotonation of the chromophore, which is also responsible for the drastic absorbance wavelength shortening of meta II.

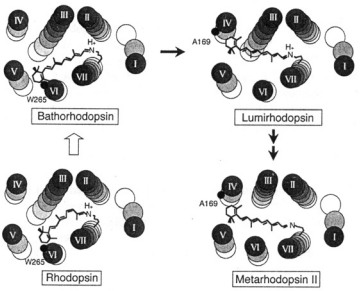


Figure 2–2: Opsin conformational movements triggered by 11-cis to all-trans photoisomerization of the chromophore.[54] In rhodopsin and bathorhodopsin, the β-ionone ring is close to Trp265 in Helix VI, but in lumirhodopsin and metarhodopsin II, it becomes cross linked to Ala169. Thus, during the batho-to-lumi transition, the β-ionone ring of the chromophore flips over the helical bundle, using the energy stored as a highly strained chromophore structure in bathorhodopsin.

## 2.3. Origin of bacteriorhodopsin

Bacteriorhodopsin is the predominant protein found in the purple membrane of *Halobacterium salinarum* (also historically referred to as *Halobacterium*

*halobium* or *Halobacterium salanarium*), a halophilic (e.g. "salt-loving") organism that functions in environments where native salt concentrations exceed six time that of seawater.[32,56] *Halobacterium salinarum* is a member of the domain Archaea.[57] Archaea is a kingdom of prokaryotic single-celled organisms that share some of the common features of eukaryotes and prokaryotes, and usually inhabit extreme environments. *Halobacterium salinarum* belongs to the Euryarchaeota phyla. The majority of the euryarchaeotes adapted to survival under extreme environmental conditions. For example, the thermophiles exist at extreme ranges in temperature, while halophiles exist at extremely high salt concentrations. *H. salinarum* grows maximally when sodium chloride (NaCl) concentrations are approximately 4 M. This organism can be seen in salt marshes across the world (i.e. the Dead Sea, the Great Salt Lake in Utah, or the crystallization pools of salt-works around the world, Figure 2–3 - Figure 2–5), and the formation of BR in the cell membrane can be associated with the purple hue characteristic of these briny marshes. Evolution optimised BR for high photochemical efficiency, thermal stability and the ability to perform its task many times in a cyclic way. The organism must be able to function in a hot, stagnant, and resources limited environment. Under conditions of low oxygen availability and high light intensities, and under the coordinate regulation of other proteins, BR formation is induced.

Figure 2–3: Great Salt Lake, Utah, U.S.A.[58]

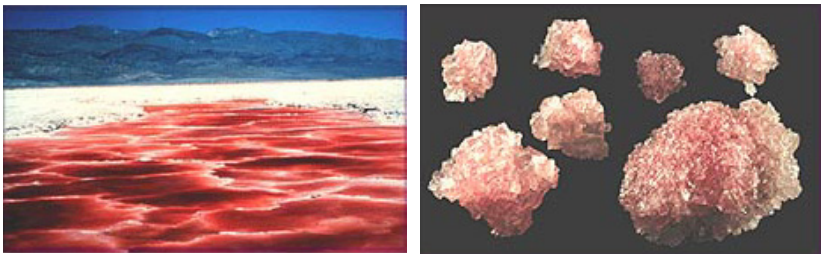

a b

Figure 2–4: a) Owens Lake b) Crystals of sodium chloride (NaCl) coloured by millions of H. salinarum from Owens Valley. California, U.S.A.[59]

Figure 2–5: Salt works of Margherita di Savoia, Italy[60]

### 2.3.1. Structure of the purple membrane

The cells of *H. salinarum* are rod shaped and measure approximately 0.5 to 1 μm in diameter by 1 to 6 μm in length. The cells stain Gram negative, a feature characteristic of the Archaea that signifies that these organisms do not contain a high concentration of peptidoglycans in the cell membrane. The purple membrane (Figure 2–6) is comprised of a trimer of BR molecules arranged in a hexagonal two-dimensional lattice. Mature BR accounts for approximately 70 to 75% of the total membrane protein. The protein exists as a trimer in the organism, but trimers and monomers show no significant spectroscopic or kinetic differences in proton pumping ability.[61]

Figure 2–6: Freeze-dried Purple Membrane[60]

The remarkable stability of BR is attributed to interactions between membrane lipids and the protein in the purple membrane. Removal of the protein or lipids by chemical means impact the stability of the lattice. The purple membrane patches were shown to be stable up to 140°C and a wide range of pH values.[62]

The purple membrane is generated under conditions of low oxygen availability and is used for photosynthetic energy production. The BR photocycle results in the transport of protons from the intracellular to the extracellular surface of the membrane. This generates an electrochemical gradient that is used for energy production as protons enter the cell through ATP synthase channels. This process of nonphotosynthetic photophosphorylation is the only example found in nature. *H. salinarum* also respires by aerobic means when the concentration of oxygen is sufficient to sustain oxidative phosphorylation. The organism is quite harmless to humans and osmotically dissociates into harmless fragments when placed in low salt environment (<2M).

### 2.3.2. The photocycle of bacteriorhodopsin

Shown in Figure 2–7 are the molecular structure of BR. The BR monomer is a 26 kDa protein that contains seven membrane-spanning α-helices. The chromophore, a non-protein moiety, is covalently linked to an internal lysine residue, Lys-216 (Figure 2–7). This chromophore is a diasteroisomer of that of visual rhodopsin; in fact, in its relaxed form, it is the protonated Schiff base of an all-*trans*-retinal.

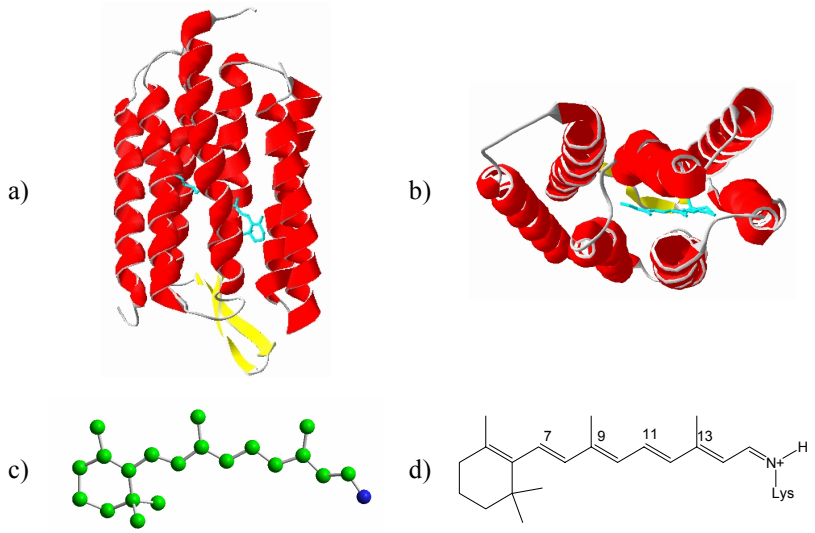


Figure 2–7: The bacteriorhodopsin molecule, side (a) and upper (b) view. In evidence the seven α-helices and the chromophore, in blue. (c) The chromophore of bacteriorhodopsin as resulting from x-ray crystallography and (d) a scheme of its structure.

The proton pumping process of bacteriorhodopsin commences when the protein-bound chromophore of the light-adapted form absorbs a photon of light and undergoes an all-*trans* 13-*cis* isomerization (Scheme 2–3).

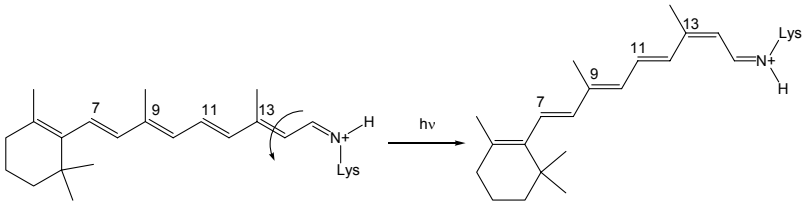


Scheme 2–3

The photoisomerization is the first step in the protein photocycle reported in Figure 2–8. Only the first step is light-activated, while all the rest of the cycle occurs via a series of thermal relaxations.

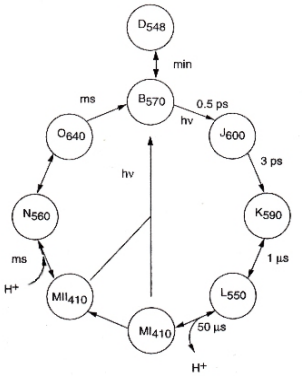


Figure 2–8: The bacteriorhodopsin photocycle. $D_{548}$ is the dark-adapted state, that can be reverted to the active $B_{570}$ upon illumination

As for the photocycle of rhodopsin, the various intermediates have been characterized by their absorbance wavelength.[25,63] Even in this case, there is a decolouring of the molecule along the cycle (photobleaching). Isomerization of the chromophore creates an electrostatic environment that destabilizes the protonated Schiff base. The Schiff base donates a proton to a nearby aspartic acid residue, Asp-85. Although the process is still poorly understood, it has be seen that concomitant with protonation of Asp-85, a proton is released in the extra-membrane environment, involving the participation of Arg-82, Glu-194, Glu-204 and a hydrogen-bonded network of internal water molecules.[64] The proton movement from the Schiff base to Asp-85 generates the blue shifted M I state. The chromophore is then re-protonated in the M II to N states transition, by transfer of a proton from another nearby aspartic acid, Asp-96. It has be seen that, apart from the already described natural photocycle, upon irradiating the M states it is possible to return directly to the B state.

Along the described photocycle, the chromophore is always covalently bound to the protein chain. It is, anyway, possible to walk another path: from state O, where the retinal is back in the all-*trans* conformation, upon irradiation, the artificial state P I is created, characterized by an 11-*cis* retinal. This causes a detachment of the chromophore from the protein, even if it doesn't exit from the protein cavity. Irradiation of the subsequent state Q photoisomerise the chromophore to all-*trans*-retinal, state Θ. Upon back-formation of the Schiff base the original B state is then generated (Scheme 2–4).

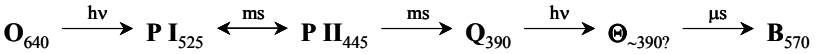


Scheme 2–4

Just like rhodopsin, a Primary Event has been observed also for bacteriorhodopsin. Using time resolved techniques (see Chapter 3) the first step of the photocycle has been subdivided as reported in Scheme 2–5. The state H represent the instantaneously generated Frank-Condon state, that transforms into I (fluorescent state) with a fs timescale. Then decay to the state J, assumed to represent the return of the molecule onto the electronic fundamental state, occurs in about 0.5 ps.

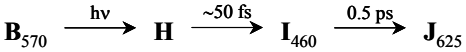


Scheme 2–5

# Chapter 3. An Introduction to Pump-Probe Time-Resolved Spectroscopy

The interaction of radiation with matter is at the base of most part of instrumental studies, as part of modern physical methods in chemistry. For example, photo-reactive molecules respond to incident radiation in the UV-visible region of the electromagnetic spectrum. In the case that the energy of the radiation matches that of a molecular transition between the ground and an electronic excited state of the molecule, a photon is absorbed by the molecule and the electronic structure is altered into a higher energy configuration. The excited molecule can eventually return to the ground state by radiative or non-radiative transition. The excited state molecule can also be stimulated to emit by photons matching the energy of a downward molecular transition to the ground state.

One of the state-of-the-art experimental techniques is the Pump-Probe Time-Resolved Spectroscopy. While the aim of this thesis is not to illustrate all aspect of this method, a brief introduction will be provided, given that most part of the computational results of the present work will be compared to experimental results obtained with this technique.

Pump-probe is a well-established time resolved spectroscopy technique that avoids the problems of poor sensitivity that usually accompany sampling or gating a fast detector. Typically, an experimental specimen is excited by a short duration pulse of light (the “pump”), while a subsequent pulse of light

(the "probe") spectroscopically senses the specimen. The two pulsed sources are synchronized, but with the probe arriving a controllable time delay Δt after the pump. Thus, the pump serves to excite the sample while the probe senses the sample's state at Δt after the pump. The process can repeat at a rapid rate, resulting in high signal throughput and good signal-to-noise using high sensitivity spectrometer and detector systems.

Given the short time range of pulses, of the order of picoseconds (ps) or femtoseconds (fs), this technique is an experimental way of creating wave-packets. Given the fact that results of time-resolved spectroscopy are explained on the basis of quantum dynamic, a short theoretical background on this subject will be given. This will be also useful to the understanding of some terms in the subsequent general description of the method, as for the rest of the thesis. Afterwards, some generalities on the various techniques will be given, without pretending of fulfilling a continuously growing field.

## 3.1. Quantum Dynamic: some Theoretical Notes

While a static situation is described by the time independent Schrödinger equation (see Appendix), if some kind of interaction (matter/matter or matter/electro-magnetic radiation) is involved in the process one is interested into, the treatment of the *full time dependent Schrödinger equation* is needed:

$$\hat{H}(t)\left|\Psi(t)\right\rangle = i\hbar\frac{\partial\left|\Psi(t)\right\rangle}{\partial t} \qquad (3\text{–}1)$$

In this equation, the Hamiltonian depends explicitly on time and is applied to a function explicitly depending on time, too. The spatial coordinate dependence is implicit. The first way to solve this equation was given by *Dirac*, and his method will be followed.[65] $\left|\Psi(t)\right\rangle$ is called a wave-packet, in the sense that it can be seen as an ensemble of waves moving in space and time. This is a differential equation of the first order, so it needs one condition: the "state" of the wave-packet at time zero: $\left|I\right\rangle \equiv \left|\Psi(0)\right\rangle$, the initial state. For realistic models, this equation cannot be solved analytically. Subsequently some approximations need to be used. For the purpose of this thesis, a simplified version of the time dependent Schrödinger equation, where time is explicit only in the wave function will be used at first. Explicit dependence on time to the rest of the equation will then be "added" without demonstrating it.

$$\hat{H}_0\left|\Psi_0(t)\right\rangle = i\hbar\frac{\partial\left|\Psi_0(t)\right\rangle}{\partial t} \qquad (3\text{–}2)$$

In this equation $\hat{H}_0$ is the molecular Hamiltonian of the time independent Schrödinger equation, $\hat{H}_0\left|n\right\rangle = E_n\left|n\right\rangle$, that can be supposed solved. The imposed initial condition is that the wave packet at time equal to zero $\left|\Psi_0(0)\right\rangle$ is known. Then, the wave packet at any given time can be expressed as:

$$\left|\Psi_0(t)\right\rangle = \hat{U}(t)\left|\Psi_0(0)\right\rangle \qquad (3\text{–}3)$$

where $\hat{U}(t)$ is the time evolution operator. Given the initial condition, there is only one $|\Psi_0(t)\rangle$. It is possible to demonstrate that the time evolution operator can be expressed as:

$$\hat{U}(t)|\Psi_0(0)\rangle = e^{-i\hat{H}_0 t/\hbar}|\Psi_0(0)\rangle \qquad (3\text{–}4)$$

Since it has been supposed that the time independent Schrödinger equation is known, $\sum_n |n\rangle\langle n|$ represents the unitary operator. Introducing it into the time evolution operator one can obtain:

$$|\Psi_0(t)\rangle = \sum_n |n\rangle\langle n|\Psi_0(0)\rangle e^{-iE_n t/\hbar} \qquad (3\text{–}5)$$

where every term is known. The notation can be simplified by calling the initial state $|I\rangle$. Then $\langle n|I\rangle$ can be written as coefficients, $C_{nI}$. Moreover, one can write $\frac{E_n}{\hbar} = \omega_n$, that has the dimensions of a frequency. So it is possible to re-write:

$$|\Psi_o(t)\rangle = \sum_n |n\rangle C_{nI} e^{-i\omega_n t} \qquad (3\text{–}6)$$

This expression is similar to the usual expansion of a wave function over a set of orthonormal eigenvector, apart from the oscillatory term, $e^{-i\omega_n t}$, which is responsible for the time dependence. That makes the function to be a

temporal wave packet. As a particular case, one can consider that the initial state is a given eigenstate of the molecular Hamiltonian: $|I\rangle = |n\rangle$. Afterwards, it is possible to substitute the coefficients with a delta function, $C_{nI} = \delta_{nI}$. In this way one can rewrite the function as: $|\Psi_0(t)\rangle = |n\rangle e^{-i\omega_n t}$, which is called a stationary state. Defining the probability of finding the wave-packet in a given state $|F\rangle$ as $P_F(t) = \left|\langle F|\Psi(t)\rangle\right|^2$, it is possible to demonstrate that for a stationary state it is independent from time (from that the name stationary).

On the other hand, the general expression for the wave-packet describes a non-stationary state. The Heisenberg's uncertainty principle, in the time-energy form $\Delta E \times \Delta t \approx \hbar$, can be used to see the difference between these two kinds of states. After exciting it by a photon, a molecule is in a higher state with energy $E_n$ for sure only if $\Delta E = 0$. This means that the observer has to wait for an "infinite" time ($\Delta t = \infty$) to achieve it. This creates a stationary state. On the other hand, a non-stationary state is created if $\Delta t = 0$ (which implies $\Delta E = \infty$). The first case ($\Delta t = \infty$) corresponds to a frequency resolved spectroscopy, while the second one ($\Delta t = 0$) corresponds to a time resolved spectroscopy.[a]

[a] Infinite time means a time longer than the molecule proper time. This time is defined as the inverse of the difference between the frequencies of two close energetic levels. At the same time, infinite difference of energy means spreading over some energy levels. On the other hand, time zero means a very short period of time, in the order of femtoseconds.

Using these equations is possible to describe the behaviour of a molecule in time as an isolated system. It is possible to write a Hamiltonian formed by the, previously written, time-independent one, plus an interaction with the external environment depending on time, in the form of a potential of interaction:

$$\hat{H}(t) = \hat{H}_0 + \hat{V}(t) \tag{3–7}$$

As Dirac suggested, one can write the wave-packet analogously to $\Psi_0(t)$, where also the coefficients depend on time:

$$\left|\Psi(t)\right\rangle = \sum_n \left|n\right\rangle C_{nI}(t) e^{-i\omega_n t} \tag{3–8}$$

Considering the transition from the initial state $\left|I\right\rangle$ to the final state $\left|F\right\rangle$, one can write the probability of the transition as $P_{FI} = \left|C_{FI}(t)\right|^2$. Then, it is possible to define the interaction potential as $\hat{V}(t) = \hat{V}_0 e^{\mp i\omega t}$. In this case $\omega$ is the frequency of the incident radiation, and has not to be confused with the frequency proper of the molecule $\omega_{FI} = \omega_F - \omega_I = \frac{E_F - E_I}{\hbar}$. The minus sign is for absorption of the radiation, while the plus sign is for emission. Frequencies are responsible for the *condition of resonance*: $\omega = \omega_{FI} \geq 0$ means perfect absorbance, while $\omega = -\omega_{FI} = \omega_{IF} \geq 0$ means induced emission. With this model is not possible to describe the spontaneous

emission, for which a quantum mechanics treatment of the electro-magnetic field is needed, too. The probability of transition can be re-written has:

$$P_{FI}(t) = \frac{2\pi t}{\hbar^2}\left|\left\langle F\left|\hat{V}_0\right|I\right\rangle\right|^2 \delta(\omega \mp \omega_{FI}) \qquad (3\text{–}9)$$

that is know as the Fermi Golden Rule.[66]

The Dirac $\delta$ function is defined as: $\delta(\omega \mp \omega_{FI}) \equiv \lim_{\Gamma \to 0} \frac{\Gamma/\pi}{(\omega \mp \omega_{FI})^2 + \Gamma^2}$; the function vanishes unless its argument vanishes. It states that energy must be conserved during the interaction, that is only in resonance conditions one can have a transition from a state to another.

The matrix element gives the selection rules for the transition. Only if the external perturbation has the correct form to mix the two states, the transition will be permitted.

Another form of the rule can be given by defining the velocity of the transition, that is the number of molecules doing the transition in the unit of time, as the time derivative of the probability.

$$W_{FI}(t) = \frac{2\pi}{\hbar^2}\left|\left\langle F\left|\hat{V}_0\right|I\right\rangle\right|^2 \delta(\omega \mp \omega_{FI}) \qquad (3\text{–}10)$$

Till now, nothing as been said about the shape of the interaction potential. It can be defined as the interaction of an electro-magnetic field, represented by the electric field $\vec{E}$, and the molecular dipole $\vec{\mu}$: $\hat{V}(t) = -\vec{E} \cdot \vec{\mu}$. It is usually more common to use the versor $\vec{\varepsilon}$ of the electric field. Moreover, it is possible to give a complete "quantistic" description of the electric field by

using explicitly the number N of photons passing through a given cubic volume with side L. In this way it is possible to define the velocity of transition for the absorption as:

$$W_{FI}^{abs} = \frac{4\pi^2 N\omega}{\hbar L^3}\left|\left\langle F\left|\vec{\varepsilon}\cdot\vec{\mu}\right|I\right\rangle\right|^2 \delta(\omega-\omega_{FI}) \qquad (3\text{–}11)$$

Similarly the emission can be written as:

$$W_{FI}^{em} = \frac{4\pi^2 (N+1)\omega}{\hbar L^3}\left|\left\langle F\left|\vec{\varepsilon}\cdot\vec{\mu}\right|I\right\rangle\right|^2 \delta(\omega+\omega_{FI}) \qquad (3\text{–}12)$$

which describes both the stimulated (N) and the spontaneous (1) emission.
The transition is, then, permitted if both the radiation wave-length is equal to the energy difference of the two molecular states, and the integral is non-zero. The last condition is achieved by symmetry. These are called *dipolar rules*. For example, the rule for the spins states that a transition between states with the same spin (i.e. singlet-singlet) is permitted, with a resulting strong band, while a transition between states with a difference on spin of 1 (i.e. singlet-triplet) is permitted but results in a weak band. Transitions between states with a spin difference of more than 1 are prohibited. Emission between states with the same spin is commonly referred to as fluorescence, while emission between states with spin difference of 1 is referred to as phosphorescence.

## 3.2. Preparation and Detection of Non-Stationary States

There exists a large variety of spectroscopic techniques that employ ultrashort laser pulses.[67] These methods may differ, for example, in the detection mechanism, and will in general monitor different aspects of the dynamics of the molecular system. In pump-probe experiments the molecular system is prepared by a first laser pulse (the pump) into a non-stationary state; the time delayed second laser pulse (the probe) interrogates the subsequent time evolution of the system. Most part of the differentiation of the various techniques is about the nature of the probe. One can assume that at $t = 0$ the system has been excited by the first pulse into the non-stationary state $|\Psi_P\rangle$. In order to probe the dynamics of the excited-state wave function $|\Psi_P(t)\rangle = e^{-i\hat{H}_0 t/\hbar}|\Psi_P\rangle$, the second pulse is used to project the evolving state $|\Psi_P(t)\rangle$ onto a known final state $|\psi_f\rangle$ involved in the experiment. A major criterion to distinguish the probe mechanism is thus given by the kind of final states $|\psi_f\rangle$ involved in the experiment. Possible choices for the electronic part of $|\psi_f\rangle$ are the electronic ground state (through time-resolved fluorescence spectroscopy), higher-lying electronic states (through excited-state absorption), and the cationic ground state as well high Rydberg states (through pulsed ionisation with ion or photoelectron detection). Alternatively, one may measure transient infrared absorption or resonance-Raman spectra of the sample.

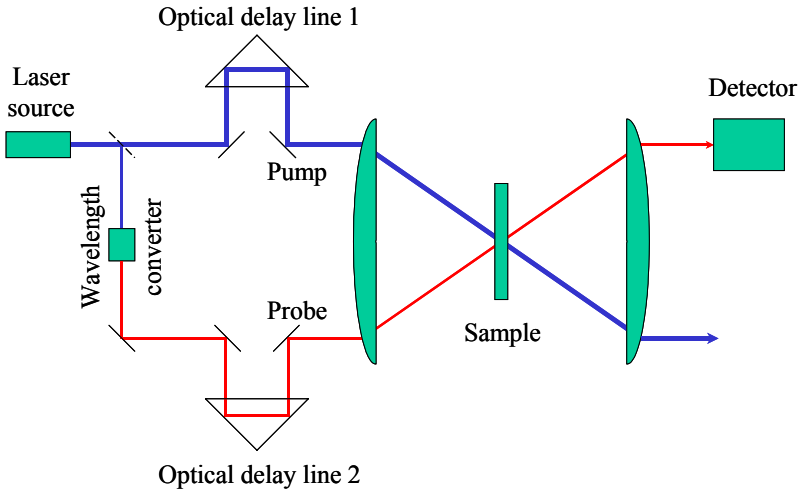


Figure 3–1: Typical pump-probe optical spectroscopy scheme.

In Figure 3–1 a typical pump-probe spectroscopy set-up is shown. A relatively strong pump beam is sent through an optical delay line and focused into the sample, where it starts some chemical reaction of interest. A fraction of the pump beam is split by an optical beamsplitter and converted to another wavelength. The probe pulse is then sent through another optical delay line and focused onto the sample. The modified pulse is then measured by some kind of detector and afterwards recorded. The signal is measured as function of the pump-probe pulses delay time.

In principle there is no difference in the information that can be obtained from a frequency resolved or a time resolved experiment. In a frequency resolved spectrum, a vibronic transition may show up as a series of sharp lines. In the equivalent time resolved experiment, one will observe quantum beats whose periods correspond to the inverse of the spacing between the

absorption lines. In practice, however, there may be differences. For example, even in the gas phase, the spacing between the absorption lines may be so small that it is hard to resolve them. More importantly, in the solution phase, the molecule under study will couple with the degrees of freedom of the surrounding bath. Strictly speaking, the Schrödinger equation for the liquid could be solved, which would show that the dynamics in the liquid, in fact, correspond to about $10^{24}$ well-defined quantum states. Most of these bath states will be coupled to the vibronic states in the molecule, resulting in the broadening of the transition. In such a case, a spectrally resolved experiment will provide little information about the dynamics of the molecule, or the dynamics of a chemical reaction that one would like to study. Only time resolved pump-probe techniques can elucidate the molecular dynamics. In the 1980s and 90s, a series of experiment were performed by a variety of groups, which came to be known as "femtochemistry" or "femtobiology".[68] *These experiments exploited the property that if a molecule is excited with a laser pulse shorter than the oscillation period of relevant vibrations in the molecule itself, a coherent vibrational wave packet is created in the excited state.*

The theoretical formalism used for interpretation of the time resolved data can be found in many reviews[69] covering various aspects. Mainly two different approaches are used, a perturbative and non-perturbative one. A more general view of the technique, along with its history, is given in the 1999 Nobel lecture by *Ahmed Zewail*.[70] This lecture has been used for the following paragraphs to describe some aspects of femtochemistry and the concept of coherence.

## 3.3. Pump-Probe "Femtoscopy"

In high-speed photography, a continuous motion is broken up into frames using a brief exposure time. For example, in *Edweard Muybridge*'s experiments in late years of the XIX century (Figure 3–2), the shutter speed (exposure time) was ~2 milliseconds and the speed of the motion was ~10 m/s, resulting in a well-defined resolution (speed x exposure time) of 2 cm; the number of frames per seconds was about twenty since the cameras were 0.5 m apart. After a century, a similar photographic technique has been used for special effects in movies, approaching 12000 frames per second (Figure 3–3).

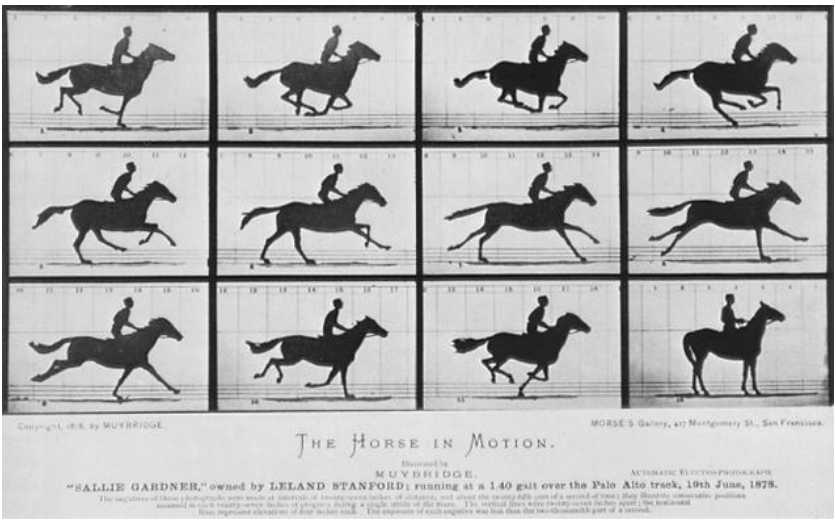


Figure 3–2: "The Horse in Motion" by Edweard Muybridge, 1878.[71]

Figure 3–3: Preparation for the "bullet-time" special effects for the movie "The Matrix", 1999.[72]

But this is nothing compared to what is needed to capture the motion of molecules. The huge contrast with molecular experiment is due to vast differences in speed (~1 km/s), resolution (~$10^{-8}$ cm) and the number (millions) of molecules involved. Given the molecular speed and resolution, the ultrashort strobes must provide exposure time on the order of 100 femtoseconds, and in one second $10^{13}$ frames could be recorded. Ultra fast pulsed laser technique have made direct exploration of this temporal realm a reality. Spectroscopy, mass spectrometry and diffraction play the role of ultra-high-speed photography in the investigation of molecular processes.

A femtosecond laser pulse provides the shutter speed for freezing nuclear motion with the necessary spatial resolution. The pulse probes the motion by stroboscopy, i.e. by pulsed illumination of the molecule in motion, and

recording or photographing the particular snapshot. A full sequence of the motion is achieved by using an accurately timed series of these probe pulses, defining the number of frames per seconds. This method of probing, although different from Muybridge's, is in principle equivalent to his use of the cameras (with shutters) as probes. For molecules there exist three additional requirements in order to study the motion. First, one needs to *clock the motion by defining its zero of time*, also accurate to tens of femtoseconds. Second, the *motion must be synchronised* since millions of molecules are typically used in the recording of molecular motion. Third, *molecular coherence must be induced to localize the nuclei*. These requirements are satisfied by using a femtosecond pump (initiating) laser pulse, in what is referred to as a *pump-probe configuration*.

With this methodology, the process to be studied is clocked from the instant that the substance under investigation absorbs radiation from the pump pulse. Passage of probe pulse through the sample at some time later provides a snapshot of the status of the system at that time. For femtosecond studies, where femtosecond control of relative timing is needed, the laser pump and probe pulses are produced in synchrony, then the probe pulse is diverted through an adjustable optical path length. The finite speed of light translates the difference in path length into a difference in arrival time of the two pulses at the sample: 1 μm corresponds to 3.3 fs. The individual snapshots combine to produce a complete record of the continuous time evolution in what may be termed femtoscopy.

## 3.4. Coherence and Atomic Motion

In a classical description, the motions of nuclei over a potential energy surface would be particle like, i.e. they would behave as "balls on a track". However, at the scale of atomic masses and energies, the quantum mechanical wave/particle duality of matter comes into play, and the notion of position and velocity common to classical systems must be applied cautiously and in accord with the uncertainty principle. In fact, the state of any material system is defined in quantum mechanics by spatially varying wave functions, with many similarities to light waves. Since the wave nature of light is a much more familiar concept that that of matter, it could be functional to use light to introduce the idea of wave superposition and interference, which plays an important role in atomic motion.

When light from two or more sources overlaps in space, the instantaneous field amplitudes (not intensities) from each source must be added together to produce the resultant light field. A well-known example is Young's two-slit experiment, in which light from a single source passes through two parallel slits in a screen to produce two phase-coherent fields of equal wavelength and amplitude. At points for which the distances from the two slits differ by n + ½ wavelengths (with n integer), the two waves add to zero at any time, and no light is seen. Elsewhere, the amplitudes do not cancel. Thus, a stationary pattern of light and dark interference fringes is produced. Knowledge of the wavelength of light and the spacing of fringes projected on a screen provide a measurement of the separation of the slits (Figure 3–4, inset). In x-ray diffraction such interference makes it possible to obtain molecular structures with atomic resolution: the atoms replace the slits.

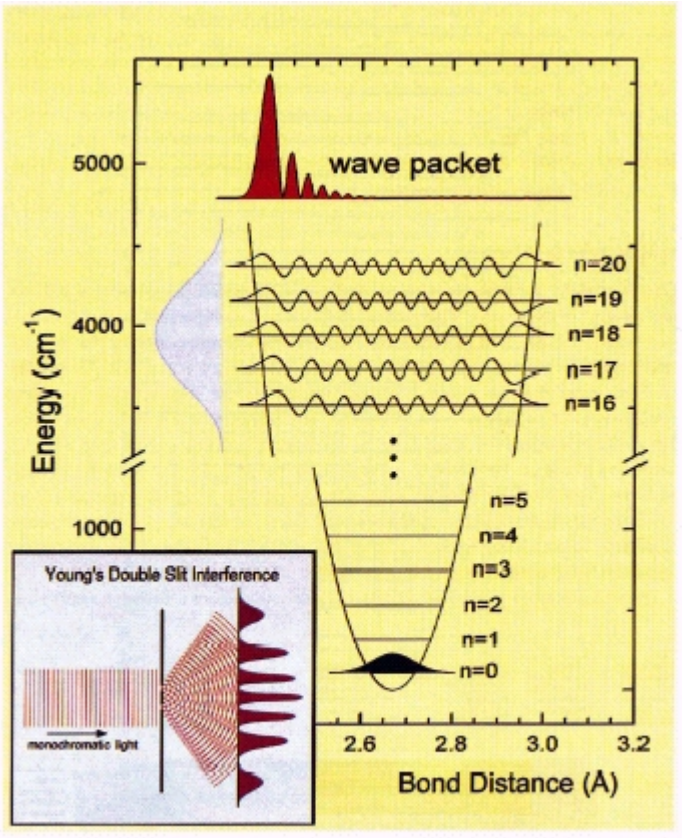


Figure 3–4: The wave packet and wave function limits for molecular system; this was calculated for the harmonic wave functions representing the vibrational states of a diatomic molecule, in the case iodine. The analogy with light interference, as in Thomas Young experiment (1801) is depicted in the inset. Adapted from ref. 70.

In studies of motion, the concept of coherence among molecular wave functions is used to achieve atomic-scale resolution of dynamics, that is the change of molecular structures with time. Molecular wave functions are spatially diffuse and exhibit no motion. Superposition of a number of separate wave functions of appropriately chosen phases can produce a spatially localized and moving coherent superposition state, referred to as a wave packet; constructive and destructive interference is the origin of spatial localization. *The packet has a well-defined velocity and position, which now makes it more resembling the classical ball, but at atomic resolution. The femtosecond light induces the coherence and makes it possible to reach atomic-scale spatial and temporal resolution, without violating the uncertainty principle.*

The Figure 3–4 shows a snapshot of the position probability (red) of a wave packet, formed from wave functions with n = 16 to 20 and with weighting according to the distribution curve at the left of the figure. It describes a non-stationary state: while time is well defined, the energy level's population is spread among various vibrational levels, following a gaussian-like distribution centred on n = 18.

The observation of motion in a real system requires not only the formation of localized wave packets in each molecule, but also a small spread in position among wave packets formed in the typically millions of molecules on which the measurement is performed. The key to achieve this condition is generally provided by (a) the well-defined initial equilibrium configuration of the studied molecule before excitation and (b) by the "instantaneous" femtosecond launching of the packet. The spatial confinement of the initial ground state of the system ensures that all molecules, each with is own coherence among the states (which form its wave packet), begin their motion

on the excited potential in a bond-distance-range much smaller than that executed by the motion. The femtosecond launching ensures that this narrow range of bond distance is maintained during the entire process of preparation. In this way, the motion is that of a classical single-molecule trajectory, unless the molecular and ensembles coherence are destroyed by intra- and/or inter-molecular perturbations.

# Chapter 4. Potential Energy Surfaces and their Exploration

This Chapter presents the basic concepts of Potential Energy Surfaces and their general features; this will be done in Sections 4.1 and 4.2. Later, Section 4.3 will present some tools for the exploration of Potential Energy Surfaces. Following Chapters will deal in depth on some peculiar aspects, about Surface Crossings (Chapter 5) and Reaction Paths (Chapter 6). At the end Chapter 7 will present the scheme for the general technique used in this work for the complete characterization of fundamental and excited states Potential Energy Surfaces.

## 4.1. Reaction Paths

A way to study a chemical reaction is that of calculating the reaction path of the process one is interested into.[73] The idea of reaction path derives, basically, from the *Born-Oppenheimer* approximation, which consists in considering the molecular nuclei movement not correlated with that of electrons (see Appendix). The approximation allows the fact that to each given nuclear geometry corresponds bi-univocally a value for the total electronic energy, which, in conjunction with the nuclear repulsion energy, gives the potential energy driving the nuclei movement (see also Appendix). The estimate of this energy for any possible disposition of nuclei let to define a Potential Energy Surface, PES. During a chemical reaction the molecular

structure evolves over this surface, by changing the relative position of nuclei.

The computation of an entire PES is a very hard task, and usually it is preferred to evaluate it only along some given sections, the most meaningful ones. Usually this sections are defined by a reference internal coordinate, which is called reaction coordinate. The reaction coordinate can be simple or composite; in the first case it can be represented by a single molecular movement, like an atom-atom stretching or a torsion along a dihedral angle. In the second case, it can be characterized by two concerted (e.g. a bending plus a stretching) or subsequent (e.g. a stretching followed by a torsion) movements.

One can imagine a potential energy surface like a landscape (Figure 4–1), where there are valleys (reagents, intermediates and products), passes between them (transition states, TS) and peaks. The roads going from one valley to another likely run along the passes with minimum difference in height with respect to the valley. As in the naive example, also chemical reactions take place with the minimum possible usage of energy. For this reason, it is useful to trace over the PES the paths connecting reagents and products, which involve the minimum energy difference along the path itself, with respect to the reagent/product valleys. These paths are called Minimum Energy Paths, MEP.[73-75]

Figure 4–1: Crete Senesi landscape, photo by L.D.V.

Given that a molecule with N atoms has 3N-6 (3N-5 if linear) possible vibrational coordinates, PES is an hypersurface of dimension 3N-6. Being this, the representation of the entire PES is impossible, apart from the special case of a diatomic molecule. Therefore, it is common to represent MEPs as a graph of the energy against the reaction coordinate, or a very significant (i.e. the most characterizing) internal coordinate. As it will be explained later in Section 4.3, the reaction coordinate is rigorously and univocally determined by the steepest descent path from a saddle point (see Section 4.2). A steepest decent path is build point by point following the local gradient direction.

## 4.2. Stationary Points: Minima and Transition States

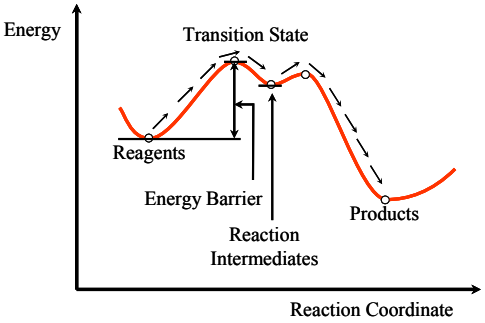


Scheme 4–1

Scheme 4–1 report a general view of the shape of a PES along the reaction coordinate; the most characteristic features are shown. First, minima on the potential energy surface represent, relatively, stable species. That means, reagents, products, and possible reaction intermediates. In between them, maxima of the curve represent the transition states of the reaction, non stable species, usually experimentally not characterizable, unless by using ultra fast time resolved spectroscopy (see Chapter 3). Both minima and maxima share one common feature, that is they have the first derivative of the energy with respect to the nuclear coordinates (i.e. the gradient) equal to zero. Hence, they are called stationary points. In a multi dimensional view, by using a quadratic approximation, a minimum can be visualized as the common vertex of 3N-6 parabolas, all of them having a positive second derivative (Scheme 4–2a). Besides, a transition state is characterized by parabolas, too, but some

of them have negative second derivative: saddle points. Based on the number of parabolas with negative second derivative (1, 2, 3 etc.) one can say saddle points of first, second, third order and so on. Anyway, the most common kind of transition state is the first order one. (Scheme 4–2b)

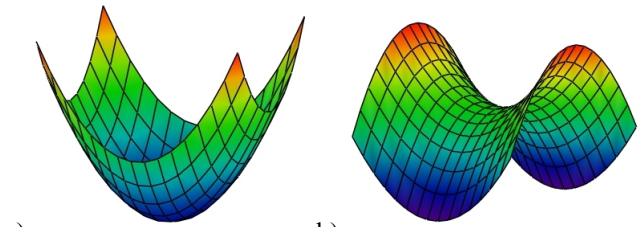

a) b)

Scheme 4–2

The difference in energy between minima and transition states represents the barrier that has to be overcome for a reaction to take place. As previously said, a first order transition state can be represented by 3N-7 parabolas with positive second derivative and only 1 with negative. The internal coordinate corresponding to this parabola is usually referred to as transition vector. The transition vector characterize the MEP in the transition state, that is it represents, locally, the movement needed to reach the reagents or products valley.

By locating the stationary points of a PES and connecting them through MEPs it is possible to describe all the possible behaviours of a chemical species, given that all the considered reactions take place on the electronic fundamental state, that is a thermal reaction. In Chapter 6 it will be described how to calculate a MEP.

## 4.3. Some Tools for Exploring Potential Energy Surfaces

The investigation of thermal reactions where only the ground electronic state is involved has become a standard practise since 1990s.[76] Indeed, modern computational tools provide a complete description of the path, which connects a transition structure to reactants and products, in a completely unbiased way. This is done by computing the *minimum energy path* (MEP)[73,75,77] along the reaction coordinate, which describes the progression of the reactant to the product through the transition state, on the 3N-6 dimensional PES of the system (N corresponds to the number of the atoms involved in the reaction mechanism).

The study of photochemical processes, where at least two electronic states are involved, each one represented by a single PES is still a difficult task. The main difficulty associated with such computations concerns the general shape of the excited state potential energy surfaces. Ground state potential energy surfaces contain only two relevant features: energy minima (reactants, products and intermediates) and saddle points (transition structures). Whereas minima and saddle points are also found in excited state potential energy surfaces, a novel feature characterizes the last ones. In fact, the photochemical reaction path is expected to have two branches; one located on the excited state and the other located on the ground state energy surface. Thus, it is very important to correctly define and compute the "funnel"[78] where the excited state reactant or intermediate is delivered to the ground

state. As will be introduced in Chapter 5, an excited state potential energy surfaces may cross the energy surface of the ground state or that of a different excited state leading to a *conical intersection* or to a *singlet-triplet crossing*.[78] Since the structure and location of these crossings play a fundamental role in determining certain excited state properties (e.g. the excited state lifetime and, as mentioned above, the photoproduct distribution) the search and characterization of these entities represent an important step in the mapping of the energy surface. However, while the computation of minima and saddle points can be carried out with standard gradient methods *the determination of crossing points requires special computational (non-conventional) tools and strategies*.

A second problem arises from the fact that the electronic configuration of excited state molecules may often present an open-shell character. A correct treatment of such systems requires a multireference wavefunction. As a consequence the type of *ab-initio quantum chemical methods required for excited state computations belong to the so-called post-SCF* methods[79] rather than the standard single-reference SCF wavefunction. These methodologies are based upon the *use of multi-reference wavefunctions* capable of describing states, which must be represented as mixture of different electronic configurations. For a review on quantum chemical methods see Appendix.

The Multiconfigurational Self-Consistent Field Theory (MC-SCF)[80,81] represents the method that has been used to carry out the theoretical investigation of the photochemical reactions presented in this thesis. The geometry optimization can be carried out with the MC-SCF method since first and second derivatives can be computed analytically. However MC-SCF

theory does not provide an adequate treatment of the electronic correlation. Thus, when using MC-SCF theory the aim is to obtain a qualitatively correct description of the PES topography. In order to improve the energetics obtained from the MC-SCF method, dynamic electron correlation must be taken into account. A treatment of dynamic electron correlation can be obtained by using the multireference MP2 method.

In recent years the CAS-SCF method[80,82] (i.e., a variant of the MCSCF method) has been extensively used for mapping excited state potential energy surfaces of organic compounds.[20] This method also provides the "natural" basis for the accurate evaluation of the excited state energetics. In fact, vertical and 0-0 excitation energies and ground and excited state energy barriers can be evaluated with just few kcal $mol^{-1}$ error by employing multireference methods, which require the multireference CAS-SCF wavefunction as the starting point. These are the multireference configuration interaction method (MR-CI[83]) and multireference perturbation theory methods (e.g. MR-MP2[84], CASPT2[85]).

In general there are two steps involved in the computation of a reaction path for an excited state system. The first step involves the evaluation, at a fixed molecular geometry, of the potential energy, its first derivatives (i.e. the *gradient* vector) and second derivatives (i.e. the *Hessian* matrix) with respect to all the 3N-6 internal coordinates of the molecule (i.e. bond lengths, bending angles and torsional angles). In the second step one evaluates the different “elements” forming a reaction path by using a series of complementary computational tools. These comprise: energy minima and saddle points, minimum energy paths and potential energy surface crossings.

In Figure 4–2 these features are illustrated in a model potential energy surfaces (where only two degrees of freedom are considered). Energy minima ($Min_1$ and $Min_2$), energy maxima (Max) and saddle points (TS) are known as *stationary point*. The nature of stationary points is determined by the fact that the first derivatives with respect to all of the internal coordinates must be zero (i.e., the gradient vector must have zero length); this means that all of the forces (proportional to the opposite of the gradient) on the atoms in a molecule are zero, and therefore the system is at a stable geometry. To locate stationary points one can use the standard tools for *geometry optimisation*[76,77,86], which search for these points on the PES, starting from an initial guess geometry. The gradient vector and the second derivative matrix (Hessian) are computed and used within a *Newton-Raphson* method for the search of minimum and transition structures.

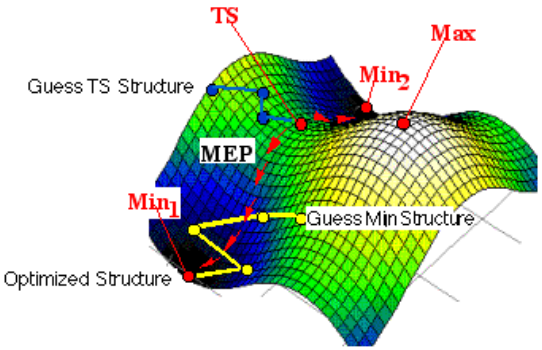


Figure 4–2: Model potential energy surface showing a maximum or peak (**Max**), and two minima (**Min1**, **Min2**) connected by a transition state **TS**. The blue and yellow lines correspond to Newton-Raphson type optimizations. The MEP describing the reaction path is indicated by a stream of arrows. The open circles and full circles indicate the "iterations" required to locate a minimum (**Min1**) and a transition structure (**TS**) respectively.

The eigenvalues of the Hessian give conclusive information concerning the nature (minimum, transition state, second order saddle point) of the located stationary points, while they represent the curvature of the PES along each mode. Vibrational frequencies, readily obtained by diagonalizing a mass-weighted force constant matrix (vibrational frequencies of the molecule are proportional to the square root of the Hessian eigenvalues), and the corresponding vibrational eigenvectors can be further used to evaluate related physical properties. Thus, if all the eigenvalues are positive or, equivalently, all frequencies are real, the point is a local minimum and it is located at the bottom of a valley of the potential surface. Contrary, a local *maximum* (also called a peak) is a point with all the eigenvalues negative, i.e. all the

vibrational frequencies are imaginary. If only one eigenvalue is negative and all the rest are positive, the point is a (first-order) saddle point: it is a maximum in one direction and a minimum in all the other (perpendicular) directions. In this case the associated frequency is imaginary, which is unphysical, but can give an idea of the shape of the transition state. For example, a high absolute value of the negative eigenvalue means that the TS is very sharp, and likely not easily accessible. On the other hand, a low absolute value of the eigenvalue can be interpreted as a smoothed transition state, likely easily reached. Transition structures are first-order saddle points. The eigenvector associated to the negative eigenvalue must indicate the direction, which connects the correct reactant and product minima. This is usually referred to as transition vector. A *n*th order saddle point has *n* negative eigenvalues, *i.e.* is a maximum with respect to *n* mutually perpendicular directions.

The concept of a PES allows one to deal with chemical structures and reaction mechanisms. The equilibrium geometry of a molecule corresponds to a minimum on the potential energy surface. If there is more than one minimum on a contiguous energy surface, several paths can be constructed that connect one minimum to the other. One way of finding the reaction path is to follow the steepest descent path from the first-order saddle point to the minima by moving along the eigenvector corresponding to the negative eigenvalue of the saddle point (termed as the transition vector). *However, it should be stressed that the steepest descent path depends on the particular choice of coordinate system.* For example, Cartesian coordinates would yield a different path from internal coordinates. Nevertheless, it is possible to define an intrinsic reaction path independently of the coordinate system by

*appealing to classical mechanics*. For a given energy surface, the movement of a classical particle must be the same regardless of whether the Cartesian coordinates are used or any of a number of different sets of internal coordinates are used. *The intrinsic reaction coordinate (**IRC**) method*[87] *can be defined as the path traced out by a classical particle sliding with an infinitesimal velocity from a saddle point down to each of the minima.* Since the classical equations of motion can be defined in any coordinate system, and since they must yield the same trajectory, this definition of IRC is unique. The classical equations of motion are simplest in mass-weighted Cartesian coordinates, where the effective mass for each coordinate is unity. In this coordinate system, the IRC is the same as the steepest descent path. The line of steepest descent in mass-weighted coordinates which connects a first-order saddle point (TS) to two minima ($Min_1$ and $Min_2$) is the minimum energy path (*MEP*) (see Figure 4–3). A MEP can be computed using standard computational tools.

A peculiarity of excited state paths (see the two dimensional model surface in Figure 4–3) is that they do not start at an energy minimum but at a non stationary point (e.g. FC point) where the system is deposited after vertical excitation. The reaction path describing the relaxation process from this point ($IRD_1$ from FC to $MIN_1$ in Figure 4–3) may be determined by the initial relaxation direction (IRD) method (the procedure required to perform this computation will be discussed in Section 6.1.1). The same tool may be used to locate the directions or relaxations on the ground state potential energy surface that originate at the vertex of the conical intersection ($IRD_2$ and $IRD_3$ in Figure 4–3). This procedure will be introduced in Section 6.2.1.

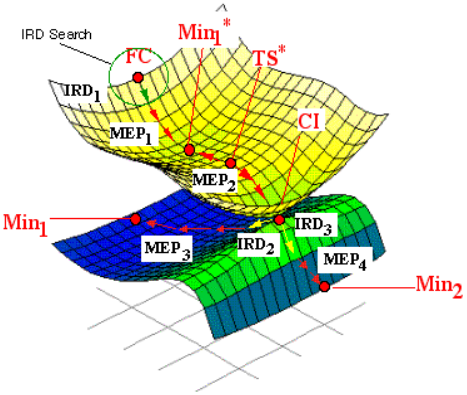


Figure 4–3: Model intersecting potential energy surfaces showing an excited state minimum (**$Min_1$***), transition state (**TS***) and a conical intersection (**CI**). The composite excited state MEP (i.e. **$MEP_1$**, **$MEP_2$**) and initial direction of relaxation from the FC point (**$IRD_1$**) are indicated by stream of arrows. The ground state initial directions of relaxation (**$IRD_2$** and **$IRD_3$**) starting at **CI** are indicated by arrows.

As said before, the most relevant mechanistic elements in a photochemical process are conical intersections and singlet/triplet crossings. A computational method for the location of such crossings and a strategy to relate them to the other features (i.e., minima and transition states) of the ground and excited state surfaces are required. The last optimised point of the MEP connecting $Min_1$ to the conical intersection (CI) may be taken as a representative point for the conical intersection geometry. This, however, might not correspond to the lowest energy intersection point. There are situations where there is no transition state connecting $Min_1$ to the intersection point or where an excited state intermediate on the upper energy

surface does not exist. In such situations, mechanistic information must be obtained by locating the lowest lying intersection point along the (n-2)-intersection space of the molecule. A computational method that allow for the minimum energy computation of the molecular structure of a real crossing is referred here as the conical intersection optimiser (**CIO**)[88,89] (the procedure will be illustrated in Section 5.3.1). A **CIO** calculation starts at suitable guess geometry. After a point of crossing has been located the optimization proceeds by following, roughly, the crossing intersection space or singlet/triplet seam in the downhill direction until an energy minimum has been reached.

Summarizing, the computational tools to investigate, theoretically, photochemical mechanisms comprise: (1) suitable *ab initio* methods to accurately compute the excited state electronic energy, (2) standard and non standard optimization procedures to determine the molecular structure of stationary points (minima, transition states) and low-lying surface crossings, and (3) methods to construct excited state reaction paths and ground state relaxation paths in terms of MEP.

# Chapter 5. Potential Energy Surface Crossings

## 5.1. Excites States: Concepts and Nature of the Photochemical Funnel

A big part of chemical reactions takes place following the absorption of a photon of light, that promotes a molecule from its fundamental state to an electronically excited one. This process has been partially treated theoretically in Chapter 3. The study of the possible routes that a molecule can take after photoexcitation is studied by photochemistry, and are called photochemical reactions, or photoreactions.

### 5.1.1. Ground and excited states pathways

As said, a photochemical reaction starts with the absorption of a photon of light that produces a change in the distribution of the electrons of the molecule. After the photoexcitation, the reactant molecule begins to relax on the *excited state potential energy surface* (PES). While, as seen, a thermal reaction is governed by the topography of a single potential energy surface (starts and ends on the ground state of the reacting system), a photochemical reaction evolves at least on two potential energy surfaces.

The mechanistic pathways for a singlet photochemical transformation involving two potential energy surfaces, the ground ($S_0$) and excited state ($S_1$) surfaces are schematically illustrated in Figure 5–1.

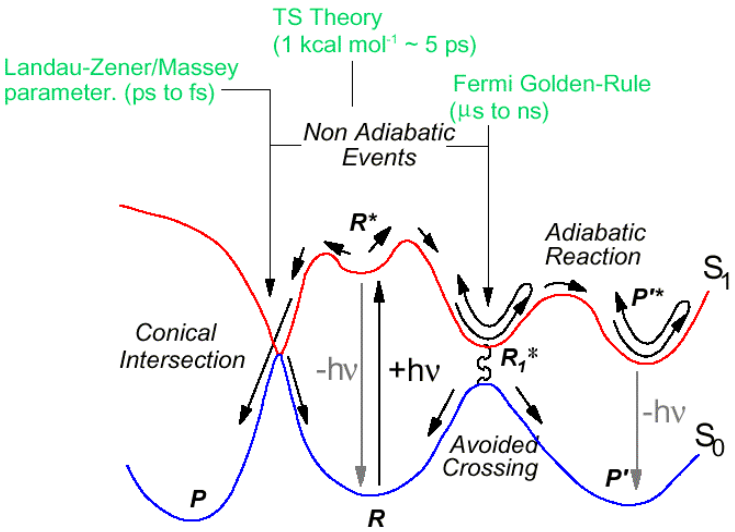


Figure 5–1: Schematic representation of the interplay between ground ($S_0$) and excited state ($S_1$) potential energy surfaces in a singlet photochemical reaction.

The absorption of a photon promotes the reactant R to the Frank-Condon (FC) region of the excited state PES, where the molecule has the same geometry of the ground state (Frank-Condon principle). Since at FC the shape of the PES is usually highly sloped the initial molecular structure becomes unstable and begins to distort toward a lower energy region of the surface which may correspond to an excited state intermediate or species R*.

The system can then return to the ground state via a radiative decay (fluorescence) from the excited state energy minima R*, or evolve on the excited state in a photochemical reaction. Regardless of the specific kind of excited state evolution, the photoexcited system will ultimately decay back to the ground state prompting the final evolution along one or more distinct pathways leading to stable (ground state) structures.

### 5.1.2. Avoided and real surface crossings

Thus the critical event in photochemistry is the non-radiative decay from the excited to the ground state. Non-radiative decays were traditionally assumed to occur at avoided crossing minima. This classical view of singlet photochemical reaction is mainly due to the 1969 computational work of *Van der Lugt* and *Oosteroff*[90] (Figure 5–2a). At such an avoided crossing, if the energy gap is larger than 1-2 kcal $mol^{-1}$, $R_1$* will rapidly thermalize and the decay probability will be determined by the *Fermi Golden Rule* (See Section 3.1). However, within this model, the probability of decay should be very small unless the energy gap is small and the radiationless decay process should occur on the same time scale as fluorescence.

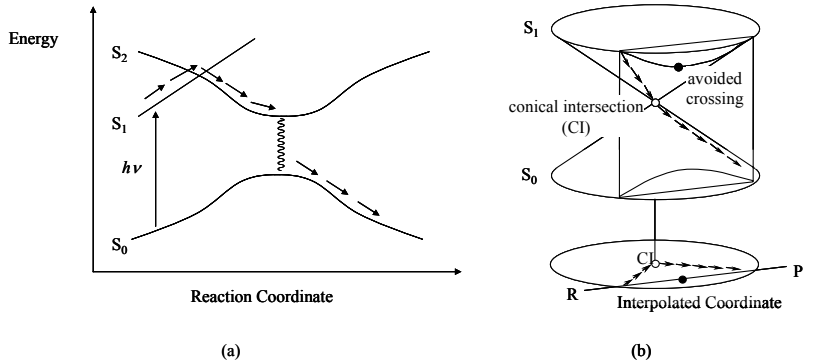


Figure 5–2: (a) Schematic illustration of the Van der Lugt and Oosteroff model of the photochemical funnel. (b) Topological relation between an avoided crossing and a real crossing (conical intersection).

On the other hand, it is well known that many photochemical processes are extremely fast (well below 1 picosecond,[50,82] i.e. on the timescale of a single molecular vibration) and associated with a complete lack of fluorescence. Furthermore, they are often stereospecific, implying a concerted mechanism.[91] Indeed, femtosecond excited state lifetimes have been observed, for instance, for simple dienes,[82] cyclohexadienes,[82,92,93] hexatrienes,[94] and in both free[95] and opsin-bound[96] retinal protonated Schiff bases.

These observations suggest that a real crossing is accessible to the system. At such surface crossing the probability of decay is very high and the corresponding molecular structure is referred as photochemical "funnel" to suggest that the excited reactant must be "funnelled" through this point to initiate product formation.

A funnel corresponds to a molecular structure that lives for only few femtoseconds ($10^{-15}$ seconds). Between 1966 and 1974 *Zimmerman*,[97]

*Michl*[98,99] and *Salem*[100] were the first to propose, independently, that for a broad class of organic reactions the structure of the funnel could be determined by locating a "cone shaped" crossing of the excited and ground state (potential) energy surfaces, known as conical intersection (CI).

The nature and the importance of the photochemical funnel has been a subject of research for at least three decades. The history of conical intersection goes back to decades ago when, in 1937,[101] at the 20th Farkas Memorial Symposium the physicist *Edward Teller* suggested that the electronic factors may play the dominant role in the efficiency of radiationless decay. Teller made two general observations:

i) In a polyatomic molecule the non-crossing rule, which is rigorously valid for diatomics, fails and two electronic states, even if they have the same symmetry, are allowed to cross at a conical intersection.

ii) Radiationless decay from the upper to the lower intersecting state occurs within a single vibrational period when the system "travels" in the vicinity of such intersection points.

On the basis of these observations, Teller proposed that conical intersections may provide a common and very fast decay channel from the lowest excited states of polyatomics, which would explain the lack of fluorescence of the funnel.

In the field of organic photochemistry, Zimmerman[97] and Michl[99] were the first to suggest, independently, that certain photoproducts originate from internal conversion at a conical intersection. Michl and collaborators[102] documented such features in *ab initio* calculations on the $H_4$ model. On the other hand, Salem's diagrams[100,103] illustrated the occurrence of conical intersections at symmetric geometries in the photochemistry of carbonyl compounds.

Subsequently, geometries of symmetry-imposed conical intersections were computed for Schiff base syn-anti isomerization by *Bonacic-Koutecky* and Michl[104], using *ab initio* procedures, and the "3x3" model of biradicaloid electronic structure[99,105] was elaborated to permit qualitative prediction of geometries at which $S_1/S_0$ conical intersections take place.[106,107] *Yarkony*[108] and *Ruedenberg*[109] identified conical intersections geometries in small molecules.

Despite the fact that the idea of Teller, Zimmerman and Michl represented an important refinement of the avoided crossing model,[90,110] *conical intersections were thought to be extremely rare or inaccessible* (i.e. located too high in energy) in organic compounds and thus were disregarded. The main difficult has to be ascribed to the fact that, in practice, *excited state quantum chemical computations require non-conventional methodologies and strategies* based upon the *use of multi-reference wavefunctions*. (i.e., *the so called post-SCF* methods) rather than the standard single-reference SCF wavefunction. For this reason excited state computations were not routinely used by chemists.

### 5.1.3. The *ab initio* quantum chemical improvement

At the end of the 80's improved *ab initio* quantum chemical methodologies became available (see Appendix) which were suitable for computing, in a balanced way, excited and ground state potential energy surfaces. In particular the *ab initio* MC-SCF method had an analytical gradient which could be employed for efficient geometry optimisation (the search for the structure corresponding to energy minima and transition states) taking into

account the complete set of the 3N-6 nuclear degrees of freedom of the reacting system (N is the number of atoms). With this new methodology it was possible to overcome the limitations (i.e. symmetry constraints and predefined reaction coordinate) of the Van der Lugt[90] and *Devaquet* calculations[110]. These limitations mainly regarded the computation of the excited state reaction path that was assumed to correspond to an interpolation between the reactant and the product structure. With the new tools one could determine available real excited state reaction path where the reaction coordinates is not assumed but computed in an unbiased way. In Figure 5–2b it is shown the relation between an avoided crossing and the double cone topology of a real conical intersection. In two dimensions, the Van der Lugt and Oosteroff model is refined by replacing the "avoided crossing" with an "unavoided crossing", i.e., a conical intersection. In other words, the Van der Lugt and Oosteroff model reaction avoided crossing path R → P is replaced by a path involving a real surface crossing R → CI → P.
A first application[111] of the *ab initio* MC-SCF method developed by *Robb* in 1990 to the photoinduced cycloaddition of two ethylene molecules showed that:

i) A conical intersection exists right at the bottom of the excited state energy surface.
ii) The molecular structure of the conical intersection is related to the observed photoproducts and stereochemistry of the reaction.

The original idea of Teller, Zimmerman and Michl has been fully supported by further computational works,[112-120] which definitely demonstrated, when taken in conjunction with modern experimental results, that the radiationless

decay process occurs via a conical intersection between excited and ground states. Radiationless decay at a conical intersection implies that:

i) The internal conversion process will be 100% efficient (*i*.e. the Landau-Zener[121] decay probability will be unity)
ii) Any observed retardation in the internal conversion or reaction rate (*i.e*. the competition with fluorescence) must reflect the presence of some excited state energy barrier which separates M* from the intersection structure and
iii) In the case where the decay leads to a chemical reaction, the molecular structure at the intersection must be related to the structure of the photoproducts.

Points i-iii provide the theoretical basis for the computational modelling of photochemical reactions. Therefore, conical intersections could, contrary to common belief, be frequent (if not ubiquitous) in organic systems and they may constitute the photochemically relevant decay channel.

### 5.1.4. Why crossing points are called conical intersections?

It is now useful to clarify why such crossing points are called *conical intersections* and whether such intersections *ever* occur in polyatomic systems.

In diatomic molecules the PES of two states (*e*.g. the ground state and the first excited state) will only intersect if the states have a different (spatial or

spin) symmetry. However, an analogous statement is *not true* for polyatomic systems:[101,122] *two PES of a polyatomic molecule can in principle intersect even if they belong to states of the same symmetry and spin multiplicity*.

It is possible to try to give a quantitative analysis of this situation.[123] Supposing all but two of the solutions of the Schrödinger equation for the electronic wavefunction have been found, and that $\phi_1$ and $\phi_2$ are any two functions that, together with the known solutions, constitute a complete orthonormal set. Of course the two missing solutions correspond to the two states (whose energy are $E_1$ and $E_2$) whose crossings one is interested in. Then it must be possible to express each of the two remaining electronic eigenfunctions (which describes the states one wants to examine) in the form

$$\Psi = c_1\phi_1 + c_2\phi_2 \tag{5–1}$$

The well-known secular eigenvalue equation is obviously expressed as:

$$\begin{bmatrix} H_{11}-E & H_{12} \\ H_{21} & H_{22}-E \end{bmatrix}\begin{bmatrix} c_1 \\ c_2 \end{bmatrix} = 0 \tag{5–2}$$

and after very simple passages one can write the expressions for the energies $E_1$ and $E_2$ of the two states as

$$\begin{aligned} E_1 &= \tfrac{1}{2}\left[ (H_{11}+H_{22}) - \sqrt{(H_{11}+H_{22})^2 + 4H_{12}^2} \right] \\ E_2 &= \tfrac{1}{2}\left[ (H_{11}+H_{22}) + \sqrt{(H_{11}+H_{22})^2 + 4H_{12}^2} \right] \end{aligned} \tag{5–3}$$

where, for the matrix elements:

$$\begin{aligned} H_{11} &= \langle \phi_1 | H | \phi_1 \rangle \\ H_{22} &= \langle \phi_2 | H | \phi_2 \rangle \\ H_{12} &= \langle \phi_1 | H | \phi_2 \rangle = H_{21} \end{aligned} \qquad (5\text{–}4)$$

Thus, in order to have degenerate solutions (i.e., an unavoided crossing), the discriminant must vanish and it is necessary to satisfy two independent conditions:

$$\begin{aligned} H_{11} &= H_{22} \\ H_{12} &= H_{21} = 0 \end{aligned} \qquad (5\text{–}5)$$

and this *requires the existence of at least two independently variable nuclear coordinates*. In a diatomic molecule there is only one variable coordinate, the interatomic distance, so the non-crossing rule follows: for states of different (spatial or spin) symmetry, $H_{12}$ is always zero and the two surfaces cross when $H_{11} = H_{22}$; this is possible for a suitable value of the single variable coordinate. Otherwise, if the two states have the same symmetry, they will not intersect.

However in a system of three or more atoms there are enough degrees of freedom for the rule to break down: the two conditions (see Equation 5–5) can be simultaneously satisfied by choosing suitable values for two independent variables, while the other $n$-2 degrees of freedom ($n = 3N$-6) are free to be varied without leaving the crossing region.

If one denotes the two independent coordinates by $x_1$ and $x_2$, and takes the origin at the point where $H_{11} = H_{22}$ and $H_{12} = H_{21} = 0$, the secular equations may be cast in the form

$$\begin{bmatrix} W + h_1 x_1 - E & l x_2 \\ l x_2 & W + h_2 x_1 - E \end{bmatrix} \begin{bmatrix} c_1 \\ c_2 \end{bmatrix} = 0 \qquad (5\text{–}6)$$

(i.e., $H_{11} = W + h_1 x_1$, etc.) or

$$\begin{bmatrix} W + (m+k) x_1 - E & l x_2 \\ l x_2 & W + (m-k) x_1 - E \end{bmatrix} \begin{bmatrix} c_1 \\ c_2 \end{bmatrix} = 0 \qquad (5\text{–}7)$$

where $m = \frac{1}{2}(h_1 + h_2)$ and $k = \frac{1}{2}(h_1 - h_2)$. The eigenvalues are

$$E = W + m x_1 \pm \sqrt{k^2 x_1^2 + l^2 x_2^2} \qquad (5\text{–}8)$$

and this is the equation of an elliptic *double cone* (i.e., with different axes) with vertex at the origin (it will be a circular cone for the case k=l) (see Figure 5–3). Hence the crossing points are called *conical intersections*. Indeed, if one plots the energies of the two intersecting states against the two internal coordinates $x_1$ and $x_2$ (whose values at the origin satisfy the two conditions $H_{11} = H_{22}$ and $H_{12} = H_{21} = 0$) obtains a typical double cone shape (see Figure 5–3a). The $x_1$ and $x_2$ coordinates are referred to as the "*branching space"* and the (n-2)-dimensional subspace of the n nuclear

coordinates is called the *intersection space*, an hyperline consisting of an infinite number of conical intersection points (see inset in Figure 5–3b).

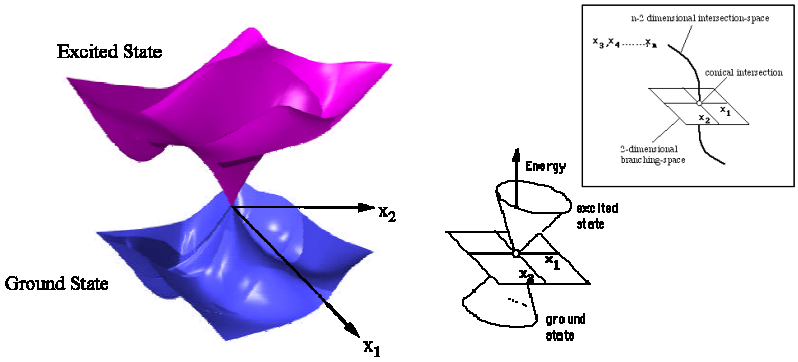


(a) (b)

Figure 5–3: (a) Representation of the typical double-cone topology for a conical intersection. (b) Relation between the "branching space" and the "intersection space".

If one moves in the *branching space* the degeneracy is lifted. Contrarily, if one move from the apex of the cone along any of the remaining n-2 internal co-ordinates defining the intersection space, the degeneracy is not lifted
Locally the co-ordinate $x_1$ is the gradient difference vector

$$x_1 = \frac{\partial(E_1 - E_2)}{\partial Q} \qquad (5–9)$$

while $x_2$ is the gradient of the interstate coupling vector

$$x_2 = \left\langle C_1^t \left| \frac{\partial H}{\partial Q} \right| C_2 \right\rangle \qquad (5\text{–}10)$$

where $C_1$ and $C_2$ are the configuration interaction (*CI*) eigenvectors in a CI problem and $H$ is the CI Hamiltonian and $Q$ represents the nuclear configuration vector of the system. The vector $x_2$ is parallel to the non-adiabatic coupling one:

$$g(Q) = \left\langle C_1^t \left| \frac{\partial C_2}{\partial Q} \right\rangle = \frac{\left\langle C_1^t \left| \frac{\partial H}{\partial Q} \right| C_2 \right\rangle}{E_1 - E_2} \qquad (5\text{–}11)$$

The vector $g(Q)$ is the coupling term that gives the magnitude of the coupling between the Born-Oppenheimer states described by $C_1$ and $C_2$ as a function of the nuclear motion along $Q$. If the intersecting potential energy surfaces have different spin multiplicity then $x_2$ is zero. Thus, a singlet-triplet crossing occurs along a (n-1)-dimensional intersection space (Figure 5–4a). In this case the branching space is one-dimensional and corresponds to the gradient difference vector $x_1$. Thus, different topological situations are possible for unavoided crossings between surfaces. One can have also intersections between two triplets (and one has an n-2 dimensional conical intersection hyperline in this case). In this last case the crossing is between two states of same spin multiplicity, similarly to the crossing of two singlet surfaces. There are situations where both types of intersection occur at the same geometry [118] (Figure 5–4b).

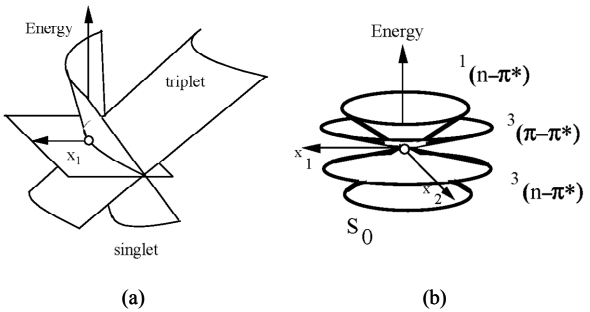


Figure 5–4: Topological possibilities for the crossing of two states: (a) (n-1)-dimensional intersection between two states of different spin multiplicity (i.e., singlet and triplet). (b) singlet and triplet conical intersection occurring at the same geometry.

### 5.1.5. Surface crossing and photochemical reactivity

To understand the relationship between the surface crossing and photochemical reactivity, it is useful to draw a parallel between the role of a transition state in thermal reactivity and that of a conical intersection in photochemical reactivity.[20] In a thermal reaction, the transition state (TS) forms a bottleneck through which the reaction must pass on its way from reactants (R) to products (P) (Figure 5–5a). The motion through the TS is described by a single vector, the transition vector $x_1$ (i.e., the eigenvector related to the imaginary vibrational frequency). A transition state separates the reactant and product energy wells along the reaction path. An accessible conical intersection (CI) (Figure 5–5b) also forms a bottleneck that separates

the excited state branch of the reaction path from the ground state branch. The crucial difference between conical intersections and transition states is that, whereas the transition state must connect the reactant energy well to a *single* product well via a single reaction path, an intersection is a "*spike*" on the ground state energy surface. The CI may connect the excited state reactant to two or more products (P and $P_1$) on the ground state via a branching of the excited reaction path (in the plane $x_1$ and $x_2$) into different ground state relaxation valleys. The nature of the products generated following decay at a surface crossing will depend on the ground state valleys (relaxation paths) that can be accessed from that particular structure.[21]

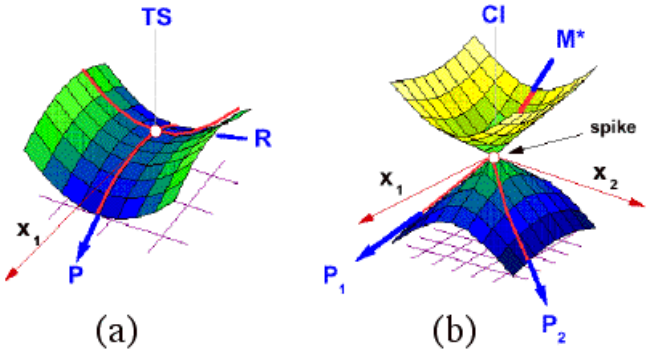


Figure 5–5: Comparison of a transition state (TS) (a) and a conical intersection (CI) (b) in photochemical reactivity

### 5.1.6. Physical meaning of the crossing conditions

The physical meaning of the two conditions $H_{11} = H_{22}$ and $H_{12} = H_{21} = 0$ will now be discussed. $\phi_1$ and $\phi_2$ of the secular equation (see Equation 5–2) correspond to the *diabatic* components of the *adiabatic* electronic eigenfunction (a diabatic function describes the energy of a particular spin-coupling or atomic orbital occupancies,[124] while the adiabatic function represents the surface of the real state), the crossing condition (real or avoided) is fulfilled when the two diabatic components $\phi_1$ and $\phi_2$ cross each other, and this happens when $H_{11} = H_{22}$, that is when the energy of the two diabatic potentials ( $H_{11}$ is the energy for the diabatic function $\phi_1$ and $H_{22}$ is the energy for the diabatic function $\phi_2$ ) is the same.

At the crossing of the diabatic functions ( $H_{11} = H_{22}$ ), the expressions for the energies of the two real states (see Equation 5–3) become

$$\begin{aligned} E_1 &= H_{11} - H_{12} \\ E_2 &= H_{11} + H_{12} \end{aligned} \qquad (5\text{–}12)$$

and the energy gap between the two real states is

$$E_2 - E_1 = 2H_{12} \qquad (5\text{–}13)$$

Thus, if the off-diagonal (resonance) term $H_{12}$ is *not zero*, the crossing will be avoided and the potential surfaces of the two real states will "split", being one of the two energies lower and the other higher then the diabatic energy

$H_{11}$. Moreover, the value of the exchange term $H_{12}$ determines how deep the avoided crossing minimum is (small values will generate deep minima, big values shallow minima). The energy separation at an avoided crossing thus depends on the magnitude of $H_{12}$. $H_{12}$ will be zero (and the crossings will be unavoided, i.e., real) when the two electronic states have a different (spatial or spin) symmetry. However, $H_{12}$ is not generally zero for states of the same symmetry (which will generate avoided crossings). Anyway, as seen above, this rule is true only for diatomic molecules and in a polyatomic system one can always have unavoided (i.e., real) crossings for suitable values of a pair of independent co-ordinates ($x_1$ and $x_2$), which will simultaneously satisfy Equation 5–5.

In conclusion the following statement is true: *for a polyatomic system two states (even with the same symmetry) will intersect along a n-2 dimensional hyperline (i.e., a line in more than three dimensions) when the energy is plotted against the n internal nuclear coordinates*.

### 5.1.7. A Valence-Bond point of view on real crossings

As discussed elsewhere,[125] it is possible to explain the origin of surface crossings using also simple VB arguments. Consider the ground and excited state potential energy surfaces for $H_3$. These surfaces can be well represented by the well know London formula for a triatomic:

$$E = Q \pm \sqrt{(K_a - K_b)^2 + (K_a - K_c)^2 + (K_b - K_c)^2} \qquad (5\text{–}14)$$

where $Q$ is the coulomb energy and the $K_a$, $K_b$ and $K_c$ are defined in terms of the two centres exchange integrals as

$$\begin{aligned} K_a &= K_{12} \\ K_b &= K_{23} \\ K_c &= K_{13} \end{aligned} \qquad (5\text{–}15)$$

The two centres exchange integrals $K_c$ involving pairs of non-orthogonal active orbitals i and j that occur in the London formula have the same interpretation as those that occur in the Heitler-London treatment of $H_2$ and can be written as

$$K_{ij} = [ij \mid ij] + 2S_{ij}\langle i|h|j\rangle \qquad (5\text{–}16)$$

The $[ij \mid ij]$ is the usual direct two-electron exchange repulsion integral, $\langle i|h|j\rangle$ is the one-electron exchange integral (kinetic plus nuclear electron attraction) and $S_{ij}$ is the overlap integral between orbitals $i$ and $j$. The exchange integral $K_{ij}$ has a simple unpredictable behaviour because it is dominated by the overlap ( $S_{ij}$ ) factor in Equation 5–16. The important point is that the $K_{ij}$ 's are proportional to the overlaps of the H1s orbitals and those depend on the $H_i$-$H_j$ distances.

Clearly, the square root vanishes in Equation 5–14 when the geometry is that of an equilateral triangle. For $H_3$ there are only three geometric variables, so the intersection space is a line consisting of all equilateral triangle geometries

where the energies of the ground and excited state are degenerated ( $E = Q$ ) along this line. Furthermore, the minimum energy point on this line is well defined. It is clear when the 3H atoms are replaced by three different one-electron atoms on the centres A, B and C one can find geometries where the square root vanishes in the absence of any symmetry.

## 5.2. Photochemistry and Photophysics Mediated by Conical Intersection Funnels

"Nowadays, it appears clear that conical intersections are a common feature in most non adiabatic singlet photoreactions. Recently, real conical intersections have been located by means of ab initio calculations for a large variety of photoreactions".[78] "Direct laboratory observation of conical intersections on the potential energy surfaces of polyatomic molecules is difficult, since they are not stationary 'points'. Their presence is surmised from the following data:[78,126,127]

- very rapid (sub-picosecond) decay of electronically excited states;
- lack of fluorescence;
- rapid formation of products.

In particular, ultrafast experiments, such as those reported in references [78,126] are readily interpreted in terms of conical intersections."

It appears evident from the previous citations, directly taken from journal articles, that a key mechanistic element of singlet photochemical reaction paths is a conical intersection *photochemical funnel.* This is the point where,

after excited state evolution, the reactant decays to the ground state and triggers photoproduct formation.

Modern laser experimental techniques,[128] femtosecond time-resolved spectroscopy (see Chapter 3), have enabled researcher to provide information on the structure and energetics of the excited state potential energy surfaces controlling fast decay. More traditional photochemistry, such as quantum yield measurements, provides information on the molecular structure of the decay channel and on the product formation paths. Thus, the detailed characterisation of the stereo- and regio-chemistry of the primary photoproducts and transient intermediates, their quantum yields and the effect of specifically designed sterically and rotationally hindered reactants on these quantities[129] is now possible. An important statement following the published results on this subject is that the observed stereoselectivity and photoproduct distribution of a photochemical organic reaction must depend on either:

- the funnel molecular structure;
- the existence of chemically or stereochemically distinct competing paths, *i.*e. funnels, on the excited state energy surface;
- the reaction path branching, *i.*e. the competing ground state relaxation paths, at a specific funnel.

### 5.2.1. A bit of history

In 1992 *Olivucci* and *Bernardi* in Bologna and Robb in London started a long-term computational project (see ref. 20 and 130 and references therein) to prove the general validity of the hypothesis supporting the existence of low-lying conical intersections in organic molecules. The systematic search

was performed on several different classes of organic molecules with the intensive use of the MC-SCF quantum chemical method. The application of powerful tools led to a detailed mapping of the potential energy surfaces of ca. 25 different organic chromophores and thus allowing the characterization of the conical intersections involved in the reaction mechanisms.

The compounds belong to one of the following classes:

- Chromophores with one double-bond (or two isolated double bonds)
- Chromophores with conjugated double-bonds
- Aromatic Chromophores and Related Compounds
- Azo-Chromophores
- Chromophores with a Carbonyl group or a Conjugated Carbonyl group
- Polysilanes
- Models of the Retinal Chromophore (Schiff Bases)
- Model Photochromic Compounds and Dyes

Conical intersections were located for all systems. A general result was that *the computed molecular structure of the intersection is related to the structure of the experimentally observed photoproducts*[112] pretty much in the same way in which, for a thermal reaction, the transition state structure is related to the molecular structure of the product.

This relationship support the validity of conical intersections as key mechanistic elements in organic photochemistry and was shown to hold for a number of different types of photochemical reactions:

- Ring-opening and Ring-closure reactions
- [1,2], [1,3] Sigmatropic Shifts
- Di-π-methane Rearrangement

- Oxadi-di-π-methane Rearrangement
- Valence Isomerization of Aromatics
- [2+2], [4+2] and [4+4] Cycloadditions
- Bicyclization of dienes
- Cis-trans isomerization
- Deazetization
- Hydrogen Transfer
- Charge Transfer
- Paterno-Buchi Addition
- Polysilane Fragmentation

Conical intersection has also been shown to provide the decay channel associated with photophysical processes such as the ultrafast (usually subpicosecond) radiationless deactivation:

- Polyenes and Polyene Schiff Bases
- Benzene
- Azulene
- Fulvene
- Indacene
- Cyanines
- Styrene

and quenching of excited states:

- n-π* states/chlorinated hydrocarbons
- n-π* states/amines

The examination of a large set of computed data allows for the formulation of a few general results that lie at the basis of the “chemistry” of conical intersections:

1. similar organic chromophores (e.g. conjugated hydrocarbons) have similar conical intersection structures.
2. all basic chemical events such as breaking, making and exchange of bonds between atoms can be mediated by conical intersections.

### 5.2.2. Some examples

This section introduces some examples of practical photochemical problems, in which conical intersections occur. In the first ($\pi$-$\pi^*$) excited state ($S_1$) benzene there is a ~3000 $cm^{-1}$ threshold for the disappearance of $S_1$ fluorescence (see refs.112, 131 and references cited therein). This observation is assigned to the opening of a very efficient, radiationless decay channel (termed "channel 3") leading to the production of fulvene and benzvalene as shown in Figure 5–6.

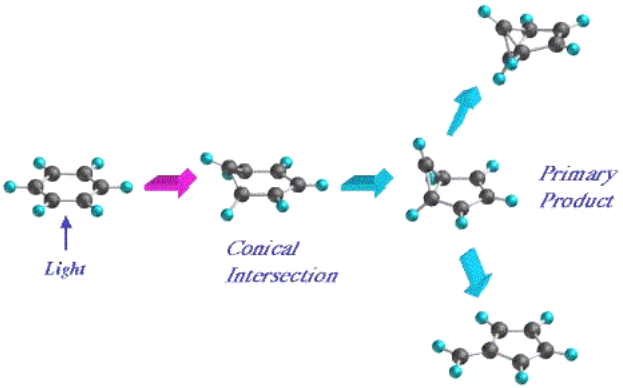


Figure 5–6: The conical intersection structure of benzene clearly shows a folded shape that precedes the formation of an envelope-like precursor (the primary product) of fulvene (bottom) and benzvalene (top).

Ab initio CAS-SCF calculations show[112] that the general surface topology of the excited state energy surface is consistent with that shown in Figure 5–7.

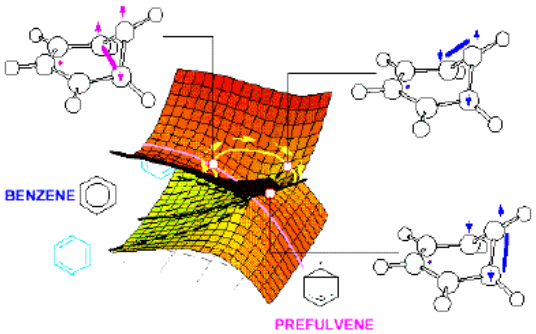


Figure 5–7: Two-dimensional model of the potential energy surface of the photochemical transformation of benzene to fulvene and benzvalene.

By examining the molecular structure of the conical intersection (Figure 5–6), one can derive information on benzene reactivity. The structure contains a triangular arrangement of three carbon centres corresponding to a -$(CH)_3$- kink of the carbon skeleton. For instance, it is obvious from the structure that the kink feature suggests formation of a cyclopropyl ring upon decay to the ground state. Thus the "primary" photoproduct of the reaction is predicted to be a diradical species characterized by a 1,3-transanular bond. The electronic structure corresponds to 3 weakly interacting electrons in a triangular arrangement, which is loosely coupled to an isolated radical centre (this is delocalised on an allyl fragment). This type of conical intersection structure appears to be a general feature in conjugated hydrocarbons systems and has been documented in a series of polyene and polyene radicals[120] with formula $C_nH_{n+2}$. The electronic origin of this feature can be understood by comparison with $H_3$ where any equilateral triangle configuration corresponds to a point on the $S_0/S_1$ conical intersection seam (this is an example of Jahn-Teller degeneracy) in which the three H electrons have identical pairwise interactions (Figure 5–8). These same features also characterize the -$(CH)_3$- kink where three singly occupied $\pi$ orbitals interact through two $\pi$ and $\sigma$ interactions.

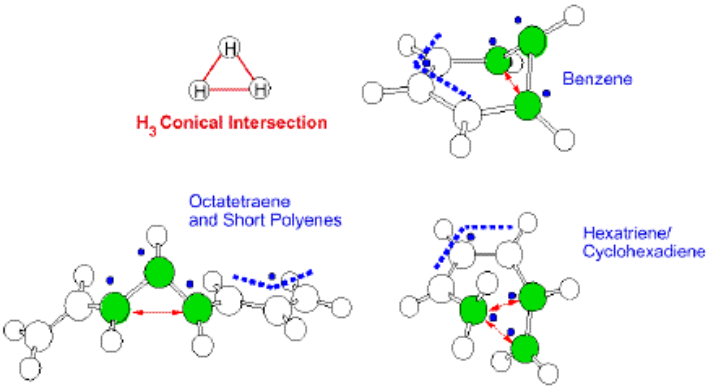


Figure 5–8: Structures of $S_1/S_0$ conical intersections in conjugated hydrocarbons (benzene, *all-trans* octatetraene, cyclohexadiene) showing the -$(CH)_3$- kink (framed).

The example of benzene shows that the same conical intersection may mediate both photophysical[a] and photochemical processes. The rate of these processes is controlled by the magnitude of an excited state barrier (a conventional TS) located between the excited state reactant and the conical intersection. Computational evidence[112,131,132] demonstrated that, when the barrier is very small or negligible, the corresponding deactivation (or chemical reaction) is ultrafast.

Comparing the conical intersection structure of linear and cyclic polyene and polyene radicals with the conical intersection structure of benzene (Figure 5–

[a] i.e., fast radiationless deactivation. For instance, in azulene the well-known lack of $S_1$ fluorescence is due to a specific conical intersection.[119]

8) (see for example the structure of all-*trans*-octatetraene and cyclohexadiene), one can see that these structures are characterized by the same kink feature. The kink structure prompts *cis-trans* isomerization and valence isomerization in polyene[120,133] and aromatics[113] respectively. Invariably, these intersections are located at the end of excited state path describing a conformational change of the molecule involving the simultaneous rotation about two C-C bonds and decreasing of one of the C-C-C angles.

As an example of conical intersection involved in photochemistry of n-π* excited states compounds in Figure 5–9 is shown the conical intersection for the hydrogen atom transfer between an azoalkane (**pyrazoline**) and a chlorinated hydrocarbons ($CH_2Cl_2$).[8,134] The structure shows an hydrogen still "moving" between the two fragment. Clearly the chemical event is not completed on the excited state but is interrupted along the reaction coordinate by the conical intersection.

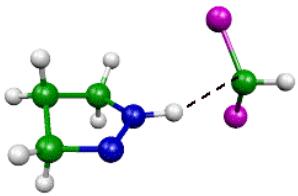

Figure 5–9: Structure of the conical intersection for the model system **pyrazoline** and $CH_2Cl_2$. This funnel accounts for the quenching of the fluorescence of azoalkanes. This figure and many other in this thesis were produced using the MOLEKEL 4.3 visualization program.[135]

A further outstanding result is the demonstration that conical intersections drive the photochemical reaction that constitutes the primary event in vision. Using a realistic model of the chromophore of the human retina visual receptor (rhodopsin) (Figure 5–10), it has been demonstrated that a conical intersection featuring a 90° twisted retinal structure controls the decay to the ground state and, as a consequence, the efficient production of the chromophore structure that initiate the receptor photocycle.[136,137] This argument is treated in depth in Chapter 9.

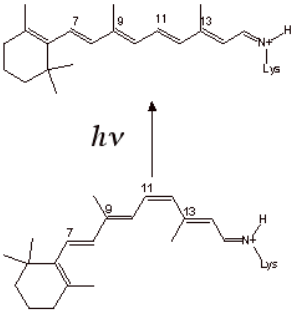


Figure 5–10: Photochemical isomerization of the retinal chromophore.

*Ab initio* semi-classical trajectory calculations have been carried out on a computationally less expensive model to investigate the time-dependent structural changes in retinal and to estimate the reaction time-scale.[138] The results show that, indeed, these types of chromophores reach the conical intersection in the subpicosecond time-scale. It has also been possible to determine the nature of the excited state reaction coordinate controlling the motion towards the conical intersection.[139] The computed coordinate (Figure 5–11) involves a sequential evolution along two different modes.[140] The

initial mode corresponds to the stretching of the double bonds that are thus prepared for torsional deformation. This initial evolution is indeed followed by torsional motion about a double bond that invariably leads to decay at a conical intersection. Such a "two-mode" coordinate, has now been experimentally confirmed for different type of rhodopsin.[141] [142]

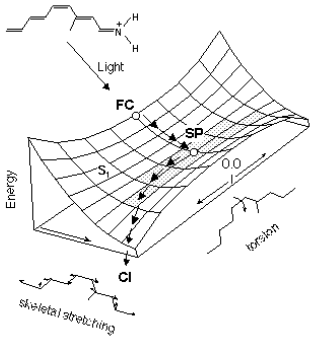


Figure 5–11: The two-mode structure (stretching + torsion) of the $S_1$ reaction coordinate of rhodopsin models.

While the photochemistry of linear conjugated hydrocarbons involves a low $\pi$ to $\pi^*$ doubly-excited singlet state, conjugated systems containing a heteroatom may feature a low-lying excited state of different nature. Recent computational studies on the $S_1$ conformational properties of protonated Schiff bases (PSB) (Structure 1) (a conjugated hydrocarbon containing a terminal $NH_2^{(+)}$ group) and $\alpha,\beta$-enones (Structure 2) (a conjugated hydrocarbon containing a terminal carbonyl group) can provide information on this regards.

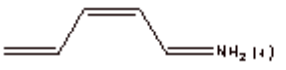

Structure 1

Structure 2

In these two species the first singlet excited states is a π to π* singly-excited state (i.e. one electron is promoted from the π-HOMO orbital to the π–LUMO orbital) and a n to p* excited state (i.e. one electron is promoted from the nitrogen or oxygen lone pair to the p-LUMO orbital) respectively.
The $S_1$ potential energy surface of Structure 1 comprises three *possible* conformational interconversion paths, which develop through the relaxation out from the FC region, as shown in Figure 5–12.

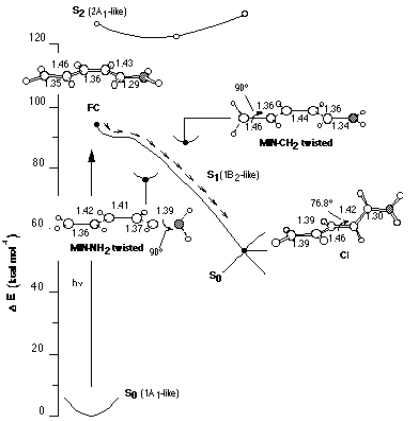


Figure 5–12: Detailed energy profile along the $S_1$ relaxation path of Structure 1 (see text).

There are two adiabatic conformational interconversion paths which lead to two excited state minima. The first minimum features a 90° twisted terminal methylene group and the other a 90° twisted amino group. In both minima the $S_0$-$S_1$ energy gap is large (~28 kcal $mol^{-1}$). As a consequence these *Z*/*E* diastereoisomers *cannot* provide efficient radiationless decay channels in this species. The third path is non adiabatic and it is dominated by a *Z* to *E* conversion of the central double bond of the molecule. This path has been fully documented[143] via a MEP computation and corresponds to a barrierless path, which leads to a 90° twisted conformation where the $S_1$ energy surface crosses the ground state energy surface at a $S_1/S_0$ conical intersection. Of course, this conical intersection provides an efficient decay channel and the *E* isomerization photoproduct accumulates on $S_0$. The 90° twisted conical intersection is the point of lowest energy on the $S_1$ energy surface and it is several kcal $mol^{-1}$ lower than the two $S_1$ twisted minima described above. The structure of the MEP coordinate and of the conical intersection (CI in Figure 5–12) indicate that the excited state relaxation path in this system involves a torsional change at one bond (i.e. at the central double-bond).[133,144]

In conclusion, the systematic investigation of different organic chromophores,[20,145] have shown that, for unsensitized photochemical reactions, the photochemical funnel is usually associated with *a conical intersection that is located <u>at the end</u> of the corresponding path*. Such conical intersections are (in analogy with transition states) critical mechanistic elements in "direct" photochemistry (including ultrafast radiationless deactivations and biological photoisomerizations).

For sensitised photochemistry, which is usually dominated by triplet excited states it has been demonstrated that the same methods used for mapping

conical intersections can be used to locate triplet/singlet crossings. The crossing between states of different spin multiplicity corresponds to a n-1 dimensional set of points where intersystem crossing (ISC) may occur and cause the relaxation of the system to a state of different spin multiplicity.[118,146]

## 5.3. Search for the Photochemical Funnel: Conical Intersections and Singlet-Triplet Crossings

### 5.3.1. Optimization of a conical intersection and analysis of Ruedenberg's branching space

As introduced in Section 4.3, there are situations where there is no transition state connecting an excited state intermediate to the conical intersection point or where an excited state intermediate on the upper energy surface does not exist. In such situations, mechanistic information must be obtained by locating the lowest lying intersection point along the (n-2)-dimensional intersection space of the molecule. The practical computation of the molecular structure of a conical intersection energy minimum can be illustrated by making an analogy with the optimisation of a transition structure. As illustrated in Figure 5–5, a transition structure is the highest energy point along the path joining reactants to products and the lowest energy point along all the other n-1 directions orthogonal to it. One can

optimise such a structure by minimising the energy in n-1 orthogonal directions, and maximising the energy in the remaining direction corresponding to the reaction path. The technique for locating the lowest energy intersection point[88] exploits the fact that the branching space directions $x_1$ and $x_2$ play a role analogous to the reaction path at the transition state. Accordingly, the lowest energy point on a conical intersection is obtained by minimising the energy in the n-2 dimensional intersection space ($x_3$, $x_4$,..., $x_n$) which preserves the degeneracy. It is important to appreciate that the gradient on the excited state PES will not be zero at an optimised conical intersection point, since it "looks like" the vertex of an inverted cone. Rather, it is the projection of the gradient of the excited state PES onto the orthogonal complement of $x_1$ and $x_2$ (*i.e.* the n-2 dimensional hyperline) that goes to zero when the geometry of the conical intersection is optimised. This situation is distinguished from an "avoided crossing minimum" of two surfaces which is a real minimum where the gradient on the excited state PES would go to zero.

Thus, in an optimised conical intersection point, the following conditions have to be fulfilled:

$$E_2 - E_1 = 0 \tag{5–17}$$

$$\frac{\partial E}{\partial x_3} = \frac{\partial E}{\partial x_4} = ... = \frac{\partial E}{\partial x_n} = 0 \tag{5–18}$$

In practice, the optimization is carried out by simultaneously minimizing the energy difference $E_2 - E_1$ in the plane spanned by $x_1$ and $x_2$ and

minimizing $E_2$ in the remaining (n-2)-dimensional space orthogonal to the $x_1$, $x_2$ plane.

For the minimisation of $E_2 - E_1$ one have:

$$\frac{\partial}{\partial Q}(E_2 - E_1)^2 = 2(E_2 - E_1)x_1 \qquad (5\text{–}19)$$

where $x_1$ is the gradient difference vector defined in Section 5.1.4. The length of $x_1$ has no significance, only its direction. ($|x_1|$ will be large if the potential energy surfaces have opposite slope but very small if they have nearly the same slope). This means that the size of the step should only depend upon $E_2 - E_1$, and suggests that one should take the gradient along the step to the minimum of $E_2 - E_1$ to be

$$f = 2(E_1 - E_2)\frac{x_1}{\sqrt{x_1 \cdot x_1}} \qquad (5\text{–}20)$$

Clearly $f$ will go to zero when $E_2 = E_1$, independently of the magnitude of $x_1$.

Note, however, that the gradient will also go to zero if $E_1$ is different from $E_2$ but the two surfaces are parallel (i.e., $x_1$, the gradient difference vector, has zero length). In this case the method would fail. This situation will occur for a pseudo Jahn-Teller case (i.e., at an avoided crossing). Of course, in this case, the geometry can be found by normal unconstrained geometry optimization.

If one now defines the projection $P$ of the gradient of $E_2$ onto the (n-2) orthogonal complement to the plane $x_1$, $x_2$ as

$$g = P\frac{\partial E_2}{\partial Q} \tag{5–21}$$

then the gradient to be used in the optimisation becomes

$$\overline{g} = g + f \tag{5–22}$$

The general behaviour of such optimization procedure is illustrated in Figure 5–13, that reports two PES intersecting along the $x_1$ and "intersection space" coordinates ( $x_3$, $x_4$ ,..., $x_n$ ). Although this example is not realistic because it starts very far from the optimised structure, notice that, starting from this initial structure (initial point), the method first finds the closest intersection point. After that, it moves downhill along the intersection space.

Notice that, starting from an arbitrary initial structure (initial point) the method locates, loosely, the closest intersection point. After that it moves downhill along the intersection space.

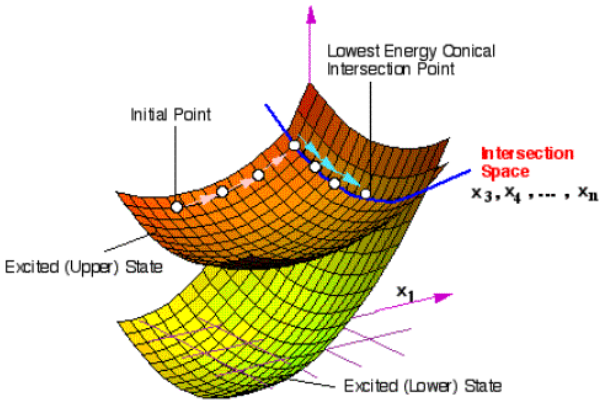


Figure 5–13: General behaviour of a conical intersection optimization procedure. This is a contrived example which was started from an almost planar geometry. The curve shows the rapid approach to the degenerate situation followed by minimization (retaining the degeneracy).

The chemically most relevant conical intersection point appears in the situation where the apex of the cone is locally the lowest energy point on the excited state surface, and the highest energy point on the ground state surface (Figure 4–3). This is called a peaked conical intersection. In fact, the topography of the potential energy surfaces in the vicinity of a conical intersection can be characterized by the relative orientation of the two potential surfaces and the terminology used is that of Ruedenberg et al.[109] There are three types of intersection. The distinction between these is shown in Figure 5–14.

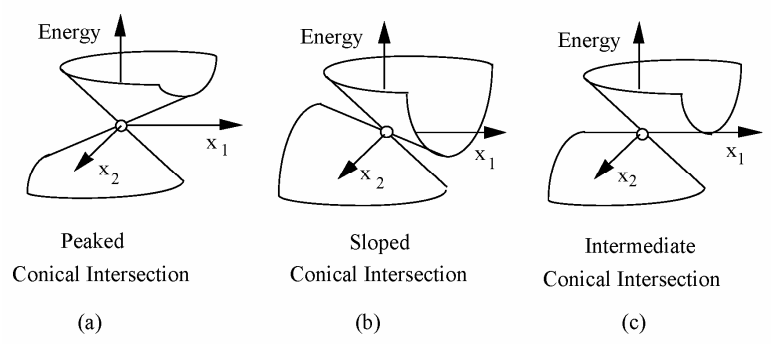


Figure 5–14: Conical intersections classified according to ref. 109: (a) peaked, (b) sloped, and (c) intermediate conical intersection.

When viewing the peaked CI, it is clear that the two intersecting curves have gradients of opposite sign. However, if the curves have gradients of the same sign then the lowest energy point on the intersection lies above the local minimum, the conical intersection is tipped (or sloped). The excited state part of the surface is almost flat in the region of the intermediate intersection, and one curve has a near-zero gradient.

In the case of the peaked conical intersection, the molecular structure of the intersection and the reaction pathway leading to it can be studied by using the tools discussed in Section 4.3, when an excited state in intermediate exist. Situations where there is no transition state connecting the excited state minimum to the intersection point correspond to a sloped conical intersection. In such situations, mechanistic information must be obtained by locating the lowest lying intersection point as described at the beginning of this section.

### 5.3.2. Case of molecules with more than one photochemical funnel: photochemical selectivity

The $S_1/S_0$ conical intersection structure documented in linear polyenes and polyene radicals (with formula $C_nH_{n+2}$) suggests that photoexcitation lead to a complex torsional deformation of the molecule. As already said in Section 5.2, the molecular geometry at the $S_1 \rightarrow S_0$ radiationless decay channel of this systems shows a special feature: a sharp "kink" located at a $-(CH)_3-$ segment. This conical intersection is accessed after simultaneous rotation about two C-C bonds and the decreasing of one of the C-C-C angles. In Figure 5–8 it has already been shown the three carbon centres arrangement for the *all-trans* octa-1,3,5,7-tetraene (*all-trans* OT).[120,147] The $-(CH)_3-$ "kink" electronic structure corresponds to three weakly interacting electrons in a triangular arrangements (like in $H_3$)[148] which are loosely coupled to an isolated radical centre delocalised on an allyl fragment.
Using the *ab initio* CASSCF method with an active space including all $\pi$ and $\pi^*$ orbitals and electrons, the same "kink" structure has been located at the end of the excited state reaction path of six *all-trans* conjugated hydrocarbons: butadiene, hexatriene[113,133] and octatetraene as polyenes; allyl, pentadienyl and heptatrienyl as polyene radicals.[120]

In longer linear polyenes, the $-(CH)_3-$ kink may be located in different positions along the hydrocarbon chain. In fact, the *all-trans* hexa-1,3,5-triene (*all-trans* HT) and the *all-trans* OT are characterized by multiple first excited state reaction paths. Each path leads to a distinct conical intersection in which the position of the $-(CH)_3-$ kink changes. The conical intersections are

different diastereoisomeric conformers and the decay from each intersection will lead to a different *Z*/*E* diastereoisomers. Furthermore, since the excited state equilibrium structure has C-C bonds whose length is closed to that of single bonds one may expect the existence of conventional adiabatic paths leading to different excited state *Z*/*E* diastereoisomers.

The computational investigation of adiabatic and non adiabatic excited state paths of *all-trans* HT and *all-trans* OT demonstrated that they have the same type of surface topology and both of them are characterized by four competitive diastereomeric reaction path channels (two diabatic and two non adiabatic) starting at the $S_1$ planar energy minimum. Each path is defined by a different transition structure and, consequently, a different barrier height. The molecular geometries for *all-trans* HT and *all-trans* OT are shown in Figure 5–15.

In *all-trans* HT the non-adiabatic transition structures of Figure 5–15a and Figure 5–15b are associated with a *non-adiabatic EZ* (because of the large ca. 50° torsion about the central double-bond) isomerization and with a *non-adiabatic* single-bond (i.e. *t*→*c*) isomerization (because of the 43° torsion about the single-bond) respectively. The adiabatic transition structures are shown in Figure 5–15c and Figure 5–15d. The first one define an isomerization paths on the excited state connecting the *all-trans* $S_1$ equilibrium structure to itself (via a 180° rotation of one terminal $CH_2$ group), the second one the *Z*-HT structure (via a 180° E→Z rotation about the central C=C bond). These structures show a ca. 90° twisted double-bond and thus lies halfway along the $S_1$ isomerization path.

The first non-adiabatic transition structure of the *all-trans* OT is associated to a $C_3$-$C_4$ trans → cis double-bond isomerization path (Figure 5–15a). In Figure 5–15f and Figure 5–15g are shown the non adiabatic and adiabatic

transition structure which define the channel for the $C_1$-$C_2$ double bond rotation where the $CH_2$ group is ~90° twisted respectively.
The last picture (Figure 5–15h) represents the transition structure for a fully adiabatic *E*→*Z* isomerization channel.

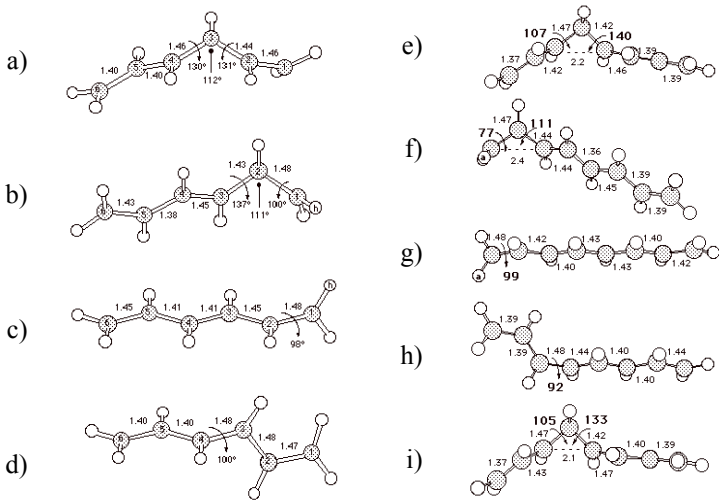


Figure 5–15: Molecular structure and relevant geometrical parameters (Å and degrees) for the $S_1$ low-lying transition structures of *all-trans* HT and *all-trans* OT (see text) in order of increasing energy: (a) $TS_{Z/E}$ (b) $TS_{t\rightarrow c}$ (c) TSCH2 adiab. (d) $TS_{Z/E}$ adiab. (e) $TS_{E\rightarrow Z}$ (non-adiab.) (f) $TS_{CH_2}$ (non-adiab.) (g) $TS_{CH2\text{-}twist}$ (adiab.) (h) $TS_{E\rightarrow Z}$ (adiab.) (i) $S_1/S_0$ **CI.** The data are from ref. 133. The relevant geometrical parameters are given in Å and degrees (Ha-C-C-C and C-C-C-C torsions are in bold style).

The results suggest that in both cases the photochemical product distribution is controlled by the non-adiabatic paths since the adiabatic paths have large

barriers. In fact, in *all-trans* HT both non-adiabatic paths are the lowest energy ones and the path associated with $E \rightarrow Z$ motion (i.e. the one with the most "central" kink) is nearly barrierless while the lowest adiabatic reactive process, which corresponds to $CH_2$ rotation, has a ca. 7 kcal $mol^{-1}$ barrier. The energetics associated to the *all-trans* OT reaction paths has the same characteristic. The lowest energy channel (ca. 7 kcal $mol^{-1}$) is a non-adiabatic channel, the one defined by the transition structure of Figure 5–15e. The remaining three channels lie at higher energies. The second non-adiabatic channel has a barrier of 10 kcal $mol^{-1}$. The adiabatic channels corresponding to the ~90 degrees twisted $CH_2$ group lies at ca. 11 kcal $mol^{-1}$ while the fully adiabatic $E \rightarrow Z$ isomerization channel lies ~7 kcal $mol^{-1}$ above the channel for non-adiabatic $E \rightarrow Z$ isomerization.

Thus, it is clear that the photochemical Z/E isomerization of these molecules must be diastereoselective. In particular the major Z/E diastereoisomer produced via photolysis of these species is expected to originate via decay at the most easily accessible diastereomeric decay channel. Finally, analysing the molecular structure of the $S_1$ transition state structure associated to the diastereomeric decay channel it is evident that the non-adiabatic Z/E isomerization may lead to a simultaneous double bond and (adjacent) single-bond conformational change.

The result of investigation of the photocyclization of the polyene *EZE*-deca-1,3,5,7,9-pentaene (see Scheme 5–1a) established that for this system it is possible to locate and determine the structure of eight photochemical funnels. Two of them are linear conical intersections characterized by a $-(CH)_3-$ kink geometrical arrangement, in two different positions: $C_3$-$C_4$-$C_5$ and $C_4$-$C_5$-$C_6$. In Scheme 5–1 is shown the photoexcitation leading to the second one.

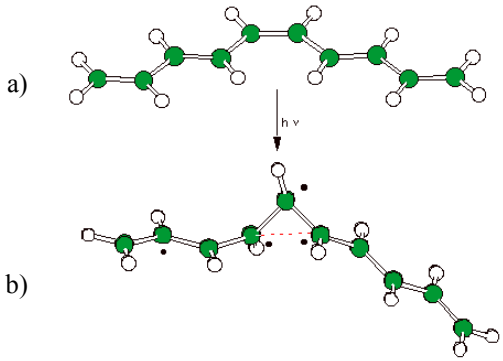


Scheme 5–1

If the molecule enters these two decay channels there will be no cyclization and the molecule remains linear. On the contrary, there are six funnels, which lead, under ground state relaxation, to three pairs of diastereomeric cyclic structures. These pairs of structures differ for the ring size (5, 7, 9 terms; Scheme 5–2).

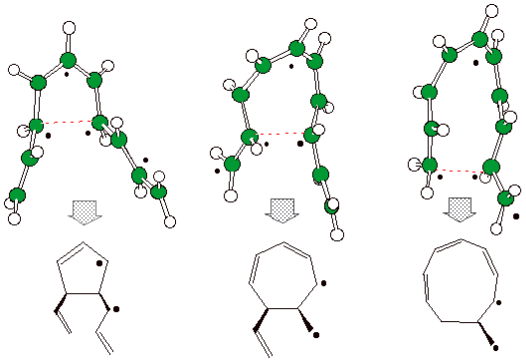

Scheme 5–2

In Scheme 5–3 are shown the two diastereomeric cyclic structures (cis/trans) for the 5-membered ring molecule. The stabilization of one of these funnels can provide an effective tool for the control of the photochemical reactivity and stereochemistry of polyenes.

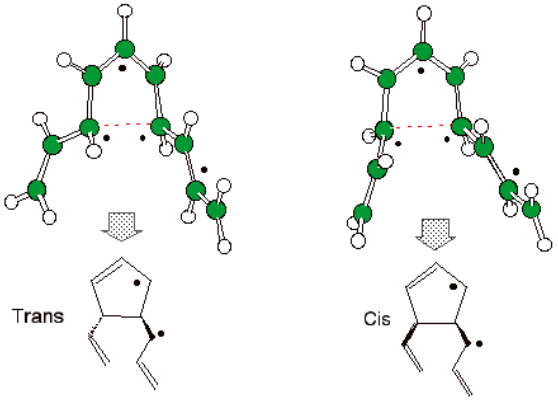


Scheme 5–3

Longer protonated Schiff bases, such as the *all-trans* epta-2,4,6-trienimminium cation, are also characterized by the presence of competitive channels[136,149]. Such molecule, with four conjugated double bonds, may undergo *trans* → *cis* isomerization at either the double bonds in position 2 and 4 as shown in Scheme 5–4.

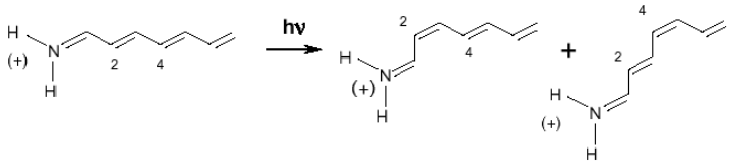


Scheme 5–4

The excited state minimum energy paths of both these isomerization processes is shown in next Figure 5–16.

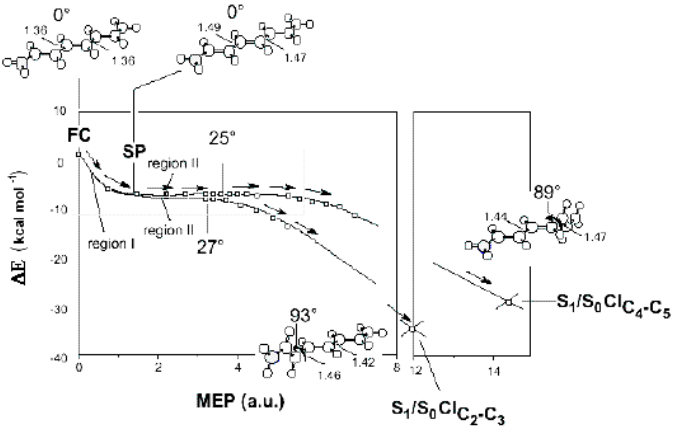


Figure 5–16: Energy profiles along the MEPs describing the competing excited state isomerization paths from the FC point (**FC**) to the decay points $\mathbf{S_1/S_0\ CI_{C2\text{-}C3}}$ and $\mathbf{S_1/S_0\ CI_{C4\text{-}C5}}$ of *all-trans* $C_7H_8NH_2^+$. Open squares define the $S_1$ ($1B_u$-like) energy. Open circles indicate the position of the conical intersections. The structures (geometrical parameters in Å and degrees) document the geometrical progression along the path. (From ref. 136)

The two paths are nearly barrierless with only less than 1 kcal $mol^{-1}$ energy difference along the long plateau region (in favour of the isomerization at position $C_2$-$C_3$). However, the initial part of the MEPs, which is dominated by double-bond expansion, is similar.
The results of analytical frequency computations and the analysis of the direction of the gradient at the **FC** point demonstrate the existence of the energy plateau and the general flatness of region II as well as competition between the two-isomerization processes. Thus, in these molecules there is not a strict diastereoselectivity due to the competition between the decay channels which have diastereomeric structures.

The diastereoselectivity is more evident in shorter protonated Schiff bases (PSBs). In fact, as already discussed in Section 2.2.2 and shown in Figure 5–12, the $S_1$ potential energy surface of the *tZt*-penta-3,5-dieniminium cation (*cis*-$C_5H_6NH_2^+$) comprises three *possible* conformational interconversion paths which develop through the relaxation out from the FC region. There are two adiabatic conformational interconversion paths which lead to two excited state minima. The first minimum features a 90° twisted terminal methylene group and the other a 90° twisted amino group (see Figure 5–12). In both minima the $S_0$-$S_1$ energy gap is large (~28 kcal $mol^{-1}$). As a consequence these *Z*/*E* diastereoisomers *cannot* provide efficient radiationless decay channels in this species. The third path is non adiabatic and it is dominated by a *Z* to *E* conversion of the central double bond of the molecule. This path leads to a 90° twisted conical intersection which provides an efficient decay channel and the *E* isomerization photoproduct accumulates on $S_0$.

A further example is reported in Section 9.3, where is demonstrated how the five double bonds *all-trans*-retinal chromophore exhibits at least three competitive excited state double bond isomerization paths, controlled by energy barriers.

### 5.3.3. Advanced topic: structure of Ruedenberg's intersection space

As already said in Section 5.2.2, the products of benzene photochemistry appear to be controlled by the topology of the $S_1/S_0$ crossing surface.[112] The excited state surface topology has been illustrated in Figure 5–7.[80,112] The optimised conical intersection structure for $S_1$ benzene is illustrated in Figure 5–8. The structure contains the "critical" three carbon centred triangular arrangement corresponding to a -$(CH)_3$- kink. Let us now discuss in more details the -$(CH)_3$ - kink electronic structure and the coupling involved in photoproduct formation. The circle around the conical intersection point in Figure 5–7 represents a "circuit" of the conical intersection which changes the coupling in the triangular arrangement of the -$(CH)_3$ – kink. In particular the two geometrical distortions that lift the degeneracy ($x_1$ and $x_2$) are shown. The nature of the two vectors, the gradient difference vector $x_1$ and the derivative coupling vector $x_2$ is illustrated in Scheme 5–5.

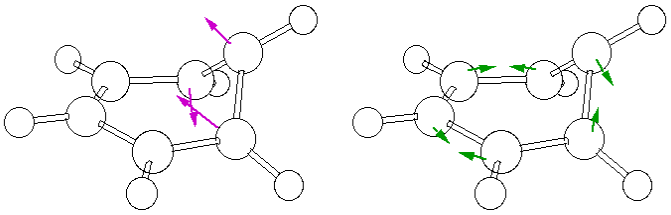


Scheme 5–5

Thus, the detailed characterization of the intersection space, defined by the $x_1$ and $x_2$ vectors, is very important to derive information on the photochemical reaction paths which lead to the final photoproducts.

The same analysis may be applied to the problem of cyclohexadiene/hexatriene photochemical interconversion.[150] In fact, the three different pairings of two out of three electrons of the -$(CH)_3$- kink can be found out mapping the branching space for this molecule (Scheme 5–6).

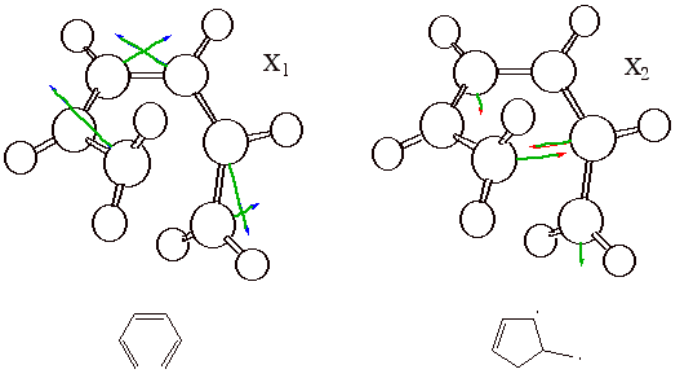


Scheme 5–6

### 5.3.4. Optimization of singlet-triplet crossings

As previously discussed, in contrast to a conical intersection, a singlet-triplet crossing belongs to n-1 dimensional space and therefore appears as a line on a two-dimensional energy surface. This is because if the intersecting potential energy surfaces have different spin multiplicity then $H_{12}$ is zero (see discussion in Section 5.1.3). In this case the branching space is one-dimensional and corresponds to the gradient difference vector $x_1$. The singlet-triplet crossing points are computed in the same fashion as the singlet-singlet crossing points, although the derivative coupling is zero. One of the first successful applications of the standard algorithm to search for a singlet-triplet crossing was in the study of the photochemistry and photophysics of acrolein.[115] The first singlet excited state of acrolein, as the simplest model of α,β-enones compound, is not a π-π* state (as in conjugated hydrocarbons, polyenes and protonated Schiff bases) but an *n*-π* state, where two unpaired electrons reside in mutually orthogonal orbitals. The different excited electronic state is due to the presence of an oxygen lone-pair in the carbonyl C=O group. One important property of the *n*-π* state is that they can give raise to extremely fast intersystem crossing to triplet states with a π-π* electronic structure. This leads, even without the need of a sensitizer, to efficient production of triplet state intermediates, which undergo an independent evolution with respect to the singlet excited state. Thus, the photochemistry of carbonyl compounds is characterized by the competition between triplet $^3$(π-π) pathways and singlet $^1$(n-π) and triplet $^3$(n-π) pathways.

The efficiency of single-triplet crossing in this system is due to the large value of singlet-triplet spin-orbit coupling (SOC) due to the different relative orientation of the two singly occupied orbitals of this system (i.e. the singly occupied orbitals n is "changed" into the orthogonal p orbitals when passing from the $n$-$\pi^*$ to the $\pi$-$\pi^*$ configuration).[78,107]

The evolution of $^1(n\text{-}\pi)^*$ *s-cis*-acrolein along the $S_1$ path involves the Z/E rotation of the terminal $CH_2$ group until a $S_1/S_0$ conical intersection is reached and the decay to $S_0$ takes place. The $S_1/S_0$ conical intersection (Scheme 5–7a) has a 90° twisted terminal $CH_2$ and corresponds to a diradical with radical centres on $CH_2$ and O with a central C-C double-bond (1.34 Å) fully formed and therefore cannot easily rotate.

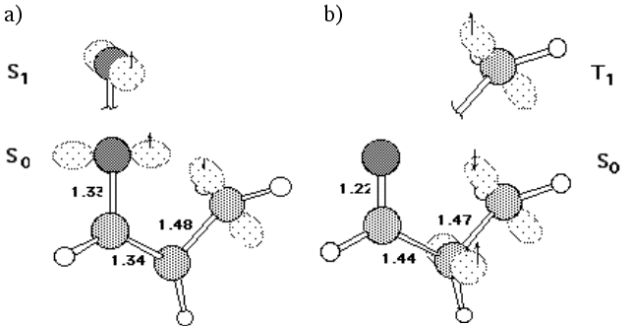


Scheme 5–7

Thus, in this structure the $S_0$ state and the $^1(n\text{-}\pi^*)$ state differ only in a 90° *rotation* of the position of the singly occupied orbital on the oxygen. Since the position of this radical centre is isolated from the $CH_2$ radical centre, the states have the same energy.

The $S_1/S_0$ conical intersection lies approximately 40 kJ mol-1 above the $S_1$ minimum. This is consistent with the observed short wavelength irradiation (254 nm) which is required to provide the necessary excess energy to populate the single decay channel.[151,152] Direct irradiation at 254 nm leads to a mixture of *cis-trans* double bond isomerization resulting from methylene rotation and ring-closure products (oxetanes). The experiments show that the cyclization is observed only when short wavelengths are used and that the oxetane production is insensitive to the use of butadiene as a triplet quencher[152] and that thus the reaction must involve the singlet manifold only.

The Z/E double-bond isomerization is also observed at 313 nm. At this wavelength the isomerization occur exclusively and the associated photochemistry comes from an alternative triplet decay route. Computations on acrolein demonstrate that the $T_1$ state is populated by ISC from the initial $S_1$ (n-π*) excited state molecule to a $T_1$ (π-π*) diradical intermediate (Scheme 5–7b).

The $^3$(π-π*) diradical intermediate is not generated directly but involves decay through successive $S_1/T_2$ and $T_2/T_1$ intersections. The $T_1$ intermediate is located at a $T_1/S_0$ intersection and is the precursor of the photoproducts which are generated via a slow ISC process. The stability and structure of this twisted excited state minima $^3$(π-π*) well explains the observed very weak phosphorescence,[153] short triplet lifetime and lack of production of the four-member ring oxetene upon <300 nm irradiation.[152] In fact, while the two radical centres are located on two vicinal carbons, the carbonyl bond is fully formed. Consequently, relaxation to the $S_0$ state can only result in α,β-enone formation structure via *cis-trans* motion.

The photochemistry of acrolein will also be discussed in Chapter 14.

The n to π* excitation is also characteristic of the singlet photochemistry of azo-compounds. Thus, as in the case of the α,β-enones, the photochemistry of this systems is complex because the intertwining of triplet $^3(\pi\text{-}\pi)$ pathways and singlet $^1(n\text{-}\pi)$ and triplet $^3(n\text{-}\pi)$ pathways. In Scheme 2–8 is illustrated the molecular and electronic structure of the 2,3-diazabicyclo[2.2.1]hept-2-ene (**DBH**), as an example of azo-compound, and its conical intersection.[146]

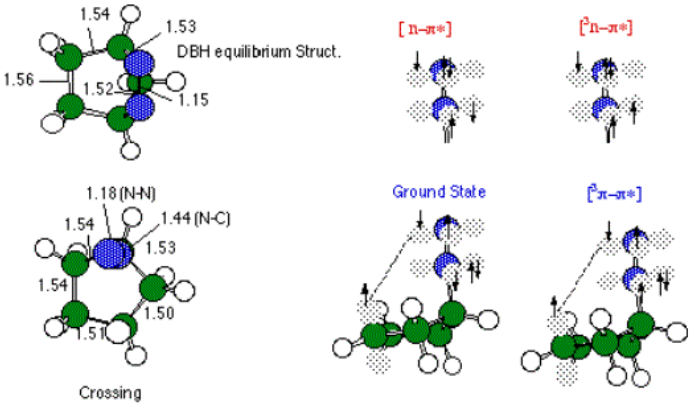


Scheme 5–8

Thus, a complete understanding of the photochemistry of this species requires the investigation of the evolution of singlet and triplet excited **DBH**. As illustrated in Figure 5–17, the reaction pathways for **DBH** form a network of routes involving 18 ground and excited state intermediates, 17 transition structure and 10 "funnels".

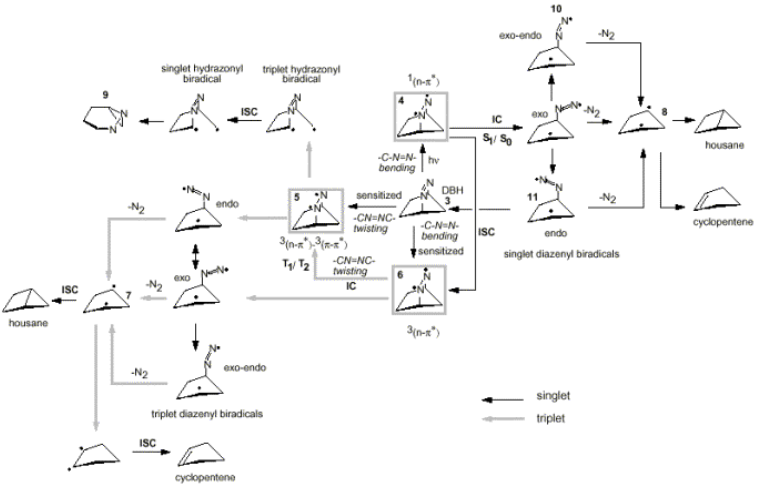


Figure 5–17: Sequence of structures along the reaction paths network computed in the photochemistry of **DBH** species (3).

The decay channel for the triplet-sensitised photolysis also has an unusual surface topology which is indicated in Figure 5–18. In the Franck-Condon region, $T_2$ has ($\pi$-$\pi^*$) character and lies ~34 kcal mol -1 above $T_1$ which has (n-$\pi^*$) character. As the structure of the molecule gets distorted from the Franck-Condon geometry, the $^3$($\pi$-$\pi^*$) and $^3$(n-$\pi^*$) states become strongly mixed so that it becomes difficult to distinguish between the two triplet states, especially at structures where the C–N=N–C bridge is twisted. In other words, the electronic structures of the $T_1$ and $T_2$ states become a combination of ($\pi$-$\pi^*$) and (n-$\pi^*$) configurations. Near the triplet (n-$\pi^*$) energy minimum (6) there is a conical intersection between the ($\pi$-$\pi^*$) and (n-$\pi^*$) triplet states. The electronic structure of the $T_1$ and $T_2$ states in the vicinity of the intersection can be understood on the basis of the derivative coupling and

gradient difference vectors. The derivative coupling vector involves an N-N-C bending, and the gradient difference vector involves twisting of the C–N=N–C bridge. The N-N-C bending distortion causes the "pure" (n-π*) and (π-π*) states to cross. Thus on one side of the upper ($T_2$) cone is the (n-π*) state and on the other side is the (π-π*) structure (this structure corresponds to a steep $T_1/T_2$ intersection point). No stable (π-π*) minimum has been located on $T_2$. The orthogonal C–N=N–C distortion has the effect of producing "mixed" (n-π*) and (π-π*) states, i.e., states which can be represented by a mixture of (n-π*) and (π-π*) character. Thus decaying from the tip of the conical intersection in the direction of the gradient difference vector generates the mixed (n-π*)-(π-π*) minimum (5) on the $T_1$ state (in this structure, the n and p orbitals are strongly mixed so that the location of the two radical centres is not unambiguous). These effects are typical of the presence of a conical intersection: as one moves in a circle centred on the conical intersection point, the wavefunction changes in a continuous fashion from (n-π*) to (n-π*)+(π-π*) to (π-π*) to (π-π*)-( n-π*) to -( n-π*).

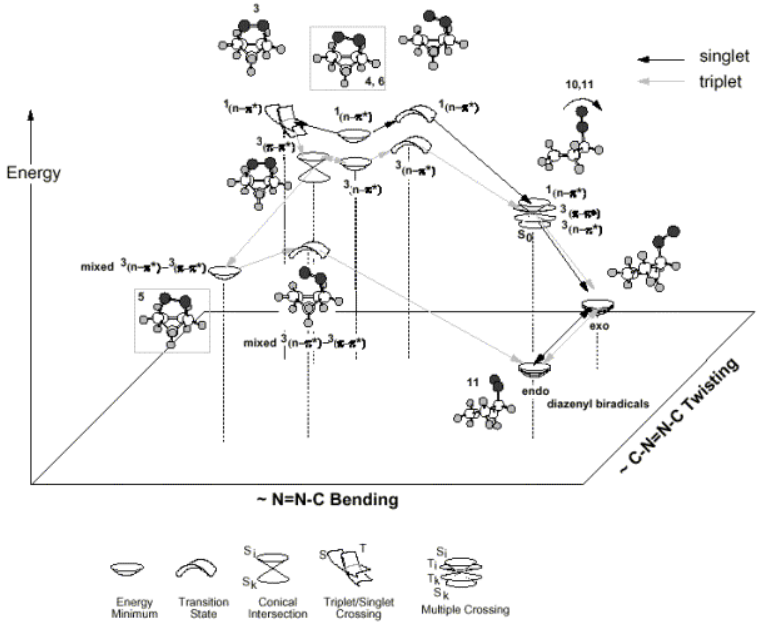


Figure 5–18: Companion schematic representation for the computed diazenyl region potential surface (the intermediates are labelled in the same way as Figure 5–17).

The results presented in this section give an idea about the complexities of the photochemistry that is typical of carbonyl and azo-compounds. A similar behaviour characterizes the photochemistry of other classes of organic molecules, such as the olefin-carbonyl Paterno-Buchi system[114], β,γ-enones[118], azo-compounds (cyclic diazoalkenes[146]) and acylcyclopropenes[118] photorearrangements.

# Chapter 6. Search for the Minimum Energy Paths

## 6.1. Excited State Relaxation

### 6.1.1. The Initial Excited State Relaxation: Computation of the Initial Relaxation Direction

As discussed in Section 4.3, the computation of excited state relaxation paths that do not start at a stationary point (e.g. the FC point) require the use of a non standard method. This is the *Initial Relaxation Direction* (IRD) method.[154] The IRD method ultimately allows one to map the possible MEP connecting the FC point to an excited state intermediate or to a conical intersection (when the excited state reaction path is barrierless). Section 6.2.1 will show that the same procedure may be used to determine the different directions of relaxation on the ground state potential energy surface starting from the crossing point.

As an example of the use of this method, this section describes the computation of the excited state minimum energy path for the photoisomerization of the minimal retinal protonated Schiff base model *tZt*-penta-3,5-dieniminium cation (*cis*-$C_5H_6NH_2^+$),[133] in which the procedure to

compute the initial direction of relaxation from the FC structure has been successful applied.

An IRD corresponds to a local steepest descent direction, in mass-weighted cartesians, starting from a given non stationary point. In practise this is computed by locating the energy minimum on a hyperspherical (i.e., *n*-1 dimensional) cross-section of the *n* dimensional potential energy surface centred on the starting point (*n* is the number of vibrational degrees of freedom of the molecule). The radius of this hypersphere is usually chosen to be small (typically ca. 0.25-0.5 au in mass-weighted cartesians) in order to locate the steepest direction in the vicinity of the starting point (i.e., the hypersphere centre). The IRD is then defined as the vector joining the starting point (i.e., the centre of the hypersphere) to the energy minimum. Once the IRD has been determined, the MEP is computed as the steepest descent line in mass-weighted cartesians using the IRD vector to define the initial direction to follow. The procedure is schematically illustrated in Figure 6–1.

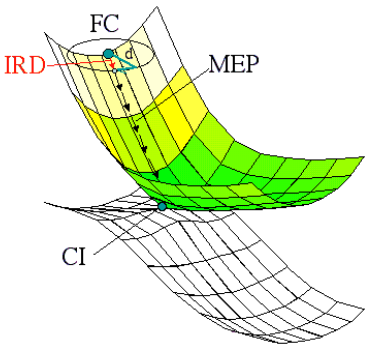


Figure 6–1: Initial Relaxation Direction (IRD) search starting from the Franck-Condon point.

The computed excited state MEP for *cis*-$C_5H_6NH_2^+$ is reported in Figure 6–2. The initial steep part of the MEP (region I) has no torsional components and terminates at an inflection of the potential energy along the MEP. The subsequent steep energy decrease towards the **CI** point (region II) can be related to the change in direction of the MEP coordinate

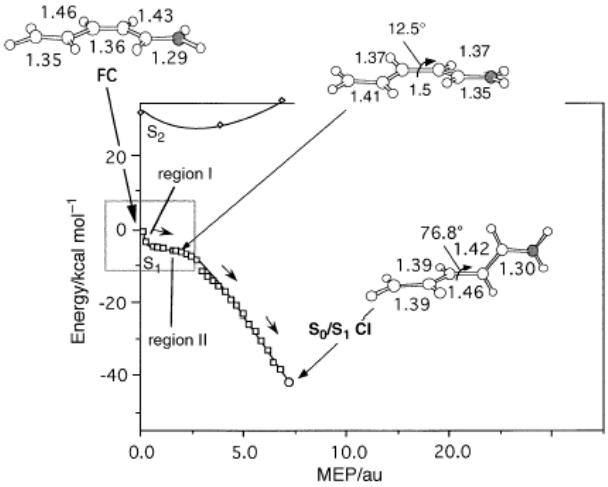


Figure 6–2: Energy profiles along the MEP describing the excited state relaxation from the FC point to the **CI** decay point of 2-*cis*-$C_5H_6NH_2^+$ (data from ref. 133). Open squares define the $S_1$ (1B u –like) branch of the cis → trans photoisomerization path; open diamonds give the energy of the $S_2$ covalent (2A g -like) state along the same path. Open circle indicates the position of the **CI.** The structures document the geometrical progression along the path. The MEP coordinate is in mass-weighted cartesians (au=$u^{1/2}$ $a_0$ ).

To determine the structure of region I, the IRD optimization method has been used to probe the force field at different distances (0.25, 0.5, 0.75, 1.0, and 1.5 au) from FC. The strategy used to compute the MEP in this region is based upon a series of IRD calculations carried out at different increasing distance values. These values coincide with the radius of the hypersphere. This is schematically illustrated in the following Scheme 6–1.[133]

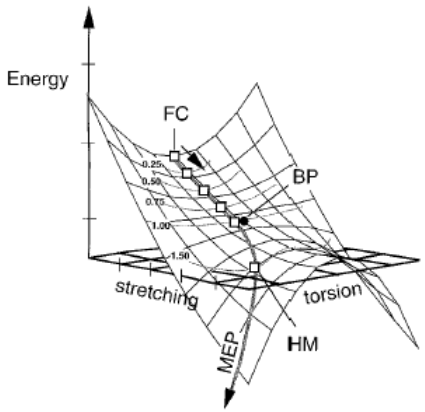


Scheme 6–1

The energy minima (open squares) on the (hyper)spherical cross-sections at 0.25-1.0 au are located at untwisted (i.e., totally symmetric) structures. This clearly indicates that in this region the potential energy surface has the shape of a stable valley. This observation has been verified by demonstrating that small torsional deformations at the FC and the following points produce an energy increase. In contrast, the hypersphere energy minimum at the 1.5 au cross-section corresponds to a ca. 12 twisted structure (HM), indicating that

the potential energy surface at this distance has the shape of an unstable energy ridge.

A rigorous demonstration of these features requires the evaluation of the vibrational frequencies along the (n-1)-coordinate space orthogonal to the computed MEP. The results of analytical frequency computations at 0.25 au and 0.75 au distance from FC and at HM confirm that a gradual change in surface shape occurs along the MEP. In particular, the change from a valley shape to a ridge shape must be localised between 0.25 and 0.75 au along the path. In fact, the frequencies corresponding to the torsional mode have a real value (212 $cm^{-1}$) at 0.25 au distance which becomes imaginary (239 i $cm^{-1}$) at 0.75 au, indicating the presence of a ridge. The curvature becomes larger (frequency 264 i $cm^{-1}$) at the stationary point located at 1.70 au. This stationary point is, therefore, a transition structure with respect to the central bond torsion.

### 6.1.2. Bimodal Excited State Relaxation and Qualitative Dynamics

The complete excited state and ground state energy profile describing the cis → trans photoisomerization path of the *cis*-$C_5H_6NH_2^+$ is shown in Figure 6–3. The reaction coordinate analysis along the $S_1$ and $S_0$ branches of the MEP shows that the cis → trans isomerization coordinate is a combination of three coupled modes: (1) twisting about the central double bond, (2) symmetric stretching of the central -CH-CH=CH-CH- fragment, and (3) in-phase stretching of the $CH_2$=CH- and -CH=$NH_2^+$ terminal fragments. In particular, the comparison of structure FC and of the slightly twisted structure located at

1.5 au (see the $S_1$ energy profile shown in Figure 6–3) reveals that the initial relaxation is dominated by double-bond expansion and single-bond contraction.

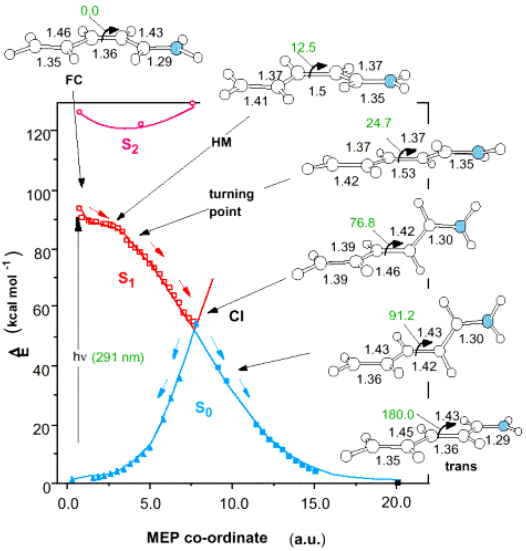


Figure 6–3: Adapted from ref. 133. Energy profiles along the three minimum energy path (MEP) describing the relaxation from the **FC** and **CI** points. Open squares and full squares curves define the excited ($1B_u$-like) and ground state branches of the cis-trans photoisomerization path. Full triangles define the ground state cis back-formation path. Open circles show the dark ($2A_g$-like) state energy along the excited state branch of the photoisomerization path. The structures (geometrical parameters in Å and degrees) document the geometrical progression along the photoisomerization path.

While the initial acceleration involves exclusively mode 3, the direction of the relaxation changes rapidly and already at 1.0 au along the MEP coordinate, mode 2 has strongly mixed with mode 3 leading to a large expansion of the cis double bond and contraction of the two adjacent bonds. It is clear that at 1.0 au the expansion along mode 3 is completed and the stretching motion becomes dominated by mode 2. Beyond this point, the torsional deformation mode 1 begins, and at 1.5 au (corresponding to the ca. 12 twisted HM structure with a 1.50 Å expanded cis double bond), the stretching along mode 2 is strongly mixed with mode 1. The stretching along mode 2 terminates at a "turning point" where the molecule has a 1.53 Å expanded central double bond but is only 25° twisted. Remarkably, the $S_1$ branch of the isomerization coordinate (open squares) correlates nicely with the $S_0$ branch (full squares) demonstrating that the $S_1$ relaxation coordinate *continues* on the ground state.

As shown in Section 6.1.1, the excited state energy surface of *cis*-$C_5H_6NH_2^+$ is characterized by a valley along the initial part of region I and by a gradual change of this valley into a ridge in region II. The structure of these regions rationalises the excited-state dynamics (see trajectory illustrated in Scheme 6–2).

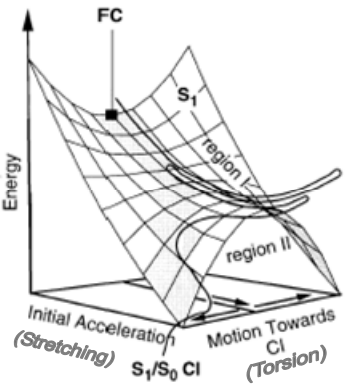


Scheme 6–2

The result of *ab initio* "on the fly" semi-classical trajectory computations[138] (for an explanation of this terminology the reader refers to Section 6.3) demonstrated that after initial acceleration through region I, the motion of the system involves high-frequency (ca. 1450 $cm^{-1}$) totally symmetric stretching oscillations. The $S_1$ skeletal oscillations can last for a few oscillations (several tens of femtoseconds) before torsional motion is initiated. However, each oscillation must pass through the highly anharmonic region II. Therefore, in the presence of a small torsional perturbation, the molecule will rapidly accelerate along the non-totally symmetric torsional mode. The steep slope connecting region II to the **CI** point will provide an increasing acceleration along the torsional coordinate. In other words, the structure of this PES induces intramolecular vibrational energy redistribution (IVR) from stretching to the torsional modes and then further acceleration along the torsional coordinate.

The results of reaction path computations for longer retinal PSB[137,139,149,155] show that the ultrafast excited-state evolution of the chromophore can be understood in terms of the same two-state two-mode model.

### 6.1.3. Multistate Excited State relaxation: Sequential Photochemical Funnels

This section discusses the origin of the observed high stereoselectivity of the photochemical *s-cis* buta-1,3-diene ring closure. This reaction provides an example where two different excited state energy surfaces ($S_2$ and $S_1$) are involved in the photochemical reaction path. In the ground state, the pericyclic reaction, which leads to the production of cyclobutene, occurs through a conrotatory motion of the two terminal methylenes of the diene. In fact, the transition state associated with this direction of rotation is more stable than the transition state that defines the disrotatory motion. Thus, the reaction is stereoselective and only the conrotatory stereoisomer is produced.
The photochemical ring closure reaction yields exclusively the disrotatory stereoisomer. The explanation of the photochemical stereoselectivity is more difficult because it cannot be easily related to a preferred conformation of a transition state structure. Anyway, it has been demonstrated[156] that the cyclobutene ring is formed via decay at the *s-cisoid* conformer of a $S_1/S_0$ conical intersection point. Therefore, it appears natural to assume that, ultimately; it must be the preferred conrotatory (*con*) or disrotatory (*dis*) orientation of the two terminal methylenes in this structure to determine the stereoselectivity of the reaction. Thus, to rationalize the disrotatory

stereochemical preference it is necessary to determine the way in which the cis or dis conformation may be generated during the photolysis.
The experimental work of *Trulson* and *Mathies*[82] has shown that the direct irradiation of butadiene at 254 nm promotes *s-cis* buta-1,3-diene to the $S_2$ state ($1B_2$ state corresponding to a single excitation from HOMO to LUMO of the π-system) and not to the $S_1$ state ($2A_1$ state corresponding to a double excitation from HOMO to LUMO).

The $S_2$ and $S_1$ potential energy surfaces and the relaxation path starting at the FC point on $S_2$ have been fully investigated in ref. 117, 157. In Figure 6–4 are shown the results of the computations of the reaction path spanning the $S_2$, $S_1$ and $S_0$ states of *s-cis* buta-1,3-diene that have $1B_2$, $2A_1$ and $1A_1$ symmetries respectively.
The initial relaxation on the $S_2$ energy surface (path VII) leads to an energy minimum of $C_s$ symmetry ($C_s$-ION) which features two 32° twisted $CH_2$ groups shown in Figure 3–4 (top). Thus along path VII one has the asynchronous *disrotatory* rotation of the two terminal methylenes, in agreement with the W. H. rules. Remarkably at this energy minimum the $S_1$ energy surface crosses the $S_2$ energy surface thus promoting a fully efficient $S_2 \rightarrow S_1$ decay. A relaxation path (path VI) starting at the $S_2/S_1$ conical intersection ends in the region of a $C_s$-MIN structure again through a motion involving a disrotatory rotation of the two terminal methylenes. The relaxed $S_1$ buta-1,3-diene has two distinct conformers ($C_s$-MIN and $C_2$-MIN) which differ for the relative direction of twisting of the two terminal methylenes. However, the most stable conformer and the one that gets populated upon decays corresponds to $C_s$-MIN where the terminal methylenes are ca. 50° twisted in a disrotatory fashion.

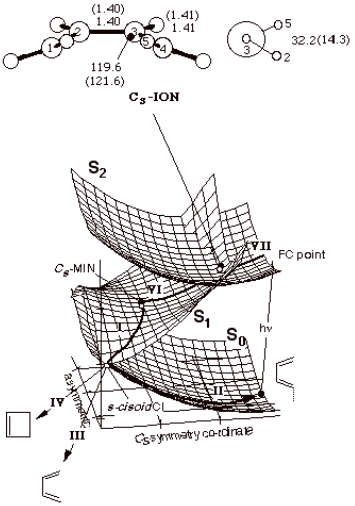


Figure 6–4: Adapted from ref. 144. Three dimensional representation of the photochemical $S_2 \rightarrow S_1 \rightarrow S_0$ reaction path for *s-cis* buta-1,3-diene from the reactant ground state equilibrium structure (the Franck-Condon (**FC**) point) to the photoproducts. Paths **VI** and **VII** indicate the relaxation from the spectroscopic state $S_2$. Path **I**, **II**, **III**, **IV** correspond to the paths illustrated in subsequent Figure 6–5. Full circles indicate equilibrium structures and open circles indicate decay channels (conical intersections).

The following relaxation of $C_s$-MIN occurs along path I leading to a $S_1/S_0$ conical intersection point (*s-cisoid*). The $S_0$ relaxation paths starting from the *s-cisoid* conical intersection are shown in Figure 6–5. Path **II** describes the reactant back formation process. Path **III**, **IV** and **V** are photochemical paths since they all describe reactive processes. In particular, path **III** describes a (single) double-bond isomerization, path **IV** cyclobutene formation and path

**V** describes the *stepwise* formation of bicyclobutane via a cyclopropylcarbonyl diradical.

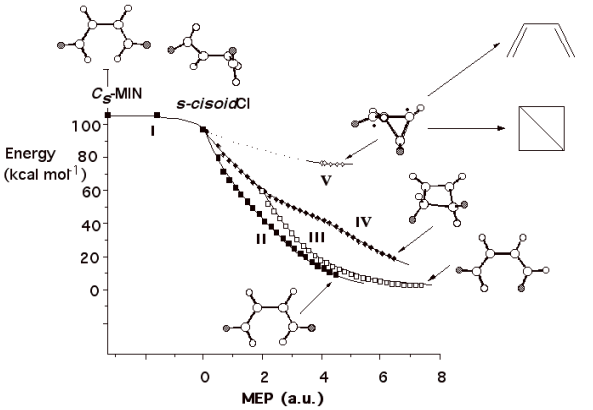


Figure 6–5: Adapted from ref. 20. *s-cis* buta-1,3-diene ground state relaxation paths departing from the *s-cisoid* conical intersection conformer. Path **II** (full squares) leads to reactant back formation. Path **III** (open square) leads to double bond *E*/*Z* isomerization. Path **IV** (full diamonds) leads to ring closure and, finally, path **V** (open diamonds) leads to a cyclopropyl diradical. The $S_1$ relaxation path **I** (full squares) connecting *Cs*-MIN and the conical intersection is also reported. All energy profiles are computed using the CAS(4,4)/DZ+d level of theory.

Inspection of the $CH_2$ deformation along the product formation paths given in Figure 6–5, shows that the path leading to cyclobutene production (path IV) describes a disrotatory motion of the two terminal methylenes. This is in good agreement with the production of the experimentally observed cyclobutene stereoisomer.

In conclusion, in agreement with both the W. H. rules and the experimental results, the ab initio CASSCF and CASPT2 computations (see Appendix) of the photochemistry of *cis*-butadiene demonstrate that:

1. The direct vertical excitation of *s-cis* buta-1,3-diene promotes the system to the $1B_2$ state as the first excited state.
2. The relaxation from the $1B_2$-excited state to the $1A_1$ ground state is characterize by the presence of two conical intersection points. The first point involves the spectroscopic $1B_2$ state and the dark $2A_1$ state while the second corresponds to the crossing between the $2A_1$ and $1A_1$ states.
3. There are two different paths which lead to the same $S_1/S_0$ conical intersection. They differ with respect to the direction of rotation of the two terminal methylenes which can be conrotatory or disrotatory. The latter is barrierless while the conrotatory motion has a barrier that is 7 kcal $mol^{-1}$ higher in energy. Thus, the formation of the disrotatory stereoisomer is favoured.
4. The following relaxation from the $2A_1/1A_1$ conical intersection yields to a mixture of cis-trans isomerization and cyclization products.

## 6.2. Ground State Relaxation

### 6.2.1. Computation of Multiple Initial Relaxation Directions

In Section 4.1 it was stressed that the search for a photochemical reaction path requires the computation of two branches. One begins on the excited state and ends at a point on a conical intersection where decay to the ground state occurs; the other branch describes the evolution of the system on the ground state from the decay point to the final product. Thus, an accessible conical intersection forms a bottleneck that separates the excited state branch of a non-adiabatic photochemical reaction path from the ground state branch. The nature of the products generated following decay at a surface crossing will depend on the ground state valleys (reaction paths) that can be accessed from that particular structure. The conical intersection can connects the excited state reactant to two or more products on the ground state via a branching of excited state reaction path to several ground state relaxation channels. If the base of the cone is circular (as in Figure 6–6) one has an infinite number of equivalent relaxation pathways on the ground state surface. On the other hand, if the base of the cone is elliptic (as illustrated in Figure 4–3) then there are two relaxation pathways corresponding to the steepest sides of the cone (minor axis of the ellipse). More generally, a number of relaxation pathways may exist at the apex of the cone, and others may develop further down the manifold, all influencing product formation.

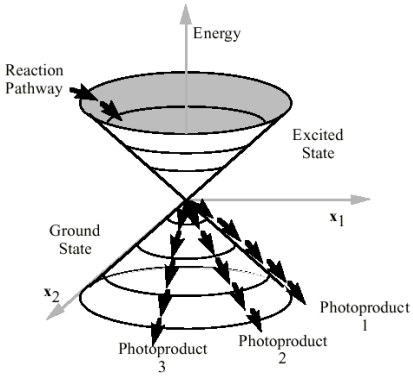


Figure 6–6: Schematic of a photochemical reaction path involving a conical intersection. The path starts on the excited state potential energy surface and decay to the ground state potential energy surface through a conical intersection to the formation of different products. The different ground state relaxation paths starting from the conical intersection and leading to Photoproduct 1, 2 and 3 respectively are shown.

In this section the focus will be on the computation of ground state branch of the photochemical reaction path and in particular, it will be outlined how the initial relaxation direction (IRD) method (already described, in general, in Section 4.3 and in Section 6.1.1 to locate the initial direction of relaxation from the FC point) is used to locate the initial relaxation directions (IRDs) from the tip of a conical intersection. The MEP generated from each IRD, which define the ground state product-formation path, provides a natural continuation of the excited state MEP connecting the photoexcited reactant to the conical intersection (i.e., excited state branch).

As illustrated in Scheme 6–3 the MEP connecting the reactant to the product of a thermal reaction is uniquely defined by the associated transition structure

(TS). The direction of the transition vector (i.e., the normal coordinate corresponding to the imaginary frequency of the TS) is used to start a MEP computation. One takes a small step along this vector (shown as $\tau$ in Scheme 6–3) to points $M_1$ and $M_2$ and then follows the steepest descent paths connecting this point to the product or reactant wells. The small step vector $\tau$ defines the IRD toward the product (taking the positive direction of $\tau$) or reactant (taking the negative direction of $\tau$). This procedure cannot be used to find the IRD for a photochemical direction since there is no such unique direction $\tau$ for the first step. As clear from Figure 6–6 the conical intersection vertex forms a singularity on each adiabatic potential energy surface (excited and ground state potential energy surfaces) since its slope and curvature along $x_1$ and $x_2$ are not smooth function of the molecular deformation. The initial motion, which lifts the degeneracy, lies in the $x_1$, $x_2$ branching plane.

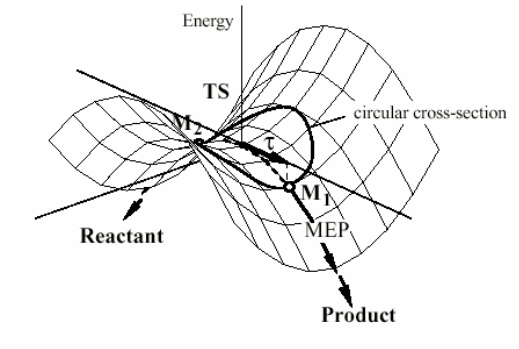


Scheme 6–3

One can devise a simple alternative procedure for defining the **IRD** at **TS** that does not use the transition vector $\tau$. If one computes the energy of the system

along a circular cross section centred on the TS as illustrated in Scheme 6–3, then provided that the radius of the circle is small enough, the energy minima $M_1$ and $M_2$ located on the circular cross section provide an alternative but equivalent definition of the direction of relaxation toward the product and reactant.

Following, it will be shown how the **IRD** can be defined in an analogous manner for a conical intersection. Figure 6–7b shows the potential energy surface for a model "elliptic" conical intersection plotted along the $x_1$, $x_2$ branching plane. Because the cone is elliptic there are two steep sides of the ground state cone surface and two ridges. It is obvious that there are two preferential directions of downhill motion located on the steep sides of the ground state cone surface. Analogous to the case of a transition state, a simple procedure for defining these directions involves the computation of the energy profile along a circular cross section of the branching plane centred on the vertex of the cone as illustrated in Figure 6–7b. This energy profile is given in Figure 6–7c as a function of the angle $\tau$ and for a suitable choice of the radius d.

It can be seen that the energy profile contains two different energy minima, $M_1$ and $M_2$. These minima uniquely define two IRDs from the vertex of the cone. The two steepest descent lines starting at $M_1$ and $M_2$ uniquely define two MEPs describing the relaxation processes. Notice that there are also two energy maxima $TS_{21}$ and $TS_{12}$ in Figure 6–7c. These can be interpreted as the transition structures connecting $M_1$ and $M_2$ along the chosen circular cross section. It can be seen in Figure 6–7b that these transition structures locate the energy ridges that separate the IRD valleys located by $M_1$ and $M_2$. Thus, while there is no analogue of the transition vector for a conical intersection,

the simple case of an elliptic cone shows that the IRDs are still uniquely defined in terms of $M_1$ and $M_2$.

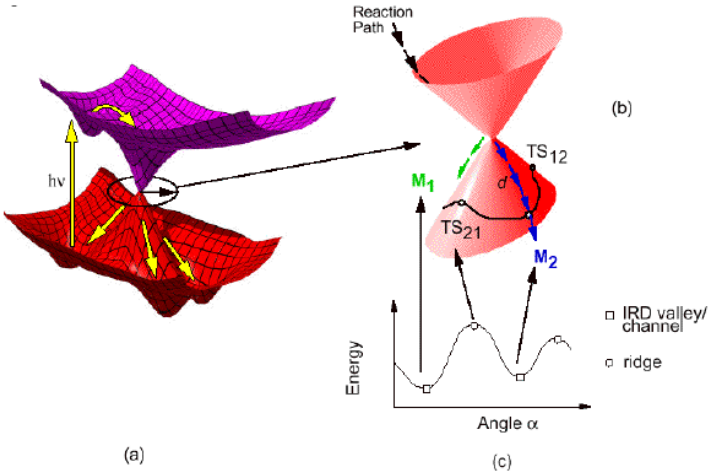


Figure 6–7: This picture illustrates the general procedure used to locate the initial relaxation direction (IRD) toward the possible decay products. (a) General photochemical relaxation path leading (via conical intersection decay) to three different final structures, (b) potential energy surface for a "model" elliptic conical intersection plotted in the branching plane, and (c) corresponding energy profile (as a function of the angle $\alpha$) along a circular cross section centred on the conical intersection point and with radius d.

The elliptic cone model of the potential energy surface at a conical intersection point discussed above is not general enough to give a correct description of all relaxation paths for a real system. Firstly, there may be more than two possible IRDs originating from the very beginning of the tip of the cone. Secondly, the first order approximation (i.e., elliptic cone) may

break down at larger distances and some IRD may lie "out" of the branching plane since the real $(x_1, x_2)$ space is, in general, curved.[109] However, the ideas introduced above can be easily extended to search for IRDs in the full n-dimensional space surrounding a conical intersection point by replacing the circular cross section with a hyperspherical cross section centred at the vertex of the cone as shown in Figure 6–8. Thus, the search for energy minima in a one-dimensional circular cross section (i.e., the circle in Figure 6–7a) is merely extended to a (n-1)-dimensional spherical cross section (i.e., hypersphere) of the ground state potential energy surface. The IRDs will then be defined by the energy minima located on the hypersphere. If the radius d defining the sphere is small enough, this hyperspherical cross-section must contain the "starting points" for *all* relaxation paths departing from the cone vertex even if they are located far from the branching plane $(x_1, x_2)$ as illustrated in Figure 6–8.

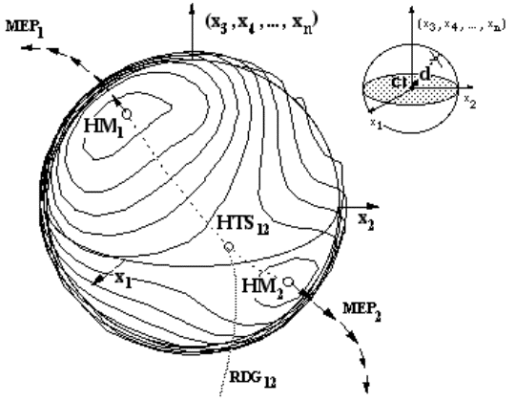


Figure 6–8: Spherical contour plot illustrating the behaviour of $\mathbf{E_{gs}}$ along a hyperspherical cross section centred on a non-ideal (*i.e.* non-elliptic) conical intersection point. The direction of the "ideal" tangent branching plane and tangent intersection space are also illustrated in the figure. Notice that the position of the hyperspherical energy minimum $\mathbf{HM_1}$ lies well above the branching plane. $\mathbf{HM_1}$ is connected to a second minimum $\mathbf{HM_2}$ via the "transition structure" $\mathbf{HTS_{12}}$. These minima on the hypersphere define two MEP in the full co-ordinate space of the system which describes the two distinct relaxation paths on the ground state potential energy sheet. Similarly $\mathbf{HTS_{12}}$ defines an energy ridge ($RDG_{12}$) which separates the two energy "valleys" where relaxation can occur.

The next section presents an example of application of the strategy illustrated above for the description of the radiationless decay and competitive photoproduct formation process in cyclohexadiene (CHD)/cZc-hexatriene (cZc-HT) system.

### 6.2.2. Are Quantum Yields Predictable?

It has been shown in the previous section that the ground state relaxation paths departing from a conical intersection point can be unambiguously defined and computed. Such information should provide a detailed description of the reaction mechanism for photoproduct formation through decay at a conical intersection. The following example illustrates the strategy outlined in the previous section. It will be demonstrated how the correct determination of the ground state relaxation paths, namely a purely structural (i.e., non-dynamics) information, may be used to predict the quantum yield of a reaction.

In ref. 113 has been reported a theoretical study of the first singlet excited state ($2A_1$) of cZc-hexa-1,3,5-triene (cZc-HT) and cyclohexadiene (CHD). These molecules are important active centres of many photochromic materials[158] and can be photochemically interconverted via direct irradiation experiments[159]. The conical intersection geometry that has been optimised on the $S_1$ surface for the CHD/cZc-HT photochemical interconversion ($CI_{CHD}$) is shown in Figure 6–9. This structure has a characteristic -$(CH)_3$- kink (this geometric triangular arrangement is typical of polyene conical intersections as already seen in Section 5.3.3), and three different ground state re-coupling paths are possible, as shown below. Thus one expects to find three ground state reaction pathways corresponding to the three different re-coupling patterns involving the triangular kink.

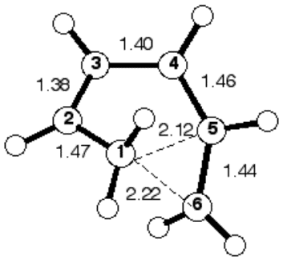


Figure 6–9: Top view of the *ab initio* optimised conical intersection structure $\mathbf{CI_{CHD}}$. The relevant geometrical parameters are given in Å.

Computational[113,150] and experimental[92,93,160,161] investigations of this problem showed that there are two almost equivalent relaxation paths, which will be populated after decay from the conical intersection: one leading to cyclohexadiene and the other to hexatriene, with very similar quantum yields. In particular, irradiation at 254 nm transforms 2,5-di-tert-butylhexa-1,3,5-triene (Scheme 3–4, left side) into the corresponding cyclohexadiene with a 0.54 quantum yield. The reverse reaction transforms 1,4-di-tert-butylcyclohexa-1,3-diene (Scheme 3–4, right side) into the corresponding hexatriene with a 0.46 quantum yield.[160]

Scheme 6–4

Consistently, the computed structure of the low-lying part of the $S_1$ ($2A_1$) potential energy surface of these molecules shows that both the direct (CHD → *cZc*-HT) and reverse (*cZc*-HT → CHD) photochemical reactions involve

the formation and decay of a common excited state intermediate (see Figure 6–10).

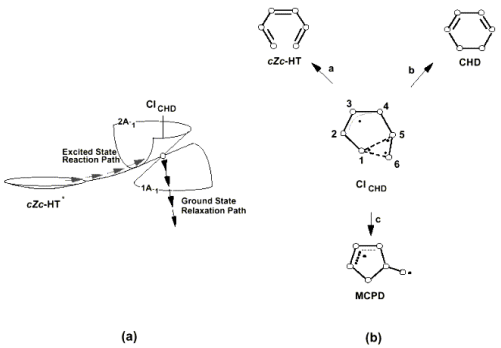


Figure 6–10: (a) the cyclohexadiene (CHD)/cZc-hexatriene (cZc-HT) photoconversion problem involves the formation of a common excited state intermediate (cZc-HT*) and its decay via a conical intersection point ($CI_{CHD}$). (b) Due to the tetraradical electronic nature of $CI_{CHD}$, relaxation on $S_0$ may occur along three different routes (a, b and c) associated with different bond formation modes and different recouplings. (From ref. 150).

This intermediate corresponds to excited state *cZc*-HT (*cZc*-HT*) and it is predicted to decay to the ground ($1A_1$) state via a conical intersection ($CI_{CHD}$) which has been located ~1 kcal $mol^{-1}$ above *cZc*-HT*.

Given the tetraradical electronic nature of this relaxation from $CI_{CHD}$ may occur along three different routes as illustrated in Figure 6–10b. Each route is associated with a different bond formation mode which is, in turn, driven by the re-coupling of four weakly interacting electrons. Accordingly, route **a** leads to relaxation towards *cZc*-HT, route **b** leads to CHD and route **c** leads

to a methylenecyclopentene diradical (MCPD). The initial relaxation directions from the $CI_{CHD}$ have been located with the IRD method discussed in the previous section and the results are illustrated in Figure 6–11.

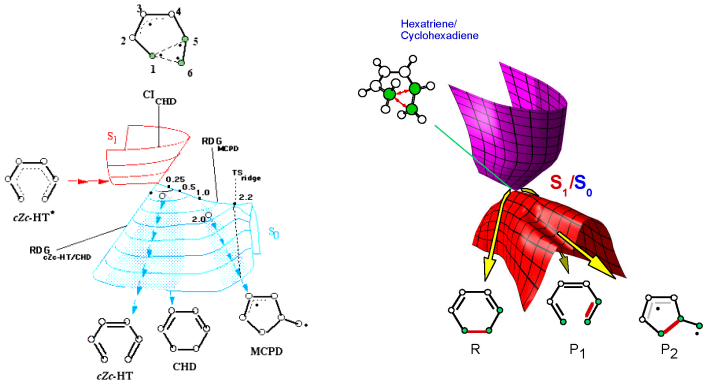


(a) (b)

Figure 6–11: (a) Key structural features controlling the product-formation process resulting from the decay of the $2A_1$ excited state intermediate ***cZc*-HT***. White areas represent energy ridges (RDG) and shaded areas represent energy valleys. (b) another viewpoint, in evidence the route c.

The *cZc*-HT* intermediate which is produced by either CHD or *cZc*-HT irradiation, decays via a facile vibrational displacement leading towards the $CI_{CHD}$ decay point. After decay, the reaction path bifurcates along two ground state relaxation valleys leading to CHD and *cZc*-HT. A third relaxation valley leading to MCPD is not directly connected to the conical intersection point $CI_{CHD}$ and originates after the energy ridge $RDG_{MCPD}$ splits into two new ridges (comprising the MCPD "valley") around 1.0 $amu^{1/2}$ bohr distance from the decay point.

The distance of the initial part of the CHD, *cZc*-HT, MCPD valleys (see shaded regions in Figure 6–11) from the decay point and the magnitude of their slope provide qualitative information on the extent of the "catchment region" associated with a specific photoproduct (see Figure 6–12). A valley (i.e. a MEP determined via IRD computations) which develops close to the conical intersection point and which is lower in energy will be associated with a larger "catchment region" and therefore there will be a higher probability of populating the associated valley upon decay from the conical intersection. Figure 6–12 suggests that the size of the CHD and *cZc*-HT "catchment regions" must be similar. Thus one can expect that the decay of *cZc*-HT* will generate the products CHD and *cZc*-HT with similar yields. Hence, the photolysis of CHD is predicted to generate *cZc*-HT with a quantum yield $\Phi_{cZc\text{-HT}} < 1$ because of the competitive CHD back formation. The MCPD product formation path is, initially, topologically inhibited since, in the immediate vicinity of the conical intersection it corresponds to a ridge (*i.e.* $RDG_{MPCD}$) and ridge-like paths will be only populated at very large kinetic energy. For this reason, the photolysis of either CHD or *cZc*-HT must have a similar outcome. In fact, since both these reactants yield the same *cZc*-HT* $2A_1$ intermediate *cZc*-HT is predicted to yield CHD with a quantum yield $\Phi_{cZc\text{-HT}\rightarrow \text{CHD}}$ which is related to the quantum yield of *cZc*-HT produced via CHD photolysis ($\Phi_{\text{CHD}\rightarrow cZc\text{-HT}}$) by the relation $\Phi_{cZc\text{-HT}\rightarrow \text{CHD}} \approx (1 - (\Phi_{\text{CHD}\rightarrow cZc\text{-HT}})$.

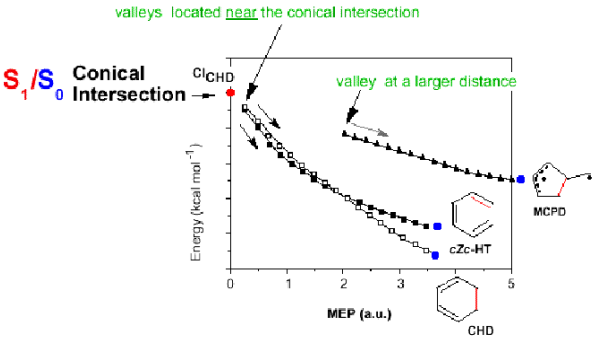


Figure 6–12: Adapted from ref. 21. Energy profiles of the three valleys located around the conical intersection $CI_{CHD}$.

The interpretation of the CHD/*cZc*-HT photolysis just presented is compatible with the available experimental data. The ca. 1 kcal mol$^{-1}$ excited state energy barrier computed via multireference MP2 theory is consistent with the observed picosecond lifetime of the $2A_1$ state following CHD direct irradiation.[93,a] While there are no measurements of $\Phi_{CHD \rightarrow CHD}$ (*i.e.* CHD back-formation during photolysis of CHD) or $\Phi_{cZc\text{-}HT \rightarrow CHD}$ (*i.e.* CHD formation during photolysis of *cZc*-HT), $\Phi_{CHD \rightarrow cZc\text{-}HT}$ is 0.41[93] *i.e.* suggesting efficient CHD back-formation. On the other hand, irradiation of 2,5-di-*tert*-butylhexa-1,3,5-triene produces 1,4-di-*tert*-butylcyclohexa-1,3-diene with a 0.54 quantum yield. The reverse reaction occurs with a 0.46 quantum yield[160] in agreement with the predicted relationship $\Phi_{CHD \rightarrow cZc\text{-}HT} \approx (1 - (\Phi_{CHD \rightarrow cZc\text{-}HT})$. In other substituted and polycyclic molecules[161] steric and strain effects may greatly differentiate the slopes of the CHD and *cZc*-HT valleys leading

[a] However, recent experiments by *Sension* and coworkers (see ref. [92]) have indicated a $2A_1$ lifetime of about 1 ps.

to values of $\Phi_{CHD}$, $\Phi_{cZc\text{-}HT}$ far from 0.5. However, the relationship given above appears to hold even in these cases.[113]

### 6.2.3. The Relationship between Thermal and Photochemical Reaction Paths

In order to gain insight into the mechanism of the $S_1 \rightarrow S_0$ decay process, it is of interest to clarify the relationship between the shapes of the $S_1$ and $S_0$ energy surfaces in the **CI** region. In general, the shape of the excited and ground state potential energy surfaces in the region of a conical intersection corresponds to that given in Scheme 6–5 where the energies are reported along the special pair of geometrical coordinates $X_1$ and $X_2$. There are two basic large-scale topographic features of the energy surface. First, the excited state branch of the reaction coordinate ends at the conical intersection point where the system decays to the ground state. Second, the ground state energy surface comprises a circular valley, centred at **CI**, comprising two energy minima $M_1$ and $M_2$ and two transition structure $TS_1$ and $TS_2$. Thus after photoexcitation of $M_1$ the excited state reactant M* evolves along the excited state branch of the reaction coordinate and, after decay at CI, generates a photoproduct $M_2$. According to the ground state surface shape this photoproduct may revert to the initial material thermally by overcoming one of the two transition states.

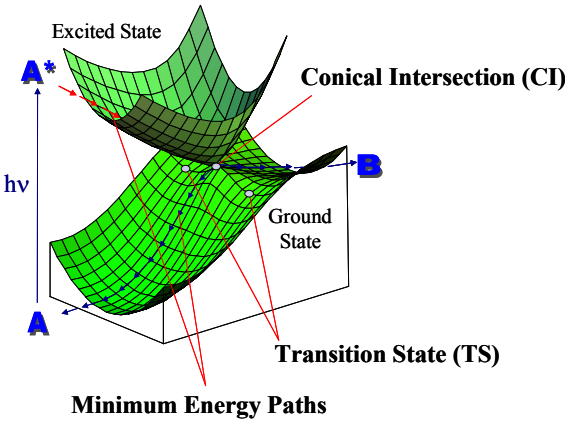


Scheme 6–5

The Introduction chapter distinguished between *successful* and *unsuccessful* photochemical reactions. In a *successful* bimolecular reaction reversion to $M_1$ will not occur and the product will accumulate in $M_2$ (of course in the presence of a moderate $M_2 \rightarrow TS$ barrier the product may slowly regenerate the reactant). Furthermore the part of the excited state material that, at the CI, decays back towards the initial reactant will undergo further photoexcitation thus returning to **CI.** This situation is schematically illustrated in Scheme 6–6a. This type of reaction path has been reported for a number of organic photochemical reactions comprising photoisomerizations (visual pigments, photochromic materials, linear conjugated hydrocarbons), ring-openings (chromene based photochromic materials) and rearrangements (benzene valence isomerizations.[20,78]

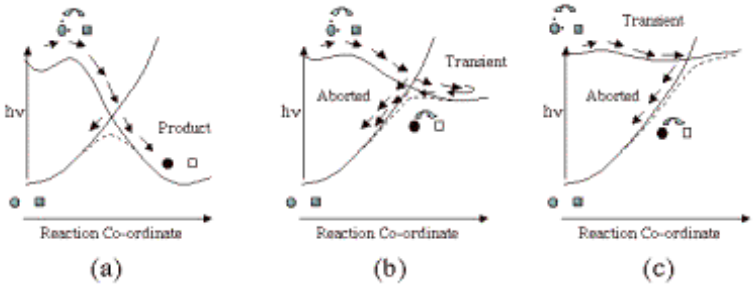


Scheme 6–6

The possible existence of unsuccessful photochemical bimolecular reactions is illustrated, on the basis of the energy surface topology given above, by Scheme 6–6b and Scheme 6–6c. When the ground state $M_2$ minimum is much higher in energy than $M_1$ and the $M_2 \rightarrow$TS barrier is very small one has the formation of a transient intermediate that will efficiently revert back to the initial reactant. For bimolecular events the rate of the reactant back formation may be comparable or even higher than the diffusion rate. Notice that in order to achieve the reaction path shape of Scheme 6–6b one needs to destabilize the electronic configuration corresponding to the $M_2$ minimum. Making a parallel with conventional correlation diagrams, this electronic structure correlates with the electronic structure of the excited state. A even less stable $M_2$ implies a flatter excited state curve. The same effect also leads to a change of the conical intersection shape. Following the nomenclature of Ruedenberg, the shape of the **CI** changes from strongly "peaked" to slightly peaked (or nearly "intermediate") going from a successful (Scheme 6–6a) to an unsuccessful (Scheme 6–6b) event. This implies a much larger slope of the $CI \rightarrow M_1$ ground state relaxation path leading to reactant back formation via an aborted chemical process. As previously shown for a photochemical

electrocyclic ring openings, a larger slope is usually associated with a larger valley.[150] As a result one expects that a larger fraction of the M* population decays directly towards the $M_1$ minimum thus further limiting the efficiency of $M_2$ production. In other words, through this path the photochemical reaction is aborted.

A further change in stability of the $M_2$ region would lead to a fully flat or even repulsive change in slope of the energy profile connecting M* to $M_2$ through **CI.** In this case the flat $M_2$ minimum may exist on the excited state rather than on the ground state energy surface as illustrated in Scheme 6–6c. Furthermore the conical intersection, which will now have an "intermediate" or "sloped" shape, will occur after the excited state minimum. Consequently in this case one predicts the formation of an excited state intermediate whose lifetime must be controlled by the barrier (or excited state energy difference) that has to be overcome to reach the **CI.** In this case the photochemical event is fully unsuccessful and the only existing relaxation path corresponds to an aborted chemical process. For a review one can see ref. 162.

Section 9.6 will show the relationship between transition structures on the ground state and nearby conical intersection for coexisting photoisomerization paths in *all-trans*-retinals. It will be shown how the shape of a conical intersection can induce changes also on the shape of the ground state, allowing the presence of one or two transition structure.

## 6.3. Semiclassical Trajectory and Wavepacket Dynamics Computations

Although in the present thesis trajectory computations will not be used, this section gives an overview of the methodology, that can be used to investigate the dynamics of excited state species. The structural analysis of critical points, crossings and minimum energy paths on the potential energy surfaces form the basis for static, i.e. non-dynamical, description and characterisation of a photochemical reaction. A full understanding of the factors that govern the photochemical reactivity can only be obtained applying molecular dynamics (MD) simulations. Nowadays, dynamics simulations are widely used to study chemical reactions in general or to deal with specific problems, such as diffusion or protein folding, but are crucial to describe ultra fast photochemical processes. A dynamic treatment can, in fact, provide information on the photochemical decay channel, on the timescale of the system evolution and on the quantum yields of the reaction. This information is becoming more and more important, because of the recent results coming from femtosecond spectroscopy and ultra fast laser techniques.

MD calculations are based on the idea of trajectory, which classically derives from the integration of the equations of motion. The trajectory can describe the positions, velocities and accelerations of a particle as they vary with time. Thus, the MD offers the possibility of a step by step mapping of the reaction path, which connects the reactant to the product, providing a series of "snapshots" of the system of atoms or molecules. However, a classical trajectory will not follow the MEP if the system on the excited state branch of the reaction coordinate possesses a high excess of vibrational energy. The

momentum developed on the excited state surface can be high enough to deviate the ground state trajectory from the ground state MEP. Two limiting situations are possible: (a) the trajectory is not representative of the "average" dynamic behaviour of a statistically meaningful initial ensemble of photoexcited molecules or (b) all trajectories belonging to such an ensemble span regions of the PES far from the MEP. In the first case the MEP provides a correct representation of the average dynamic behaviour of a photoexcited reactant. In contrast in case b the MEP only provides information of the surface structure but not on the reactive motion.

In a different language, it is also possible to say that the centre of the vibrational wavepacket prepared on the excited state follow the MEP or run away from the MEP. In general trajectory of small reactive systems (e.g., triatomics) in the gas phase or in isolated conditions my deviate considerably. On the other hand, the information derived from a MEP approach is usually a correct description of the photochemical reaction mechanism where the excited state reactants are vibrationally "cold" such as those found in solutions, in cold matrices or in sizable organic molecules. More in general MEP and trajectory computations provide highly complementary information on the reaction mechanism and dynamics.

In classical trajectory calculations, the nuclear motion is assumed to be classical and is obtained solving the Newton's equations of motion that are numerically integrated on a single *Born-Oppenheimer* (BO) surface. In many applications the integration can be done using a known analytical function that represents the PES that is, for example, a molecular mechanics forcefield or a parameterised function obtained by fitting the experimental and computational data. No Hessian evaluation is required so very small timesteps are possible. Unfortunately, the classical molecular mechanics

forcefields are not accurate enough to describe the complex bond making and bond breaking processes that occur in a photochemical reaction. On the other hand, the fitted functions have a limited applicability. Another drawback of such molecular dynamics methods is that the quantum mechanical effects, such as tunnelling, and the quantization of the vibrational energy level are not considered. Furthermore, they cannot describe the transition between potential energy surfaces and this is particularly important in the photochemical reactions where more than one PES is involved. A quantum mechanical treatment has to be included in the dynamics simulations to describe the decay at a conical intersection.

A rigorous treatment of the nuclear and electronic motion can be gained following the wavefunction evolution by the time-dependent Schrödinger equation (see Section 3.1)

$$\hat{H}(t)\left|\Psi(t)\right\rangle = i\hbar\frac{\partial\left|\Psi(t)\right\rangle}{\partial t} \qquad (6\text{–}1)$$

Under the *Born-Oppenheimer* approximation, which allows treating the motion of the nuclei separately from the motion of the electrons, is possible to follow the motion of the system as a function of the nuclei, known as a delocalised quantum wavepacket that evolves on the potential energy surface (provided by the motion of the electrons) according to the time-dependent Schrödinger equation. The wavepacket dynamics application, in which the time-dependent Schrödinger equation can be solved directly, is limited to systems with 3-6 degrees of freedom. This is done by solving the equations presented in Section 3.1.

The multi-configuration time-dependent Hartree (MCTDH) method offers the possibility to study systems with less than 30 degrees of freedom.[163]
A semiclassical approach has been introduced to apply wavepacket dynamics simulations also to larger systems. The semiclassical or quasi-classical methods employ different level of theory: namely, they use a full quantum chemical approach to solve the electronic problem and an approximation, based on trajectories, to treat the nuclear motion.
In the *Born-Oppenheimer molecular dynamics*[164] the nuclear wavepacket motion is emulated by a large number of pseudo-particles trajectories, called "swarm" of trajectories, driven by the classical Newton's equations of motion.

The nuclear wavepacket can be described also by one or more Gaussian functions as it is implemented in the *Gaussian wavepacket method*.[165]
In 1990, *Helgaker* and co-workers[166] developed a new method that overcomes the problem of studying systems with many degrees of freedom. In the so called *"direct dynamics"*, in fact, the potential energy surface is never computed completely but the gradient which drives the nuclear motion is evaluated "on the fly" from an adiabatic wavefunction at each step during the dynamics simulation. This is achieved computing a series of local second order model surfaces along the trajectory. Using this quadratic approximation, the timestep has to be sufficiently small in order to minimize the anharmonic contribution. The region around the expansion point for which the quadratic approximation is valid is referred to as the *trust-region* and a trust radius determines the stepsize. In order to increase the stepsize and since the rate-limiting step of this method is the computation of the local

second order model surface, *Chen* and co-workers in 1994[167] proposed a method in which a local fifth-order surface is used.

More recently, *ab initio* semiclassical trajectory calculations based on direct dynamics have been reported where the gradient is computed at CASSCF level. Even if running CASSCF trajectories is still a computationally expensive tool, its implementation significantly increases the accuracy of the investigation of photochemical reactions. The CASSCF method in fact is the most suitable method for the computation of the excited states properties. Furthermore, CASSCF is particularly appropriate for direct dynamics because permit the gradient to be calculate analytically and with a relatively low computational cost.

In principle, the motion of a wavepacket can be "simulated" using a suitable ensemble of semiclassical trajectories. In fact, in a semiclassical description, the initial wavepacket has to be represented by an appropriate set of initial positions and momentum. Given an initial geometry, the initial conditions are determined by random sampling each normal modes within an energy threshold $E_{limit}$. The total energy is randomly distributed in the kinetic and potential energy of the system. Therefore, an ensemble of trajectory ("classical wavepacket") is generated. The "centre" of the packet is the initial geometry and can correspond to a geometry near the Franck-Condon region or a point along the excited state reaction path.

The sampling procedure in the classical phase-space is also known as microcanonical sampling.[168] The Hamiltonian for a system of n normal modes is the sum of the energies for independent harmonic oscillators and is given by:

$$H = E = \sum_{i=1}^{n} E_i = \sum_{i=1}^{n} \frac{P_i^2 + \omega_i^2 Q_i^2}{2} \qquad (6\text{–}2)$$

To form a microcanonical ensemble, random values of $P_i$ and $Q_i$, that is of the momentum and initial position, have to be chosen giving each normal mode a random phase, so that:

$$Q_i = \frac{\sqrt{2E_i}}{\omega_i} \cos(2\pi R) \qquad (6\text{–}3)$$

$$P_i = -\sqrt{2E_i} \sin(2\pi R) \qquad (6\text{–}4)$$

where $\omega_i = 2\pi\nu_i$ .

The **Q** and **P** vectors are then transformed in Cartesian coordinate q and momentum p and those are then scaled taking into account the energy conservation (E=cost).
The outcome of the "swarm" of trajectory calculations can be analysed statistically and depending on the size and properties of the ensemble it is possible to acquire reliable information on excited state lifetimes or product yield distributions.

Scheme 6–7 illustrates the methods for *ab initio* (where the potential energy is computed at the *ab initio* level) dynamics.

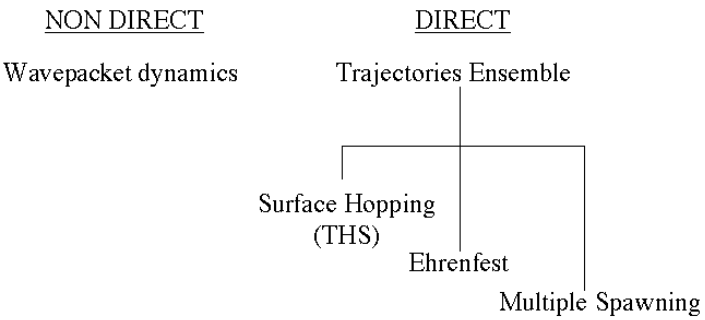


Scheme 6–7

The classical trajectories cannot correctly describe the cases where the *Born-Oppenheimer* approximation breaks down, namely when there is a strong non-adiabatic coupling between two or more PES. Many photochemical processes are known to involve a non-radiative decay at a conical intersection where the *Born-Oppenheimer* approximation is not more valid. Outside these regions the classical trajectory method remains applicable. The non-adiabatic correction can be incorporated in the trajectory computation through an *Ehrenfest* type methodology or through a surface-hopping algorithm. The "Multiple spawning" method of *Levine* and *Martínez*[169] is also available in which the Gaussian wavepacket method have been extended to include the non-adiabatic effects. To successfully describe the non-adiabatic event, the trajectory has to sample all the different surfaces in order to simulate the population transfer between the electronic states. The main difference with the classical trajectory methods is that *a wavepacket for each electronic state it is now required*, whilst the equations of motion that have to be integrated are the same. The simplest way to add the non-adiabatic correction is using the trajectory-surface-hopping (TSH) algorithm implemented by *Tully* and

*Preston* in 1971.[170] In the TSH method the integration of the equations of motion is switched between two or more *Born-Oppenheimer* surfaces. The TSH method is used to propagate the excited state trajectories onto the ground state in the conical intersection region. The probability of a surface hop is determined from the solution $a_i(t)$ of the usual semi-classical equations of motion:

$$\sum a_{i\alpha}\left\langle \phi_\beta \left| H \right| \phi_\alpha \right\rangle - i\left[ Q \cdot \left\langle \phi_\beta \left| \nabla_Q \right| \phi_\alpha \right\rangle \right] = i a_{i\beta} \qquad (6\text{–}5)$$

where $\phi_\beta$ etc. are zeroth order wavefunctions and $\left\langle \phi_\beta \left| H \right| \phi_\alpha \right\rangle$ is the *Born-Oppenheimer* **CI** matrix element. The trajectory is represented by **Q** (t), the inter nuclear configuration vector. Most importantly $\left\langle \phi_\beta \left| \nabla_Q \right| \phi_\alpha \right\rangle$ represent the non-adiabatic coupling vector. The probability of finding the system in wavefunction i is represented by $\left| a_i \right|^2$ with $\sum_{i=1}^{2} \left| a_i \right|^2 = 1$. After a hop, the difference in energy between $S_0$ and $S_1$ is redistribute along the component of the momentum parallel to the non-adiabatic coupling vector, as described by Truhlar.[171]

The surface hop method is not correctly defined in cases for which the trajectory can cross the region of strong non-adiabatic coupling more than only once. This is the case, for example, when a “sloped” conical intersection is involved in the reaction mechanism. One solution to this problem could be the “spawning method” mentioned above.

A different approach is the mixed state method, also called "classical path" (CP) approach, which uses the Ehrenfest force to solve the equations of the motion. *Gadea* and co-workers first applied the method to the study of excited $Ar^{3+}$ cluster ions.[172] The main feature of the method is that the electronic wavefunction is propagated at the same time of the local nuclear wavepacket. Consequently, the method can provide results that approach the exact quantum mechanic solution more than with the surface hop approach. The nuclei experiment a mean-field potential and the trajectory sample the potential and the non-adiabatic coupling during all the simulation. A drawback of the method is that provides unreliable results in the case in which the two interacting surfaces are very different from each other. The main evident example is when a bound state is coupled with a dissociative state.

The ab initio "on the fly" semiclassical trajectory calculations with surface hopping driven by CASSCF force field in the full space of coordinates has been applied to the study of the *cis*-trans photoisomerization of the minimal retinal model 2-*cis*-$C_5H_6NH_2^+$.[138]

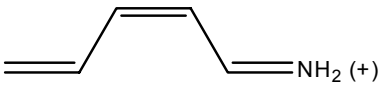


tZt-penta-3,5-dieniminium cation (*cis*-$C_5H_6NH_2^+$)

The dynamics simulations were carried out by sampling a limited region of the phase space that is by randomly choosing the initial starting geometries (i.e. with a random twist of a few degrees around the central bond) and with no initial kinetic energy. The trajectory calculations show that isomerization

path is barrierless and in all of them a radiationless decay through a conical intersection takes place. The initial motion of the systems after excitation is dominated by the skeletal stretching modes, followed by relaxation over the torsional mode. This is an example of two state two-mode pathway. The decay occurs within the first half-oscillation of the torsional mode. No excited state equilibrium is reached. This is consistent with the experimentally observed short excited state lifetime (50-60 fs) of 11-*cis*-retinal-protonated Schiff base (PSB11, the chromophore of rhodopsin) and the vibrational coherency of the photoproduct.
One of the photoisomerization trajectories is shown in Figure 6–13 were the twist around the central bond is 10°. The crossing is reached after ca. 60 fs and the trans photoproduct well is entered on a 90 fs time scale.

A more recent application of the ab initio "on the fly" dynamics using the CASSCF gradient has been performed for the trimethine cyanine $NH_2$-($CH_3$)-$NH_2^+$,[173] as a model compound for short chain cyanines. The initial excited state evolution of the cyanines can be described using the same two state two-mode model reported for the retinal model.

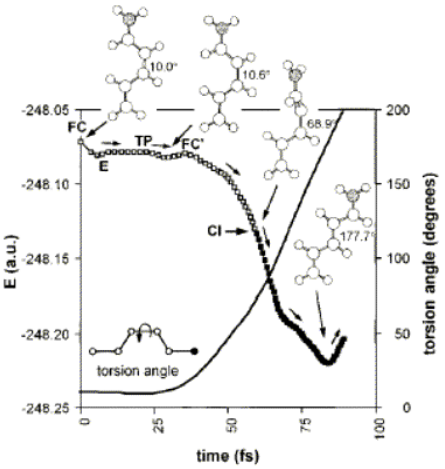


Figure 6–13: Full potential energy profile (E) along the photoisomerization trajectory discussed in the text (10 degree initial twist). Open squares for the $S_1$ and filled squares for the $S_0$ state. The structures (geometrical parameters in Å and degrees) document the geometrical progression along the trajectory as a function of time.

# Chapter 7. Application: the CASPT2//CASSCF/6-31g* strategy

In this thesis, structure optimization and relaxation path mapping are carried out to perform fully unconstrained *ab initio* quantum chemical computations in the framework of the CASPT2//CASSCF/6-31G* strategy. The resolution of a photochemical mechanism implies the detailed knowledge of all the events that follow photon absorption and ultimately lead to photoproduct formation. The final purpose is that of building a mechanistic scheme of the studied photoreaction. This is done by mapping the potential energy surfaces involved in the photochemical reaction, usually following the MEP connecting the Franck-Condon structure to the ground state photoproduct through the point of intersection. The first step is the computation of the structures of stationary points and low-lying crossings. In the case of the model surface topology of Figure 4–3, the reaction path from the FC point to the final photoproducts can be determined in a completely unbiased way by computing the minimum energy path (MEP) in three steps, connecting respectively FC to $Min_1$*, TS * to $Min_1$* and CI, and finally **CI** to P and P'. The first two parts, $MEP_1$ and $MEP_2$, describe the excited state branch of the reaction coordinate (i.e., from the FC point to the decay point), and the third part, $MEP_3$ and $MEP_4$, describes the ground state branch (i.e., from the decay point to reactant and product wells).

The surface of Figure 4–3 is characterized by a crossing between two singlet states (e.g. the $S_1$ and $S_0$ states). The presence of a surface crossing in correspondence of local energy minimum on the excited state energy surface

allows for the existence of a peculiar type of reaction path that, however, has been demonstrated to be a common feature in different classes of organic compounds. This path connects an excited state intermediate M* to a crossing point via a standard transition structure TS*. This is a *non-adiabatic* path, which includes a radiationless decay channel where the system continues its relaxation motion along the ground state energy surface (and, therefore, along the energy surface of a different state). The minimum energy path ($MEP_2$) connecting the transition state on the excited state potential energy surface (TS*) to the excited state intermediate is computed with a standard methodology. An IRC is computed starting at TS* in both forward and reverse direction. The initial relaxation directions (IRDs) to follow are provided by the transition vector (normal mode corresponding to the imaginary frequency at the transition structure). The conical intersection lies at one end of the MEP and is located following the MEP until the $S_1$ and $S_0$ energies become degenerate.

To calculate $MEP_1$ it is necessary to defines the IRD to use as the starting direction to be used in a subsequent IRC computation. The IRD method locates one or more local steepest descent directions among all the possible directions of a rotating vector (see circle centred at FC in Figure 4–3) of a fixed length and centred on the initial point (e.g. FC).

In the case of the two-dimensional model surface of Figure 1–3 there is only one steepest descent direction at FC, which corresponds, to the one pointing towards the energy minimum (see arrow). In general the search can be extended to *all* possible relaxation paths starting at a *non stationary point* on a 3N-6 dimensional energy surface.

Finally, the ground state relaxation paths are computed in the same way as for $MEP_1$, the only difference being in the hypersphere, which is now centred

on the conical intersection point. In this case there are different types of IRDs depending on the number of different $S_0$ relaxation pathways connecting the intersection point to the final photoproducts or to certain unstable ground state intermediates. For example, in the case of the model surface topology of Figure 4–3, the excited state reaction path "bifurcates" into two ground state relaxation valleys ultimately leading to the original reactant regeneration ($Min_1$) and to product formation ($Min_2$).

A different reaction path is shown in Figure 5–13 where the crossing does not lie at the bottom of an excited state energy valley but above it. Thus, the reaction path mapping involves the location of the lowest energy point located on the crossing seam and then the computation of the excited state steepest descendent path, which connects this point with the excited state intermediate.

Obviously, not always the procedure is so straightforward. It could happen that following a MEP one encounters a previously unknown local minimum or crossing point. Furthermore, it could happen that the localized minima or crossings don't agree with data from previous works or from experiments. In these cases, the chemical intuition must supply the researcher for other possible ways for the reaction to follow.

When it is possible, that is the computational time is reasonable, minima and transition states nature is confirmed by frequency calculation.

All the optimization of minima, transition states and conical intersections, along with the MEP calculations that will be presented in this thesis were performed using the Gaussian98[174] suite of programs and the methods therein. They were all performed at the CASSCF level of theory (see Appendix). The chosen active space is reported in each calculation. The used basis set (see Appendix) was the 6-31g*, since previous works demonstrated

it has the capabilities of describing the orbitals of organic compounds, similar to those studied, so that results (e.g. spectroscopic data) are consistent with experimental data.
Once all the critical points, crossing points and reaction paths are determined, it is necessary to apply the CASPT2 correction to the CASSCF-optimised geometries, in order to obtain the correct energetics and corrected reaction path energy profile. This means, the energy of each molecular geometry (i.e. minima, TSs, crossings and selected points of the MEPs) is re-estimated at the CAPST2 higher level of theory (see Appendix). This was obtained by using the MOLCAS 4.1[175] and MOLCAS 5.4[176] suites of program.

The general procedures described above are schematically illustrated in the following flow-chart.

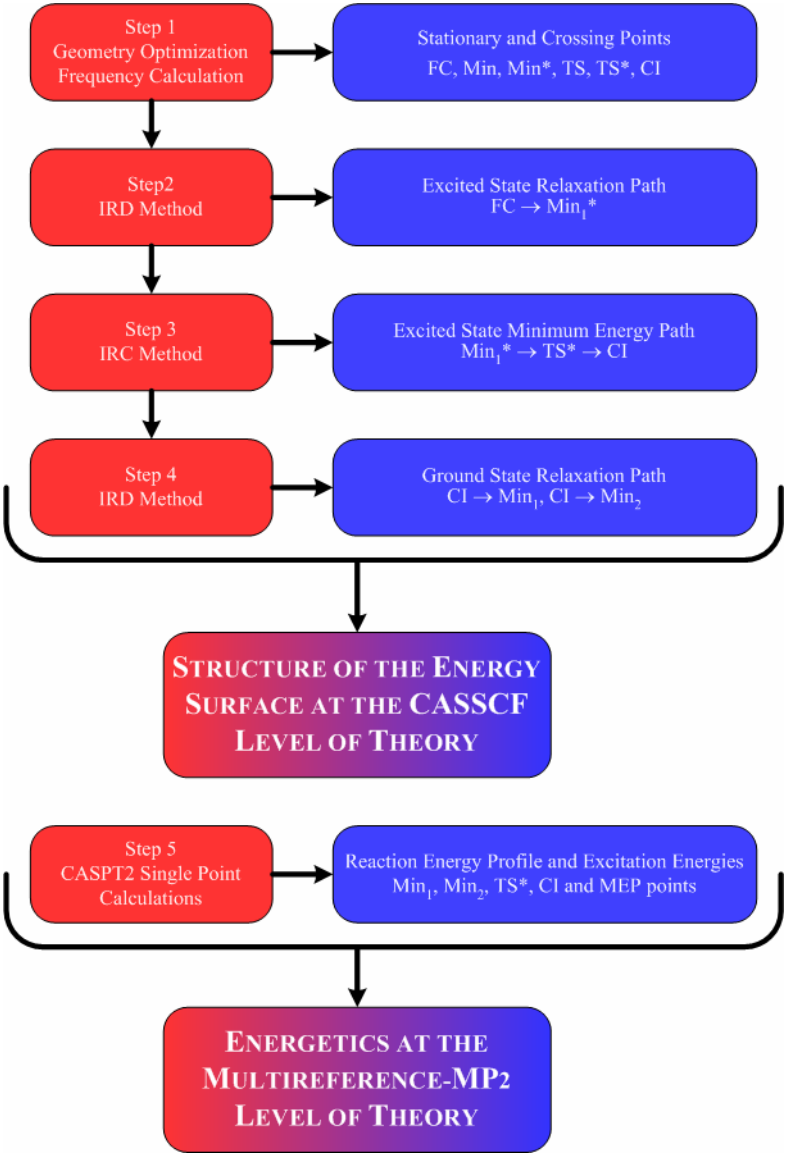
Step 1
Geometry Optimization
Frequency Calculation
Stationary and Crossing Points
FC, Min, Min*, TS, TS*, CI
Step2
IRD Method
Excited State Relaxation Path
FC → Min1*
Step 3
IRC Method
Excited State Minimum Energy Path
Min1* → TS* → CI
Step 4
IRD Method
Ground State Relaxation Path
CI → Min1, CI → Min2
STRUCTURE OF THE ENERGY SURFACE AT THE CASSCF LEVEL OF THEORY
Step 5
CASPT2 Single Point
Calculations
Reaction Energy Profile and Excitation Energies
Min1, Min2, TS*, CI and MEP points
ENERGETICS AT THE MULTIREFERENCE-MP2 LEVEL OF THEORY

# Chapter 8. Introduction to Retinal Chromophores

## 8.1. The Importance of the Primary Event

Chapter 2 presented the main characteristics of rhodopsin and bacteriorhodopsin proteins. In this chapter some more details will be given. As previously said, the entire signal cascade of vision in rhodopsin, or the proton transfer in bacteriorhodopsin, are triggered by the cis-trans photoisomerization of the retinal chromophore. What happens between the photon absorption and the appearance of the first trappable intermediate is usually referred to as the primary event of the photoreaction.

The biological function of these proteins is given by the thermal transition from an intermediate to another. However, the energy to perform these steps is given by the first one, where a photon is captured and its energy transformed into "chemical force". Hence, the importance of the primary event is stated.[177] Moreover, the primary event represents one of the fastest reactions known in the biological world; in fact, the first intermediate of bacteriorhodopsin appears in less then 500 fs,[140,178] while the appearance of the first intermediate of rhodopsin is even faster, 200 fs.[95] As previously said, the very first intermediates of the photocycles haven't been isolated, yet. In fact, even at very low temperature, they are still not isolable. The initial event of rhodopsin[23] (and bacteriorhodopsin)[25,179] after absorption of a photon is now confirmed to be a cis-trans (or trans-cis, respectively) isomerization of

the retinal chromophore. This isomerization starts on the electronic excited state as a consequence of the photon absorption. After a few femtoseconds, the chromophore evolves into a fluorescent state (in the sense that it could be detected by fluorescence time-resolved pump-probe spectroscopy), called FL state or I for rhodopsin and bacteriorhodopsin, respectively. These intermediates evolve into photorhodopsin, in ~200 fs, and J, in ~500 fs, respectively. These intermediates are supposed to represent the return of the chromophore on the fundamental state. These series of events is reported in Scheme 8–1. After a few picoseconds, the first trappable intermediates appear, bathorhodopsin and K, respectively again.

Rhodopsin

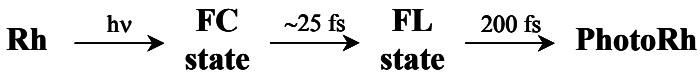


Bacteriorhodopsin

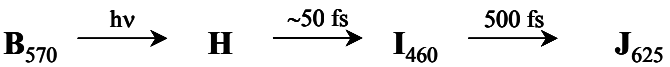


Scheme 8–1

The possible nature and origin of the two events before the decay on the fundamental state will be discussed later in Chapter 9.

The assignment of photorhodopsin as the first intermediate on the fundamental state will be treated in more details (and argued) in Chapter 11.

## 8.2. Experimental Studies: Speed, Yield and Specificity

Even if the protein chain come into action in first person with thermal steps after the primary event, the effects of the protein cavity on the chromophore during the isomerization are quite relevant. In particular, with respect to the photoreaction of the chromophores in solution, the protein cavity gives to the isomerization process higher speed, bigger quantum yield and specificity over the photoproducts. All these three aspects are tightly bounded one to another. One possible hypothesis is that the protein cavity induces changes on the structural properties of the chromophore and/or on the shape of the excited state potential energy surface, such that the photoexcited molecule has to "travel" a shorter and/or steeper path prior relaxing on the fundamental state. All these possibilities will be explored in Chapter 10. In this paragraph a sum of the experimental evidences of the protein cavity activity will be presented.

The photoisomerization process inside the protein cavity is very efficient and stereospecific. In fact, the chromophore of rhodopsin has a quantum yield for photoisomerization of 65%,[180] and the only photoproduct is the all-*trans*-retinal. The bacteriorhodopsin's chromophore, too, has a quantum yield of around 60%,[181] and the only photoproduct of the isomerization is the 13-*cis*-retinal. The situation is very different in solution, as reported in Table 8–1.

Table 8–1: Photoisomerization quantum yields and photoproducts of various isomers of retinal chromophore, when irradiated in solution.[182]

| Isomer | Solvent | Quantum yield $\phi$ | Photoproduct (from HPLC) |
|---|---|---|---|
| 9–cis | hexane | ≤ 0.05 | all–trans |
| | methanol | ≤ 0.05 | all–trans |
| 11–cis | hexane | 0.23 ± 0.04 | all–trans |
| | methanol | 0.25 ± 0.03 | all–trans |
| 13–cis | hexane | ≤ 0.05 | all–trans |
| | methanol | ≤ 0.05 | all–trans |
| all–trans | hexane | 0.14 ± 0.02 | 13–cis, 11–cis, 9–cis, 7–cis (18%, 70%, 11%, traces) |
| | methanol | 0.13 ± 0.02 | 13–cis, 11–cis, 9–cis, 7–cis (9%, 71%, 15%, 5%) |

As can be seen, quantum yields are very low, and the all-*trans*-retinal has got all possible cis isomers as photoproducts. More over, the more abundant photoproduct, in solution, for the all-trans chromophore is the 11-cis isomer, and not the in cavity occurring 13-cis. Thus, the action of the protein cavity can be summarised in i) guides the photoisomerization towards only one product, ii) select an otherwise un-favoured product, and iii) is essential to achieve efficiency. i and ii give stereospecificity.

Through time resolved pump-probe spectroscopy, another important difference of behaviour of the chromophores inside and outside the protein cavity has been seen. In fact, inside the protein cavity, the stimulated emission decaying time is less than 1 ps for both chromophores;[95,140,178] otherwise, when the retinals are in solution, the decaying time reaches 1.5

ps[183] and 2-3 ps[95] for the all-trans and 11-cis retinal chromophores, respectively. This is a forth aspect of the action of the cavity over the photoisomerization process: speeding up of the reaction.

Later on, experiments tried to probe the protein cavity by modifying natural chromophores, adding some rings to enclose the isomerising double bond; the ring-locked chromophores that will be treated in following chapters are reported in Scheme 8–2.

Some artificial pigments showed longer decaying times both in the protein cavity and in solution, even if some were faster in the protein cavity than outside. Other ring locked retinals could be compared to the natural ones when placed in solution, while, quite surprisingly, with the increasing of the ring size, the artificial chromophores showed a decaying time in the protein cavity just like the wild type ones, and even faster.

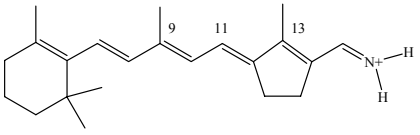


all-trans PSB13.5

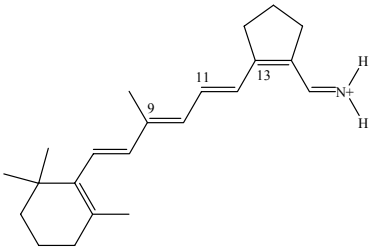


13-cis PSB13.5

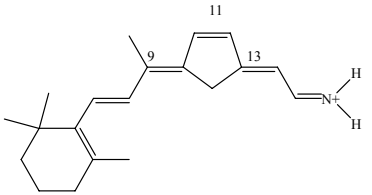


11-cis PSB11.5

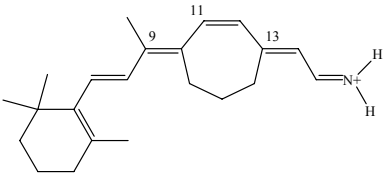


11-cis PSB11.7

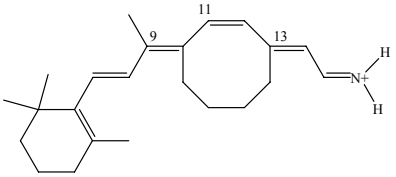


11-cis PSB11.8

Scheme 8–2

A list of the artificial chromophores that will be treated in this thesis along with the available femtosecond time resolved spectroscopy data about decaying time inside and outside the protein cavity are given in Table 8–2. 11-cis PSB11.7 has not been studied by time-resolved spectroscopy with femtosecond time resolution, but only by picosecond time resolution.[184] However, available data show that its behaviour is similar to the wild type rhodopsin chromophore.

Table 8–2: Decaying time of the stimulated emission from femtosecond time resolved spectroscopy of various chromophore

| Artificial Chromophore | Protein | Solution |
|---|---|---|
| all-trans PSB13.5 | 19 ps[140,178] | 2.3 ps[185] |
| 13-cis PSB13.5 | No data available | 2.5 ps[185] |
| 11-cis PSB11.5 | 6 ps[95] | 19 ps[95] |
| 11-cis PSB11.8 | 0.1 ps[186] | No data available |

The origin of the multiple routes for the photoisomerization of the natural chromophores, along with an analysis of the photoisomerization paths of artificial retinals with five-member rings will be given in Chapter 9. Artificial pigments with seven- and eight-member rings will be deeply analysed in Chapter 11.

# Chapter 9. Retinal Chromophores: Preliminary Computational Studies

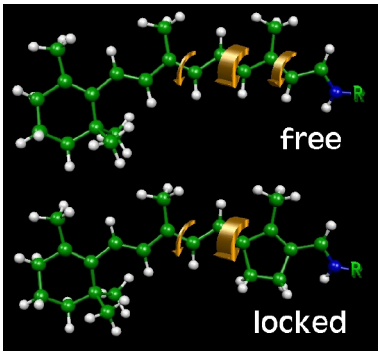


In the last years, a sort of protocol has been proven to be effective in describing the behaviour of retinal chromophores in isolated condition.[139] The computational analysis of the chromophores *in vacuo* gave, also, a new insight of the effects of the protein cavity onto the behaviours of the chromophores. The basis of this method is the use of *ab initio* multiconfigurational second-order perturbation theory computations on models of the chromophores.

## 9.1. Model Choice and Validation

Most part of this testing and validation was done using the PSB11 model 4-cis-γ-methylnona-2,4,6,8-tetraeniminium cation **1**.[139,149] This model is

constituted by five conjugated double bonds, being the last one formed by the C=N bond of the protonated Schiff base. The sixth double bond embedded into the β-ionone ring was not included because of the computational cost. Anyway, computations and experimental evidences (see later) justified this choice. Even if the β-ionone ring was absent, the carbon atoms were numbered as in the natural chromophore, to maintain coherence. Being a model of the chromophore of rhodopsin, the molecule is in 11-cis conformation. To lighten the computation, only one methyl group was added, the one that could have some steric influence over the isomerization.

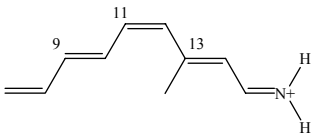


Model **1**

The molecular structures defining the reaction coordinates for the relaxation path after photoexcitation of **1** have been obtained via fully unconstrained geometry optimisation and minimum energy path (MEP) computations on the basis of the CASPT2//CASSCF/6-31g* scheme presented earlier in Chapter 7. The considered active space comprised 10 electrons in 10 π-orbitals, spanning over all the conjugated double bonds. The computations were carried out in isolated condition and in the absence of a counterion.

The usage of this model and the computational strategy have been validated by computing the absorption and fluorescence maxima, the change in dipole moment and by simulating the resonance Raman spectra of PSB11 and its $^{13}C$ isotopomers in solution.[155] The computed data compare well with the

corresponding experimental quantity, suggesting that the terminal double bond of PSB11, which is part of the β-ionone ring, does not conjugate effectively with the remaining part of the π-system in the ground state equilibrium geometry. This conclusion is supported by the twisted conformation of the β-ionone ring recently computed and observed in the structure of rhodopsin obtained by x-ray diffraction[43] and nmr spectroscopy.[187] Given all of these evidences, **1** and similar models can be used as realistic models of the retinal chromophores.

## 9.2. The Two-State-Two-Mode Model

The results of reaction path computations for the PSB11 model **1** (Figure 9–1) show that the $S_1$ ($S_1$ corresponds to the 1 $B_u$-like – i.e. hole-pair - spectroscopic state of polyenes) reaction coordinate is sequentially dominated by two substantially uncoupled modes. The first mode is totally symmetric and drives the initially planar system out of Franc-Condon point (**FC**) through a concerted double-bond stretch and single-bond compression. The second mode is non-totally symmetric and is dominated by a torsional motion about the central double bond of the system. The following evolution along the torsional coordinate leads to a conical intersection funnel (**CI**) where the chromophore displays a ca. 90° twisted central double bond and where, finally, fully efficient decay to the ground state occurs.

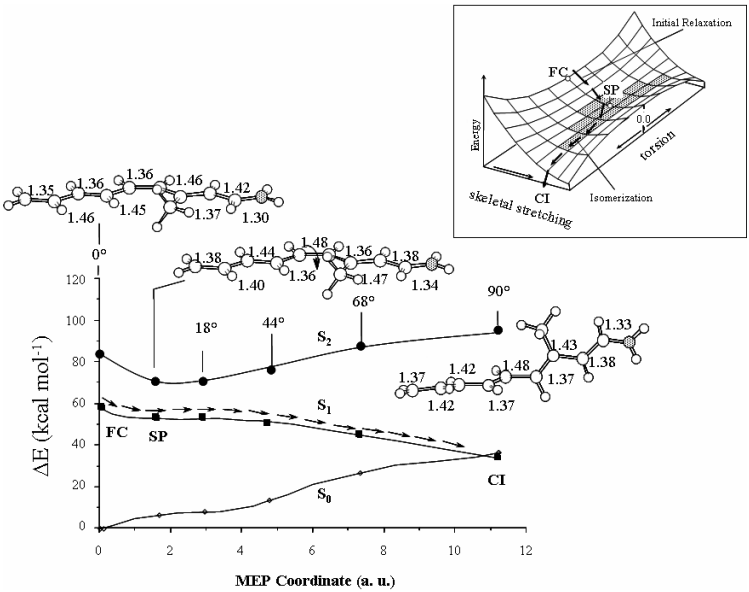


Figure 9–1: Energy profiles along the $S_1$ 11-cis→all-trans photoisomerization coordinate of **1**. The structures (geometrical parameters in Å and degrees) document the progression of the molecular structure along the co-ordinate (data are from ref. 149). Full circles, full squares and full diamonds indicate the $S_2$, $S_1$ and $S_0$ energies, respectively. The two-mode structure (stretching + torsion) of the $S_1$ reaction coordinate is illustrated in the inset. **FC** is the Franck-Condon structure, **SP** corresponds to the relaxed planar species and **CI** is the 90° twisted $S_1/S_0$ conical intersection decay channel.

Isomerization is then completed on the fundamental state. Thus, along the reaction coordinate, the double-bond isomerization motion does not start immediately after photoexcitation, but only after relaxation of the PSB carbon skeleton. Indeed, the initial $S_1$ relaxation leads to a "metastable" planar species (stationary point, **SP**) where the single-double bond order is

inverted. Also, no evidence of an avoided crossing between $S_1$ and $S_2$ ($S_2$ corresponds to the singlet $2A_g$-like – i.e. dot-dot - dark excited state of polyenes) has been found, on the contrary to what was previously suggested. All these data are collectively called two-state-two-mode mechanistic model.[139] This sequence, fast **FC→SP** relaxation, vibrational energy redistribution, nearly barrier-less partial isomerization before decay, compares well with the experimental timings presented earlier. The energy profile computed for the isomerization of the model will be used as a touchstone for the evaluation of possible effects given by structural changes of the chromophores.

## 9.3. Photoisomerization Pathways of the all-trans Retinal: Relationship Between Energy Barriers and Photoproducts in Solution

On the basis of the results obtained with **1**, an analysis of a model of the chromophore of bacteriorhodopsin was done, using the same methodology.[137] One goal of this research was to elucidate the lack of stereospecificity of the photoisomerization of the all-trans chromophore (PSBT) in solution. Analogously to the previous work, **2** was used as a model of the PSBT chromophore. The lack of stereospecificity observed in solution suggests that competitive or nearly competitive excited state reaction paths exist in the isolated PSB chromophores, which correspond to torsional deformation about different double bonds (e.g. the double bonds in position 9, 11 and 13). In order to support this hypothesis, excited state reaction path computations

were carried out for different realistic PSB models in isolated conditions and in the absence of a counterion.

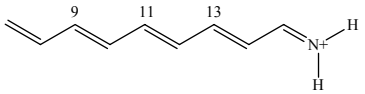


Model **2**

As **1**, after photoexcitation **2** evolves to a planar **SP** intermediate. Given this planarity, the **FC→SP** part of the path must be common to all possible isomerizations. Thus in the following the results of a series of reaction path computations will be presented, documenting different **SP→CI** routes.

The molecular structures defining the **SP→CI** reaction coordinates for the cation **2** have been obtained via fully unconstrained geometry optimisation and minimum energy path (MEP) computations using the CASPT2//CASSCF/6-31g* procedure (Chapter 7). Progression along the MEP is measured in mass-weighted cartesians (au=amu1/2$a_0$). An active space of 10 electrons in 10 π-orbitals (10e/10o) has been used in all calculations.

The $S_0$, $S_1$ CASSCF and $S_0$, $S_1$ and $S_2$ CASPT2 energy profiles for the all-trans→11-cis isomerization of model **2** are given in Figure 9–2.

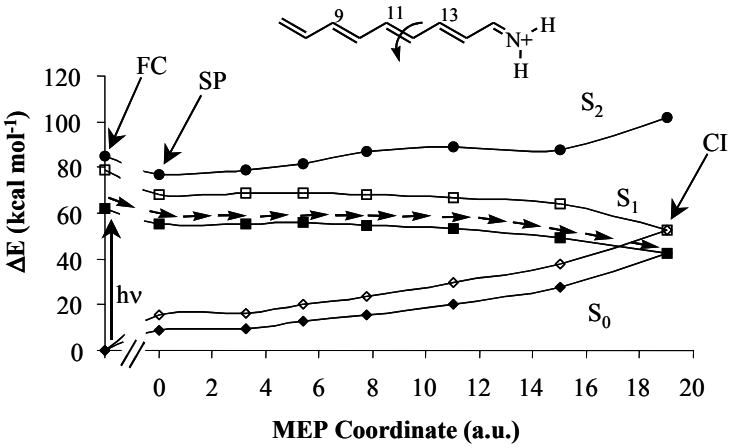


Figure 9–2: Energy profiles along the $S_1$ all-trans→11-cis photoisomerization coordinate of **2**. Full circles, full squares and full diamonds indicate the $S_2$, $S_1$ and $S_0$ CASPT2 energies. Open squares and open diamonds show the $S_1$ and $S_0$ CASSCF energies (i.e. before PT2 correction).

Notice that, while there is a considerable correction in the interstate energy gaps when passing from CASSCF to CASPT2, the general shape of the energy profile remains unchanged. In general the use of CASPT2 to improve the energy accuracy is not recommended in any region where the two states may be highly coupled (i.e. the corresponding wave functions may be mixed), such as in the case of avoided crossings and in the regions surrounding conical intersections. In Section 9.5 is demonstrated that is valid to discuss the structure of the CI on the basis only of the CASSCF data.

Given the general flatness of the $S_1$ energy profile along the computed reaction paths, it is not always technically possible to locate a transition structure at the CASSCF level. Furthermore, even when this is possible, the energy profile recomputed at the CASPT2 level often shows a shifted energy

maximum. Thus, throughout this chapter and the followings, the position of the $S_1$ "transition structures" (**TS**s) and of the corresponding energy barriers are evaluated as the CASPT2 energy difference between the energy of the **SP** intermediate and that of the CASPT2 energy profile maximum.

The $S_0$, $S_1$ and $S_2$ energy profiles computed along the 11-cis→all-trans indicate that the $S_2$ energy profile is always more than 20.0 kcal $mol^{-1}$ higher in energy than the $S_1$ state. Thus, as previously reported, PSB photoisomerization involves only two electronic states, suiting to the two-state-two-mode mechanistic model. In the following, discussion will be limited to the structure of the $S_1$ and $S_0$ energy profiles as well as of the $S_1/S_0$ conical intersection region.

In Figure 9–3 the energy profiles associated with the reaction coordinates of the PSBT model **2** leading towards the 9-cis, 11-cis and 13-cis forms are reported. There are three general features.

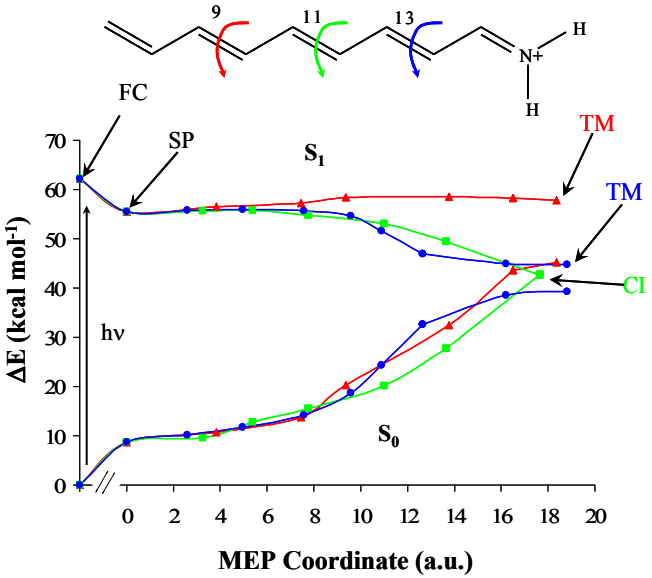


Figure 9–3: CASPT2 energy profiles along the $S_1$ all-trans→9-cis (full triangles, red line), all-trans→11-cis (full squares, green line) and all-trans→13-cis (full circles, blue line) photoisomerization coordinates of **2**. The all-trans→9-cis and all-trans→13-cis photoisomerization paths end in a twisted energy minimum (**TM**), while the all-trans→11-cis path ends at a $S_1/S_0$ conical intersection (**CI**).

In all cases the $S_1$ energy profiles display a flat plateau (i.e. with a barrier less than 3.0 kcal $mol^{-1}$) that develops from the planar **SP** point to a significantly twisted structure. The energy plateau ends after ca. 40 degrees twisting along the all-trans→11-cis coordinate, at ca. 50 degrees along the all-trans→13-cis coordinate and persists all along the all-trans→9-cis coordinate. The $S_1$ energy barriers are (in ascending order) all-trans→11-cis (0.2 kcal $mol^{-1}$), all-trans→13-cis (0.5 kcal $mol^{-1}$), all-trans→9-cis (3.0 kcal $mol^{-1}$).

In all cases, the energy profile ends at a ca. 90 degrees twisted structure. However, while the all-trans→11-cis reaction coordinate ends at a $S_1/S_0$ intersection **CI**, both the all-trans→13-cis and all-trans→9-cis path first lead to a ca. 90 degrees twisted energy minimum (**TM**) on the $S_1$ surface. As previously demonstrated by Martinez, Ben-Nun et al.[188] for the all-trans→13-cis case, these minima are located near two **CI**s (not reported in Figure 9–3) that are entered via a displacement along a single bond contraction - double bond expansion stretching mode. These **CI**s lie at a slightly higher energy than the minima (ca. 2.5 kcal $mol^{-1}$) and their relationship to the corresponding **TM**s will be discussed in Section 9.6. The CIs relative to the all-trans→13-cis and all-trans→9-cis paths have been located via a two-dimensional scan carried out at the CASSCF level of theory. The grid corresponding to the search of the CI near TM relative to the all-trans→13-cis path has been computed by applying a step of +0.02 Å and -0.02 Å to the C-C bond and C-N bond of the -CH-CH-$NH_2$ moiety respectively. The results are reported in Scheme 9–1.

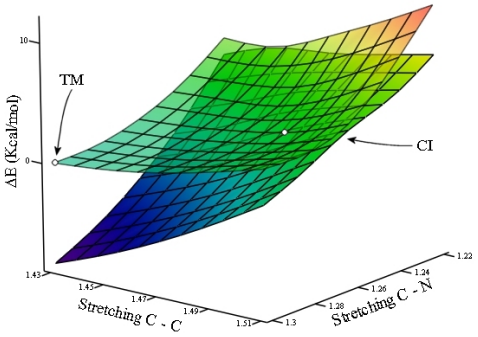


Scheme 9–1

While the $S_1$ lifetimes must depend exclusively on the evolution of the chromophore along its $S_1$ potential energy surface, this is not the case for the photoisomerization quantum yields. Indeed the relative population of the all-trans → 9-cis, all-trans → 11-cis, all-trans → 13-cis paths is only one factor that contributes to determine the final quantum yield distribution. A second critical factor is the unavoidable path branching occurring upon $S_1 \rightarrow S_0$ decay at the corresponding conical intersections. This branching reflects the wave packet motion in the region of the conical intersection. In principle, only semi-classical or quantum dynamics methodologies can provide a rigorous answer to this problem. However, very regrettably, the application of these methodologies to realistic (accurate) multidimensional potential energy surfaces of **2** is still substantially out of reach. A characterization of the shape of the $S_1$ surface associated with the all-trans → 11-cis, all-trans → 13-cis **CI**s will be presented in Section 9.6. However, qualitatively one can consider that the all-trans → 11-cis **CI** should be accessed more easily then those near **TM**s.

A qualitative difference between the all-trans → 11-cis and all-trans → 13-cis (and 9-cis) cases is immediately apparent. In the first case the trajectories will enter the conical intersection directly while in the second case the trajectories must undergo a number of oscillations (in a direction orthogonal to the torsional motion) in the region of **TM** before entering the **CI**. Thus as suggested by Martinez, Ben-Nun et al.[189] the different topologies may be related to different quantum yields for the 11-cis and 13-cis products.

In conclusion, there are at least two factors determining the quantum yield of the all-trans → 11-cis process with respect to the all-trans → 13-cis process. The first is related to the structure of the different competitive excited state paths that leads to a different population of the competitive isomerization

paths. In this respect one would predict a similar population for the all-trans → 11-cis and all-trans → 13-cis paths since these are both nearly barrierless. The second factor is related to the reactant/product branching occurring upon decay at the funnel. According to this factor the first process shall be favoured with respect to the second. The all-trans → 9-cis process is predicted to be disfavoured by both factors. This model provides a qualitative rationalization of the quantum yields observed for PSBs in methanol solution.[182] Indeed, the 11-cis>13-cis>9-cis photoproduct ratio observed for the photolysis of PSBT is readily explained.

## 9.4. Five Member Ring Lock Usage: No Change in the Primary Event

The excited state dynamics of rhodopsin and bacteriorhodopsin have been recently investigated by carrying out time-resolved spectroscopic studies on artificial pigments where the natural PSB chromophores have been substituted with synthetic locked chromophores (see, for instance, the structures presented in Section 8.2).[95,140,178,185] In locked chromophores the torsional deformation of the reactive double bond (e.g. the double bond 11 in rhodopsin and the double bond 13 in bacteriorhodopsin) is prevented since the double bond is part of a cyclopentene moiety (see structures PSB13.5 and PSB11.5).

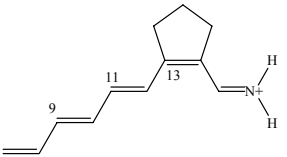


Model **3**

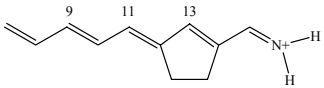


Model **4**

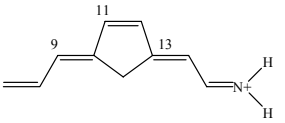


Model **5**

By using the all-trans PSB13.5 chromophore, Ottolenghi, Ruhman, Sheves, Atkinson and co-workers[178] demonstrated that the timescale (less than 50 fs) of the initial excited state dynamics of bacteriorhodopsin (i.e. the timescale for formation of a transient relaxed $S_1$ species) is not sensitive to the presence of the lock. Based upon this experiment the authors concluded, in agreement with the two-mode reaction coordinate of Figure 9–1, that the all-trans→13-cis isomerization motion couldn't dominate the initial excited state relaxation. In further agreement with a two-mode model, the same experiment revealed that the rate of decay of such transients is very sensitive to the locking. In fact, while the excited state of native bacteriorhodopsin has a ca. 200 fs lifetime (with a product appearance time of 500 fs), the artificial pigment has a ca. 15 ps lifetime, thus indicating that all-trans→13-cis motion must be involved in the excited state decay. On the other hand it must be

stressed that a 15 ps lifetime still corresponds to a fast decay rate. This raises the problem of defining the nature of the radiationless decay channel operative in *locked* retinal proteins. Thus the results of excited state reaction path computations for locked PSB models are now presented, too.

Figure 9–4: Energy profiles along (a) the $S_1$ *all-trans*→11-*cis*, photoisomerization co-ordinate of **4** (b, next page) the 13-*cis*→11-*cis,* 13-*cis*. photoisomerization co-ordinate of **3** (c, next page) the $S_1$ 11-*cis*→11-*cis,* 13-*cis* photoisomerization co-ordinate of **5**. Full squares and full diamonds indicate the CASPT2 $S_1$ and $S_0$ energies along the same co-ordinate, respectively. Open squares and diamonds show the $S_1$ and $S_0$ CASSCF energies (i.e. before PT2 correction).

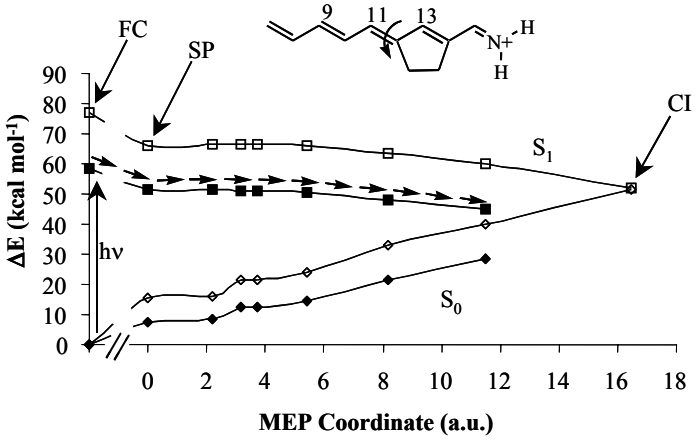


a)

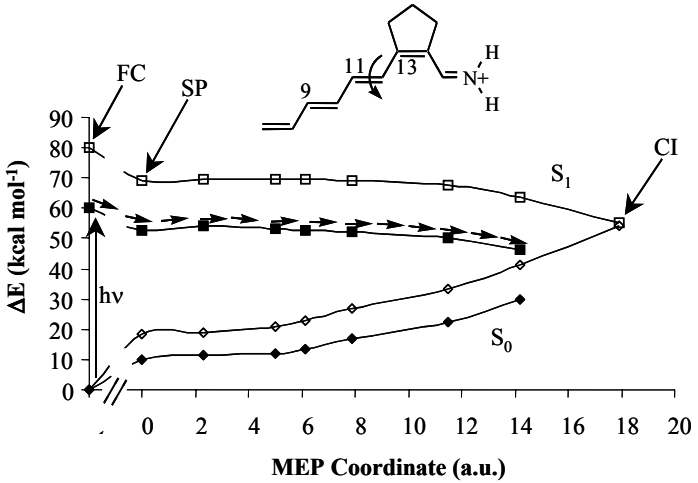


b)

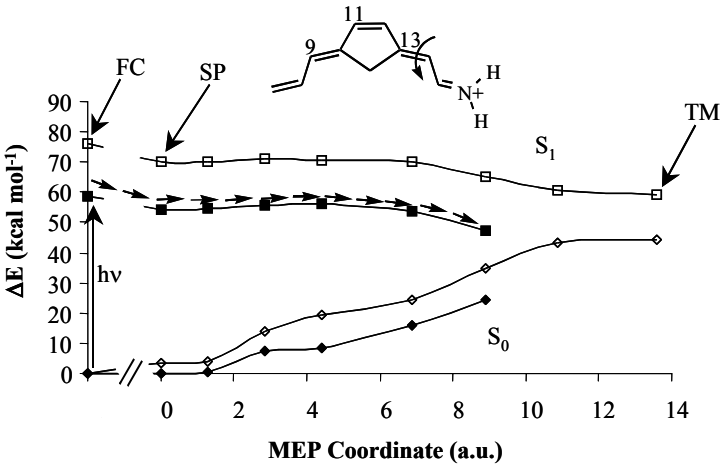


c)

In Figure 9–4a the photoisomerization path for the all-trans PSB13.5 model **4** is reported. This path must be compared with the corresponding all-trans→11-cis path of Figure 9–3. It is evident from the figure that the presence of the lock does not alter the general behaviour described for the

free chromophore and the reaction path is barrierless. This indicates that, in **4**, the presence of the lock in a position adjacent to the reactive double bond does not lead to stabilization of the SP structure. Furthermore, as with the free chromophore, the path ends at a ca. 90° twisted $S_1/S_0$ **CI**. In Figure 9–4b is reported the photoisomerization energy profile of model **3**. This second type of lock (i.e. the five-member ring lock now comprises 2 rather than 3 atoms of the conjugated chain) shows a similar behaviour. In fact the computed 13-cis-locked→11-cis,13-cis-locked path is again substantially barrierless.

In Figure 9–4c the behaviour of model **5** is shown, with respect to the 11-cis-locked→11-cis-locked,13-cis process. Similar to the cases of **4** and **3**, the lock (which is structurally different from the previous two since it comprises 4 rather than 2 or 3 atoms of the conjugated chain) is expected to have a limited effect on the reaction energy profile about adjacent unlocked double bonds. However, for this chromophore, a substantial $S_1$ barrier was computed for both the isomerization of the double bond in position 13 and the double bond in position 9. Indeed the 11-cis-locked→9-cis,11-cis-locked process has a 5.0 kcal mol-1 barrier and the 11-cis-locked→11-cis-locked,13-cis process of Figure 9–4c has a 2.0 kcal mol-1 barrier. Due to the absence of a barrierless path the planar **SP** intermediate of **5** must have the longer excited state lifetime among the PSBs.

### 9.4.1. Photoisomerization Takes Place Around Different Double Bonds. Relationship Between Energy Barriers and Photoproducts in Solution.

The photoinduced dynamics of both native and locked PSBs in methanol solution have been investigated by means of time-resolved spectroscopic methods. These experiments have provided a measure of the $S_1$ excited state lifetime and, in turn, of the effect of the lock on the $S_1$ decay rate. Below it is shown that the observed changes in lifetime correlate with the changes in the magnitude of the barrier located along the $S_1$ paths discussed in the previous section.

Both $S_1$ all-trans and 11-cis PSBs have a 2-3 ps $S_1$ lifetime.[95,183] This lifetime is associated with the timescale required for $S_1$ vibrational energy redistribution and evolution along the barrierless energy plateau of the all-trans→11-cis (see Figure 9–2) and 11-cis→all-trans (see Figure 9–1) paths respectively. In fact, as discussed above for **1**, the bimodal nature of the excited state reaction coordinate implies that, immediately after the initial **FC→SP** relaxation, the vibrational energy is located on totally symmetric stretching modes. This energy must thus be redistributed before evolution along the weakly coupled asymmetric **SP→CI** torsional coordinate begins (ultimately leading to $S_1 \rightarrow S_0$ decay). Notice that for model **1** the retinal methyl group in position 13 has been preserved in order to describe the steric interaction with the hydrogen in position 10 that contributes to 11-cis→all-trans torsional destabilization of PSB11 (this destabilization contributes to

speed up the 11-cis→all-trans motion in rhodopsin).[190] The all-trans→11-cis path of Figure 9–2 indicates that such steric interaction is not a prerequisite for barrierless isomerization about the double bond in position 11.

The all-trans PSB13.5 and 11-cis PSB11.5 locked chromophores provide two cases where the effect of the lock on the excited state timescale can be probed. In fact, according to the results presented in Figure 9–4a and c for **4** and **5**, one can predict distinct behaviours for these two PSB chromophores. In particular, upon locking of all-trans PSB a barrierless all-trans→11-cis path remains operative and one would not predict a significant change in excited state lifetime. In contrast, upon locking of 11-cis PSB, no barrierless isomerization path remains operative and the most favourable path shows a 2.0 kcal mol-1 energy barrier. As a consequence a marked increase in excited state lifetime is predicted. Consistent with these predictions, the measured lifetimes of all-trans PSB13.5 and 11-cis PSB11.5 in methanol solution are 2-3 ps[185] and 19 ps[95] respectively. It is therefore apparent that the results of calculations correlate qualitatively with the experiment. Further evidence for this correlation comes from the observed excited state lifetime of the 13-cis locked chromophore 13-cis PSB13.5. In fact, similarly to all-trans PSB13.5, this chromophore decays in 2-3 ps indicating that a substantially barrierless isomerization path is still operative in the locked molecule. Indeed, as reported in Figure 9–4b for the 13-cis PSB13.5 model **3**, the path corresponding to the isomerization of the double bond in position 11 is essentially barrierless.

### 9.4.2. Possible Effects of the Protein Cavity

The correlation between the computed $S_1$ energy profiles and observed $S_1$ lifetimes also provides indirect information on the effect of the protein cavity on the potential energy surface of the PSB chromophores. For instance, in bacteriorhodopsin the excited state lifetime of all-trans PSB is reduced from 2-3 ps to 0.2 ps.[140,178] Furthermore, in contrast to the solution environment where the all-trans→11-cis motion prevails, the isomerization corresponds to an all-trans→13-cis stereospecific process. The reduced excited state lifetime suggests that, in the protein, the all-trans→13-cis energy profile of Figure 9–3 becomes favoured. In other words, the long energy plateau is greatly reduced or even removed. On the other hand, it is not clear if the protein acts exclusively by "catalysing" the all-trans→13-cis route or if it also inhibits the favoured all-trans→11-cis path as suggested by the stereospecificity. The results of a recent spectroscopic investigation[140,178] of an artificial bacteriorhodopsin containing the all-trans PSB13.5 chromophore have revealed that, upon locking, the excited state lifetime of the protein undergoes a ca. 10-fold increase up to ca. 20 ps. This behaviour is substantially different from that of the corresponding locked chromophore in solution where the lock does not change the lifetime.[185] Thus the locked bacteriorhodopsin lifetime increase suggests that the all-trans→11-cis energy profile is destabilized by the protein cavity in such a way that a few kcal $mol^{-1}$ barrier impairs the access to the conical intersection. Such models would then suggest that photoisomerization in bacteriorhodopsin is the result of simultaneous specific "catalysis" (all-trans→13-cis path) accompanied by specific "inhibition" (all-trans→11-cis path).

The above model must also be valid for rhodopsin. In this case the protein environment catalyses the 11-cis→all-trans path making it more attractive (and also coupling the stretching and the torsional modes to speed up vibrational energy redistribution). Again in the artificial protein containing the 11-cis PSB11.5 locked chromophore the observed lifetime is ca. 4 times longer (ca. 85 ps) than the lifetime of the corresponding locked chromophore in solution.[95] This suggests that, in rhodopsin, the protein cavity, which specifically catalyses the 11-cis→all-trans, also "inhibits" the alternative 11-cis →11-cis, 13-cis motion.

The reaction paths of Figure 9–4b and c support the idea that the 13-cis PSB13.5 and 11-cis PSB11.5 locked chromophores could undergo trans to cis photoisomerization at positions 11 and 13 respectively. While the observable production of the resulting di-cis locked retinals may be limited by an unfavourable branching at the corresponding conical intersection, careful experimental work on the solution photochemistry of 13-cis PSB13.5 and 11-cis PSB11.5 would be important as a test of the mechanistic view proposed above. Indeed, while production of di-cis retinals has not been observed during photolysis of a 11-cis PSB11.5 in rhodopsin, irradiation of a six-member ring 11-cis locked PSB in rhodopsin afforded 11,13 and 11,9 di-cis photoproducts.[191]

## 9.5. Validation of CASSCF against MS-CASPT2 Conical Intersections

In order to demonstrate that a conical intersection point located at the CASSCF level remains degenerate after the inclusion of a correction for dynamic correlation, MS-CASPT2[192] computations have been carried out. MS-CASPT2 (see Appendix), in principle, is able to treat avoided crossings and conical intersections in a balanced way. At a true conical intersection, the coupling is zero and so the MS-CASPT2 treatment becomes equivalent to CASPT2 (i.e. the relevant off-diagonal elements of the effective Hamiltonian used in the MS-CASPT2 treatment will be close to zero). The MS-CASPT2 method is, however, very sensitive to the choice of active space, and in order to obtain correct results it is often necessary to augment an active space with additional virtual orbitals. Since an expanded active space MS-CASPT2 re-evaluation of the energy profile of model **2** or, even worse, a MS-CASPT2 re-optimisation of the corresponding conical intersection was too expensive to be carried out, a MS-CASPT2 conical intersection optimisation[88,89] for the minimal PSB model penta-2,4-dieniminium cation[133] was run, by using a finite difference method recently developed.[193] In this calculation the active space comprised 6 electrons in 8 $\pi$ orbitals.

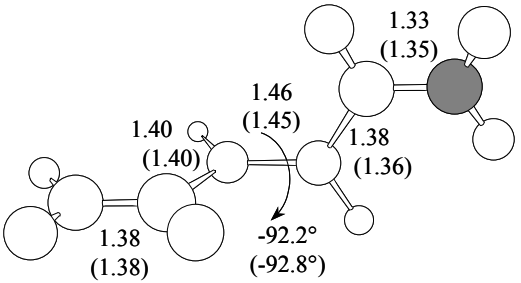


Figure 9–5: MS-CASPT2 and CASSCF optimized structures of the penta-2,4-dieniminium cation $S_1/S_0$ conical intersection (geometrical parameters in Å and degrees). The MS-CASPT2 geometrical parameters are given in brackets.

In Figure 9–5 it is shown that, for this minimal model, a true conical intersection exists on the dynamically correlated potential energy surfaces. Comparison of the geometrical parameters of this structure with the corresponding CASSCF structure shows that there are substantially no structural changes.

## 9.6. Conical Intersections Topology

The results of trajectory and wave packet calculations depend critically on the shape of the $S_1$ and $S_0$ potential energy surfaces in the region close to the conical intersection. For this reason, in this chapter a characterization of the shape of the $S_1$ surface, associated with the all-trans→11-cis, all-trans→13-cis **CI**s, is presented. As shown above, the all-trans→13-cis pathway does not lead directly to a conical intersection but to an energy minimum **TM**

displaying a ca. 90° twisted double bond in position 13. In agreement with previous studies,[188] the **CI** point located slightly *above* the minimum can be entered by progression along a mode dominated by a double bond expansion – single bond contraction of the N-containing moiety. This stretching mode is nearly orthogonal to the **SP→TM** coordinate characterized by a 90° torsion change and nearly parallel to one of the vectors defining the conical intersection branching plane (Figure 9–6).[109] This mode (the gradient difference vector) is shown in Figure 9–6b and corresponds to a single bond contraction - double bond expansion mode localized exclusively along the N-containing moiety of **2**. The same features are found for the all-trans→9-cis process.

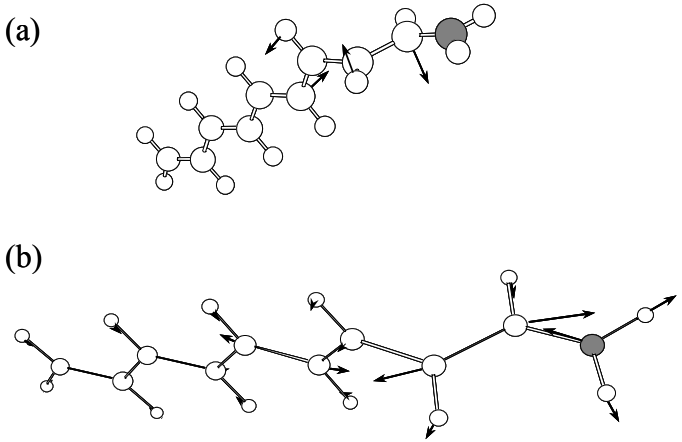


Figure 9–6: Branching plane vectors for the **CI** of **2** along the all-trans→13-cis photoisomerization co-ordinate. (a) Nonadiabatic coupling vector and (b) gradient difference vector.

In order to gain insight into the mechanism of the $S_1 \rightarrow S_0$ decay process, it is of interest to clarify the relationship between the shapes of the $S_1$ and $S_0$ energy surfaces in the **CI** region. This has been accomplished by carrying out, for both the all-trans→11-cis and all-trans→13-cis **CI**s of **2**, a one-dimensional scan of the CASSCF energy surfaces along the direction of the branching plane mode discussed above. The results of the scan are given in Figure 9–7.

The first general feature of the shape of the $S_0$ energy surface in these regions is that it contains the transition structures for the *thermal* cis-trans isomerization. In fact, in the case of the conical intersection associated to the all-trans→11-cis process, on opposite sides of the cone tip, two different $S_0$ minima could be located (see Figure 9–7a). This finding indicates the energy surface shape given in Scheme 9–2a, where the minima correspond to the distinct $S_0$ transition structures **TS1** and **TS2** and the conical intersection is "peaked".[109] Thus the scanning coordinate defines a **TS1→CI→TS2** $S_0$ energy ridge that divides the $S_0$ reactant (trans) and product (cis) valleys. In Figure 9–7b it is shown that, for the alternative case of the conical intersection associated to the all-trans→13-cis process, the computed energy profile shows only one $S_0$ energy minimum.

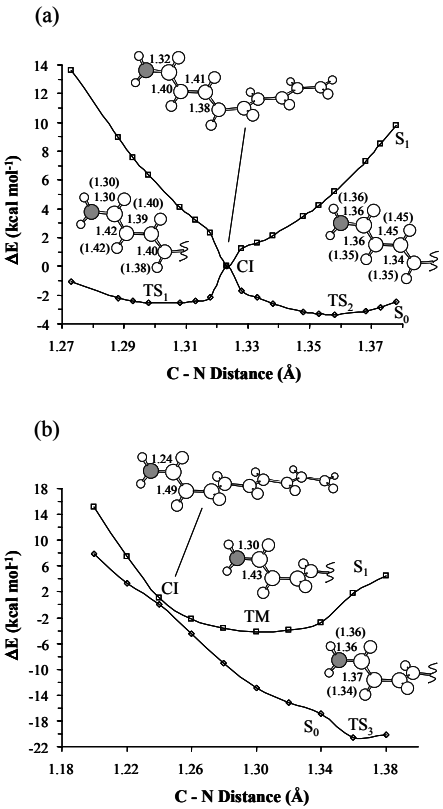


Figure 9–7: CASSCF energy profiles along a double bond expansion – single bond contraction mode defined in Section 9.3 for: (a) the **CI** point of the *all-trans*→11-*cis* path of **2** and (b) the **TM** point of the *all-trans*→13-*cis* path of **2.** The geometrical parameters of the optimized transition state structures (**TS$_1$**, **TS$_2$**, **TS$_3$**) are given in brackets (values in Å). The **CI** located in (b) is ca. 4.8 kcal mol$^{-1}$ higher in energy then the **TM**: this is due to the less comprehensive mono-dimensional scan performed in this case, with respect to that of Scheme 9–1.

This finding suggests an energy surface shape of the type illustrated in Scheme 9–2b where the minimum corresponds to a transition structure **TS3** and the conical intersection is "sloped".[109] Notice that the $S_1$ 90° twisted energy minimum **TM** is located in the region above the $S_0$ **TS3** structure. Thus, these two points differ in electronic structure and are related by an intramolecular charge transfer. Evidence in favour of the potential energy surface topologies of Scheme 9–2a and b has been produced by rigorous $S_0$ transition state searches in the full space of the nuclear degrees of freedom of the system. Three transition structures have indeed been located in the strict vicinity of the $S_0$ energy minima of Figure 9–7. Their relevant geometrical parameters are given in the same figure.

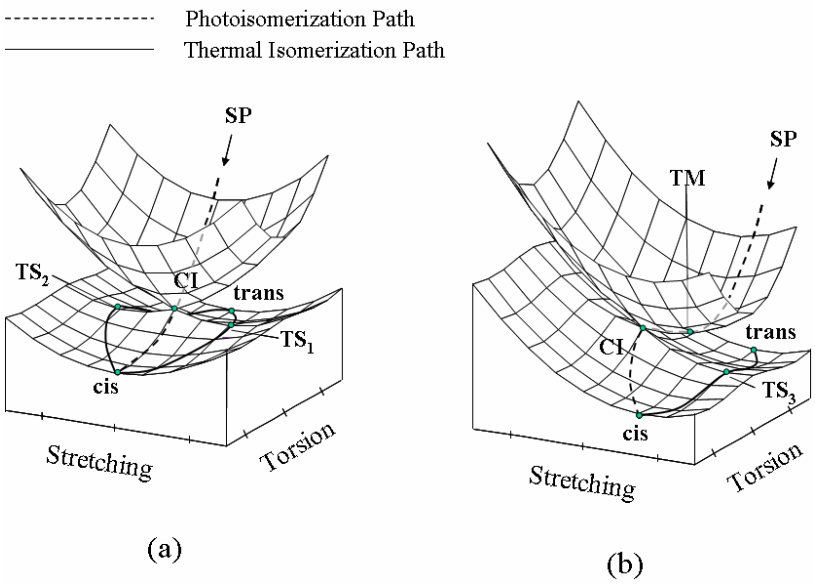


Scheme 9–2

# Chapter 10. How to Achieve a Photoisomerization “Speed Up” in Retinal Protonated Schiff Base Models

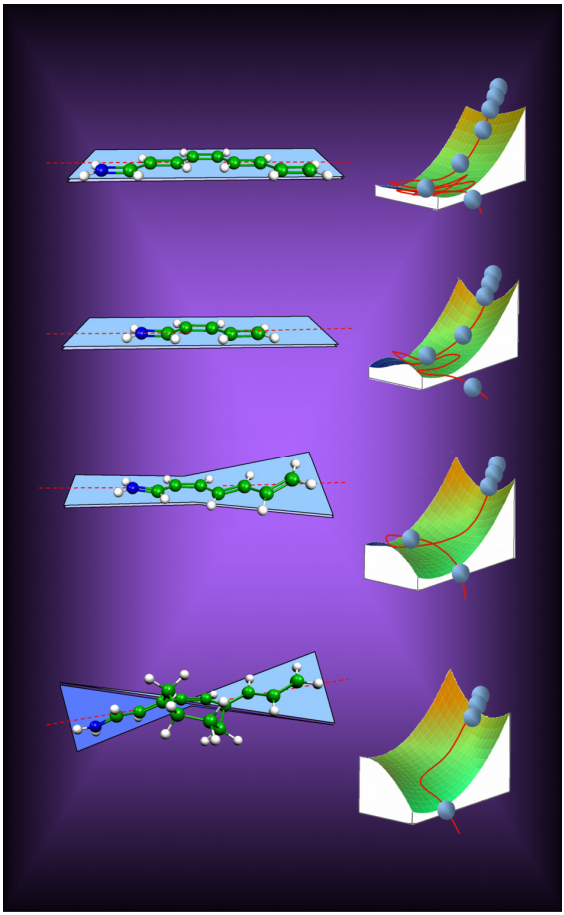

## 10.1. Introduction

In the present chapter the results of CASSCF/6-31G* photoisomerization path computations of a series of models of the 11-*cis*-retinal chromophore of the visual pigment rhodopsin are discussed.[194] The results indicate that, with respect to chromophore *in vacuo*, certain intramolecular and environmental factors are capable of speeding up the excited state decay associated with cis→trans isomerization motion. Using suitable protonated Schiff base models it is shown that three structural factors can potentially speed up the isomerization: (a) the reducing of the length of the conjugated chain, (b) the twisting of the hydrocarbon end of the conjugated chain with respect to the protonated Schiff base end and (c) the ring locking of the hydrocarbon end of the conjugated chain with an eight member ring. All factors operate via increasing the slope of the excited state energy surface and enhancing the coupling between stretching and torsional modes. It is then possible to argue that the protein catalysis seen in rhodopsin may, at least partly, exploit the same type of principles.

Results presented in Section 9.2 (see Figure 9–1) represent the basis to analyze the possible ways to speed-up the isomerization of rhodopsin-like retinals. While reaction paths provide structural (i.e. static) rather than dynamics information, the idea behind these computations is that the isomerization speed must primarily be a consequence of the structure of the path or, in other words, of the force field prompting PSB11 relaxation. Two factors appears to be critical for an isomerization speed up. The first is that

the reaction coordinate must be dominated by the cis-trans torsional mode. The second is that the energy profile along such coordinate must not only be barrierless but display a large slope.

According to the computational results on model **1**, the slower excited state dynamics observed when PSB11 is isolated from the protein environment has been attributed to:

(i) the fact that the $S_1$ isomerization coordinate is bimodal (see Figure 9–1 inset). Namely, the relaxation along a totally symmetric stretching mode (**FC→SP**) precedes the relaxation about the 11-cis→all-trans torsional mode (**SP→CI**) leading to $S_1 \rightarrow S_0$ decay at the conical intersection **CI**.

(ii) the existence of an extended (0°-40°) $S_1$ energy plateau (or even a small barrier) along this second mode (see Figure 9–1) that prevents effective acceleration of the excited state molecule towards decay.

The results (i) and (ii) suggest that the photoisomerization (and, in turn, the decay) may be speed up in systems that have a larger coupling between stretching and torsional modes or/and a reduced energy plateau along the torsional mode.

Reaction path computations indicate that, with respect to model **1**, certain *intramolecular and, loosely, environmental factors* can speed up the photoisomerization in PSBs. In particular:

(a) decreasing the length of the conjugated chain drastically reduces the $S_1$ energy plateau.

(b) *twisting the hydrocarbon end of the conjugated chain with respect to the protonated Schiff base end* not only decreases the length of the energy plateau but increases the stretching-torsion coupling.

(c) *ring locking with an eight member ring* leads to an even larger stretching-torsion coupling and reduction of the energy plateau.

Interestingly factors (b) and (c) are explained by the same light-triggered *conformational "spring" effect*. Such effect, that can be more correctly described in terms of photoinduced torsional (i.e. Pitzer) strain, is prompted by the light-triggered change in the position of the double and single bonds along the PSB skeleton.

## 10.2. Computational Details

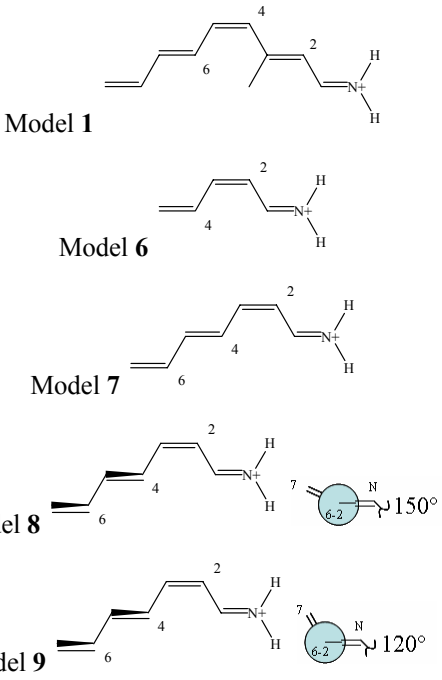

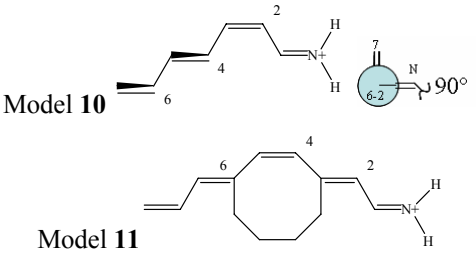


The molecular structures defining the FC→CI branch (i.e. the $S_1$ branch) of the reaction coordinates have been obtained via fully unconstrained (for cations **1**, **6, 7** and **11**) and partially constrained (for cations **8-10**) geometry optimization and minimum energy path (MEP) computations using the complete active space self consistent field (CASSCF) level of theory with the 6-31G* basis set. In all cases the chosen active space comprises the full π-system of the PSB11 models. In particular, an active space of 10 electrons in 10 π-orbitals was used for structures **1** and **11**, 8 electrons in 8 π-orbitals for structures **7-10** and 6 electrons in 6 π-orbitals for structure **6**. The MEP for structure **1** is from ref. 139, 149 (see also Section 9.2), the MEP for structure **6** was taken from ref. 195 while that of structure *all-trans* **7** from reference 136. A two root ($S_0$, $S_1$) state average procedure has been used to avoid CASSCF convergence problems in all excited state calculations. The procedure adopted to carry out these computations is reported in ref. 89, 154. In all cases progression along the MEP is given in mass-weighted cartesians (a.u.=amu$^{1/2}a_0$). The method is analogue to that described in Chapter 7, apart for the CASPT2 dynamic energy contribution correction.

Notice that in this part of the thesis the focus is on the changes of the *shape* and *slope* of the energy profile along the computed paths. For this reason the

calculations are limited to the CASSCF level of theory. While, in contrast to the CASPT2 level, CASSCF does not include the treatment of dynamics electron correlation and cannot correctly reproduce the excitation energy (i.e. the $S_0$-$S_1$ gap is overestimated), it is apparent from Figure 9–2 that, for PSBs, the general shape of the $S_1$ energy profile is substantially unchanged.

Structures **8-10** correspond to different conformations of the 2-*Z* stereoisomer of structure **7** and are characterized by fixed (i.e. constrained) dihedral angle. As illustrated in the corresponding model structures above and stressed in Scheme 10–1 below, the constraint is imposed on the dihedral angle N-$C_2$-$C_6$-$C_7$ and ensures a fixed conformational relationship between the carbon and nitrogen ends of the models. In particular, because of the constraint, the dihedral angle between the plane $\delta$ and the axis **a** is conserved along the MEP at ca. 150°, 120° and 90° for **8**, **9** and **10** respectively. (Notice that the centre $C_1$ will still be free to move above or below the $\pi$-plane $\alpha$.). The effect of the geometrical constraint is not straightforward. In fact, as illustrated in Scheme 10–1 for structure **9**, it imposes a ground state helical equilibrium structure that is also maintained along the computed excited state MEP. Such molecular (negative) helicity is due to the fact that, because of the constraint, planes $\gamma$ and $\beta$ are twisted out-of-plane of different amounts with respect to the reference plane $\delta$ or to the plane $\alpha$. Notice also that, because of the imposed constraint, the $\pi$-subsystems lying on the planes $\gamma$ and $\beta$ will be free to reorient with respect to the plane $\gamma$ and the axis **a** along the excited state MEP changing the magnitude of the helicity. Also notice that the N-$C_1$-$C_2$ $\pi$-subsystem lying on the plane $\alpha$ will be able to reorient about the same axis.

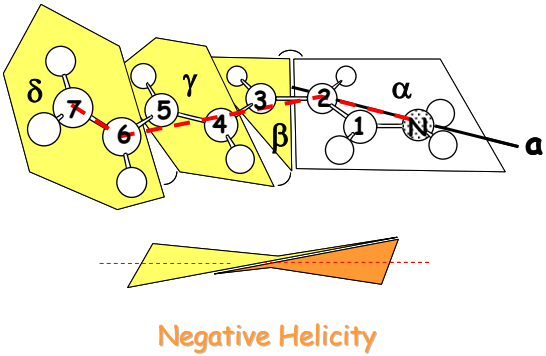


Scheme 10–1

## 10.3. Results and Discussion

### 10.3.1. Effect of the decrease of the length of the conjugated chain.

Figure 10–1 report the $S_1$ energy profile for the computed **FC→CI** path for models **1**, **6** and for two stereoisomers of **7** (the previously reported *all-trans*[136] and the *2-Z* forms). It is apparent that the more than 40° long energy plateau of model **1** is monotonically reduced when the length of the conjugated chain is decreased. In fact, both stereoisomer of **7** (i.e. the models with four double bonds) display an $S_1$ energy plateau that ends after a ca. 20° torsional deformation. This plateau is further reduced in the model with three double bonds **6**. Indeed, in **6** the energy plateau is abandoned after a ca. 10° torsional deformation.

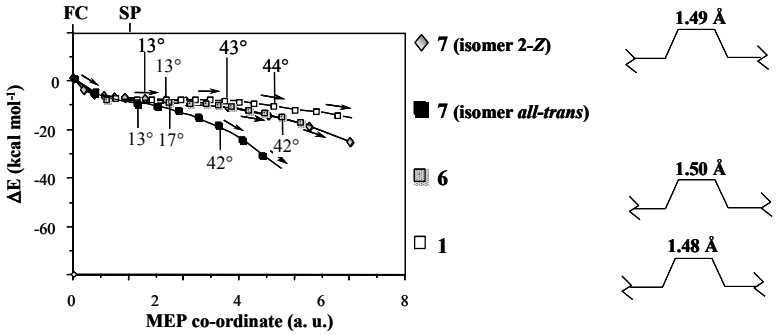


Figure 10–1: Comparison of the initial part of the unconstrained $S_1$ photoisomerization path of **1**, **6** and **7** (isomer all-trans and isomer 2-Z). The geometrical parameters in degrees document the progression of the dihedral angles $C_3$-$C_4$-$C_5$-$C_6$ for **1**, $C_1$-$C_2$-$C_3$-$C_4$ for **6** and $C_1$-$C_2$-$C_3$-$C_4$ for **7** along the relaxation path. **FC** and **SP** are defined as in Figure 9–1. The geometrical parameters in Å (on the right) document the bond length shortening of the central bond going from short to longer PSBs.

Analysis of the reaction coordinate for models **6** and **7** confirms the reaction path structure seen in the inset of Figure 9–1. Nevertheless, consistently with a strong reduction of the energy plateau, the shape of the potential energy near **FC** is different in **1** and **6**. This difference is illustrated in Scheme 10–2 that displays the shape of the $S_1$ energy surface region surrounding the planar relaxed structure **SP** in the two systems. In fact, **SP** corresponds to a flat energy minimum in **1** (see Scheme 10–2a) and to a transition structure in **6** (see Scheme 10–2b). While, due to the planarity of the **FC** structure, the totally symmetric stretching mode and the non-totally symmetric torsional mode are uncoupled, a small deviation from planarity will have the effect of leading to a prompt decay in **6** but not in **1**. This is schematically illustrated

by the hypothetic trajectories reported in Scheme 10–2a and b. Semiclassical trajectory computations[138] have confirmed such mechanistic idea, indicating that **6** should decay on ca. 50 fs time scale.

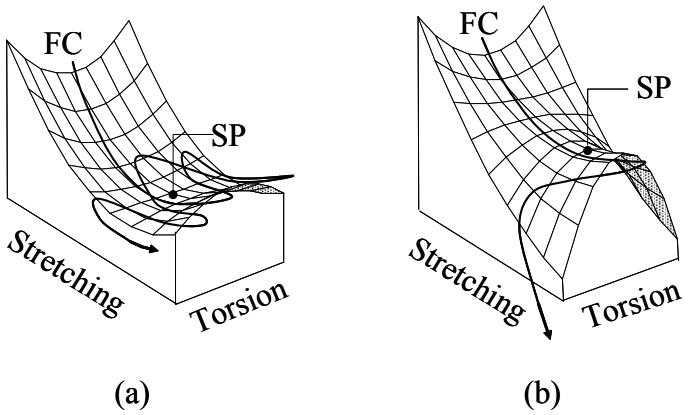


Scheme 10–2

As reported in ref. 133 the behaviour seen in Figure 9–1 must be related to the extension of the π-system and amount of residual π-bonding in the excited state. Briefly, the stretching relaxation leads to an inversion of the double bond/single bond position. This step is obviously preparatory with respect to torsional deformation as the reacting double bond is turned into a single bond after photoexcitation. The amount of double bond character maintained by the single bonds after photoexcitation must be related to the shape of the $S_1$ energy profile about the isomerization torsional coordinate. In short PSBs this residual character increases with the number of conjugated double bonds, thus, along the torsional coordinate, longer PSB11 models will display a flat $S_1$ energy plateau while shorter ones will display a highly

unstable energy profile. A direct evidence of this residual conjugation is provided by the bond length of the central bond (see Figure 10–1) that decreases going from shorter to longer PSBs.

### 10.3.2. Effect of the helicity.

The comparison of the FC→CI energy profile for PSB11 models featuring an imposed out-of-plane helical structure provides information on the effect of the planar symmetry breaking (e.g. due to certain specific environmental constraints) of the structure of the $S_1$ force field. In particular, as stressed in points (i)-(ii) of the introduction, the effect of such helical distortion on the length of the energy plateau and on the coupling between the stretching and torsional modes (see also Scheme 10–1 above) is quite interesting.

Figure 10–2 reports the initial part of the $S_1$ **FC→CI** energy profiles for models **6**-**10**. The reference energy profile will be the one of models **6** and 2-*Z* **7** already seen in Figure 10–1. These profiles represent two limiting cases: (1) model **6** represents a case where a three double bond π-system is fully unperturbed and (2) model **7** represents a case where the same π-system is maximally perturbed via conjugation with an additional terminal double bond (i.e. a terminal vinyl group). Again, as described above, model **7** displays a longer energy plateau.

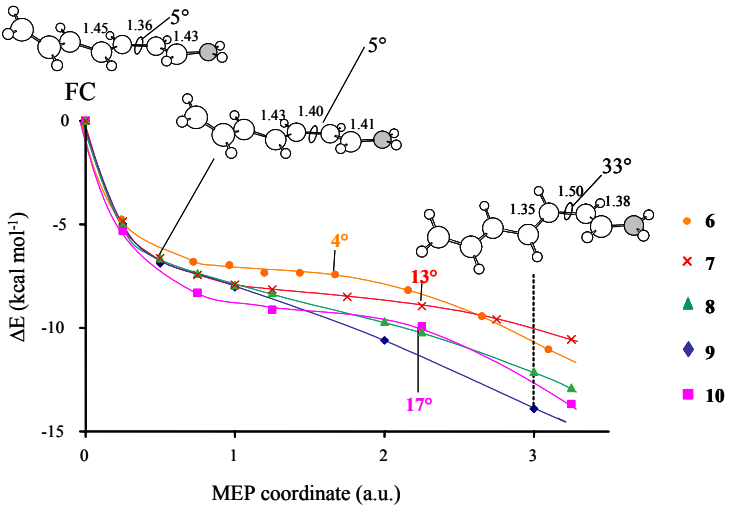


Figure 10–2: Comparison of the initial part of the $S_1$ **FC→CI** energy profile for models **6**-**10**. The geometrical parameters in degrees correspond to the value of the dihedral angle $C_1$-$C_2$-$C_3$-$C_4$ along the relaxation path. Notice that for models **6**,**7** and **10** the values at the end of the plateau are shown. The structures (geometrical parameters in Å and degrees) correspond to model **9** and document the progression of the bond length and dihedral angles $C_1$-$C_2$-$C_3$-$C_4$ along the relaxation path.

The different values of the constrained N-$C_2$-$C_6$-$C_7$ dihedral angle impose a different degree of helicity on models **8**-**10**. Thus for a N-$C_2$-$C_6$-$C_7$ angle of 150° (model **8**) one has a modest helicity that increases for a N-$C_2$-$C_6$-$C_7$ angle of 120° (model **9**) and becomes strong for a N-$C_2$-$C_6$-$C_7$ angle of 90° (model **10**). Of course, the helicity perturbs the conjugation along the model chain. Thus, model **8** is weakly deconjugated while model **10** is strongly deconjugated. Comparison of the energy profile of the fully unperturbed

model **6** with the strongly deconjugated model **10** confirms that, indeed, the length of the energy plateau must depend on the extension of the conjugation. In fact the two models display the same short (c.a. 4°) energy plateau (substantially an inflection) in the energy profile. Consistently the reaction coordinate analysis confirms a substantially decoupled stretching and torsional modes in both cases. The fact that the energy plateau of model **10** lies ca. 2 kcal $mol^{-1}$ below the plateau of the unperturbed model is readily explained by the preferential excited state stabilization effect of the additional (terminal) vinyl unit. In fact, as previously reported,[133] in the ground state PSBs display a positive charge located on the terminal C=N moiety. However, upon photoexcitation 40% to 50% of the charge is moved towards the carbon end of the molecule. As can be shown via simple resonance formula (i.e. valence bond) analysis, such charge translocation is coupled with the initial excited state stretching relaxation described by the exchange in the position of the single and double bonds. Thus alkyl and, even more importantly, vinyl substitution at the carbon end of the PSB model will also stabilize $S_1$ with respect to $S_0$, but will also stabilized the relaxed **SP** vs. **FC** structure.

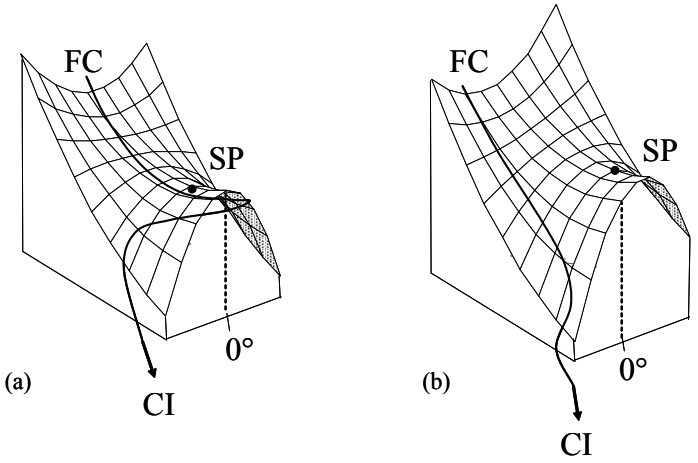


Scheme 10–3

Comparison of the weakly perturbed and maximally perturbed energy profiles of structures **10** and **7** with the energy profiles of the perturbed (i.e. partially conjugating) structures **8** and **9** reveals a completely different scenario. In structures **8** and **9** the short energy plateau of **10** or the longer energy plateau of **7** are not found. In contrast, the energy profiles display an energy slope that is larger for the helical model **9** than for the weakly helical model **8**. Reaction coordinate analysis reveals that along this slope the stretching modes become highly coupled with the torsional mode. In this way stretching relaxation does not precede torsional relaxation. This behaviour that must prompt a speed up of the isomerization motion on $S_1$ and leads to a faster $S_1$ decay is rationalized on the basis of the energy surface structure presented in Scheme 10–3. The presence of an helical structure breaks the torsional symmetry of the $S_1$ energy surface already at **FC**. Thus, in these systems the clockwise and counter-clockwise deformations will not be

equivalent and the $S_1$ relaxation must also involve the torsional mode (see Scheme 10–3b).

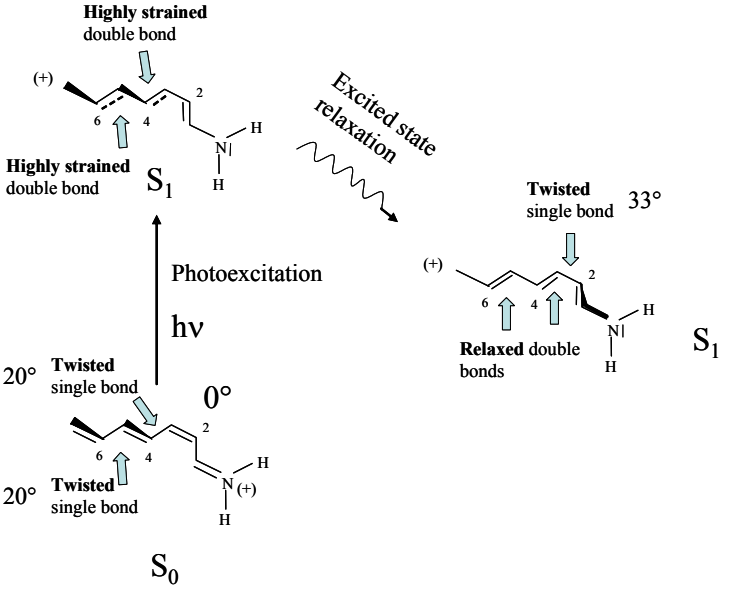


Scheme 10–4

The energy surface of Scheme 10–3b provides a structural explanation for the disappearance of the energy plateau and for the increased stretching-torsion coupling. However, the molecular mechanism responsible for such energy surface structure is illustrated in Scheme 10–4 for structure **9**. Immediately after photoexcitation the twisted $C_5$-$C_6$ and $C_3$-$C_4$ single bonds become torsionally strained due to the $S_0 \rightarrow S_1$ change in the electronic wavefunction. Again, as discussed above, in $S_1$ PSBs the original single bonds are turned into double bonds and *vice versa*. Thus, at **FC**, the gradients of structure **8** or

**9** must have important components along the $C_5$-$C_6$ and $C_3$-$C_4$ torsional modes. In particular, these components prompt planarization at these sites (that have now a double bond character). At the same time, due to the imposed geometrical constraint, the double bond at $C_2$-$C_3$ (i.e. the one that describes the isomerization process) becomes torsionally strained. For this reason this bond (that has now single bond character) relaxes along the corresponding torsional mode. In conclusion, the torsional components combine with the double bond expansion / single bond contraction mode described in the previous section and thus the excited state relaxation occurs along a highly coupled torsional and stretching mode.

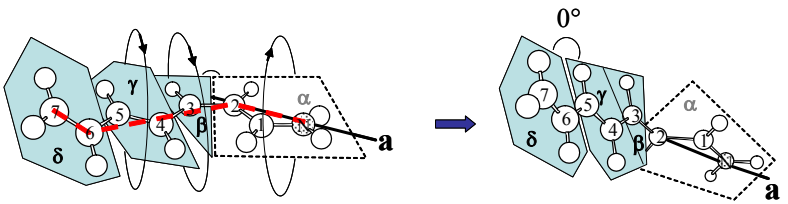


Scheme 10–5

The synchronous torsional motion about the $C_5$-$C_6$, $C_3$-$C_4$ and $C_2$-$C_3$ bonds is reminiscent of the previously proposed hula-twist motion.[196] However due to the imposed helical structure the torsional deformation occurs between not adjacent and multiple single and double bond pairs. For models **8** and **9** this motion can be described as a rotation of planes **γ** and **β** with respect to plane **δ** coupled with an opposite rotation of plane **α** about the axis **a**. This is illustrated in Scheme 10–5 that displays the computed geometry for **9** at 3.3 a.u. along the MEP.

The analysis of the results reported above indicates that since $S_0 \rightarrow S_1$ excitation results in a large torsional strain imposed on the **FC** structure, the geometrical constraint characterizing the perturbed structures **8** and **9** turns these system in photoactivated conformational springs that display enhanced acceleration along the reaction coordinate (and, of course) about the isomerising double bond. This additional acceleration is mediated by the augmented slope of the energy profiles seen in the perturbed models. Again, the ultimate, mechanistic reason for this acceleration has to be ascribed to changes in the equilibrium position of double and single bonds.

### 10.3.3. Effect of eight member ring-locking.

This section reports about a speed up effect of the same nature of the one seen above. However this time the constraint is not imposed externally (i.e. mimicking an environmental steric effect) but is due to the presence of a specific type of intramolecular ring-locking. In particular, it will be shown that in structure **11** two excited state double bonds contribute to the excited state torsional strain leading to a **FC→CI** energy profile with a large slope.

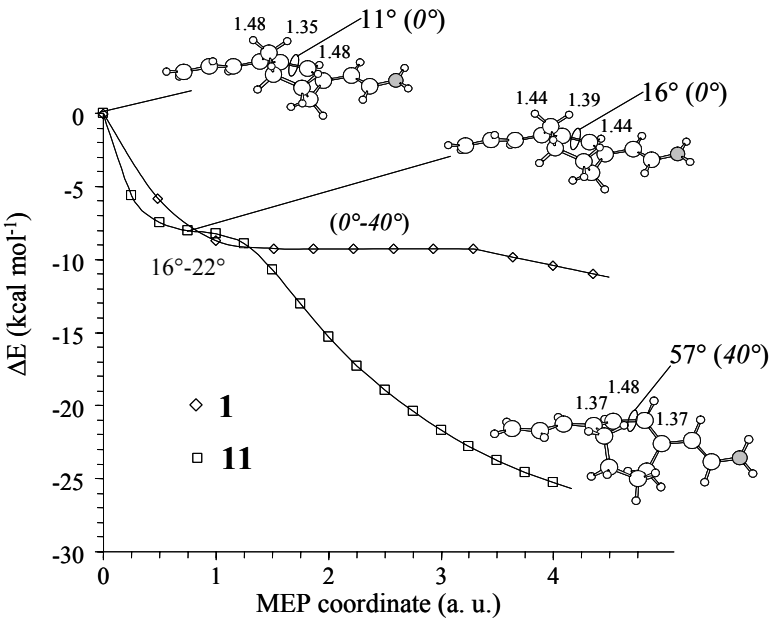


Figure 10–3: Comparison of the initial part of the $S_1$ **FC→CI** energy profile for the PSB11 model 1 (open diamonds) with that of structure **11** (open squares). The geometrical parameters (in Å and degrees) document the progression of the molecular structure along the relaxation path of 11. The corresponding progression for the dihedral angle $C_3$-$C_4$-$C_5$-$C_6$ of **1** is shown in brackets.

Figure 10–3 shows the comparison of the energy profile of the reaction path of the PSB11 model **1** with that of structure **11**. It is clear that **11** displays a reduced (i.e. only ca. 6° long) energy plateau of ca. the same length of that found for model **6**. After the plateau the energy decreases very quickly yielding an energy profile that is even steeper than the one found for models **8** and **9**. Since **1** has a planar **FC** structure, one has, again, the behaviour

shown in Scheme 10–2a where the clockwise and counter-clockwise torsional deformations lead to enantiomeric $S_1$ paths. In fact, in **11** the asymmetric lock removes the symmetry and, in principle, one must now have a structure of the potential energy surfaces where **FC** and **SP** correspond to structures twisted in opposite directions (see Scheme 10–3).

The mechanistic explanation for this behaviour will be given in Chapter 11.

## 10.4. Conclusions

The classification of the structural factors that may (or may not) result in a speed up of the photoisomerization of PSBs with respect, for instance, to PSB11 *in vacuo*, appears to have a wide interest. In fact, while these factors may help to unveil the nature of the rhodopsin protein "catalysis" of photoisomerization, PSBs may also serve as models for the development of efficient bio-mimetic switches or, ultimately, single-molecule molecular motors. This technological issue calls for a detailed comprehension of the mechanism and catalytic effects on the isomerization process in such a way to assist the design of novel functional materials. Accordingly, above three different structural factors have been reported, appearing able to speed up the excited state decay of PSBs.

The first factor corresponds to the decreasing in length of the π-system and operates by reducing the excited state energy plateau documented for model system **1**. The second factor suggests that asymmetric environmental (*intermolecular*) constraints yielding a helical conformation of the PSB

conjugated backbone speed up the photoisomerization by both eliminating the excited state energy plateau and increasing the slope of the energy surface. Finally the same effect has been reported when suitable *intramolecular* constraints such as those imposed by an eight member ring lock, acts on the conjugated chain.

Going back to the problem of determining the factors driving the rhodopsin protein catalysis it is interesting to point out that the x-ray crystallographic structure of bovine rhodopsin[43] clearly shows a PSB11 chromophore with a distorted helical structure. Furthermore an artificial rhodopsin where an eight member ring locked chromophore replaces the native retinal[186] show an even more enhanced excited state decay rate. All these facts will be also treated in next Chapter 11.

# Chapter 11. Photoisomerization Mechanism of 11-cis-Locked Artificial Retinal Chromophores: Acceleration and Primary Photoproduct Assignment

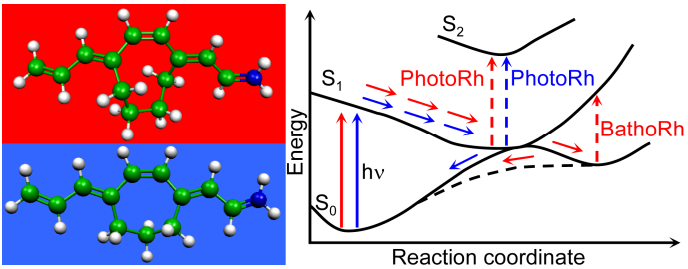


## 11.1. Introduction

This chapter will deal with the large changes in excited state lifetime observed along a series of artificial pigments where the native PSB chromophores have been substituted with synthetic 11-cis *locked* chromophores.[186,197] As already seen in Sections 8.2 and 9.4, in these molecules the torsional deformation of the reactive double bond (e.g. the 11-cis double bond) is restrained since the double bond is part of a cyclic moiety. For this reason the formation of a stable PSBT photoproduct is not expected and the photolysis of the artificial pigment leads to a rapid

reconstitution of the starting material. On the other hand, a varied spectrum of excited state lifetimes has been observed as a function of the ring size. For instance, an 85 ps *increase* in excited state lifetime, along with fluorescence, is observed in an artificial rhodopsin (Rh5) where the chromophore features an 11-cis double bond embedded in a five member ring (PSB11.5).[184] In contrast, in the different artificial rhodopsins (Rh7 and Rh8) where the 11-cis double bond is embedded in a seven (PSB11.7) and an eight (PSB11.8) member ring, respectively, one observes no fluorescence, suggesting that these chromophores are flexible enough to allow for rapid excited state relaxation. Furthermore, Rh8 features a 90 fs *decrease*[186] in excited state lifetime with respect to the ca. 150 fs of wild-type Rh. In other words while, as expected, the five member ring lock prevents the 11-cis→all-trans excited state motion dominating the evolution towards the $S_1 \rightarrow S_0$ decay channel, *the eight member ring lock of PSB11.8 seems to be able to accelerate this process*.

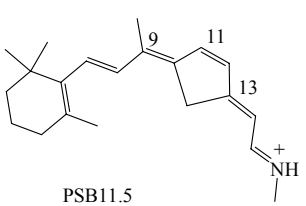


PSB11.5

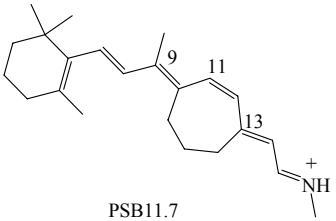


PSB11.7

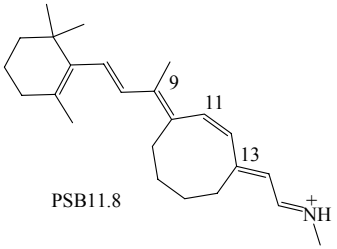


PSB11.8

Along the previous series of artificial rhodopsins, one observes also a remarkable difference in the appearance of the transient photoproducts. In fact, while no photoproduct has been detected for Rh5, photolysis of Rh7 leads to a transient photoproduct with a 580 nm $\lambda_{max}$.[184] Similarly, photolysis of the less strained Rh8 system leads to the appearance of two distinct and sequential photoproducts, with a 585 nm and 577 nm $\lambda_{max}$, respectively.[198]

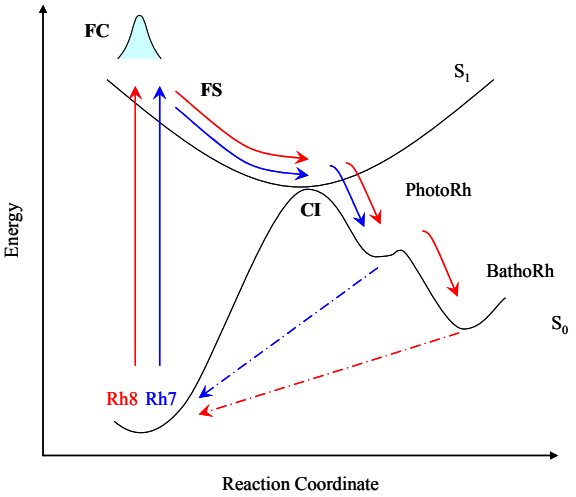


Scheme 11–1

These results have been interpreted according to a reaction mechanism proposed by Mizukami et al.,[198] where the transients absorbing at 580 and 585 nm are assumed to correspond to analogues of the primary photoproduct photorhodopsin (photoRh) and the absorption at 577 nm is assumed to be associated to production of a bathorhodopsin (bathoRh) analogue. The fact that locks of different size determine the appearance of a different number of Rh photoproducts, as well as the fact that the eight member ring lock speeds up the excited state decay, appears of great interest in the context of the investigation of the photoisomerization mechanism of PSBs. Indeed, it is apparent that the different degree of torsional flexibility associated to each ring lock must be related to the type and number of transient species generated, as well as augmented excited state decay rate. As stressed below, the investigation of these ring strain effects, via the mapping of the intrinsic

excited state reaction path of PSB11.7 and PSB11.8, represents the main research target of the present chapter.

Chapter 10 reported the CASSCF photoisomerization paths of a series of PSB models, showing the relationship between molecular structure and the shape of the potential energy surface. This chapter reports CASPT2//CASSCF photoisomerization and relaxation path computations to achieve information about the intrinsic behaviour of locked retinal chromophores after photoexcitation. As in previous chapters, the studied models did not include the terminal double bond of PSB11, which is part of the β-ionone ring, since it does not conjugate effectively with the remaining part of the π-system.

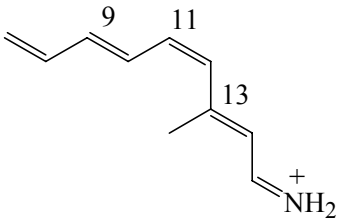


**1**

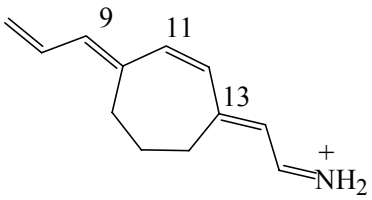


**2**

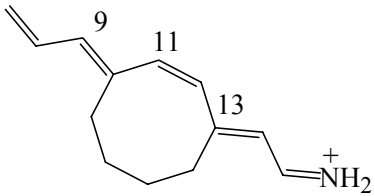


**3**

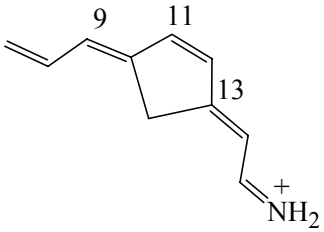


**4**

As reported in Section 9.2, photoisomerization path computations for **1** have demonstrated that the $S_1$ reaction co-ordinate ($S_1$ corresponds to the 1 $B_u$-like – i.e. hole-pair - spectroscopic state of polyenes) is sequentially dominated by two substantially uncoupled modes (see Figure 11–1a for a schematic view of the structure of the $S_1$ potential energy surface of **1**). The first mode is totally symmetric and drives the initially planar system out of the Franck-Condon point (**FC**) through a concerted double-bond stretch and single-bond compression. The second mode is asymmetric and is dominated by a cis-trans isomerization motion initiated after depopulation of a very flat planar energy minimum (**SP**). Evolution along this mode leads to a conical intersection funnel (**CI**) where the chromophore displays a ca. 90° twisted central double bond and where fully efficient decay to the ground state takes place.

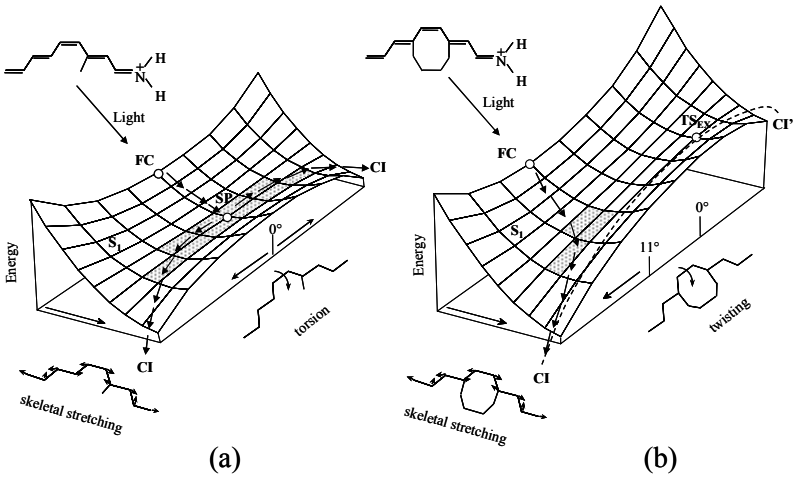


Figure 11–1: Schematic illustration of the two-mode structure of the $S_1$ energy surface along the excited state isomerization path for (a) the PSB11 model **1** (as in Section 9.2) and (b) the PSB11.8 model **3** in isolated conditions. The stream of arrows on the $S_1$ surfaces represents the two-mode reaction co-ordinate starting at **FC**. The dashed line represents the path connecting the two conical intersection funnels entered via "clockwise" and "counter clockwise" torsional deformation respectively. Point **SP** corresponds to a flat energy minimum (i.e. a metastable species) where the torsional deformation leading to two degenerate $S_1 \rightarrow S_0$ decay channels **CI** begins. Similarly, point $\mathbf{TS_{ex}}$ represents a transition structure connecting the non degenerate **CI** and **CI'** decay channels. The shaded areas corresponds to the flat $S_1$ energy plateau discussed in the text.

In analogy with model **1**, in this chapter the 4-*cis*-nona-2,4,6,8-tetraeniminium cation derivative **2** is used as a model of PSB11.7 and **3** as a model of PSB11.8. It will be shown that, while **2** features an $S_1$ energy

surface remarkably similar to that of the unlocked model PSB11 (see Figure 11–1a), **3** displays an $S_1$ energy surface with the structure shown in Figure 11–1b. This surface is asymmetric with respect to the clockwise and counter-clockwise torsion due to the lack of planarity of the chromophore. As a consequence, ***3*** *will experience an initial relaxation characterized by a coupled stretching-torsional motion and not by the only stretching as in* ***1***. The same models will also be used to investigate the *effect of the different size locks on the photoproducts appearance*, assuming that this is a consequence of *intrinsic* chromophore factors. In other words in PSB11.7 and PSB11.8 the ring strain (in particular the Pitzer strain[199]) would alter the structure of the $S_1$ force field of the native PSB11 conjugated backbone in such a way to restrain (or allow) the formation of certain intermediates and, in the case of Rh8, accelerate the evolution towards the $S_1 \rightarrow S_0$ decay channel. In the framework of this hypothesis, the results of relaxation path computations starting at the CI point of **2** and **3** call for a substantial revision of Scheme 11–1 and provide evidence that, indeed, the formation of a single photoproduct or of two sequential photoproducts associated to photoRh and bathoRh analogues is a function of the ring size.

## 11.2. Computational Details

Structure optimization and relaxation path mapping have been carried out using fully unconstrained *ab initio* quantum chemical computations in the framework of the CASPT2//CASSCF/6-31G* strategy, as reported in Chapter 7.

All computations employed the 6-31G* basis set and an active space comprising 10 electrons in 10 orbitals. This includes the full π-system.

Energy minima and transition structures of the electronic ground state were optimized using a single root CASSCF wave function, while minima and transition structures of the electronic first excited state were optimized using a two roots ($S_0$, $S_1$) state average (0.5, 0.5) CASSCF wave function. The $S_1$ and $S_0$ potential energy surfaces were connected through Conical Intersections (CI).

A two roots ($S_1$, $S_0$) state average (0.5, 0.5) CASSCF wavefunction $S_1$ MEP calculation was performed to connect the Franck-Condon point of **3** to the $S_1/S_0$ CI; analogously, two MEP calculations were performed along the potential energy surface of **2** to connect the $S_1$ transition state to the minimum and to the $S_1/S_0$ CI. For each CIs a $S_0$ MEP was computed using a single root wavefunction, connecting the chosen CI to the $S_0$ reagent or product minimum.

For each geometry, a three roots ($S_0$, $S_1$, $S_2$) state-average (0.33, 0.33, 0.33) CASSCF wavefunction was used as reference function for evaluating the CASPT2 energies, to include the dynamic correlation effect.

The energy of the CIs of the two models were also re-evaluated at the CASPT2 level of theory using the larger basis-set 6-31G(d,p) that includes diffuse functions. The calculation was performed to check the consistency of the previous results when adding diffuse function. Since no sensible variation in $S_0/S_1$ energy difference was found, the usage of diffuse function can be considered not influent on the considered models. This effect can be explained by considering the ionic nature of the models. Indeed, a large effect given by diffuse functions can be expected when dealing with anionic species; that's because of the larger electron density of the molecule which,

otherwise, could be artificially constrained on atoms. On the other hand, cation are not expected to need expansion of the basis-set, given that electron density is naturally contracted.

## 11.3. Results

### 11.3.1. Conformational Structure of the PSB11.8 Chromophore Model

While the PSB11 model **1** admits a single planar conformer,[139] the eight member ring lock in the PSB11.8 model **3** induces an out-of-plane deformation of the originally planar 4-*cis* nona-2,4,6,8-tetraeniminium cation moiety ultimately leading to different conformers of close energy. The **Half-chair**, **Boat-1** and **Boat-2** structures displayed in Figure 11–2 were located within a 1 kcal $mol^{-1}$ energy range.[a] It is apparent from Figure 11–2 that, in all conformers, the conjugated chain appears to be considerably twisted. However, while in **Half-chair** the axis of the conjugated chain is substantially linear, both the **Boat-1** and **Boat-2** structures display a considerably bent chain. As reported in Table 11–1, **Boat-1** is 0.8 kcal $mol^{-1}$ more stable than **Half-chair**. Despite the computed energy order, in the

[a] A molecular mechanics/mm3 conformational search was first performed. Afterwards, the obtained structures showing all trans double bonds (with the exception of the one embedded into the ring) were optimized at the CASSCF/6-31G* level of theory. The refined geometries were then re-evaluated at the CASPT2 level of theory.

present chapter the focus will only be on the photoisomerization of **Half-chair**, since this appears to be the only structure that could fit into the rhodopsin cavity.

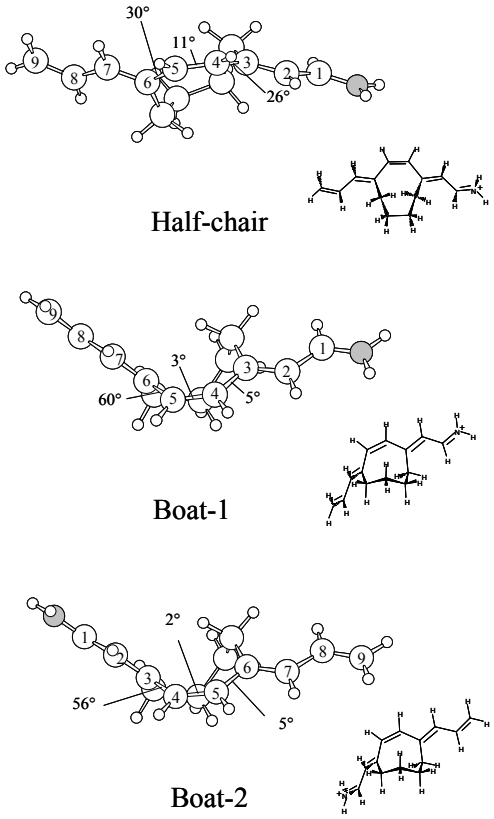


Figure 11–2: Ground state conformers of the PSB11.8 model **3**. The values of the three central twisting deformations correspond to the $C_7$-$C_6$-$C_5$-$C_4$, $C_6$-$C_5$-$C_4$-$C_3$ and $C_5$-$C_4$-$C_3$-$C_2$ dihedral angles.

The computed absorption maximum for **Half-chair** is 503 nm and therefore it is only 20 nm red-shifted with respect to the 481 nm computed for **1.**[139] This behaviour seems in line with the protein absorption maxima where one has a 498 nm and 500 nm absorption maximum for Rh and Rh8 respectively.[a] The fact that the absorption maximum of **Half-chair** is slightly red-shifted with respect to **1** can be explained taking into account two basic properties of conjugated chains:

(i) twisting about single bonds leads to deconjugation and therefore to a blue-shift in the absorption maximum,

(ii) twisting about double bonds leads to bond breaking and therefore to a red-shift.

**Half-chair** features an 11° twisted central 4-cis double bond (i.e. the one corresponding to the 11-cis double bond of PSB11.8) and the two adjacent single bonds (positions 3 and 5) twisted of 26° and 30° respectively. Thus, in this conformer, the red-shift and blue-shift effects partially cancel each other. This appears to be in line with the 481 nm blue-shifted computed absorption maximum of **Boat-1**. In fact, this conformer features a substantially planar 4-cis double bond but a 60° twisted adjacent single bond (position 5), leading to a dominant de-conjugating effect. The same explanation is in line with the fact that the PSB11.5 model **4,** featuring a fully planar conjugated backbone, has a computed absorption maximum of 485 nm,[137] i.e. virtually the same as

[a] The fact that the absorption maximum of PSB11 and PSB11.8 are only slightly displaced from each other is also true in solution as these quantities are 445 nm and 435 nm respectively in methanol (when chloride is the counterion).

that of the unlocked chromophore **1** (481 nm). In the following the label **3** will be used to indicate exclusively the **Half-chair** conformer.

### 11.3.2. Excited State Isomerization Path of Models 3 and 2

Figure 11–3 (next page): Energy profiles along the (a) $S_1$ 4-cis→all-trans (11-cis→all-trans in PSB11.8) photoisomerization coordinate of **3,** (b) $S_1$ 4-cis→all-trans (11-cis→all-trans in PSB11.7) photoisomerization coordinate of **2** and (c) $S_1$ 4-cis→all-trans (11-cis→all-trans in PSB11) photoisomerization coordinate of **1** (data from ref. 149; see also Section 9.2). Full circles, full squares and full diamonds indicate the $S_2$, $S_1$ and $S_0$ CASPT2 energies. Open squares show the $S_1$ CASSCF energies (i.e. before PT2 correction). The structures (geometrical parameters in Å and degrees) document the progression of the molecular structure along the co-ordinate. **FC** is the Franck-Condon structure, **SP** corresponds to the relaxed planar species, $\mathbf{TS_{EX}}$ is a transition state, **TM** represents a relaxed twisted minimum and **CI** is the ca. 90° twisted $S_1/S_0$ conical intersection decay channel.

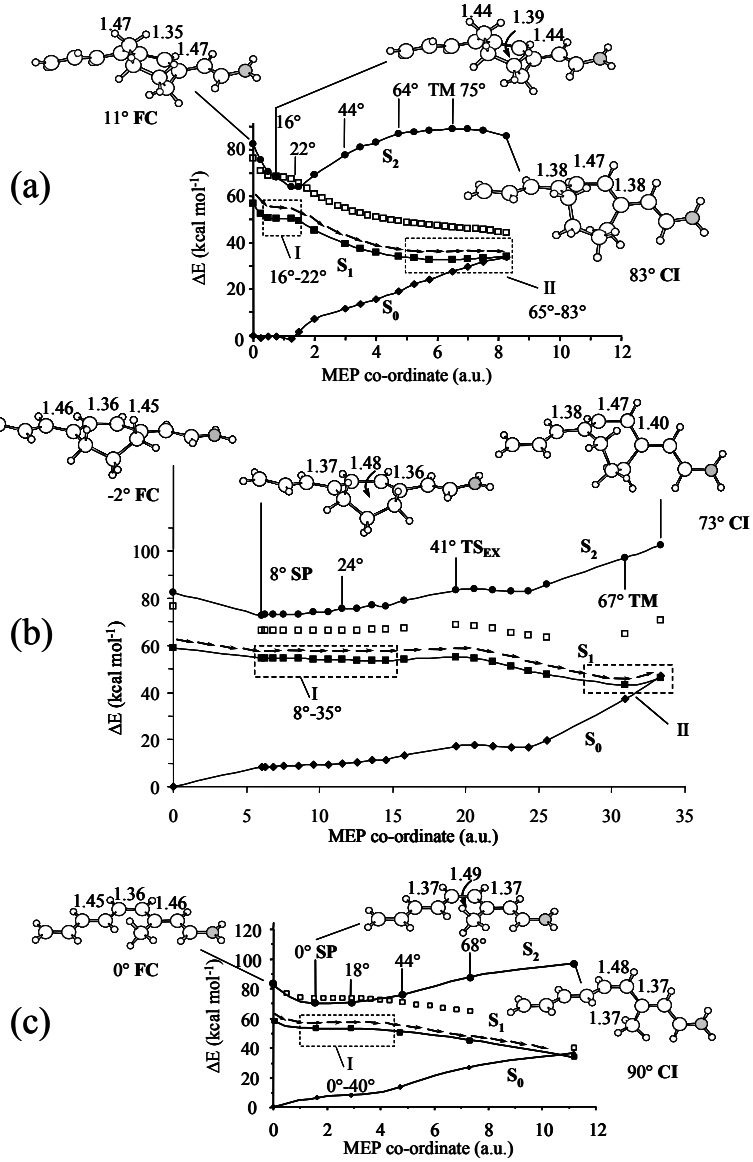
(a)
1.47
1.35
1.47
11° FC
1.44
1.39
1.44
64°
TM
75°
16°
44°
22°
S2
1.38
1.47
1.38
83° CI
I
S1
16°-22°
II
S0
65°-83°
ΔE (kcal mol-1)
MEP co-ordinate (a.u.)
(b)
1.46
1.36
1.45
-2° FC
1.38
1.47
1.40
73° CI
1.37
1.48
1.36
41° TSEX
S2
8° SP
24°
67° TM
S1
I
8°-35°
II
S0
ΔE (kcal mol-1)
MEP co-ordinate (a.u.)
(c)
1.45
1.36
1.46
0° FC
1.49
1.37
1.37
0° SP
18°
44°
68°
S2
1.48
1.37
1.37
90° CI
S1
I
0°-40°
S0
ΔE (kcal mol-1)
MEP co-ordinate (a.u.)

Figure 11–3a presents the result of excited state MEP computations for **3**. In order to describe the effect of the Pitzer (i.e. torsional) strain introduced by the eight member ring lock on the shape of the 4-cis→all-trans $S_1$ photoisomerization path, Figure 11–3c reports the corresponding path for **1** taken from ref. 149 (see also Section 9.2). As already stated above, the major difference between the two $S_0$ equilibrium structures (i.e. the **FC** points) is the large twisting deformation of the central portion of the conjugated chain of **3**. Despite this difference it is apparent from inspection of Figure 11–3a and c that the two paths display the same general structure. In particular, for both paths the $S_0$, $S_1$ and $S_2$ energy profiles have the same structure with the $S_2$ ($S_2$ corresponds to the singlet $2A_g$-like – i.e. dot-dot - dark excited state of polyenes) energy profile always more than 15.0 kcal $mol^{-1}$ higher than the $S_1$ state. Thus, as previously reported,[139] the computations show that only the $S_1$ and $S_0$ potential energy surfaces are involved in photoisomerization of PSBs. For this reason, in the following the discussion will be exclusively centred on these two energy surfaces.

In contrast to their general structures, the reaction coordinates and energy profiles of the excited state isomerization path of **3** and **1** are remarkably different. A first difference is found in the **FC** region. In fact, as mentioned above (Section 11.1, see Figure 11–1), the initial relaxation of the unlocked chromophore is dominated by an in-plane stretching motion leading to a planar stationary point **SP**. The following torsional relaxation starts at **SP** and develops along an extended energy plateau that ends after a ca. 40° twisting deformation (see dashed frame in Figure 11–3c). In contrast, **3** relaxes along a coordinate characterized by highly coupled stretching and torsional

deformations. In fact, as shown in Figure 11–3a, the relaxation of the 11° twisted **FC** structure yields a 16° twisted structure (i.e. with a net +5° torsion increase) where, with respect to the **SP** structure of **1**, the length of the central double bond has only been slightly expanded (e.g. for the central double bond one has a 1.35Å→1.39Å and 1.36Å→1.49Å change for **3** and **1** respectively). Inspection of Figure 11–3a reveals a second difference between the relaxation paths of **1** and **3**. In fact, while **3** displays the same energy plateau feature observed for **1** (see dashed frames I) this does not start at a planar stationary point **SP**, but at a transient 16° twisted structure. Such plateau is very short since it ends at only 22° twisting revealing a net 6° length i.e. much shorter than the 40° long energy plateau of **1**. A third difference regards the shape of the $S_1$ isomerization path beyond 40° torsional deformation. As shown in Figure 11–3c, in this region **1** leaves the energy plateau and evolves along a slope leading to a 90° twisted conical intersection **CI**. In contrast, in **3** the **CI** is located at the end of a low lying flat region of the $S_1$ energy surface spanned by structures featuring 65° to 83° twisting (see dashed frame II), and featuring a twisted minimum **TM** located 4 kcal $mol^{-1}$ below the **CI**.

The excited state MEP of model **2** shows a structure remarkably similar to that of the unlocked model **1** (compare Figure 11–3b and c). Indeed, the nearly planar **FC** structure evolves toward an 8° twisted minimum **SP** located just 4 kcal $mol^{-1}$ lower in energy. Similar to **1**, at **SP** the change in bond order is already completed, while the torsional deformation has only increased of 10°. A nearly 30° long energy plateau (dashed frame I in Figure 11–3b), connects **SP** to the transition state ($\mathbf{TS_{EX}}$), located 0.5 kcal $mol^{-1}$ above **SP** and featuring a torsional deformation of 41°. After the transition state, the path evolves along a slope, reaching a twisted minimum (**TM**) which features

a 67° torsional deformation and gives access to a conical intersection **CI**, located 3 kcal $mol^{-1}$ higher in energy.

From a more quantitative point of view, the excited state relaxation path of **2** appears to be flatter than that of **1**: for example there is a 15 kcal $mol^{-1}$ difference in energy between **FC** and **TM** against the 25 kcal $mol^{-1}$ energy difference between **FC** and **CI** of **1**.

### 11.3.3. Ground state Relaxation and Reactant Reconstitution of Models 3 and 2

At **CI** the excited state species undergoes a fully efficient decay to $S_0$ prompting ground state relaxation and, ultimately, photoproduct formation. In order to provide mechanistic information on the decay process the relaxation paths departing from **CI** were computed. (See Chapter 6)

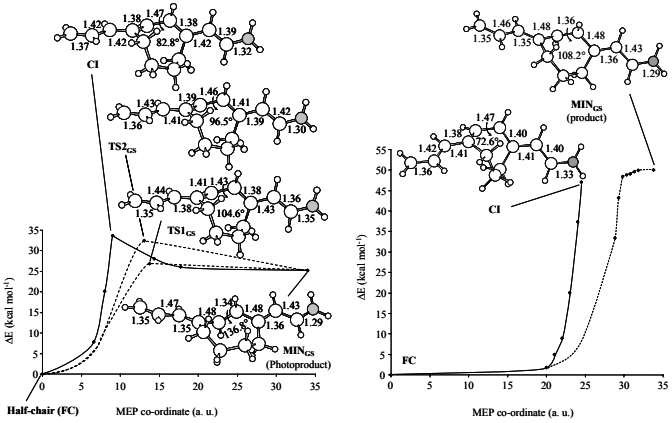


Figure 11–4: (a) CASPT2 energy profiles along the $S_0$ relaxation paths (**CI→MIN$_{GS}$** and **CI→FC**, full line) and reactant reconstitution paths (**MIN$_{GS}$→TS1$_{GS}$→FC** and **MIN$_{GS}$→TS2$_{GS}$→FC**, dashed line) for the PSB11.8 model **3**. (b) CASPT2 energy profiles along the $S_0$ relaxation paths (**CI→FC**, full line) and reactant reconstitution paths (**MIN$_{GS}$→ FC**, dashed line) for the PSB11.7 model **2**. Structures corresponding to the energy minimums and transition states are also reported (geometrical parameters in Å and degrees). The structure of the conical intersections of Figure 11–3a and b are also reported to allow comparison with the other structures.

Figure 11–4a reports two relaxation paths of **3** leading to (i) the reactant and (ii) a high energy minimum **MIN$_{GS}$** displaying an *all-trans* nona-2,4,6,8-tetraeniminium cation moiety. Because of the high torsional strain imposed by the ring, **MIN$_{GS}$** is located ca. 25 kcal mol$^{-1}$ higher in energy than the reactant and displays a 137° twisted "trans" central double bond. Thus route i constitutes a photochemical reactant back-formation path while route ii leads to production of a relatively unstable all-trans photoproduct. In order to

provide a quantitative estimate of the degree of stability of $\mathbf{MIN_{GS}}$ two different transition structures $\mathbf{TS1_{GS}}$ and $\mathbf{TS2_{GS}}$ have been located, both associated with the all-trans → 4-cis thermal isomerization of the primary photoproduct (i.e. to thermal reactant reconstitution).[a] The magnitude of the associated reaction barriers is 1.6 and 7.2 kcal $mol^{-1}$ respectively, indicating that $\mathbf{TS1_{GS}}$ defines the most efficient thermal isomerization route for the return of $\mathbf{MIN_{GS}}$ to the original **Half-chair** structure of **3**.

In Figure 11–4b is reported the reactant back-formation determined for **2**. This is the only relaxation path for this model. In fact, a minimum $\mathbf{MIN_{GS}}$ displaying a 108° twisted "trans" central double bond was located 3 kcal $mol^{-1}$ above **CI**.

In the region of the CI, the $S_1$ energy surfaces of model **2** and **3** appear to be similar (both showing a **TM** and a higher in energy **CI**). However, the $S_0$ ones are quite different, giving rise to different conical intersections. Indeed, **2** shows a conical intersection with a more "sloped"[109] topography than that of **3**. (See Section 5.3.1) As a consequence, the relatively unstable photoproduct $\mathbf{MIN_{GS}}$ of **3** can be reached via the photoisomerization path through the **CI**, while $\mathbf{MIN_{GS}}$ of **2** could be reached only via a thermal one as the **CI** gives access only to the reagent's valley. A three dimensional representation of the two CIs is reported in Scheme 11–2.

[a] It is quite common that transition state's saddles controlling thermal cis-trans isomerization are split in two by a conical intersection peak. (see for example ref. [200] and also Section 9.6) This, ultimately, leads to the appearance of two different transition states, as depicted in Scheme 11–2.

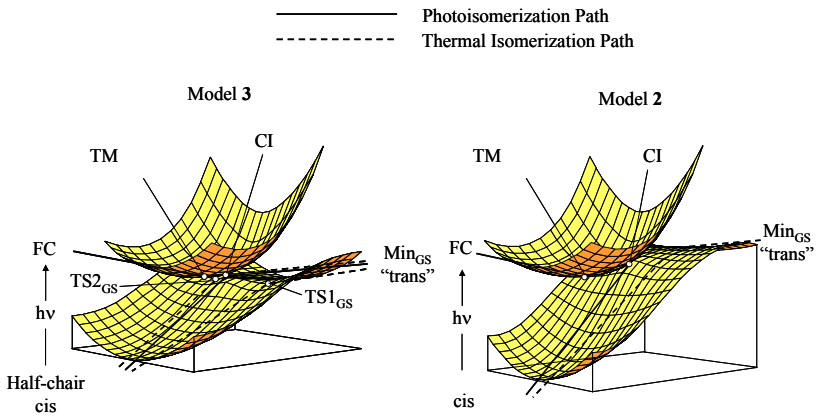


Scheme 11–2

# 11.4. Discussion

## 11.4.1. Structure of the Excited State Isomerization Path of Model 3

This section examines the effects of the eight member ring strain on the structure of the $S_1$ potential energy surface along the $C_3$-$C_4$-$C_5$-$C_6$ torsion. In the Introduction Section 11.1, it was mentioned that **3** features an asymmetric excited state potential energy surface (see Figure 11–1b). Indeed, transition state optimization on $S_1$ leads to a stationary point with a -5° twisted 4-cis double bond ($\mathbf{TS_{EX}}$), that plays the role of the asymmetric structure SP. As shown in Figure 11–5, this structure connects two $S_1/S_0$ conical intersections, **CI'** and **CI**. **CI'** is located ca. 6 kcal $mol^{-1}$ below $\mathbf{TS_{EX}}$ and features a –74° twisted double bond. Torsional deformation in the opposite direction

displaces $\mathbf{TS_{EX}}$ towards an extended energy plateau beginning at the energy minimum $\mathbf{MIN_{EX}}$ located 2 kcal $mol^{-1}$ below $\mathbf{TS_{EX}}$ and featuring a 0° twisted 4-cis double bond. Inspection of the **CI'**, $\mathbf{TS_{EX}}$ and $\mathbf{MIN_{EX}}$ structures reveals that the deformation along the $C_3$-$C_4$-$C_5$-$C_6$ torsion (i.e. the original central double bond) is not the only variable involved in the **CI'**→$\mathbf{TS_{EX}}$→$\mathbf{MIN_{EX}}$ structural change. In fact, the molecule also undergoes a 70° torsional change about the single bond in position 3 (i.e. along the $C_2$-$C_3$-$C_4$-$C_5$ torsion). Evolution beyond $\mathbf{MIN_{EX}}$ leads towards the energy plateau described in Section 3.2 (this starts at the 16° twisted structure of Figure 11–3 a. The associated MEP, starting at **FC**, is indicated by a stream of arrows), and ultimately towards the conical intersection **CI**.

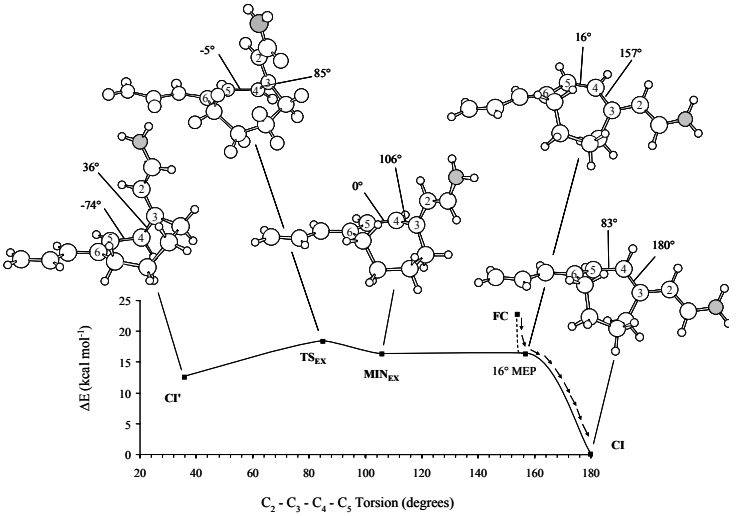


Figure 11–5: Structure of the $S_1$ potential energy surface of **3** along the **CI'→TS$_{EX}$→MIN$_{EX}$→CI** path as a function of the $C_2$-$C_3$-$C_4$-$C_5$ torsion. The structures document the progression of the $C_3$-$C_4$-$C_5$-$C_6$ and $C_2$-$C_3$-$C_4$-$C_5$ dihedral angles along the coordinate. The stream of arrows illustrates the qualitative relationship between the excited state reaction pathway documented in Figure 11–3a and the **CI →CI'** path.

### 11.4.2. Excited State Lifetime Tuning: the "Spring" Effect

As mentioned in the Introduction, Section 9.2 and Chapter 10 provides computational evidence that excited state lifetime is associated with the timescale required for $S_1$ vibrational energy redistribution (from totally symmetric stretching modes to the weakly coupled asymmetric torsional ones) and evolution along the *barrierless* energy plateau located along the

11-cis → all-trans reaction coordinate. This section will show that this mechanism provides the basis for the comprehension of the effect of the ring locks on the excited state lifetime of the PSB11 chromophore. A *decrease* of the excited state lifetime (i.e. a faster $S_0 \rightarrow S_1$ decay) should occur when:

- *the coupling between the stretching and torsional coordinates is increased so that to increase the rate of vibrational energy redistribution from the initially populated* ***FC→SP*** *mode to the* ***SP→CI*** *isomerization mode and*
- *the length of the energy plateau located along the* ***SP→CI*** *torsional mode is reduced so that the $S_1$ chromophore is more rapidly accelerated towards the decay channel.*

The artificial PSB11.5 retinal chromophore provides one extreme case where the lock induces a dramatic *decrease* of the excited state decay rate. As reported in Section 9.4, due to the planarity of the five member ring lock, this structure maintains a planar ground state and thus does not feature an increased coupling between stretching and torsional modes.

In contrast to PSB11.5, the PSB11.8 chromophore investigated in the present chapter provides a case of dramatic *increase* of the excited state decay rate in rhodopsin. The analysis of the computed photoisomerization path (Figure 11–3a) and $S_1$ stationary points (Figure 11–5) of **3** indicates that the PSB11.8 $S_1$ energy surface satisfies both the properties i and ii. In particular, the out-of-plane distortion of the conjugated chain induced by the lock dramatically enhances the coupling between stretching and torsional modes along the initial part of the reaction path.

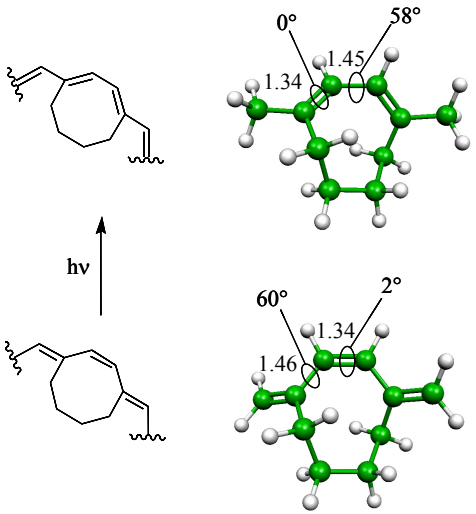


Scheme 11–3

In mechanistic terms the computed data indicate that *the eight member ring "lock" operates like a spring triggered by light absorption*. In fact, as described above, the computations show that, upon absorption of a photon of light, the double bond pattern of the central part of the PSB chain of **3** is changed in such a way that the positions of single and double bonds are exchanged, thus imposing a large torsional strain about the $C_3$-$C_4$, $C_4$-$C_5$ and $C_5$-$C_6$ bonds. The origin of this effect can be explained as followed (see Scheme 11–3). Upon photoexcitation the eight member ring moiety changes its electronic (i.e. bonding) structure passing from that of a cyclooct*ene* to that of a cyclooctad*iene* moiety. This change prompts a rapid adaptation of the initially planar configuration of the 4-cis double bond towards that of the skewed single bond of a cyclooctadiene moiety. This is demonstrated in Scheme 11–3 that displays the computed ground state equilibrium

conformation of a triene (with a cyclooctene moiety) and a diene as models of the $S_0$ and $S_1$ structure of the eight member ring moiety of **3** (and, in turn, PSB11.8) respectively. The cyclooctadiene in Scheme 11–3 has a ca. 60° equilibrium angle about the $C_4$-$C_5$ bond (i.e. the initial 4-cis double bond). Since the diene is a model for the excited state of **3**, 60° is the equilibrium value "imposed" by the eight member ring "spring" to the torsional deformation of the reactive bond. In other words while the presence of the eight member ring prompts a very rapid torsional deformation away from the fluorescent state it would also partially restrain complete deformation towards the 90° **CI** decay channel. This appears to be in line with the computed energy profile of Figure 11–3a and with the discussion reported in Section 11.3.2. In other words, in contrast to **1**, structure **3** has a flat low lying segment of the $S_1$ path spanned by structures featuring 65° to 83° torsional deformations (frame II in Figure 11–3a). One could even detect a flat energy minimum at ca. 75° torsional deformation. This behaviour can be assigned to the effect of the cyclooctadiene-like structure of the excited state lock.

To confirm the above assignment, the same kind of analysis was performed to compare the computed ground state equilibrium conformation of a cycloheptatriene with a cycloheptadiene, as models of the $S_0$ and $S_1$ structure of the seven member ring moiety of **2** (and, in turn, PSB11.7) respectively. Both structures show a planar central bond (see Scheme 11–4), so *no speed-up is expected from the seven member ring moiety*.

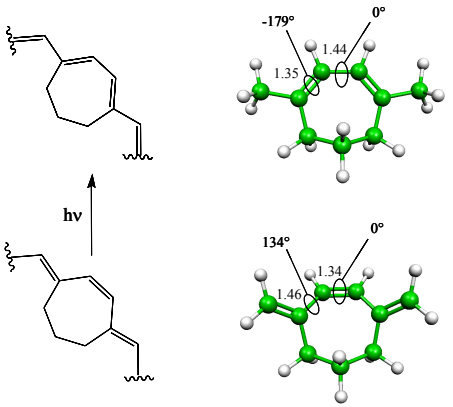


Scheme 11–4

Consistently, the computed MEP indicates a slower **FC** → **CI** motion, with respect to **3**. In fact, while there is a coupling between the stretching and torsional modes in the motion out of **FC**, the presence of the long plateau and, most of all, of a transition structure (**$TS_{EX}$**) along the path are not consistent with an acceleration of the photoisomerization process.

As mentioned in Section 11.1, the assumed working hypothesis is that the fluorescence lifetime decrease observed in Rh8[186] is the consequence of an intrinsically faster decay of the locked chromophore with respect to PSB11. The results reported so far provide evidence that this is indeed the case, as the *$S_1$ force field of the isolated PSB11.8 chromophore must effectively accelerate the chromophore towards the $S_1 \rightarrow S_0$ decay channel*. Thus in Rh8 both the protein environment and the "environment" provided by the eight member ring lock accelerate the decay of PSB11 with respect to the solution environment. This leads to the idea that the protein cavity could modify the

$S_1$ energy surface structure of PSB11 in a way similar to the eight member ring. For instance, Scheme 11–5 compares the observed out-of-plane deformation of PSB11 in Rh (data obtained from x-ray diffraction[43] and NMR[187]) with the ground state equilibrium structure of the PSB11.8 model **3**. It is evident that, while there are important quantitative differences between the two structures, the directions of torsional deformation is the same (in particular the deformations about the $C_{11}$-$C_{12}$ (8° counterclockwise) and $C_5$-$C_4$ (11° counterclockwise). In other words one can think that the asymmetric protein cavity imposes a torsional strain on the chromophore backbone that reinforces that imposed by the eight member ring lock.

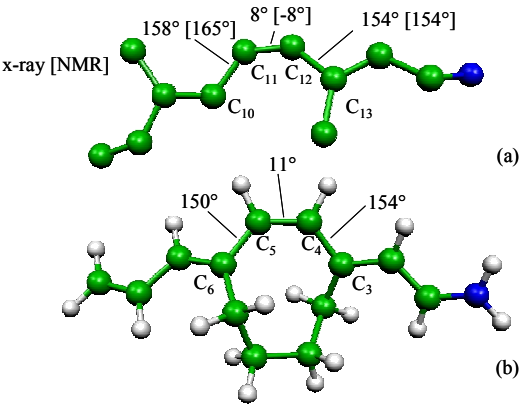


Scheme 11–5

### 11.4.3. Correlation between Computed and Experimental Results: Hypothesis on the Primary Photoproduct Appearance

This Section re-examines the reaction mechanism for the photoisomerization of PSB11.7 and PSB11.8 on the basis of the computational results reported above.

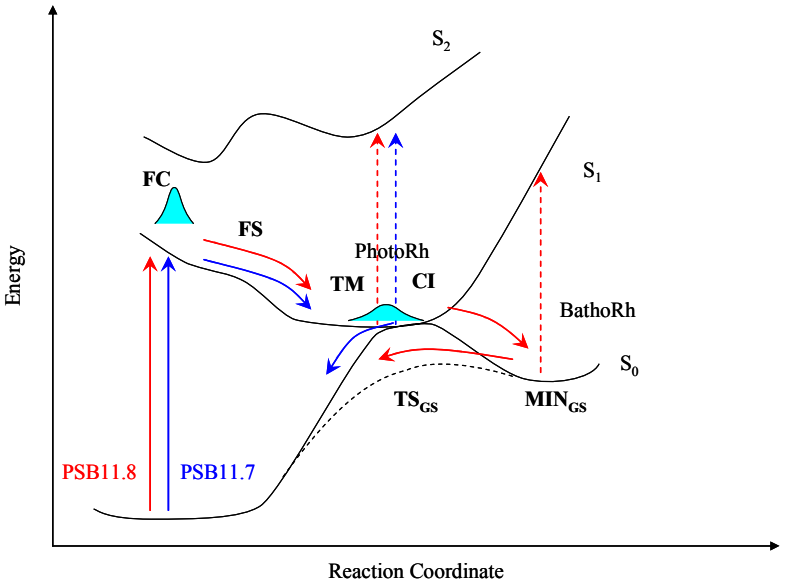


Scheme 11–6

As shown in Scheme 11–6, the results of the computational investigation of the PSB11.7 and PSB11.8 models agree with the initial part of the mechanistic picture of Scheme 11–1. An initial combined stretching/torsional

relaxation from **FC** leads, within a single oscillation, to a fluorescence state (**FS**) that is assigned to the first energy plateau seen in Figure 11–3 (dashed frames I). After that, the system reach a low-lying and flat non fluorescent (i.e. the $S_1$-$S_0$ energy gap is <20 kcal $mol^{-1}$) region where it could reach the conical intersection funnel. Following the decay on the ground state, the chromophore could evolve towards a ground state intermediate featuring a ca. 140° torsion about the reconstituted "trans" double bond.[a] This intermediate can be thermally reverted to the starting material by overcoming a small energy barrier. Since:

- **3** is capable to access a 137° twisted "trans" intermediate via the photochemical path, while **2** cannot do it (See Section 11.3.3)
- experimentally, Rh7 and Rh8 show a primary photoproduct analogue to photorhodopsin, while only Rh8 shows also the bathorhodopsin analogue photoproduct
- comparing the computed minimum energy paths of **3** and **2** in Figure 11–3, one can observe that the two potential energy surfaces show a region, centred on the **TM** structures, where the wavepacket could spread (see dashed frames II in Figure 11–3)

it is possible to make the assumption that this *flat region of **2** and **3** could be associated with the photorhodopsin primary photoproduct analogue*. Of course, **2** doesn't show any evidence of a bathorhodopsin photoproduct analogue because the molecule immediately reverts to the initial form after decay at **CI**.

[a] Despite extensive search, a $S_0$ trans conformer of **3** featuring a fully planarized $C_4$-$C_5$ double bond could not be located.

In other words, PSB11.7 and PSB11.8 reach the end of the $S_1$ slope before vibrational cooling. Then they cool down vibrating in the **TM - CI** flat region (which means also back and forth between the $S_1$ and $S_0$ potential energy surfaces); it is possible to associate this condition with the photorhodopsin primary photoproduct. Finally, the chromophores relax on the ground state, triggering reactant back formation (PSB11.7) or bathorhodopsin analogue production (PSB11.8).

## 11.5. Conclusions

Above computational evidence have been provided in favour of an efficient "catalysis" of the departure of a PSB11 chromophore from its fluorescent state **FS**. An eight member ring lock acts like a light-triggered spring that imposes a considerable Pitzer strain on the central part (i.e. $C_3$-$C_4$-$C_5$-$C_6$ and $C_{10}$-$C_{11}$-$C_{12}$-$C_{13}$ moieties in **3** and PSB11.8 respectively) of the conjugated chain of the chromophore. As discussed in Section 11.4.2, the strain mainly originate by the change in bond order occurring during vertical excitation (see Scheme 11–3) that pushes the torsional deformation of the reactive (4-*cis*) double bond. As a result the 40° long energy plateau documented in the native PSB11 model **1** is reduced to a short 6° long segment suggesting a strongly decreased fluorescence lifetime.

A hypothesis onto the nature of the primary photoproduct of Rh7 and Rh8 have been presented, on the basis of detailed comparison of the potential energy surface shape of **2** with that of **3** (along with the experimental data). Such hypothesis implies that the photorhodopsin-like first intermediate of these chromophores could correspond to the flat region surrounding the

twisted minimum at the end of the excited state slope, where the chromophore may oscillate many times before decaying at the conical intersection funnel. Finally, the Rh8 bathorhodopsin-like photoproduct could be assigned to a ground state structure displaying a nearly trans conformation of the central double bond.

The PSB11.8 model does not comprise the β-ionone ring. However, as previously documented for the PSB11 model **1** and discussed in the Introduction section, this approximation can be accepted if one is interested in a mechanistic description of the initial excited state dynamics of the chromophore (say from **FC** to **FS**) where the double bond residing in the β-ionone ring does not effectively conjugate with the rest of the PSB chain. Partial or total planarization of the β-ionone moiety may occur later along the reaction, due to the bond order inversion occurring in the excited state. This bond order change together with the effect of the protein cavity must be taken into account when trying to model more rigorously the behaviour of Rh7 and Rh8 beyond the bottom of the $S_1$ surface.

Table 11–1: CASSCF/6-31G* Absolute, CASPT2/6-31G* Absolute and Relative Energies along with Wave Function Reference Weights of the Structures Discussed in Chapter 11

| Structure | State | CASSCF energy (hartree) | CASPT2 energy (hartree)[a] | reference weight[a] | CASPT2 level relative energy (kcal mol$^{-1}$)[b] |
|---|---|---|---|---|---|
| *2-(4-allylidene-cyclohepta-2-enylidene)-ethyliminium cation model **2*** | | | | | |
| **FC** | $S_0$ | -518.0385 | -519.6694 | 0.65 | 0.0 |
| | $S_1$ | | -519.5756 | 0.64 | 58.9 |
| | $S_2$ | | -519.5376 | 0.63 | 82.7 |
| **SP** | $S_0$ | -518.0022 | -519.6560 | 0.65 | 8.4 |
| | $S_1$ | -517.9215 | -519.5822 | 0.64 | 54.7 |
| | $S_2$ | | -519.5533[c] | 0.64[c] | 72.9 |
| **$TS_{EX}$** | $S_0$ | -517.9846 | -519.6421 | 0.65 | 17.1 |
| | $S_1$ | -517.9187 | -519.5817 | 0.64 | 55.0 |
| | $S_2$ | | -519.5361[c] | 0.64[c] | 83.6 |
| **TM** | $S_0$ | -517.9486 | -519.6096 | 0.64 | 37.6 |
| | $S_1$ | -517.9319 | -519.6002 | 0.64 | 43.4 |
| | $S_2$ | | -519.5144[c] | 0.64[c] | 97.3 |
| **CI** | $S_0$ | -517.9294 | -519.5955 | 0.64 | 46.4 |
| | $S_1$ | -517.9294 | -519.5943 | 0.64 | 47.1 |
| | $S_2$ | | -519.5062 | 0.58 | 102.4 |
| **$MIN_{GS}$** | $S_0$ | -517.9612 | -519.5896 | 0.64 | 50.1 |
| | $S_1$ | | -519.4974 | 0.63 | 107.9 |
| | $S_2$ | | -519.4702[c] | 0.63[c] | 125.0 |
| *2-(4-allylidene-cycloocta-2-enylidene)-ethyliminium cation model **3*** | | | | | |
| **Half-chair (FC)** | $S_0$ | -557.0472 | -558.8322 | 0.63 | 0.0 |
| | $S_1$ | -556.9255 | -558.7415 | 0.62 | 56.9 |
| | $S_2$ | | -558.6991 | 0.63[c] | 82.5 |
| **Boat-1** | $S_0$ | -557.0648 | -558.8334 | 0.63 | -0.8 |
| | $S_1$ | | -558.7387 | 0.61 | 58.7 |
| | $S_2$ | | -558.6971[c] | 0.63[c] | 84.8 |
| **Boat-2** | $S_0$ | -557.0644 | -558.8319 | 0.63 | 0.2 |
| | $S_1$ | | -558.7423 | 0.62 | 56.4 |
| | $S_2$ | | -558.6872 | 0.55 | 91.0 |
| **CI** | $S_0$ | -556.9778 | -558.7785 | 0.63 | 33.6 |
| | $S_1$ | -556.9766 | -558.7777 | 0.62 | 34.2 |
| | $S_2$ | | -558.6954[c] | 0.61[c] | 85.8 |
| **$MIN_{GS}$** | $S_0$ | -556.0283 | -558.7919 | 0.62 | 25.3 |
| | $S_1$ | | -558.6910 | 0.60 | 88.6 |
| | $S_2$ | | -558.6632[c] | 0.63[c] | 106.0 |
| **$TS1_{GS}$** | $S_0$ | -556.9897 | -558.7894 | 0.62 | 26.8 |
| | $S_1$ | | -558.7442 | 0.62 | 55.2 |
| | $S_2$ | | -558.6952[c] | 0.60[c] | 86.0 |
| **$TS2_{GS}$** | $S_0$ | -556.9937 | -558.7805 | 0.62 | 32.4 |
| | $S_1$ | | -558.7578 | 0.62 | 46.7 |
| | $S_2$ | | -558.6869[c] | 0.63[c] | 91.2 |
| **$MIN_{EX}$** | $S_0$ | -557.0163 | -558.8109 | 0.62 | 13.4 |
| | $S_1$ | -556.9417 | -558.7518 | 0.62 | 50.5 |
| | $S_2$ | | -558.6845 | 0.56 | 92.7 |
| **$TS_{EX}$** | $S_0$ | -557.0028 | -558.8036 | 0.63 | 17.5 |
| | $S_1$ | -556.9225 | -558.7396 | 0.61 | 58.2 |
| | $S_2$ | | -558.7074[c] | 0.63[c] | 78.1 |
| **CI'** | $S_0$ | -556.9545 | -558.7569 | 0.62 | 47.2 |
| | $S_1$ | -556.9545 | -558.7578 | 0.62 | 46.7 |
| | $S_2$ | | -558.7000[c] | 0.56[c] | 82.9 |

[a] A three roots ($S_0$, $S_1$, $S_2$) state average (0.33, 0.33, 0.33) CASSCF wave function (energies not shown) was used as zeroth order wave function for the CASPT2 results quoted (energies and weights)

[b] Energies are relative to the $S_0$ state energy value of **FC** of each model

[c] CASPT2 energy obtained applying a level shift procedure, with level shift equal to 0.1

# Chapter 12. The Importance of Protein Folding

Alzheimer's disease. Cystic fibrosis. Mad Cow disease. An inherited form of emphysema. Even many cancers. Recent discoveries show that all these apparently unrelated diseases result from protein folding gone wrong. As though that weren't enough, many of the unexpected difficulties biotechnology companies encounter when trying to produce human proteins in bacteria also result from something amiss when proteins fold. This chapter will sketch some aspect of protein folding,[201] to introduce in Chapter 13 a possible tool to investigate this phenomenon.

What exactly is protein folding? It is well know that proteins are fundamental components of all living cells: our own, the bacteria that infect us, the plants and animals we eat. The haemoglobin that carries oxygen to our tissues, the insulin that signals our bodies to store excess sugar, the antibodies that fight infection, the actin and myosin that allow our muscles to contract, and the collagen that makes up our tendons and ligaments (and even much of our bones) all are proteins.

To make proteins, ‘machines’ known as ribosomes string together amino acids into long, linear chains. Like shoelaces, these chains loop about each other in a variety of ways (i.e., they fold). But, as with a shoelace, only one of these many ways allows the protein to function properly. Yet lack of function is not always the worst scenario. For just as a hopelessly knotted shoelace could be worse than one that won't stay tied, too much of a misfolded protein

could be worse than too little of a normally folded one. This is because a misfolded protein can actually poison the cells around it.

## 12.1. Early Studies

The importance of protein folding has been recognized for many years. Almost a half-century ago, *Linus Pauling* discovered two quite simple, regular arrangements of amino acids, the α-helix and the β-sheet, that are found in almost every protein.[202] And in the early 1960s, *Christian Anfinsen* showed that the proteins actually tie themselves.[203] If proteins become unfolded, they fold back into proper shape of their own accord; no shaper or folder is needed.

Of course, neither Pauling nor Anfinsen nor the committees that awarded them their respective Nobel prizes knew at the time that these discoveries would be so important for understanding Alzheimer's disease or cystic fibrosis. And when Pauling, at least, was doing his breakthrough studies, he could hardly have imagined the enormity of today's biotechnology industry. What scientists did know is that any process that was so fundamental to life as protein folding would have to be of the utmost practical importance.

But research did not stop with Pauling and Anfinsen. Indeed, it is now known that Anfinsen's conclusions needed expansion: sometimes a protein will fold into a *wrong* shape. And some proteins, aptly named chaperones, keep their target proteins from getting off the right folding path. These two small but important additions to Anfinsen's theory hold the keys to protein folding diseases.

Humans have known since antiquity (but didn't know we knew) that protein folding can go wrong. When we boil an egg, the proteins in the white (which constitute the 10%) unfold, trapping in a gel the other 90% of water. But when the egg cools, the proteins don't return to their original shapes. Instead, they form a solid, insoluble (but tasty) mass. This is misfolding. Similarly, biochemists have always cursed the tendency of some proteins to form the insoluble lumps in the bottom of their test tubes. We now know that these, too, were proteins folded into the wrong shapes.

Until recently, biochemists lacked the tools to study these insoluble lumps. Nor did they expect such masses would be particularly interesting. The prevailing view at the time was that the lumps were just hopelessly tangled and completely amorphous masses of protein fibres (aggregation). Researchers eventually discovered that these aggregates of incorrect folding could be highly structured, but before this crucial insight and before proper investigative tools were developed, biochemists simply threw their fouled test tubes away.

## 12.2. 'Gunking Up' Tissues

As far back as the start of this century, physicians have been noticing that certain diseases are characterized by extensive protein deposits in certain tissues. Most of these diseases are rare, but Alzheimer's is not. It was *Alois Alzheimer* himself who noted the presence of "neurofibrillary tangles and neuritic plaque" in certain regions of the brain of his patient Frau August D.[204] Tangles are more or less common in diseases that feature extensive nerve cell death; plaque, however, is specific to Alzheimer's. The major

question, which has only recently been answered, is whether plaque *causes* Alzheimer's or, like tangles, is a *consequence* of it.

Further investigation showed that neuritic plaque (unrelated to the plaque that clogs atherosclerotic blood vessels and causes heart attacks) is composed almost entirely of a single protein. Deposits of large amounts of a single, insoluble protein around the degenerating nerve cells of Alzheimer's disease eventually provided a key to understanding the disorder.

It was development of the biotechnology industry that unexpectedly spurred interest in insoluble protein gunk. This industry can produce proteins (often otherwise difficult-to-obtain human proteins) quickly and economically in bacteria. To their surprise, however, scientists who worked for biotech companies often found two things: a protein that was supposed to be soluble, instead precipitated as insoluble inclusion bodies within the bacteria, and proteins that were supposed to be secreted into the surrounding medium instead got stuck at the bacterial cell wall.

This puzzling activity led scientists, almost for the first time, to seriously study just what goes wrong during protein folding.

## 12.3. Further Studies

In the decades after Anfinsen's work, the National Institutes of Health and the National Science Foundation continued to finance research in several laboratories. Working in relative obscurity, these protein biochemists tried to discover how a completely unfolded protein, with hundreds of millions of potential folded states to choose from, consistently found the “correct” one, and did so within seconds to minutes.

Could there be specific, critical intermediates (partially folded chains) in the folding process? This turned out to be a difficult question to answer. Partially folded chains don't stay that way very long; they become fully folded chains in a fraction of a second. Nevertheless, by the early 1980s researchers had not only found clear evidence for the existence of *partially* folded proteins, but also realized the key role these played in the folding process. This shows the need for a technique able to explore protein folding in real time, such as the possibility opened by the usage of light activated rotors inside a protein chain, as described in next Chapter 13.

One study involved the difficulty in getting bovine growth hormone to fold properly. Although the unfolded proteins were not sticky, and the fully folded proteins were not sticky, the partially folded molecules stuck to each other, a first clue as to the origins of misfolded lumps (at least for purified proteins in test tubes). It still remained unclear why misfolding occurred in cells under certain circumstances but not under others.

## 12.4. Temperature Sensitivity

The early 1980s also saw one of the first serious investigations of protein *misfolding*. These studies focused on temperature-sensitive mutations (mutations allowing growth at 24° C but not at 38° C) in the tailspike protein of bacteriophage P22. Neither bacteriophage P22, a virus that infects certain bacteria, nor its tailspike protein has any practical importance in themselves. Faced with thorny problems, however, scientists often look for experimental systems that will allow them to get a foothold or find a way around them. In this case, they thought that a large protein, whose folding passes through

multiple stages, would be a good system for looking at folding pathways within cells. Many temperature-sensitive mutations had already been isolated in bacteriophages, but never examined for their effect on folding.

Their hopes were realized: The majority of the temperature-sensitive mutations they found, despite having only one amino acid altered, caused the tailspike protein to end up as insoluble gunk at high temperatures. Since these folding failures were occurring in bacterial cells that were growing in the laboratory, it was now possible to analyze what went wrong in a protein's folding process.

The obvious guess at the time was that the mutant proteins were less stable. After all, the temperature scale is fundamentally defined by how much atomic-scale shaking or motion is going on; in other words, the higher the temperature, the more shaking there is. This implies that a less stable protein is more likely to fall apart at elevated temperatures and might therefore be more likely to end up (like cooked eggs) as insoluble gunk.

But this turned out not to be the case. If the mutant chains were allowed to fold up at low temperature, and were then heated, they were as stable as wild-type. It turned out to be a partially folded intermediate, on the route from the random shoelace to the correctly folded protein, that was sensitive to temperature. At higher temperatures these intermediates would stick to themselves and be unable to reach the properly folded state.

This turned out to be a general problem in the folding of many proteins: They have to pass through partially folded states in which they are delicately poised between folding all the way to the correct state or becoming seriously stuck as a result of premature entanglement with other molecules. Recognizing that it was the intermediates and not the fully folded protein that

were in trouble opened the way to understanding some aspect of a range of diseases.

Since nowadays many disease causes are recognized to be in misfolding of proteins (for example: Alzheimer's disease, Mad Cow disease and its human equivalent, Creutzfeldt-Jacob disease, cystic fibrosis), more and more research groups are focusing on studying this subject. Even if at a very early stage of study, the next chapter will present what could, in principle, open new possibilities for the study in real time of the process of folding, unfolding and refolding of proteins.

# Chapter 13. *N*-methylthioacetamide: a Preliminary study for a Rotor Inside a Peptide Chain

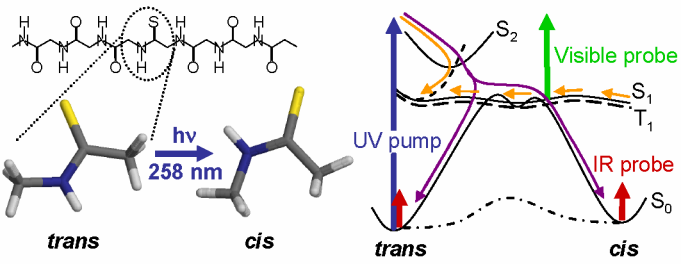


## 13.1. Introduction

While amides are usually most stable in the trans conformation, they can be converted into the cis conformation with relatively high quantum yield by photoisomerization upon π-π* excitation.[181] In *N*-methylacetamide (NMA) the corresponding absorption band peaks at 186 nm.[205] Substitution of oxygen by sulphur in a peptide bond yields a thioamide, and leads to significantly red-shifted π-π* and n-π* absorption, thus lowering the excitation energy needed for photoisomerization. When a thioamide is integrated into the backbone of a polypeptide, it is therefore possible to selectively excite this unit and to photoinduce a conformational change via trans-cis isomerization at a well defined position in the peptide chain. For the thionated endorphins Tyr-$\phi$[CS-N]-Pro-X-Phe-$NH_2$ (X=Trp or Phe)

*Schutkowski* and co-workers[206] have shown that the concentration of molecules with the Tyr-Pro bond in the cis-conformation can be significantly enhanced by photoisomerization. *Seebach* and co-workers[207] have synthesized β-thiohexapeptides with one, two and three C=S groups in the N-terminal position, and report drastic changes in the CD-spectra upon π-π* excitation of the thionated peptide units. In a very recent work, *Zhao* et al. report on efficient photoswitching of secondary thiopeptide bonds in α-polypeptides.[208] This is particularly interesting as the possibility to selectively introduce thio amino acids into polypeptides, which are capable of forming secondary structures, has recently been demonstrated by *Miwa* and co-workers.[209,210] Both the incorporation of a thioamide linkage between the residues of a β-turn[209] and within a helical peptide[210] resulted only in minor changes to the native hairpin- and α-helical structures. As an alternative to the more widely used, but much bulkier azobenzene photoswitches[211] O→S substitution in a single peptide unit may thus provide a method to study the dynamics of photoinduced conformational changes in practically *unperturbed* (i.e. substantially native) peptides and proteins, provided that isomerization of the thioamide takes place on a sufficiently fast time scale.

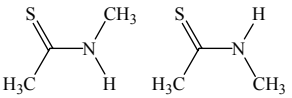


*trans*-NMTAA *cis*-NMTAA

*N*-methylthioacetamide (NMTAA) is among the simplest thioamides, and it has been subject to many studies of photoisomerization, using UV-Vis, Raman and NMR spectroscopy.[212-214] It has been shown that trans-cis

isomerization[a] leads to significant shifts both in the electronic and the vibrational spectra, which in turn can be used to monitor the kinetics and dynamics of photoisomerization. However, these experiments, as well as similar measurements on regular amides[181,215] provide only limited information on the underlying mechanism and the timescales involved. The best time resolution so far was achieved by resonance Raman experiments, which have put a 5 ns upper limit for the time of trans → cis isomerization of NMTAA.[213] While the high isomerization efficiency upon UV-excitation has been interpreted as a signature of a twisted π-π* excited state in NMA and NMTAA,[181] torsional modes are not enhanced in the resonance Raman spectra of NMA,[215] indicating that isomerization may occur later in the relaxation process. Early *ab initio* calculations[216] have reported optimized structures with twisted geometry in both the n-π*, π-π* and the triplet excited states of NMA.

Here, in order to establish the photoisomerization mechanism of NMTAA, transient visible and infrared spectroscopy with high time resolution have been used, to follow the photoreaction in real time. In addition kinetic measurements of the isomerization quantum yields and photostability at different irradiation wavelengths have been performed. In order to provide a rigorous basis for the formulation of a mechanism consistent with the observed results *ab initio* CASPT2//CASSCF quantum chemical calculations

[a] Since the isomerization takes place about the formally single bond C-N, one should refer to s-*trans*-NMTAA and s-*cis*-NMTAA conformations. However, to conform to previous works, the labels cis or trans will be used as determined by the relative positions of the two NMTAA methyl groups.

have been performed, to map out the intrinsic (i.e. *in vacuo*) photoisomerization path of NMTAA.[217]

## 13.2. Methods

### 13.2.1. Experimental setup

NMTAA was prepared from NMA employing standard procedures based on Lawesson's reagent[218] and purified by vacuum distillation. For time-resolved IR measurements, 50-250 mM solutions of NMTAA in $D_2O$ were circulated through a flow cell made of $CaF_2$ windows spaced 50 μm apart at a rate sufficient to ensure complete exchange of excited sample volume between subsequent excitation pulses.[219]

In order to completely avoid signals from the window material in measurements in the visible spectral range, experiments had to be performed in a jet of NMTAA, dissolved in doubly distilled water, with a thickness of about 70 μm. A high optical density of the NMTAA solution of about 100 OD/mm ($c \approx 80$ mM) provided a low effective interaction path length between pump light and the water, to further minimize contributions from the solvent.

Femtosecond (fs) pulses for IR measurements (1 kHz, 700 μJ /pulse, 80 fs) were obtained from an amplified titanium-sapphire laser system (Spectra Physics), operating either at 840 nm or at 777 nm. UV pulses for the excitation of NMTAA at 280 nm or at 259 nm were generated by frequency tripling. The third harmonic beam was then isolated by dielectric mirrors, and the UV pulses were stretched to 1.4 ps duration by guiding them through 15

cm of fused silica. This significantly increased the threshold for the onset of undesired non-linear effects in the sample cell, like white-light generation and/or colour centre formation, and allowed to excite a larger fraction of the molecules.

Mid-infrared pulses near 1400 $cm^{-1}$ (100 fs, 1 μJ, 250 $cm^{-1}$ bandwidth) were produced in a home-built double-stage optical parametric amplifier (OPA) followed by frequency mixing in a $AgGaS_2$ (Silver thiogallate) crystal.[220] The IR pulses were split into two parts (of ~ 50 nJ each). One part (the probe pulse) was overlapped with the UV-pump pulse in the sample cell. The second part was used as a reference beam in order to correct for intensity fluctuations, and crossed the flow-cell approximately 500 μm further up-stream than the pump pulse. Both IR beams were dispersed in a spectrometer and detected with a double MCT array (2 x 32 pixels) on a single shot basis with 3 $cm^{-1}$ resolution.

For transient UV-pump/Vis-probe spectroscopy a Clark MRX CPA-2001 regenerative amplifier system (1 kHz, 800 μJ /pulse, 160 fs) provided pulses with a central wavelength of 775 nm, and frequency tripling yielded UV pulses at 258 nm. The pulse energies for excitation were chosen low (between 300 nJ and 2 μJ) to minimize the formation of solvated electrons by multiphoton excitation. Transient absorbance changes in the UV-visible spectral range were recorded by a single filament white light continuum, generated in a 2 mm-thick $CaF_2$ plate, which covered a wavelength range from 300-1000 nm. For spectral resolution two spectrometers (for probe and reference beams) equipped with 42-diode arrays were used and operated in single shot detection.

Narrow bandwidth light for kinetic measurements was generated by passing the output of a high pressure Xe lamp through a monochromator. The UV-

light was directed onto the sample, either inside an FTIR or a UV-Vis spectrometer, allowing to record spectra as a function of irradiation without having to move the sample. A flow cell allowed to introduce or exchange the sample in the FTIR spectrometer without opening the thermally equilibrated and nitrogen-flushed chamber, and guaranteed identical optical path lengths, window absorption and scattering conditions in all experiments. All data were recorded with a liquid nitrogen-cooled MCT detector and baseline drifts were less than 1 mOD over several hours. Care was taken that the spot size used for irradiation was larger than the sample cell window. The photon flux could thus be determined from a measurement of the light power immediately behind an empty sample cell. The same excitation source was used for fluorescence measurements in combination with a photomultiplier and a photon counting system. A lower limit for the sensitivity of this home-built setup was determined from the fluorescence signal of a laser dye of identical optical density at the excitation wavelength.

$^{1}$H-NMR spectra in thermal equilibrium and of the photostationary state were recorded with an Avance DRX-600 MHz spectrometer. To assure full saturation of the large amount of sample needed, it was irradiated with 3-6 mW UV-light from the fs-laser, while circulating the sample inside the flow cell and monitoring its UV-absorption spectrum. The saturated sample was then transferred to the NMR-spectrometer and spectra were recorded within 10 minutes after the end of irradiation.

### 13.2.2. Computational methods

Structure optimization and relaxation path mapping have been carried out using fully unconstrained *ab initio* quantum chemical computations in the

framework of the CASPT2//CASSCF/6-31g* strategy showed in Chapter 7, with the only exception of two triplet energy minima (**Min $T_1$ Planar Trans** and **Min $T_1$ Planar Cis**) that were optimized by imposing a planarity constraint.

All computations employed an active space comprising 10 electrons in 8 orbitals. This includes the full N-C-S π-system (4 electrons in 3 π-orbitals), the sulphur p lone pair (2 electrons in 1 orbital) plus the C-N and C-S bonds (4 electrons in 4 σ-orbitals). The σ/σ* orbitals were added after test calculations because they were seen to mix with the π/π* and lone pair systems when the geometry becomes highly pyramidalized.

When possible, energy minima and transition structures were optimized using a single root CASSCF wave function and confirmed via analytic frequency computations. However, the $S_2$ minimum (**Min $S_2$**) was located using a two roots ($S_1$, $S_2$) state-average (0.5, 0.5) CASSCF wavefunction and subsequently confirmed via a numerical frequency calculation. Similarly, due to wavefunction instability, the four $S_0$ transition states (**TS $S_0$ A1**, **TS $S_0$ A2**, **TS $S_0$ B1**, **TS $S_0$ B2**) were located using a two roots ($S_0$, $S_1$) state-average (0.5,0.5) CASSCF wavefunction.

The $S_2$, $S_1$, $T_2$, $T_2$ and $S_0$ potential energy surfaces were connected by computing five $S_2/S_1$, $S_1/S_0$ Conical Intersections (CI)[21,144] and eight $T_2/S_1$, $T_1/S_0$ Inter System Crossings (ISC). The optimization of both CIs and ISCs was found to be technically difficult due to the fact that the "sloped"[109]

topography of these points[89,a] decreases the convergence efficiency. *For this reason, the reported structures represent a compromise between the quality of energy minimization on the upper state and the complete energy degeneracy between the two intersecting states*.

A $S_2$ MEP calculation was performed to connect the Franck-Condon point to the $S_2$ minimum and $S_2/S_1$ CI, using a two roots ($S_1$, $S_2$) state-average (0.5, 0.5) CASSCF wavefunction. A $S_1$ MEP connecting the $S_2/S_1$ CI to one of the $S_1$ minimum has been computed using a two roots ($S_0$, $S_1$) state-average (0.5, 0.5) wavefunction. Finally, for each $S_1/S_0$ CI and $T_1/S_0$ ISC a $S_0$ MEP connecting the chosen CI or ISC point to the $S_0$ reagent or product minimum was computed using a single root wavefunction.

As stated before, energies of stationary points, CIs, ISCs and selected points along the MEPs have been re-evaluated using single point calculations performed at the CASPT2 level of theory. For each geometry, a three roots ($S_0$, $S_1$, $S_2$) state-average (0.33, 0.33, 0.33) CASSCF wavefunction was used as reference function for evaluating the CASPT2 energies of the singlet states, while a two roots ($T_1$, $T_2$) state-average (0.5, 0.5) wavefunction was used for the triplet states. Also, for each energy minimum on $S_1$ and $T_1$ a four roots ($S_0$, $S_1$, $S_2$, $S_3$ or $T_1$, $T_2$, $T_3$, $T_4$) state-average (0.25, 0.25, 0.25, 0.25) CASSCF wavefunction was used as reference function for evaluating the CASPT2 energies of third and forth roots.

[a] Energies and energy gaps oscillate during the geometry optimization and never converge, or if energy gap tends to converge the energy increases endlessly. This behaviour has been found to be associated with highly sloped conical intersections.

## 13.3. Experimental Results

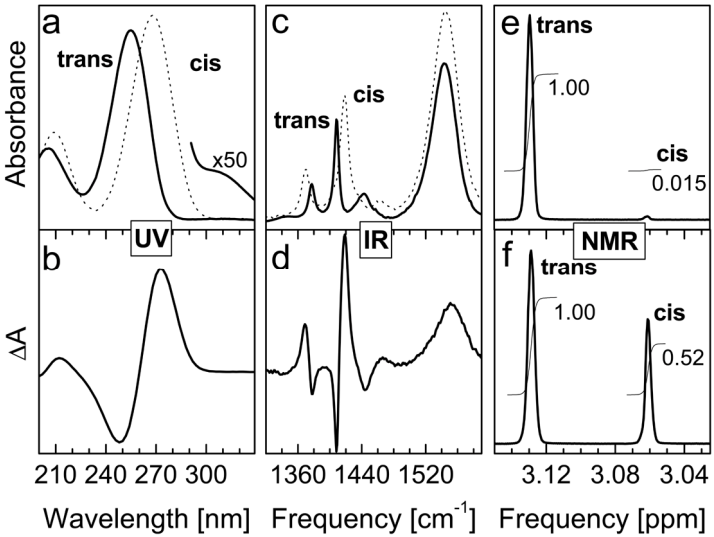


Figure 13–1: a) solid lines: UV-absorption spectrum of *trans*-NMTAA in deuterated water b) difference absorption spectrum under UV-irradiation. c) solid line: FTIR absorption spectrum of *trans*-NMTAA before irradiation d) FTIR difference absorption spectrum under UV-irradiation. The dotted lines in a) and c) show the *cis*-NMTAA absorption spectra, which were constructed from the trans and difference spectra. e) NMR spectrum at room temperature before irradiation and f) in photo equilibrium after 256 nm irradiation. The numbers indicate the normalized peak areas.

### 13.3.1. Steady state absorption and kinetic studies

The solid lines in Figure 13–1a and c show the UV and infrared absorption spectra of *trans*-NMTAA in $D_2O$ at room temperature. The $S_2$ state, which is due to a $\pi$-$\pi^*$ excitation (see below), gives rise to the main UV absorption band centred at 255 nm, while a much weaker shoulder at 305 nm is due to the $S_1$ state (n-$\pi^*$ transition). In the infrared spectrum, three prominent bands were of main interest in this study. They were assigned on the basis of a normal mode calculation on BLYP 6-31G(d) level (GAUSSIAN98), which was capable of reproducing approximate frequencies, relative intensities and energy shifts upon isomerization. The band at 1545 $cm^{-1}$ is the amide II band, which is strongly blue-shifted with respect to matrix isolation spectra of NMTAA[221] and broadened due to strong interaction with the $D_2O$ solvent. The band at 1409 $cm^{-1}$ and the weaker band at 1372 $cm^{-1}$ can best be characterized as 'symmetric' and 'antisymmetric' stretch motion of the C-C-N-C backbone. Both modes also involve an umbrella-like motion of the methyl groups (The extinction coefficients for *trans*-NMTAA are 12400 L $mol^{-1}cm^{-1}$ at 255 nm and 200 L $mol^{-1}cm^{-1}$ at 1545 $cm^{-1}$). The changes in UV and infrared absorption due to UV irradiation are shown in the Figure 13–1b and d. In the UV, a red-shift is observed for the $\pi$-$\pi^*$ absorption band and this shift obscures any changes that may occur in the region of the n-$\pi^*$ band. In the IR vibrational spectrum, the trans band at 1409 $cm^{-1}$ undergoes a blue-shift, and gains in oscillator strength upon photoisomerization, while a red shift is observed for the 1372 $cm^{-1}$ band. The amide II band of the cis species is stronger and peaks at slightly larger energies than the trans band. Kinetic measurements, based on both UV and FTIR absorption data, show an

exponential decrease of the *trans*-NMTAA concentration and a simultaneous growth of the *cis*-NMTAA photoproduct. There are well-defined isosbestic points in the difference absorption spectra, which is an indication of simple two-state kinetics cis $\overset{h\nu}{\rightleftharpoons}$ trans. Indeed, due to the strongly overlapping UV-absorption bands of the two isomers, the photoreaction can take place in both directions and a photoequilibrium between cis and trans species is eventually established.

Table 13–1: Cis concentrations $c_{cis}$ in photoequilibrium and quantum efficiencies of trans→cis isomerization $\eta_{t\rightarrow c}$ for different irradiation wavelengths obtained from kinetic and from transient absorption measurements. The ratio $\eta_{c\rightarrow t}/\eta_{t\rightarrow c}$ was estimated from the concentrations in photoequilibrium and the absorption cross sections of *cis*- and *trans*-NMTAA.

| λ/nm | $c_{cis}$ % | $\eta_{c\rightarrow t}/\eta_{t\rightarrow c}$ | $\eta_{t\rightarrow c}$ (kinetic), % | $\eta_{t\rightarrow c}$ (transient), % |
|---|---|---|---|---|
| 256 | 34 (NMR) | 2.3-3.1 | 40[a] | 30-40 |
| 280 | 4.4 (NMR) | 2.1-3.5 | 28 | 30-40 |
| 308 | (14±2)[b] | 3-6 | - | - |

The *cis*-NMTAA concentration in the photostationary state under 256 nm irradiation is 34%, compared to only 1.5% in thermal equilibrium before irradiation (Figure 13–1e and f). Mainly due to the differences in the relative absorption cross sections of *cis*- and *trans*-NMTAA, their concentrations in

[a]The error due to the uncertainty in the photon flux is estimated to be 50 %

[b]determined by IR difference spectroscopy (calibrated by the NMR value at 256 nm)

photoequilibrium vary strongly as a function of irradiation wavelength, as shown in Table 13–1.[a] The table also shows the ratio of the quantum efficiencies for trans → cis and cis → trans isomerization, which can be determined directly from the concentrations in photoequilibrium and the absorption cross sections. Although associated with large error bars due to uncertainties in the photon flux, the estimates for the trans → cis isomerization quantum efficiency (20-40% for π-π* excitation) from the kinetic data is very similar to the more reliable value (30-40%) obtained from the transient measurements (see below).

[a] Since the irradiation wavelength can be changed without removing the sample from the FTIR spectrometer, the concentrations in photoequilibrium for different irradiation wavelength can be determined with high accuracy (and independent of any spectrometer drifts) relative to the value at 255 nm by comparing the peak-to-peak differences in the FTIR-differences spectra shown in Figure 13–1d.

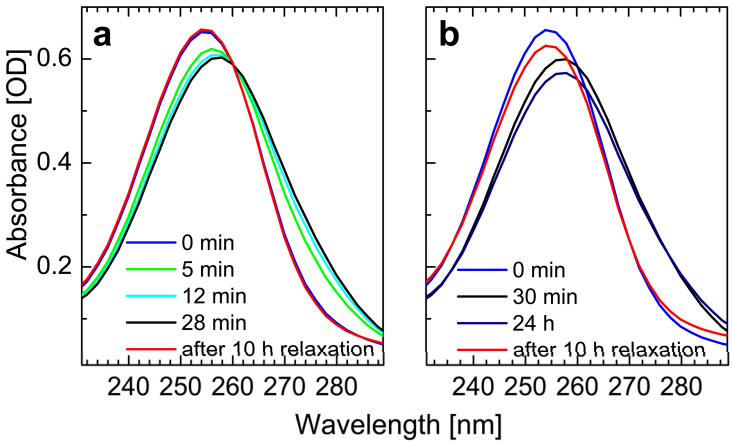


Figure 13–2: a) UV-absorption spectra of NMTAA before irradiation (blue line, 98% trans) and after 5, 12, and 28 minutes of irradiation at 255 nm. After 10 h in the dark at room temperature the original absorption spectrum has completely recovered (red line). b) irradiation for much longer than 30 minutes leads to a very slow degradation of the sample without further isomerization, and only partial recovery of the initial absorption spectrum after thermal relaxation.

In previous work sample degradation and trans → cis isomerization were found to occur with equal probability and their combined quantum efficiency was estimated to be 24%.[213] In contrast, it was find very little to no degradation of the NMTAA samples during the time needed to reach photoequilibrium. When irradiation was stopped in photoequilibrium the original trans-absorption spectra completely recovered due to thermal relaxation back to trans (Figure 13–2a). Only after an irradiation dose that corresponds to approximately 50 photo excitations per molecule it was observed an irreversible 5% loss and a small red shoulder in the UV

absorption spectrum of NMTAA after thermal relaxation (Figure 13–2b). At the same time, however, no new vibrational bands could be detected in the FTIR spectrum.[a] Thus it was concluded that NMTAA in $D_2O$ is photostable upon $\pi$-$\pi^*$ excitation with a quantum efficiency for decomposition below 0.1%. These findings are in agreement with recent measurements on small thio-substituted dipeptides.[208]

## 13.3.2. Time-resolved measurements

### 13.3.2.1. UV-Vis spectral range

Transient absorption changes of an aqueous solution of *trans*-NMTAA were recorded over a wide spectral range and compared to the contribution of the pure solvent $H_2O$ under identical conditions. Figure 13–3a and b show transients at two selected probe wavelengths (371nm and 483nm) after UV-excitation at 258 nm. The graphs are composed of two different data sets, one for delay times $\Delta t < 10$ ps (plotted on a linear scale) with a small temporal increment in order to facilitate detection of fast components, and one for $\Delta t > 10$ ps (plotted on a logarithmic scale).

[a] Note, however, that the sample can be efficiently destroyed upon irradiation with an unfiltered low-pressure Hg lamp, which it is attributed to excitation by light from the 193-nm line.

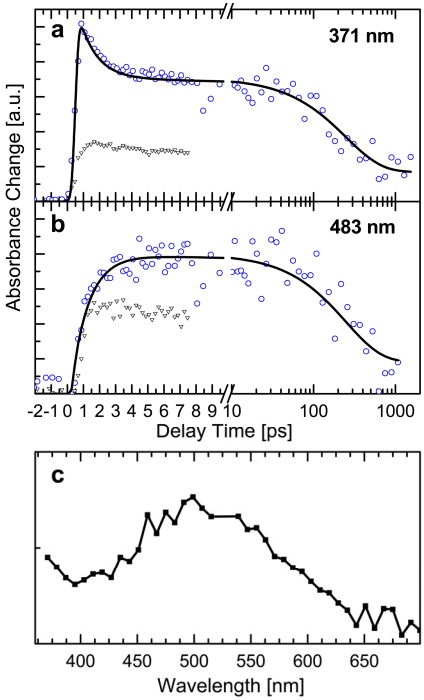


Figure 13–3: Transient absorption signals of NMTAA in $H_2O$ (circles) and pure $H_2O$ (triangles) at characteristic probe wavelengths of a) 371 nm and b) 483 nm, upon UV-excitation at 258 nm. The solid lines show double-exponential fits with time constants of 1.1 ps and 260 ps. c) Spectrum associated with the 260 ps time constant in fits to a set of transients between 350 nm and 700 nm.

At 371 nm an absorption increase is observed for the NMTAA solution (open circles) which rises within the time resolution of the setup and decays with a fast (1.1 ps) and a slow (260 ps) time constant. Both time constants can also be observed at a probing wavelength of 483 nm. However, the fast

component has a smaller relative amplitude and now appears as a rise time. Pure $H_2O$ also shows positive transient absorption at the two wavelengths (triangles), but these signals contain no comparable fast components. This rise in solvent absorption is attributed to the photoinduced formation of solvated electrons, with a lifetime of the order of microseconds in pure liquid water.[222] Their contribution to the signal of the concentrated NMTAA solution should be significantly smaller due to the high optical density and the resulting much shorter (< 15 μm) effective sample thickness. The true size of the background signal can in fact be estimated from the long-delay offset in the NMTAA data, which is much smaller than for pure $H_2O$.

The transient measurements thus clearly identify absorption of an excited state of NMTAA with a lifetime of ~250 ps. A pronounced maximum around 500 nm is found in the decay associated spectrum related with this slow time constant (Figure 13–3c), which may be interpreted as the spectral characteristics of this long-lived excited state band. Unfortunately, fast-varying solvent contributions to the signal do not allow an unambiguous identification of the spectrum associated with the 1.1 ps time constant. Over compensatory effects by strong positive contributions from the solvated electron and the excited state absorption of NMTAA may also obscure stimulated emission signals, which could not be identified in the accessible spectral range between 300 nm and 1000 nm.

#### 13.3.2.2. Mid-infrared spectral range

Changes in the mid-infrared absorption at different time delays after 259 nm excitation of *trans*-NMTAA are shown in the left column of Figure 13–4.

Apart from a positive offset, the transient spectra at very early times after photoexcitation have the same shape as the FTIR absorption spectrum of *trans*-NMTAA. Within the first 30 ps the initial bleaching signal is reduced

to little more than half of its original size, and positive absorption bands grow in at the spectral positions of the *cis*-NMTAA vibrations. This dynamics subsequently continues on a much slower timescale.

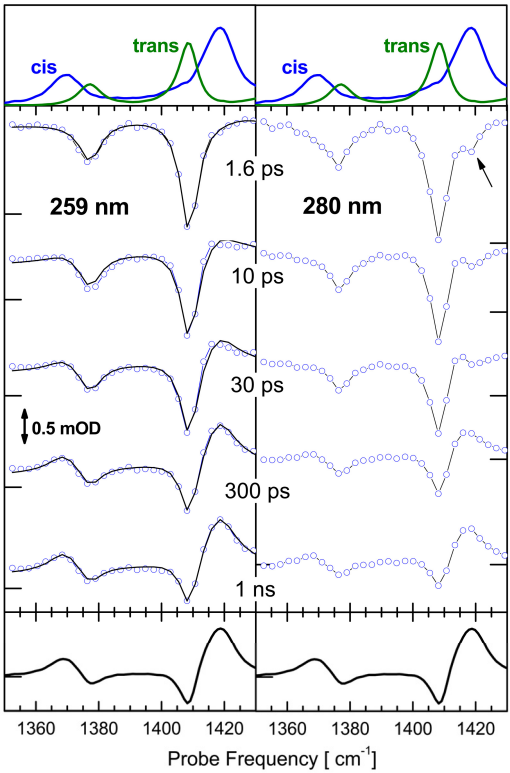


Figure 13–4: Magic angle transient infrared absorption spectra at different time delays after 259 nm (left) and 280 nm (right) excitation of NMTAA in $D_2O$. Thick black lines in the left column show least square fits using a linear combination of the cis and trans FTIR absorption spectra (shown on top). Horizontal ticks mark the zero-lines. The FTIR difference absorption spectrum (bottom) is also shown for comparison.

After 1 ns, the difference spectra fully reproduce the FTIR difference spectrum and no further changes are observed for longer time delays.[a] These results were found to be independent of concentration in the range of 50-250 mM.

The right column of Figure 13–4 shows transient spectra recorded for 280 nm excitation, where the *cis*-NMTAA absorption is approximately 5-10 times stronger than that of *trans*-NMTAA (see Figure 13–1). Thus, although only a small fraction of the molecules are initially in the cis-conformation (≤2% cis at room temperature), these do contribute to the transient signal, when exciting at this wavelength. Indeed, immediately following excitation, a bleaching signal is now also observed at the cis transition energies (see the arrow, right column in Figure 13–4). This signal increased during long series of measurement as a result of cis accumulation, but never exceeded 10-20% of the trans bleaching signal. Apart form the additional contribution due the

[a] The background underlying the NMTAA signal has two origins: A broad, unstructured positive signal, which decays to a small, constant value within approximately 10 ps is also observed for pure $D_2O$. The intensity of this background signal changes when the sample cell is moved, suggesting contribution from the cell windows. The main cause for the long-time background signal is, however, the temperature rise in $D_2O$ as the excess photon energy is dissipated to the solvent. FTIR measurements show that a small increase in temperature (1 K) leads to a positive, nearly flat, difference signal in the 1300-1450 $cm^{-1}$ region, which can be easily subtracted as a linear background from the transient data. It stays constant at delay times longer than 100 ps, indicating the end of the main energy dissipation.

excitation of *cis*-NMTAA no significant differences in the dynamics after excitation at the two wavelengths were observed. The larger change in amplitude of the signal for 280 nm excitation is due to the fact that cis → trans isomerization diminishes the trans → cis difference spectrum at long time delays. Taking this into account, it was found that the trans → cis isomerization quantum yields for 280 nm and 259 nm excitation are equal within experimental error and lie in the range of 30-40%.[a]

In order to extract the relevant time scales involved in the dynamics, the magic angle signals for 259 nm excitation were analyzed using singular value decomposition (SVD). The resulting basis spectra contain no features that do not already appear in the steady state absorption spectra of *cis*- and *trans*-NMTAA. The corresponding time traces can be fit simultaneously to a bi-exponential function, yielding global time constants of 8.5 ± 0.5 ps and 250 ± 20 ps.

[a] The isomerization quantum yields were determined in the following way: the FTIR trans-absorption spectrum was fit to the magic angle transient signal at 1-ps delay (maximum bleach) by simple rescaling. This determines the amount of initially excited trans species. Next, a FTIR trans-cis difference spectrum was rescaled to fit to the 1-ns transient spectrum. The rescaled absorption spectrum A, multiplied by a variable factor $\eta_{t\rightarrow c} \leq 1$ can now be added to the rescaled difference spectrum D, until a smooth product-spectrum P with symmetric line shapes is obtained; $\eta_{t\rightarrow c}$ is the quantum efficiency of isomerization. This method yields $\eta_{t\rightarrow c} = 0.35 \pm 0.05$. At 280 nm, where *cis*-NMTAA is also excited, the product spectrum is proportional to $D + (\eta_{t\rightarrow c} - \eta_{t\rightarrow c}\eta_c / \eta_t)A$, where $\eta_c / \eta_t$ is the ratio of initially excited cis and trans molecules.

It wasn't possible to identify any vibrational bands that may be assigned to NMTAA in an electronically excited state. The IR absorption bands of these species may either have shifted out of the spectral window used for detection, or their distribution may be so broad, that their absorption remains hidden in the unstructured background signal. A strong spectral shift could be caused by the fact that all the normal modes in the investigated spectral region include stretch motion of the central C-N bond, which have a significantly reduced bond order in the electronically excited states in which the molecule can isomerise (see below). Indeed, it was found that the transient spectra can be well reproduced by simply fitting the dataset with linear combinations of the cis and trans FTIR spectra (solid black lines in Figure 13–4). The quality of the fits is very good with only small deviations at intermediate delays, where there is a small red shift of the product absorption band near 1420 $cm^{-1}$ with respect to the FTIR spectrum of *cis*-NMTAA. This red-shift is maybe better seen with respect to the bleaching signal of *cis*-NMTAA in the spectra recorded upon 280 nm excitation (right column in Figure 13–4) and is a typical signature of a (cis) molecule at a more elevated temperature. It arises from anharmonic coupling of the high energy mode to low-frequency vibrations that have become excited thermally (or non-thermally) as a result of photoexcitation and energy dissipation.[223] Given the large amount of energy per normal mode that is delivered to the molecule by a 259 nm photon, the observed shifts are however surprisingly small. The transient infrared measurements thus appear to be sensitive only to ground state molecules that have dissipated most of the excitation energy. They monitor the arrival of population in either the relaxed cis or trans conformation of NMTAA, and the observed dynamics is therefore due to the joint processes of electronic relaxation and vibrational cooling.

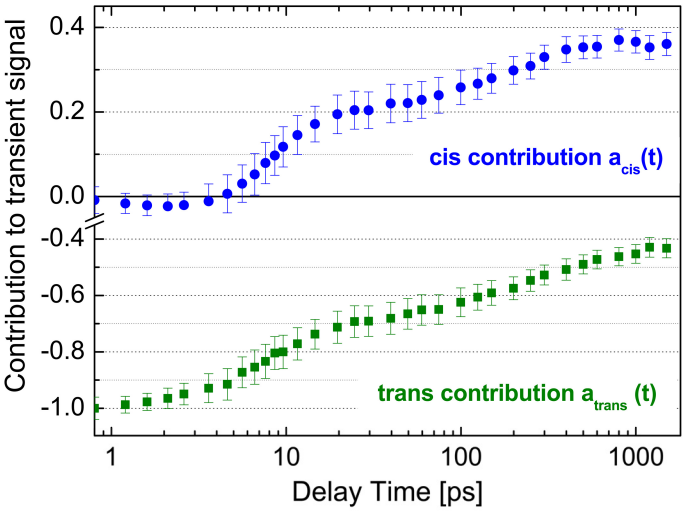


Figure 13–5: Time-dependent contributions of cis and trans absorption spectra in a least square fit $a_{cis}A_{cis}(\nu) + a_{trans}A_{trans}(\nu)$ + linear background to the magic angle transient spectra between 1350 $cm^{-1}$ and 1450 $cm^{-1}$. $A_{cis}(\nu)$ and $A_{trans}(\nu)$ denote the FTIR absorption spectra, which were scaled to yield $a_{trans} = -1$ at the earliest pump probe delay. The linear term $c(t)\nu + d(t)$ was added in the fit to account for the time-dependent background signal, caused mainly by the temperature rise in the $D_2O$ solvent. Error bars represent confidence intervals.

Figure 13–5 shows the contributions of cis and trans species to the transient spectra at different time delays, extracted from the fits using their ground state absorption spectra. It can be seen that both the recovery of the initial trans ground state and the formation of *cis*-NMTAA occur on two distinct timescales, with time-constants compatible with those obtained from the

SVD analysis (8.5 ps and 250 ps). About 30% of the initially excited trans population returns to the (cold) trans ground state within the first 20-30 ps following the 259 nm pump pulse. At the same time, another 15-20% is converted into ground-state *cis*-NMTAA. This early recovery of the IR absorption bands of cold ground state species indicates fast electronic decay and very efficient excess energy dissipation from the thioamide to the solvent. A strong interaction of NMTAA with $D_2O$ is already apparent from the broad amide II absorption band, that is strongly blue-shifted compared to the matrix-isolated molecule,[221] and efficient energy dissipation could take place for example via dipolar coupling to the $D_2O$ molecules of the first hydration shell as is the case of NMA in water,[224] and more directly through intermolecular hydrogen bonds. As a result, the 8-9 ps time constant very probably reflects the cooling of photoexcited NMTAA in deuterated water.

Further reduction of the initial *trans*-NMTAA bleach and the growth of the *cis*-NMTAA absorption bands take place on a much slower timescale which is comparable to the time of excited state decay in the visible measurements. Just as on the fast timescale, roughly two times more trans species than cis species are formed in the slow process. Overall, 35-40% of the excited NMTAA molecules are converted into cis, and the remaining molecules return back to the ground state in the trans conformation.

## 13.4. Photochemical Reaction Path Computations

Table 13–2: Molecular orbital occupation of *trans*-NMTAA in the $S_0$, $S_1$ and $S_2$ states: only the p-type sulphur lone pair and the $\pi/\pi^*$ orbitals are depicted. Occupations were calculated using a three roots ($S_0$, $S_1$, $S_2$) state average (0.33, 0.33, 0.33) CASSCF wave function.

| | sulphur lone pair | $\pi$ | $\pi$ | $\pi^*$ |
|---|---|---|---|---|
| | 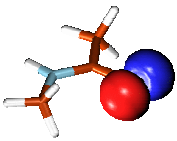 | 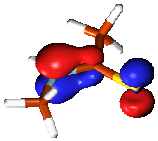 | 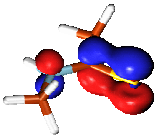 | 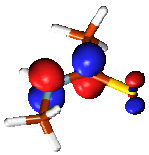 |
| $S_0$ | 1.998 | 1.981 | 1.955 | 0.064 |
| $S_1$ | 1.000 | 1.993 | 1.998 | 1.008 |
| $S_2$ | 1.995 | 1.972 | 1.413 | 0.616 |

The only energy minima located on the $S_0$ potential energy surface correspond to *trans*-NMTAA and *cis*-NMTAA. These are planar structures featuring $C_S$ symmetry with the cis stereoisomer located 1.9 kcal $mol^{-1}$ above the trans stereoisomer. Two fully asymmetric $S_0$ transition states (**TS $S_0$ A1** and **TS $S_0$ B1**) describe the trans → cis *thermal* isomerization reaction. They are located 24.9 and 20.7 kcal $mol^{-1}$ above *trans*-NMTAA respectively. These values compare very well with *cis*-NMTAA concentrations of 4% at room temperature, and a free activation enthalpy of 22 kcal $mol^{-1}$ in dilute $CCl_4$ solution.[225] Notice that the presence of the pyramidalized nitrogen

centre allows for the existence of one enantiomeric form (**TS $S_0$ B2** and **TS $S_0$ A2**) for each transition state.

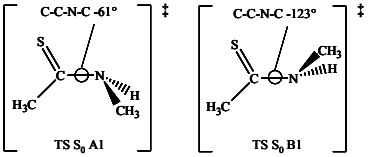


Wavefunction analysis at *trans*-NMTAA establishes that the $S_2$ state corresponds to a $\pi$-$\pi^*$ excitation, while the $S_1$ corresponds to a n-$\pi^*$ excitation (see Table 13–2).

### 13.4.1. Excited State Relaxation

As shown in Figure 13–6, relaxation from the Franck-Condon point (**FC**) of *trans*-NMTAA is dominated by C-S bond expansion: the C-S bond passes from 1.69 Å to around 1.96 Å, while the C-N bond stretches from 1.33 Å to 1.37 Å. Later along the same relaxation path the sulphur atom is lifted out of plane as the thiocarbonyl carbon starts to pyramidalize. At **Min $S_2$** the C-S bond distance is 2.07 Å, while the C-N bond distance goes back to 1.35 Å; the S atom makes a -55° dihedral angle with the carbon-nitrogen frame which, in turn, remains nearly planar. A further expansion of the C-S bond of **Min $S_2$** leads to a $S_2/S_1$ conical intersection (**CI $S_2/S_1$**) located ca. 14 kcal $mol^{-1}$ higher than the minimum.

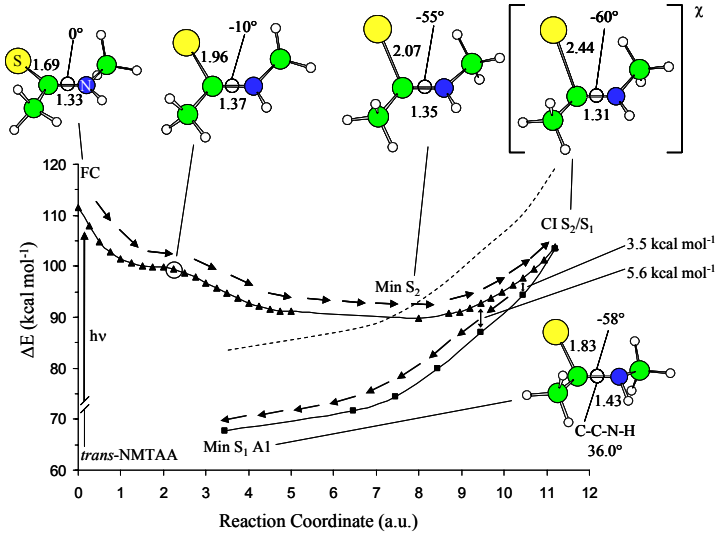


Figure 13–6: **FC → Min $S_2$ → CI $S_2/S_1$** and **CI $S_2/S_1$ → Min $S_1$ A1** paths computed at the CASPT2//CASSCF level of theory. The reaction coordinate is in mass-weighted cartesians (a.u. = $amu^{1/2}a_0$). Full triangles and full squares represent $S_2$ and $S_1$ energies respectively. C-S and C-N bond distances are given in Å; the S-C-N-C dihedral angle is given in degrees. For **Min $S_1$ A1** the C-C-N-H angle is also reported. The χ symbol indicates the CI. The dashed line represents the estimated shift in the position of the n-π* state due to solvent effects (see Section 13.5.1).

Relaxation from **CI $S_2/S_1$** to the $S_1$ potential energy surface is achieved via a path dominated by back-contraction of the C-S bond length to 1.83 Å and expansion of the C-N bond distance to 1.43 Å. During the relaxation the thiocarbonyl carbon centre remains pyramidalized while the originally planar nitrogen centre pyramidalizes. The existence of two pyramidalized centres

implies the existence of two diastereoisomers for the $S_1$ minimum. These have indeed been located and are referred to as **Min $S_1$ A1** (A stands for S,R) and **Min $S_1$ B1** (B stands for S,S). As a consequence the low-lying region of the $S_1$ potential energy surface is spanned by two flat "valleys" (Path A and Path B) that originate from the diastereoisomers **Min $S_1$ A1** and **Min $S_1$ B1** respectively. Starting from **Min $S_1$ A1** on Path A it was possible to map the entire conformational space corresponding to the torsional deformation about the central C-N bond. As shown in Figure 13–7, this path intercepts three conformational minima and three conformational transition states, in the order **Min $S_1$ A1** → **TS $S_1$ A1** → **Min $S_1$ A2** → **TS $S_1$ A2** → **Min $S_1$ A3** → **TS $S_1$ A3**. From **TS $S_1$ A3** the molecule goes back to **Min $S_1$ A1**.

Transition between Path A and Path B is possible through inversion transition states. For instance, the passage between **Min $S_1$ A1** and **Min $S_1$ B1** is driven by a transition state, **TS $S_1$ Pyr1**, located 2.6 kcal $mol^{-1}$ higher than **Min $S_1$ A1**.

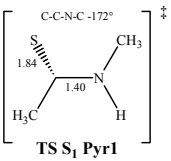


**TS $S_1$ Pyr1**

As reported in Figure 13–7, and similar to Path A, Path B comprises three conformational minima and three conformational transition states (in the order **Min $S_1$ B1** → **TS $S_1$ B1** → **Min $S_1$ B2** → **TS $S_1$ B2** → **Min $S_1$ B3** → **TS $S_1$ B3**. From **TS $S_1$ B3** the molecule goes back to **Min $S_1$ B1**). The maximum energy difference between the entire set of minima and transition

states is ca. 3.5 kcal $mol^{-1}$, so, at room temperature, the molecule can explore the entire conformational space of both Path A and Path B.

Figure 13–7 (next page): $S_1$ (full line), $T_1$ (dashed line) and $S_0$ (dot-dashed line) isomerization paths and $S_1(T_1) \rightarrow S_0$ relaxation paths (full line) computed at the CASPT2//CASSCF level of theory. Full circles, full squares and open squares represent $S_0$, $S_1$ and $T_1$ energies respectively. C-S and C-N bond distances in Å, and C-C-N-C dihedral angles in degrees. For the CIs and the ISCs the S-C-N angle is also given. Values in parentheses refer to $T_1$. While the C-C-N-C dihedral angle has been chosen as the internal coordinate that represents the trans-cis isomerization path, relaxation on $S_0$ is also characterized by planarization at the carbon and nitrogen centres. The nitrogen atoms of all structures along Path A are in the R conformation, while on Path B the nitrogens have a S conformation. The χ symbol indicates the CIs and the ISCs, the ‡ indicates the transition states.

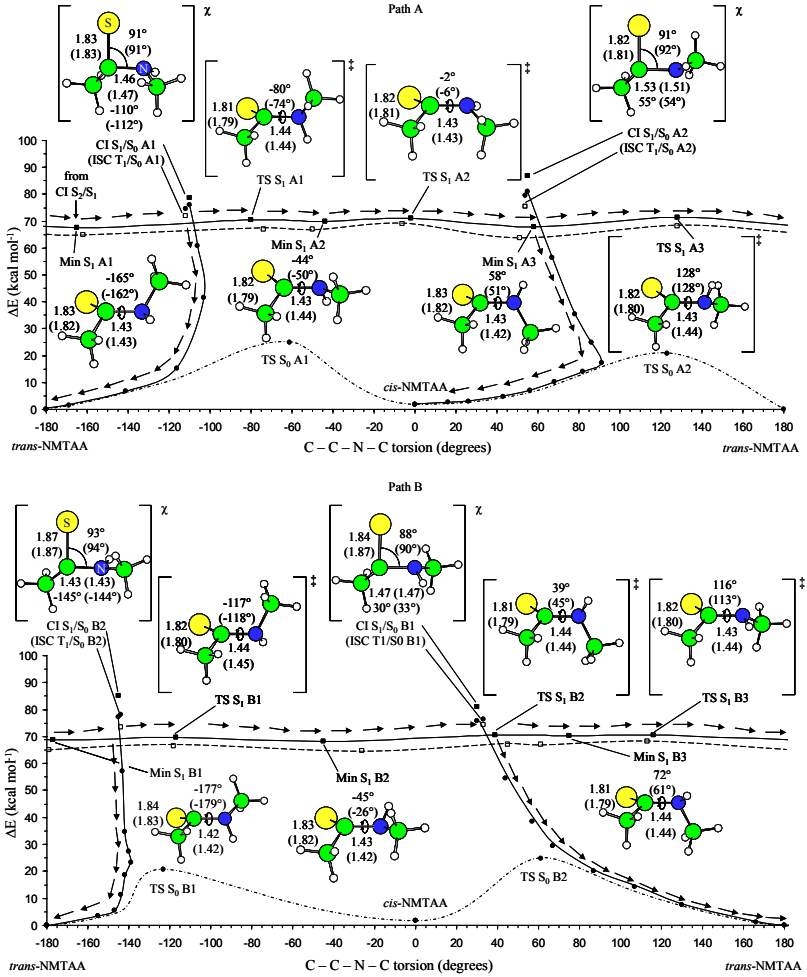
Path A
χ
91°
(91°)
1.83
(1.83)
1.46
(1.47)
-110°
(-112°)
-80°
(-74°)
1.81
(1.79)
1.44
(1.44)
-2°
(-6°)
1.82
(1.81)
1.43
(1.43)
1.82
(1.81)
91°
(92°)
1.53 (1.51)
55° (54°)
CI S1/S0 A1
(ISC T1/S0 A1)
from
CI S2/S1
TS S1 A1
TS S1 A2
CI S1/S0 A2
(ISC T1/S0 A2)
Min S1 A1
-165°
(-162°)
1.83
(1.82)
1.43
(1.43)
Min S1 A2
-44°
(-50°)
1.82
(1.79)
1.43
(1.44)
Min S1 A3
58°
(51°)
1.83
(1.82)
1.43
(1.42)
TS S1 A3
128°
(128°)
1.82
(1.80)
1.43
(1.44)
TS S0 A1
TS S0 A2
cis-NMTAA
ΔE (kcal mol-1)
trans-NMTAA
C – C – N – C torsion (degrees)
trans-NMTAA
Path B
χ
93°
(94°)
1.87
(1.87)
1.43 (1.43)
-145° (-144°)
-117°
(-118°)
1.82
(1.80)
1.44
(1.45)
88°
(90°)
1.84
(1.87)
1.47 (1.47)
30° (33°)
39°
(45°)
1.81
(1.79)
1.44
(1.44)
116°
(113°)
1.82
(1.80)
1.43
(1.44)
CI S1/S0 B2
(ISC T1/S0 B2)
CI S1/S0 B1
(ISC T1/S0 B1)
TS S1 B1
TS S1 B2
TS S1 B3
Min S1 B1
-177°
(-179°)
1.84
(1.83)
1.42
(1.42)
Min S1 B2
-45°
(-26°)
1.83
(1.82)
1.43
(1.42)
Min S1 B3
72°
(61°)
1.81
(1.79)
1.44
(1.44)
TS S0 B1
TS S0 B2
cis-NMTAA
ΔE (kcal mol-1)
trans-NMTAA
C – C – N – C torsion (degrees)
trans-NMTAA

### 13.4.2. Relaxation to the ground state

Decay to $S_0$ occurs via four different CIs. Two CIs are located along Path A (**CI $S_1/S_0$ A1** and **CI $S_1/S_0$ A2**) and two along Path B (**CI $S_1/S_0$ B1** and **CI $S_1/S_0$ B2**). All CIs are characterized by a S-C-N angle of ca. 90°. As mentioned in Section 13.2.2, these energy surface crossings are difficult to locate and therefore the structures reported are the best compromise between the requirement of stability and degeneracy. All decay channels are located in the range of 9.7-16.3 kcal $mol^{-1}$ above **Min $S_1$ A1**.[a] As reported in Figure 13–7, relaxation path computations indicate that the photochemical outcome of a $S_0$ relaxation process depends on the specific decay channel (i.e. the specific surface crossing) prompting the relaxation. Remarkably, only **CI $S_1/S_0$ A2** gives access to the cis product (*cis*-NMTAA), while decay at the other three CIs results in production of the initial trans molecule. One may explain this result by comparing the value of the C-C-N-C dihedral angle along a specific relaxation path to the value of the same dihedral angle for the ground state transition structures. In fact, these define the ridge between the cis and trans valleys on the $S_0$ potential energy surface (see Figure 13–7).

The analysis of the relaxation coordinates starting at **CI $S_1/S_0$ A1** and **CI $S_1/S_0$ B2** (C-C-N-C dihedral angles of -110° and -145° respectively) shows that the initial relaxation is dominated by replanarization of the thiocarbonyl

[a] Reported energies for CIs represent the mean between the $S_1$ and $S_0$ CASPT2 energy values reported in Table 13–6. Energy degeneracy was achieved at the CASSCF level of theory, but the CASPT2 treatment split the two energies. The mean values represent a good approximation of the energy of the CI.

carbon centre. As shown in Figure 13–7, after replanarization the molecule finds itself in the trans valley and goes back to the trans form. In contrast, the analysis of the relaxation coordinates starting at **CI $S_1/S_0$ A2** and **CI $S_1/S_0$ B1** (C-C-N-C dihedral angle of 55° and 30° respectively) shows that, due to the steric repulsion between the two fairly eclipsed methyl groups, thiocarbonyl carbon replanarization occurs simultaneously to a C-C-N-C dihedral angle increase of ca. 35°. For this reason, when the relaxation starts at **CI $S_1/S_0$ A2** the molecule achieves a dihedral angle of ca. 90° that is lower than the 123° angle of **TS $S_0$ A2** and right on top of the cis valley. Thus, the cis form is generated. In contrast, when relaxation starts at **CI $S_1/S_0$ B1**, after thiocarbonyl carbon replanarization the structure displays a dihedral angle of ca. 65° which is larger then the dihedral angle of **TS $S_0$ B2** and right on top of the trans valley. *In conclusion the given relaxation path analysis shows that relaxation from three out of four decay channels leads to the trans form*.

### 13.4.3. Population and Decay of the Triplet States

These computations establish the existence of triplet trans-cis isomerization pathways that, ultimately, lead to the same photoproduct distribution. In fact, as shown in Figure 13–7, the structure of the $T_1$ energy surface is analogue to the one seen for $S_1$. Indeed, it was possible to locate six different $T_1$ conformers (three along Path A and three along Path B). These conformers may decay to $S_0$ via four different $T_1/S_0$ ISCs (two for Path A and two for Path B) featuring a geometrical structure very close to the corresponding $S_1/S_0$ CIs described above. Thus, substantially, ground state relaxation from $T_1$ may occur along the same paths already described for the $S_1$ relaxation. However, notice that the energy difference between the $T_1$ minima and the

ISCs is considerably smaller then the energy difference between the $S_1$ minima and the $S_1/S_0$ CIs.

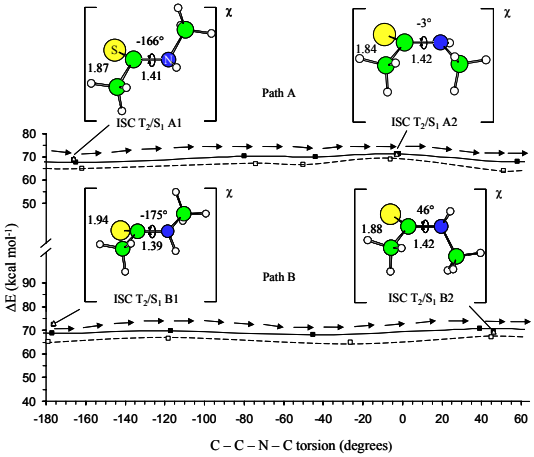


Figure 13–8: $T_1/S_0$ intersystem crossings computed at the CASPT2//CASSCF level of theory. Full squares, open squares and open triangles represent $S_1$, $T_1$ and $T_2$ energies. Geometrical parameters, symbols and lines as in Figure 13–7.

In principle efficient population of the $T_1$ energy surface may occur via intersystem crossing from $S_1$ to $T_2$ followed by internal conversion from $T_2$ to $T_1$. Indeed, as shown in Figure 13–8 the $S_1$ conformers can access the $T_2$ state via four different $T_2/S_1$ ISC channels located near the region of **Min $S_1$ A1**, **TS $S_1$ A2**, **Min $S_1$ B1** and **TS $S_1$ B2**. Following the El-Sayed rules for inter system crossings,[226] the $T_2$ state (corresponding to a triplet π-π* excitation) can be accessed quite efficiently from a degenerate singlet n-π* state. Since, in the same region, the $T_2$ and $T_1$ potential energy surfaces are substantially

degenerate,[a] it is reasonable to assume that the $T_1$ state is readily accessed allowing for the efficient population of the six different $T_1$ conformers of Figure 13–7.

### 13.4.4. Comparison with Spectroscopic Data

Table 13–3: Comparison of Experimental and CASPT2//CASSCF Calculated Absorption Wavelengths and CASSCF Oscillator Strengths. The calculated $S_2 \rightarrow S_0$ fluorescence maximum is also reported. Data are in nm, while kcal $mol^{-1}$ values are given in brackets.

| | experimental | | | calculated | | | |
|---|---|---|---|---|---|---|---|
| | n-π* | π-π* | *f* | n-π* | *f* | π-π* | *f* |
| absorption trans | 305 (94) | 255 (112) | 2.5 x $10^{-1}$ | 366 (78) | 1.43 x $10^{-2}$ | 257 (111) | 3.06 x $10^{-1}$ |
| absorption cis | | 268 (107) | | 374 (76) | 0.92 x $10^{-2}$ | 267 (107) | 3.26 x $10^{-1}$ |
| fluorescence[b] | | | | | | 796 (36) | |

In order to validate the computational strategy (see Section 13.2.2), the experimental absorption and phosphorescence energies were compared with the corresponding calculated data. Absorption maxima were calculated as the

[a] For example, the energy difference between the $T_2$ and $T_1$ states at the $T_2/T_1$ ISCs is in the range 1.7-4.8 kcal mol-1. See Table 13–6.

[b] Vertical energy difference between $S_2$ and $S_0$ energy values of **Min $S_2$**.

difference between the $S_1$ (for the $S_0 \rightarrow S_1$ transition) or $S_2$ (for the $S_0 \rightarrow S_2$ transition) energy and the $S_0$ energy at *trans*-NMTAA and *cis*-NMTAA. The resulting values are summarized in Table 13–3.

It can be seen that the π-π* absorption and the absorption red-shifts observed when passing from the trans to the cis form are well reproduced. On the other hand, there is a large discrepancy between the calculated and the observed n-π* absorption maximum, possibly because the solvent effects were not considered in the computation. Indeed, $S_0$, $S_1$ and $S_2$ have calculated dipole moments of 4.9 D, 2.7 D and 5.3 D respectively. Thus a polar solvent is expected to induce a similar stabilization in $S_0$ and $S_2$ (since these states have roughly the same dipole moment). On the other hand, the stabilization effect on $S_1$ is expected to be smaller, due to the lower dipole moment of this state. Previous works[227] showed that a quite sophisticated treatment of the solvent bulk is needed to predict n-π* excitation energies in good agreement with the experimental data.

To reproduce the phosphorescence maximum recorded in a methanol:ethanol low-temperature glass,[214] the maximum was calculated as the energy difference between $T_1$ (for the $T_1 \rightarrow S_0$ transition) or $T_2$ (for the $T_2 \rightarrow S_0$ transition) and $S_0$ at different structures as reported in Table 13–4.

Table 13–4: CASPT2//CASSCF Calculated Maxima of Phosphorescence for different Molecular Geometries and Experimental Values Observed in a Methanol:Ethanol Low-Temperature Glass. Data are in nm, while kcal mol$^{-1}$ values are given in brackets.

| experimental value[214] | calculated | structure | transition |
|---|---|---|---|
| 485 (59) | 757-945 (38-30)[a] | Min $T_1$ A1 – B3 | $T_1 \rightarrow S_0$ |
| | 605-727 (47-39)[a] | Min $T_1$ A1 – B3 | $T_2 \rightarrow S_0$ |
| | 426-448 (67-64)[a] | Min $T_1$ A1 – B3 | $T_1 \rightarrow S_0$ non-vertical[b] |
| | 470 (61) | Min $T_1$ Planar Trans | $T_1 \rightarrow S_0$ |
| | 462 (62) | Min $T_1$ Planar Cis | $T_1 \rightarrow S_0$ |

The calculated energy differences between $T_1$ and $S_0$ at the optimized geometry of the various energy minima on $T_1$ are not consistent with the experimental value. However, since the experiment was carried out in the constrained environment of a cold glass, one can assume that the molecule had sufficient space only to relax along the stretching coordinates (e.g. it could not relax along pyramidalization coordinates), and that radiative decay was the only way for the molecule to go back to $S_0$. This view is supported by the fact that the calculated $T_1$-$S_0$ energy difference at the **Min $T_1$ Planar Trans** and **Min $T_1$ Planar Cis** are in good agreement with the value of $\lambda_{max}$ for the observed phosphorescence.

[a] Data represent the range of the phosphorescence maximum calculated for the various minima on $T_1$ energy surface.

[b] These values were calculated comparing $T_1$ energies of the **Min $T_1$ A1 – B3** minima with the $S_0$ energy of ***trans*-NMTAA**.

Table 13–5: Calculated absorption wavelength and oscillator strength of the minima along $S_1$ and $T_1$ Path A and B. Data are in nm, while kcal $mol^{-1}$ values are given in brackets. Corrected values were estimated from calculated by subtracting the energy difference between experimental and calculated energy difference of the n-π* transition (15.6 kcal $mol^{-1}$).

| Structure | Transition | *f* | Calculated | Corrected |
|---|---|---|---|---|
| Min $S_1$ A1 | S1 – S3 | $7.5 \cdot 10^{-2}$ | 309 (93) | 371 (77) |
| Min $S_1$ A2 | S1 – S3 | $6.6 \cdot 10^{-3}$ | 403 (71) | 517 (55) |
| Min $S_1$ A3 | S1 – S3 | $1.6 \cdot 10^{-1}$ | 378 (76) | 477 (60) |
| Min $S_1$ B1 | S1 – S3 | $4.3 \cdot 10^{-2}$ | 365 (78) | 455 (63) |
| Min $S_1$ B2 | S1 – S3 | $7.5 \cdot 10^{-2}$ | 321 (89) | 389 (74) |
| Min $S_1$ B3 | S1 – S3 | $4.8 \cdot 10^{-3}$ | 407 (70) | 524 (55) |
| | | | | |
| Min $T_1$ A1 | T1 – T3 | $2.2 \cdot 10^{-2}$ | 386 (74) | 489 (58) |
| Min $T_1$ A2 | T1 – T3 | $2.0 \cdot 10^{-1}$ | 578 (49) | 845 (34) |
| Min $T_1$ A3 | T1 – T3 | $5.6 \cdot 10^{-1}$ | 549 (52) | 783 (36) |
| Min $T_1$ B1 | T1 – T3 | $7.4 \cdot 10^{-2}$ | 557 (51) | 800 (36) |
| Min $T_1$ B2 | T1 – T3 | $4.0 \cdot 10^{-1}$ | 383 (75) | 484 (59) |
| Min $T_1$ B3 | T1 – T3 | $1.8 \cdot 10^{-1}$ | 647 (44) | 1000 (29) |

The possible origins of the visible transient absorption signals (Figure 13–3c) were also investigated. The $S_1/S_2$ transition being energetically out of the recorded range, the singlet forth root was calculated for each $S_1$ minimum and the triplet third and forth roots were calculated for each $T_1$ minimum. (See Table 13–5) As for the n-π* excitations the computed $S_1 \rightarrow S_3$ or $T_1 \rightarrow T_3$ absorption will be shifted by a polar solvent due to the higher dipole moment of $S_3$ and $T_3$ (both π-π* states) with respect to $S_1$ and $T_1$. With the

rough assumption that the energy shift would be similar to the one reported for n-π* excitations, one can estimate the absorption wavelengths of the $S_1$ and $T_1$ minima as reported in Table 13–5. Remarkably these values are in the range of those reported in Figure 13–3c; in particular, at least one minimum per Path (**Min $S_1$ A3**, **Min $S_1$ B1**, **Min $T_1$ A1**, **Min $T_1$ B2**) shows an absorption wavelength in the 500 nm region, along with a not negligible calculated oscillator strength. Unfortunately this analysis cannot distinguish between $S_1$ or $T_1$ absorptions.

## 13.5. Discussion

Excited state vibrational bands do not appear in the transient infrared spectra of photoexcited NMTAA and well-defined bands are only observed at, or very near, the spectral positions of the room-temperature absorption bands of *cis*- and *trans*-NMTAA. Thus, the IR experiment provides information about the return of the photoexcited population to the two isomeric ground state minima. Two distinct timescales of approximately 8 and 250 ps are observed for both the formation of *cis*-NMTAA and the recovery of *trans*-NMTAA. On both timescales, the same branching ratio between the two isomers is found, with a cis yield of approximately 30-40%. The UV-visible measurements yield complementary information on the dynamics in the electronically excited states, revealing that the 250 ps time-constant represents the lifetime of an electronically excited state with an absorption band near 500 nm. These findings in combination with the computational results of Section 13.4 provide a detailed picture of the mechanism underlying the photoisomerization of *trans*-NMTAA.

### 13.5.1. Fast relaxation dynamics

The IR experiment shows that 50% of the exited molecules relax to the ground state of either *cis*- or *trans*-NMTAA within a few picoseconds after excitation. This implies, that isomerization and electronic relaxation from the initially excited $\pi$-$\pi^*$ state must take place on a faster timescale. Although the computations reveal that a $S_2/S_1$ conical intersection is located relatively high in energy with respect to **Min $S_2$**, suggesting a too long $S_2$ lifetime, the analysis of the $S_2$ relaxation path indicates that fast radiationless decay may still occur since:

i) The $S_2$ and $S_1$ surfaces become nearly degenerate well before the conical intersection. In fact already at a point located only 2.8 kcal $mol^{-1}$ above **Min $S_2$** there is an energy gap of only 5.6 kcal $mol^{-1}$ (see Figure 13–6). Thus one may assume that the non-adiabatic transition from one surface to the other starts to occur before the intersection.

ii) Both position and relative energy of **CI $S_2/S_1$** are expected to be sensitive to the solvent environment, which can affect (e.g. lower or remove) the energy barrier controlling the decay. This effect is consistent with the solvent dependence of the $S_1$ absorption maximum discussed above and can be roughly estimated in terms of the difference between the experimental (in solution) and the calculated (*in vacuo*) n-$\pi^*$ excitation energies (see Table 13–3).

As shown in Figure 13–6, the crossing point moves close to the $S_2$ minimum when the resulting energy of ~ 15 kcal $mol^{-1}$ is added to the $S_1$ curve (dashed

line). Another considerable solvent effect has been documented in NMA, the carbonyl analogue on NMTAA,[228] where the calculated C-O and C-N bond distances for π-π* differ significantly between vacuum and solution: indeed, *in vacuo* the C-O bond of NMA lengthens more than the C-N one, consistent with what it was found for C-S versus C-N in NMTAA (see above). On the other hand, in solution the C-N bond expansion is greater than that of the C-O bond, as also indicated by Resonance Raman data.[229] This has been attributed mainly to a more elongated C-O bond in the electronic ground state due to hydrogen bonding. While the relative C-N and C-S contributions to the initial relaxation path appear to change from the gas-phase to solution and may be different in amides and thioamides, such effects clearly deserve further research efforts to be fully understood.

Notice that the prediction that initial relaxation on $S_2$ is dominated by C-N and C-S bond expansion (and not by torsional deformations) is consistent with the resonance Raman spectra recorded on NMA, where torsional modes are not enhanced.[215] It is also consistent with the observation that the quantum efficiency of isomerization does not depend on the irradiation wavelength (259 or 280 nm), which indicates that the initial excess energy plays no role in the trans-cis photo-isomerization.

According to the above discussion the photoreaction must be determined by events occurring at lower energy. In fact, trans → cis isomerization motion is predicted to occur predominantly on the $S_1$ (and/or $T_1$) potential energy surface, where the molecule can sample all torsional angles without having to overcome significant energy barriers (see Figure 13–7). This can also explain the observation of trans-cis isomerization upon direct excitation of the $S_1$ state at 308 nm (n-π* transition). From $S_1$ (or $T_1$) fast relaxation to the ground state is possible via four CIs (ISCs), that predetermine the final conformation

adopted by the molecule. Indeed, making the rough assumption that the four different $S_1/S_0$ CIs have the same probability of being accessed, it is possible to estimate a quantum yield for the trans → cis process close to 25%. This is remarkably close to the measured quantum efficiency of 30-40%. It must be stressed that the same conclusions are drawn if one considers decay from $T_1$ via the four $T_1/S_0$ intersystem crossing points documented above. Thus the involvement of a "triplet" pathway cannot be excluded (see below).

The solvent is expected to have a similar effect on all four $S_1/S_0$ CIs (and the four $T_1/S_0$ ISCs), since the calculated dipole moments remain more or less at the value of *trans*-NMTAA along the isomerization path. This implies that the energy barrier between minima and intersection points should be higher in water than calculated *in vacuo*, while there is no evidence that one decay route may become preferred.

### 13.5.2. Slow relaxation dynamics

Half of the photoexcited molecules follow an ultrafast relaxation pathway back to the ground state. An approximately equal fraction of NMTAA relaxes much more slowly with a time constant of 250 ps. The observation of excited state absorption with the same lifetime clearly shows that this slow dynamics is due to population trapping in an electronically excited state, which subsequently relaxes non-radiatively. However, just like in the fast process the ratio of cis and trans yield is approximately 1:2, which indicates a similar relaxation pathway on both time scales. The given computational results offer two different explanations:

i) Branching and population trapping occur on the $S_2$ surface, in which case the 250 ps time constant may be proportional to the time required to

surmount the barrier between **Min $S_2$** and **CI $S_2/S_1$** (or a decay region close to it). Subsequent relaxation and isomerization would then be identical for temporarily trapped molecules and for the molecules that reach the $S_2 \rightarrow S_1$ decay point directly (e.g. impulsively).

In this case, however, fluorescence (predicted at a wavelength of 800 nm, see Table 13–3) should be observable from $S_2$, even in the presence of non-radiative relaxation with a rate of 250 $ps^{-1}$. In agreement with earlier work,[213,230] it wasn't possible to detect any fluorescence from NMTAA in the 300-850 nm region, which, given the sensitivity of the setup, excludes trapping in a state with an oscillator strength $\geq 5 \times 10^{-2}$ for the transition to $S_0$, or implies a much smaller energy difference (i.e. emission at $\lambda > 850$ nm) between excited state minimum and the ground state. Note, however, that no stimulated emission could be detected in a spectral window up to 1000 nm. Furthermore, the 1 ps rise time in the transient signal at 483 nm and the corresponding fast decay at higher energies is rather untypical for spectral dynamics due to vibrational cooling (in the $S_2$ state), for which one would expect a blue-shift of the excited state absorption. The 1 ps dynamics is therefore more likely due to electronic relaxation, suggesting that population trapping occurs after relaxation from $S_2$ to $S_1$.

ii) Population trapping occurs on $S_1$ or $T_1$. This implies that an initial vibrationally hot $S_1$ population, produced by $S_2 \rightarrow S_1$ decay, either immediately decays to $S_0$ (giving rise to the fast time-constant) or undergoes internal vibrational energy re-distribution and get temporarily trapped in the $S_1$ or $T_1$ excited state.

According to this scenario, competition between immediate electronic relaxation and cooling in the excited state would be at the origin of the two reaction regimes. An alternative scenario involves that branching of the $S_1$

population that either decays directly to $S_0$ via the $S_1/S_0$ intersections, or to $T_2$ via the $T_2/S_1$ crossings. The $T_2$ population would then decay to $S_0$ via the $T_2/T_1$ and $T_1/S_0$ crossings in a somehow slower process. Indeed, the observation of blue-green phosphorescence from NMTAA in a low-temperature glass by Tasumi et al.[214] could be an indication for the involvement of a triplet pathway. Notice that, as documented in Figure 13–7 and Figure 13–8 respectively, there is the same number of $S_1 \rightarrow T_2$ and $S_1 \rightarrow S_0$ decay channels and that they have similar energies. It is therefore not unlikely that the $S_1$ population evenly decays to $S_0$ and $T_2$, which could explain why approximately one half of the molecules decay via the fast and the other half via the slow channel. In addition, very similar *cis*-NMTAA quantum yields are predicted for these two channels, since the possible relaxation pathways of the molecule upon reaching the $S_0$ ground state via a $S_1/S_0$ conical intersection or via the corresponding $T_1/S_0$ intersystem crossing are almost identical.

### 13.5.3. Photoequilibrium and back reaction

Although it wasn't possible to follow the back-reaction from *cis*- to *trans*-NMTAA with time-resolved spectroscopy, it can be deduced from the low cis concentrations at photo equilibrium that cis → trans isomerization must be much more efficient than the trans → cis process. The most reliable ratio of cis → trans over trans → cis isomerization efficiency was determined for 256 nm irradiation, where cis → trans isomerization is 2.3-3.1 times more likely. At the lower error limit of these measurements the sum of both quantum efficiencies may add up to unity. If confirmed by complementary measurements, this could indicate that isomerization proceeds in both

directions via a common intermediate state, which then determines the outcome of the photoreaction. This is consistent with a scenario, where the same "region" of the $S_1$ or $T_1$ states are populated from either the trans or cis conformers. In other words, in agreement with the proposed mechanism, the decay channels would always correspond to the same set of crossings.

## 13.6. Conclusion

Time resolved infrared experiments and *ab initio* CASPT2//CASSCF reaction path computations for $\pi$-$\pi^*$ excitation of *trans*-NMTAA yield consistent mechanistic information on the trans → cis isomerization of NMTAA, which is summarized in Figure 13–9. The initial $S_2$ population (schematically represented by a Gaussian wave packet) evolves on $S_2$ mainly via C-S bond expansion (and out-of-plane deformation) leading to efficient $S_2 \rightarrow S_1$ decay in the region of the $S_2/S_1$ conical intersection.

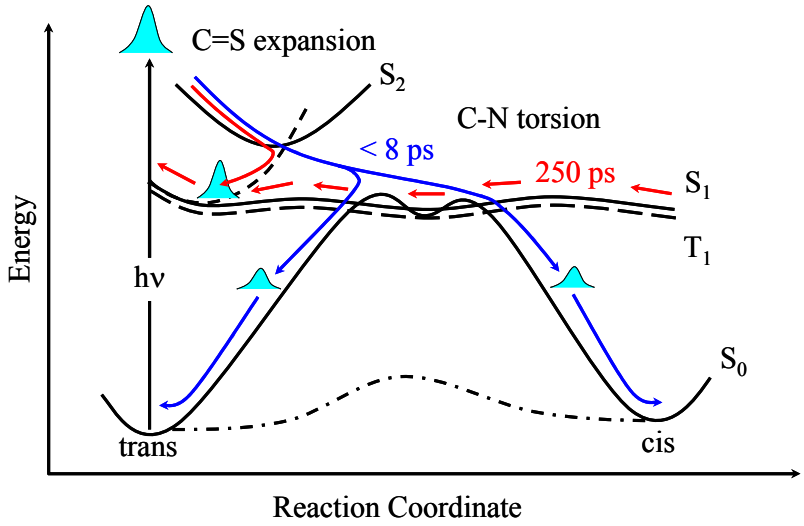


Figure 13–9: Schematic representation of the photoisomerization reaction of *trans*-NMTAA. The multiple intersections between the $S_1$, $T_1$ and the $S_0$ energy profiles represent the CIs and ISCs documented in Figure 13–7. See text for details.

Relaxation on $S_1$ delivers the system to a very flat region of the potential energy surface, characterized by multiple conformers and multiple $S_1/S_0$ conical intersections located a few kcal $mol^{-1}$ above them. Decay to the ground state may then occur *directly* (blue arrows) via the $S_1/S_0$ CIs or *indirectly* (red arrows). Approximately half of the excited molecules seem to follow the direct relaxation pathway, and return to the electronic ground state with a time constant of less than 7 ps. The second half of the excited molecules become temporarily trapped in an electronically excited state and reach the electronic ground state with a much longer time constant of ~ 250 ps. This population trapping can either be the result of competition between

vibrational energy relaxation on $S_1$ and $S_1 \rightarrow S_0$ electronic decay, or competition between fast $S_1 \rightarrow S_0$ decay and a somehow slower relaxation process via the triplet states. On both the fast and the slow timescale, *cis*-NMTAA is formed with a quantum efficiency of 30-40%. It has been demonstrated that the final ground state conformation of NMTAA is predetermined by the molecular geometries of the $S_1/S_0$ CIs and $T_1/S_0$ ISCs and is therefore independent of the followed route, provided nearly full sampling of the torsional coordinate in $S_1$ and/or $T_1$ is possible prior to decay. The replacement of one oxygen atom by sulphur in the backbone of a peptide is probably the least "invasive" way to render it photoswitchable. This study indicates that a thio-photoswitch is photostable and potentially capable of inducing conformational change with a high quantum yield on a sub-nanosecond timescale. This timescale is much faster than the time-resolution needed to investigate, for example, the formation of secondary structure elements in proteins. However, notice that, due to the flatness of the $S_1$ and $T_1$ isomerization paths, it is likely that a fully relaxed peptide conformation will not be perturbed by the photoexcitation of a NMTAA unit. In other words, the $S_1$ or $T_1$ force field of NMTAA may not be able to efficiently force a peptide chain out of its equilibrium conformation. On the other hand, if the peptide is exerting a certain amount of torsional strain on the NMTAA unit which is contrasted by the thioamide C-N partial double bond, then promotion to the flat $S_1$ or $T_1$ energy surfaces can act as an "unlocking event" (compare the $S_0$ energy profile with the $S_1$ and $T_1$ energy profiles in Figure 13–7), and allow for trans to cis isomerization. In this case NMTAA may be seen as a photoreleasable lock.

Table 13–6: CASSCF/6-31G* Absolute, CASPT2/6-31G* Absolute and Relative Energies along with Wave Function Reference Weights of the Structures Discussed in Chapter 12

| structure | state | CASSCF reference energy (hartree) | CASPT2 energy (hartree) | reference weight | relative energy CASPT2 level (kcal mol$^{-1}$)[a] |
|---|---|---|---|---|---|
| ***trans*-NMTAA** | $S_0$ | -569.7080 | -570.3427 | 0.83 | 0.0 |
| | $S_1$ | -569.5707 | -570.2180 | 0.82 | 78.3 |
| | $S_2$ | -569.5016 | -570.1651 | 0.80 | 111.4 |
| | $T_1$ | -569.5791 | -570.2215 | 0.82 | 76.0 |
| | $T_2$ | -569.5723 | -570.2156 | 0.82 | 79.7 |
| ***cis*-NMTAA** | $S_0$ | -569.7052 | -570.3397 | 0.83 | 1.9 |
| | $S_1$ | -569.5710 | -570.2177 | 0.82 | 78.4 |
| | $S_2$ | -569.5053 | -570.1685 | 0.80 | 109.3 |
| | $T_1$ | -569.5793 | -570.2215 | 0.82 | 76.1 |
| | $T_2$ | -569.5759 | -570.2197 | 0.82 | 77.1 |
| **TS $S_0$ A1** | $S_0$ | -569.6674 | -570.3030 | 0.83 | 24.9 |
| | $S_1$ | -569.5767 | -570.2240 | 0.82 | 74.4 |
| | $S_2$ | -569.4953 | -570.1654 | 0.80 | 111.2 |
| | $T_1$ | -569.5903 | -570.2314 | 0.82 | 69.9 |
| | $T_2$ | -569.5552 | -570.1910 | 0.83 | 95.2 |
| **TS $S_0$ B1** | $S_0$ | -569.6743 | -570.3097 | 0.83 | 20.7 |
| | $S_1$ | -569.5775 | -570.2255 | 0.82 | 73.5 |
| | $S_2$ | -569.4991 | -570.1687 | 0.80 | 109.2 |
| | $T_1$ | -569.5885 | -570.2313 | 0.82 | 69.9 |
| | $T_2$ | -569.5599 | -570.1977 | 0.82 | 91.0 |
| **Min $S_1$ A1** | $S_0$ | -569.6669 | -570.3001 | 0.83 | 26.7 |
| | $S_1$ | -569.5948 | -570.2349 | 0.82 | 67.7 |
| | $S_2$ | -569.5337 | -570.1838 | 0.81 | 99.7 |
| | $T_1$ | -569.6030 | -570.2389 | 0.82 | 65.1 |
| | $T_2$ | -569.5956 | -570.2319 | 0.82 | 69.5 |
| **Min $S_1$ A2** | $S_0$ | -569.6537 | -570.2876 | 0.83 | 34.6 |
| | $S_1$ | -569.5904 | -570.2314 | 0.82 | 69.9 |
| | $S_2$ | -569.5015 | -570.1637 | 0.80 | 112.3 |
| | $T_1$ | -569.5992 | -570.2353 | 0.82 | 67.4 |
| | $T_2$ | -569.5822 | -570.2173 | 0.82 | 78.7 |
| **Min $S_1$ A3** | $S_0$ | -569.6620 | -570.2942 | 0.83 | 30.4 |
| | $S_1$ | -569.5947 | -570.2346 | 0.82 | 67.8 |
| | $S_2$ | -569.5290 | -570.1813 | 0.81 | 101.3 |
| | $T_1$ | -569.6031 | -570.2398 | 0.82 | 64.6 |
| | $T_2$ | -569.5889 | -570.2237 | 0.82 | 74.6 |
| **Min $S_1$ B1** | $S_0$ | -569.6608 | -570.2931 | 0.83 | 31.1 |
| | $S_1$ | -569.5940 | -570.2332 | 0.82 | 68.7 |
| | $S_2$ | -569.5356 | -570.1868 | 0.81 | 97.8 |
| | $T_1$ | -569.6030 | -570.2386 | 0.82 | 65.3 |
| | $T_2$ | -569.5914 | -570.2270 | 0.82 | 72.6 |
| **Min $S_1$ B2** | $S_0$ | -569.6656 | -570.2989 | 0.83 | 27.5 |
| | $S_1$ | -569.5940 | -570.2341 | 0.82 | 68.1 |
| | $S_2$ | -569.5336 | -570.1839 | 0.81 | 99.6 |
| | $T_1$ | -569.6020 | -570.2377 | 0.82 | 65.8 |
| | $T_2$ | -569.5959 | -570.2324 | 0.82 | 69.2 |
| **Min $S_1$ B3** | $S_0$ | -569.6532 | -570.2885 | 0.83 | 34.0 |

[a] Energies are relative to the $S_0$ state energy value of ***trans*-NMTAA**.

| | | | | | |
|---|---|---|---|---|---|
| | $S_1$ | -569.5877 | -570.2309 | 0.82 | 70.2 |
| | $S_2$ | -569.4937 | -570.1625 | 0.80 | 113.1 |
| | $T_1$ | -569.5971 | -570.2350 | 0.82 | 67.6 |
| | $T_2$ | -569.5795 | -570.2158 | 0.82 | 79.6 |
| **TS $S_1$ A1** | $S_0$ | -569.6447 | -570.2775 | 0.83 | 40.9 |
| | $S_1$ | -569.5894 | -570.2304 | 0.82 | 70.5 |
| | $S_2$ | -569.4974 | -570.1642 | 0.80 | 112.0 |
| | $T_1$ | -569.5985 | -570.2349 | 0.82 | 67.6 |
| | $T_2$ | -569.5740 | -570.2070 | 0.83 | 85.1 |
| **TS $S_1$ A2** | $S_0$ | -569.6693 | -570.3021 | 0.83 | 25.5 |
| | $S_1$ | -569.5893 | -570.2292 | 0.82 | 71.2 |
| | $S_2$ | -569.5309 | -570.1826 | 0.81 | 100.5 |
| | $T_1$ | -569.5968 | -570.2322 | 0.82 | 69.3 |
| | $T_2$ | -569.5916 | -570.2280 | 0.82 | 71.9 |
| **TS $S_1$ A3** | $S_0$ | -569.6605 | -570.2938 | 0.83 | 30.7 |
| | $S_1$ | -569.5874 | -570.2290 | 0.82 | 71.4 |
| | $S_2$ | -569.5064 | -570.1699 | 0.80 | 108.4 |
| | $T_1$ | -569.5966 | -570.2332 | 0.82 | 68.7 |
| | $T_2$ | -569.5803 | -570.2151 | 0.82 | 80.1 |
| **TS $S_1$ B1** | $S_0$ | -569.6550 | -570.2877 | 0.83 | 34.5 |
| | $S_1$ | -569.5902 | -570.2318 | 0.82 | 69.6 |
| | $S_2$ | -569.5059 | -570.1693 | 0.80 | 108.8 |
| | $T_1$ | -569.5990 | -570.2357 | 0.82 | 67.1 |
| | $T_2$ | -569.5803 | -570.2135 | 0.83 | 81.1 |
| **TS $S_1$ B2** | $S_0$ | -569.6468 | -570.2794 | 0.83 | 39.7 |
| | $S_1$ | -569.5895 | -570.2301 | 0.82 | 70.6 |
| | $S_2$ | -569.5003 | -570.1657 | 0.80 | 111.1 |
| | $T_1$ | -569.5982 | -570.2347 | 0.82 | 67.8 |
| | $T_2$ | -569.5743 | -570.2078 | 0.83 | 84.7 |
| **TS $S_1$ B3** | $S_0$ | -569.6700 | -570.3035 | 0.83 | 24.6 |
| | $S_1$ | -569.5890 | -570.2300 | 0.82 | 70.7 |
| | $S_2$ | -569.5165 | -570.1717 | 0.81 | 107.3 |
| | $T_1$ | -569.5968 | -570.2332 | 0.82 | 68.7 |
| | $T_2$ | -569.5868 | -570.2233 | 0.82 | 74.9 |
| **TS $S_1$ Pyr 1** | $S_0$ | -569.6658 | -570.2981 | 0.83 | 28.0 |
| | $S_1$ | -569.5910 | -570.2307 | 0.82 | 70.3 |
| | $S_2$ | -569.5446 | -570.1925 | 0.81 | 94.2 |
| | $T_1$ | -569.6004 | -570.2365 | 0.82 | 66.6 |
| | $T_2$ | -569.5937 | -570.2303 | 0.82 | 70.5 |
| **CI $S_1/S_0$ A1** | $S_0$ | -569.5815 | -570.2171 | 0.82 | 78.8 |
| | $S_1$ | -569.5792 | -570.2215 | 0.82 | 76.0 |
| | $S_2$ | -569.4664 | -570.1304 | 0.80 | 133.2 |
| | $T_1$ | -569.5862 | -570.2277 | 0.82 | 72.1 |
| | $T_2$ | -569.5336 | -570.1685 | 0.82 | 109.3 |
| **CI $S_1/S_0$ A2** | $S_0$ | -569.5680 | -570.2043 | 0.82 | 86.9 |
| | $S_1$ | -569.5673 | -570.2134 | 0.82 | 81.1 |
| | $S_2$ | -569.4696 | -570.1331 | 0.80 | 131.5 |
| | $T_1$ | -569.5732 | -570.2179 | 0.82 | 78.3 |
| | $T_2$ | -569.5234 | -570.1599 | 0.82 | 114.7 |
| **CI $S_1/S_0$ B1** | $S_0$ | -569.5769 | -570.2218 | 0.82 | 75.8 |
| | $S_1$ | -569.5768 | -570.2136 | 0.82 | 81.0 |
| | $S_2$ | -569.4544 | -570.1222 | 0.80 | 138.4 |
| | $T_1$ | -569.5826 | -570.2259 | 0.82 | 73.3 |
| | $T_2$ | -569.5262 | -570.1622 | 0.82 | 113.2 |
| **CI $S_1/S_0$ B2** | $S_0$ | -569.5755 | -570.2197 | 0.82 | 77.2 |
| | $S_1$ | -569.5709 | -570.2072 | 0.82 | 85.0 |

| | | | | | |
|---|---|---|---|---|---|
| | $S_2$ | -569.4848 | -570.1428 | 0.81 | 125.4 |
| | $T_1$ | -569.5804 | -570.2239 | 0.82 | 74.6 |
| | $T_2$ | -569.5356 | -570.1718 | 0.82 | 107.2 |
| **ISC $T_2/S_1$ A1** | $S_0$ | -569.6606 | -570.2938 | 0.82 | 30.7 |
| | $S_1$ | -569.5938 | -570.2335 | 0.82 | 68.5 |
| | $S_2$ | -569.5402 | -570.1881 | 0.81 | 97.0 |
| | $T_1$ | -569.6018 | -570.2374 | 0.82 | 66.1 |
| | $T_2$ | -569.5962 | -570.2323 | 0.82 | 69.2 |
| **ISC $T_2/S_1$ A2** | $S_0$ | -569.6679 | -570.3009 | 0.83 | 26.2 |
| | $S_1$ | -569.5889 | -570.2288 | 0.82 | 71.5 |
| | $S_2$ | -569.5349 | -570.1858 | 0.81 | 98.5 |
| | $T_1$ | -569.5962 | -570.2316 | 0.82 | 69.7 |
| | $T_2$ | -569.5923 | -570.2288 | 0.82 | 71.4 |
| **ISC $T_2/S_1$ B1** | $S_0$ | -569.6378 | -570.2699 | 0.83 | 45.7 |
| | $S_1$ | -569.5903 | -570.2276 | 0.82 | 72.2 |
| | $S_2$ | -569.5475 | -570.1916 | 0.81 | 94.8 |
| | $T_1$ | -569.5993 | -570.2337 | 0.82 | 68.4 |
| | $T_2$ | -569.5914 | -570.2261 | 0.82 | 73.2 |
| **ISC $T_2/S_1$ B2** | $S_0$ | -569.6582 | -570.2916 | 0.82 | 32.1 |
| | $S_1$ | -569.5923 | -570.2318 | 0.82 | 69.6 |
| | $S_2$ | -569.5412 | -570.1894 | 0.81 | 96.2 |
| | $T_1$ | -569.6004 | -570.2359 | 0.82 | 67.0 |
| | $T_2$ | -569.5959 | -570.2320 | 0.82 | 69.5 |
| **Min $T_1$ A1** | $S_0$ | -569.6662 | -570.2994 | 0.83 | 27.1 |
| | $S_1$ | -569.5947 | -570.2349 | 0.82 | 67.6 |
| | $S_2$ | -569.5334 | -570.1838 | 0.81 | 99.7 |
| | $T_1$ | -569.6031 | -570.2392 | 0.82 | 64.9 |
| | $T_2$ | -569.5955 | -570.2320 | 0.82 | 69.4 |
| **Min $T_1$ A2** | $S_0$ | -569.6529 | -570.2872 | 0.83 | 34.8 |
| | $S_1$ | -569.5895 | -570.2316 | 0.82 | 69.7 |
| | $S_2$ | -569.4963 | -570.1635 | 0.79 | 112.5 |
| | $T_1$ | -569.5994 | -570.2362 | 0.82 | 66.8 |
| | $T_2$ | -569.5789 | -570.2138 | 0.82 | 80.9 |
| **Min $T_1$ A3** | $S_0$ | -569.6619 | -570.2946 | 0.83 | 30.2 |
| | $S_1$ | -569.5944 | -570.2349 | 0.82 | 67.6 |
| | $S_2$ | -569.5317 | -570.1837 | 0.81 | 99.7 |
| | $T_1$ | -569.6034 | -570.2409 | 0.82 | 63.9 |
| | $T_2$ | -569.5889 | -570.2245 | 0.82 | 74.2 |
| **Min $T_1$ B1** | $S_0$ | -569.6608 | -570.2931 | 0.83 | 31.1 |
| | $S_1$ | -569.5940 | -570.2332 | 0.82 | 68.7 |
| | $S_2$ | -569.5356 | -570.1868 | 0.81 | 97.8 |
| | $T_1$ | -569.6030 | -570.2386 | 0.82 | 65.3 |
| | $T_2$ | -569.5914 | -570.2270 | 0.82 | 72.6 |
| **Min $T_1$ B2** | $S_0$ | -569.6579 | -570.2917 | 0.83 | 32.0 |
| | $S_1$ | -569.5930 | -570.2333 | 0.82 | 68.6 |
| | $S_2$ | -569.5380 | -570.1876 | 0.81 | 97.3 |
| | $T_1$ | -569.6027 | -570.2396 | 0.82 | 64.7 |
| | $T_2$ | -569.5923 | -570.2290 | 0.82 | 71.4 |
| **Min $T_1$ B3** | $S_0$ | -569.6497 | -570.2839 | 0.83 | 36.9 |
| | $S_1$ | -569.5880 | -570.2307 | 0.82 | 70.3 |
| | $S_2$ | -569.4946 | -570.1628 | 0.80 | 112.9 |
| | $T_1$ | -569.5984 | -570.2357 | 0.82 | 67.2 |
| | $T_2$ | -569.5745 | -570.2085 | 0.83 | 84.2 |
| **TS $T_1$ A1** | $S_0$ | -569.6458 | -570.2794 | 0.83 | 39.7 |
| | $S_1$ | -569.5889 | -570.2310 | 0.82 | 70.1 |
| | $S_2$ | -569.4961 | -570.1637 | 0.80 | 112.3 |

| | | | | | |
|---|---|---|---|---|---|
| | $T_1$ | -569.5986 | -570.2359 | 0.82 | 67.0 |
| | $T_2$ | -569.5720 | -570.2054 | 0.83 | 86.2 |
| **TS $T_1$ A2** | $S_0$ | -569.6689 | -570.3021 | 0.83 | 25.5 |
| | $S_1$ | -569.5892 | -570.2295 | 0.82 | 71.0 |
| | $S_2$ | -569.5285 | -570.1812 | 0.81 | 101.3 |
| | $T_1$ | -569.5969 | -570.2327 | 0.82 | 69.0 |
| | $T_2$ | -569.5909 | -570.2277 | 0.82 | 72.1 |
| **TS $T_1$ A3** | $S_0$ | -569.6617 | -570.2956 | 0.83 | 29.6 |
| | $S_1$ | -569.5870 | -570.2294 | 0.82 | 71.1 |
| | $S_2$ | -569.5046 | -570.1695 | 0.80 | 108.7 |
| | $T_1$ | -569.5968 | -570.2340 | 0.82 | 68.2 |
| | $T_2$ | -569.5789 | -570.2140 | 0.82 | 80.8 |
| **TS $T_1$ B1** | $S_0$ | -569.6608 | -570.2934 | 0.83 | 30.9 |
| | $S_1$ | -569.5939 | -570.2334 | 0.82 | 68.6 |
| | $S_2$ | -569.5373 | -570.1882 | 0.81 | 97.0 |
| | $T_1$ | -569.6031 | -570.2391 | 0.82 | 65.0 |
| | $T_2$ | -569.5919 | -570.2279 | 0.82 | 72.0 |
| **TS $T_1$ B2** | $S_0$ | -569.6470 | -570.2804 | 0.83 | 39.1 |
| | $S_1$ | -569.5889 | -570.2308 | 0.82 | 70.2 |
| | $S_2$ | -569.4981 | -570.1655 | 0.80 | 111.2 |
| | $T_1$ | -569.5982 | -570.2356 | 0.82 | 67.2 |
| | $T_2$ | -569.5719 | -570.2056 | 0.83 | 86.0 |
| **TS $T_1$ B3** | $S_0$ | -569.6696 | -570.3035 | 0.83 | 24.6 |
| | $S_1$ | -569.5887 | -570.2303 | 0.82 | 70.5 |
| | $S_2$ | -569.5131 | -570.1698 | 0.81 | 108.5 |
| | $T_1$ | -569.5970 | -570.2338 | 0.82 | 68.3 |
| | $T_2$ | -569.5857 | -570.2226 | 0.82 | 75.3 |
| **ISC $T_1/S_0$ A1** | $S_0$ | -569.5847 | -570.2198 | 0.82 | 77.1 |
| | $S_1$ | -569.5798 | -570.2238 | 0.82 | 74.6 |
| | $S_2$ | -569.4695 | -570.1323 | 0.80 | 132.0 |
| | $T_1$ | -569.5866 | -570.2281 | 0.82 | 71.9 |
| | $T_2$ | -569.5365 | -570.1717 | 0.82 | 107.3 |
| **ISC $T_1/S_0$ A2** | $S_0$ | -569.5764 | -570.2150 | 0.82 | 80.1 |
| | $S_1$ | -569.5706 | -570.2159 | 0.82 | 79.6 |
| | $S_2$ | -569.4745 | -570.1375 | 0.80 | 128.8 |
| | $T_1$ | -569.5771 | -570.2224 | 0.82 | 75.5 |
| | $T_2$ | -569.5282 | -570.1655 | 0.82 | 111.2 |
| **ISC $T_1/S_0$ B1** | $S_0$ | -569.5815 | -570.2170 | 0.82 | 78.9 |
| | $S_1$ | -569.5775 | -570.2211 | 0.82 | 76.3 |
| | $S_2$ | -569.4636 | -570.1280 | 0.80 | 134.7 |
| | $T_1$ | -569.5830 | -570.2244 | 0.82 | 74.3 |
| | $T_2$ | -569.5345 | -570.1693 | 0.82 | 108.8 |
| **ISC $T_1/S_0$ B2** | $S_0$ | -569.5790 | -570.2160 | 0.82 | 79.5 |
| | $S_1$ | -569.5764 | -570.2181 | 0.82 | 78.2 |
| | $S_2$ | -569.4912 | -570.1488 | 0.81 | 121.7 |
| | $T_1$ | -569.5829 | -570.2257 | 0.82 | 73.4 |
| | $T_2$ | -569.5413 | -570.1772 | 0.82 | 103.8 |
| **Min $S_2$** | $S_0$ | -569.6275 | -570.2568 | 0.83 | 53.9 |
| | $S_1$ | -569.5798 | -570.2157 | 0.82 | 79.7 |
| | $S_2$ | -569.5615 | -570.1995 | 0.82 | 89.8 |
| | $T_1$ | -569.5912 | -570.2244 | 0.82 | 74.2 |
| | $T_2$ | -569.5889 | -570.2223 | 0.82 | 75.5 |
| **CI $S_2/S_1$** | $S_0$ | -569.5762 | -570.1951 | 0.83 | 92.6 |
| | $S_1$ | -569.5501 | -570.1780 | 0.82 | 103.4 |
| | $S_2$ | -569.5496 | -570.1772 | 0.82 | 103.9 |
| | $T_1$ | -569.5685 | -570.1986 | 0.82 | 90.4 |

| | | | | | |
|---|---|---|---|---|---|
| | $T_2$ | -569.5674 | -570.1976 | 0.82 | 91.1 |
| **Min $T_1$ Planar Trans** | $S_0$ | -569.6937 | -570.3243 | 0.83 | 11.5 |
| | $S_1$ | -569.5832 | -570.2236 | 0.82 | 74.7 |
| | $S_2$ | -569.5266 | -570.1795 | 0.81 | 102.4 |
| | $T_1$ | -569.5896 | -570.2256 | 0.82 | 73.5 |
| | $T_2$ | -569.5854 | -570.2225 | 0.82 | 75.4 |
| **Min $T_1$ Planar Cis** | $S_0$ | -569.6914 | -570.3222 | 0.83 | 12.9 |
| | $S_1$ | -569.5827 | -570.2231 | 0.82 | 75.1 |
| | $S_2$ | -569.5308 | -570.1839 | 0.81 | 99.7 |
| | $T_1$ | -569.5889 | -570.2251 | 0.82 | 73.8 |
| | $T_2$ | -569.5887 | -570.2268 | 0.82 | 72.7 |
| **Min $S_1$ A1** | $S_0$ | -569.6644 | -570.3000 | 0.82 | 26.8 |
| | $S_1$ | -569.5909 | -570.2350 | 0.82 | 67.5 |
| | $S_2$ | -569.5318 | -570.1839 | 0.81 | 99.7 |
| | $S_3$ | -569.4139 | -570.0872 | 0.79 | 160.3 |
| | $T_1$ | -569.5944 | -570.2390 | 0.82 | 65.1 |
| | $T_2$ | -569.5887 | -570.2331 | 0.82 | 68.7 |
| | $T_3$ | -569.4568 | -570.1188 | 0.80 | 140.5 |
| | $T_4$ | -569.4477 | -570.1137 | 0.80 | 143.7 |
| **Min $S_1$ A2** | $S_0$ | -569.6504 | -570.2874 | 0.82 | 34.7 |
| | $S_1$ | -569.5875 | -570.2324 | 0.82 | 69.2 |
| | $S_2$ | -569.5010 | -570.1661 | 0.80 | 110.8 |
| | $S_3$ | -569.4512 | -570.1193 | 0.80 | 140.2 |
| | $T_1$ | -569.5914 | -570.2361 | 0.82 | 66.9 |
| | $T_2$ | -569.5747 | -570.2185 | 0.82 | 77.9 |
| | $T_3$ | -569.4865 | -570.1528 | 0.80 | 119.1 |
| | $T_4$ | -569.4261 | -570.0962 | 0.80 | 154.7 |
| **Min $S_1$ A3** | $S_0$ | -569.6585 | -570.2937 | 0.82 | 30.7 |
| | $S_1$ | -569.5916 | -570.2361 | 0.82 | 66.9 |
| | $S_2$ | -569.5281 | -570.1837 | 0.81 | 99.8 |
| | $S_3$ | -569.4402 | -570.1155 | 0.78 | 142.5 |
| | $T_1$ | -569.5960 | -570.2408 | 0.82 | 64.0 |
| | $T_2$ | -569.5815 | -570.2243 | 0.82 | 74.3 |
| | $T_3$ | -569.5024 | -570.1622 | 0.81 | 113.2 |
| | $T_4$ | -569.4154 | -570.0894 | 0.79 | 158.9 |
| **Min $S_1$ B1** | $S_0$ | -569.6576 | -570.2927 | 0.82 | 31.4 |
| | $S_1$ | -569.5906 | -570.2343 | 0.82 | 68.0 |
| | $S_2$ | -569.5349 | -570.1888 | 0.81 | 96.6 |
| | $S_3$ | -569.4336 | -570.1093 | 0.77 | 146.5 |
| | $T_1$ | -569.5948 | -570.2387 | 0.82 | 65.2 |
| | $T_2$ | -569.5846 | -570.2279 | 0.82 | 72.0 |
| | $T_3$ | -569.4995 | -570.1575 | 0.81 | 116.2 |
| | $T_4$ | -569.4173 | -570.0898 | 0.79 | 158.7 |
| **Min $S_1$ B2** | $S_0$ | -569.6628 | -570.2989 | 0.82 | 27.5 |
| | $S_1$ | -569.5903 | -570.2344 | 0.82 | 67.9 |
| | $S_2$ | -569.5315 | -570.1841 | 0.81 | 99.5 |
| | $S_3$ | -569.4200 | -570.0923 | 0.80 | 157.1 |
| | $T_1$ | -569.5937 | -570.2381 | 0.82 | 65.6 |
| | $T_2$ | -569.5890 | -570.2338 | 0.82 | 68.3 |
| | $T_3$ | -569.4530 | -570.1147 | 0.80 | 143.1 |
| | $T_4$ | -569.4485 | -570.1103 | 0.80 | 145.8 |
| **Min $S_1$ B3** | $S_0$ | -569.6498 | -570.2881 | 0.82 | 34.2 |
| | $S_1$ | -569.5853 | -570.2320 | 0.82 | 69.5 |
| | $S_2$ | -569.4930 | -570.1645 | 0.80 | 111.8 |
| | $S_3$ | -569.4545 | -570.1200 | 0.80 | 139.7 |
| | $T_1$ | -569.5893 | -570.2356 | 0.82 | 67.2 |
| | $T_2$ | -569.5717 | -570.2167 | 0.82 | 79.1 |
| | $T_3$ | -569.4892 | -570.1585 | 0.80 | 115.6 |
| | $T_4$ | -569.4191 | -570.0940 | 0.79 | 156.0 |

| | | | | | |
|---|---|---|---|---|---|
| **Min $T_1$ A1** | $S_0$ | -569.6638 | -570.2994 | 0.82 | 27.2 |
| | $S_1$ | -569.5909 | -570.2351 | 0.82 | 67.5 |
| | $S_2$ | -569.5318 | -570.1840 | 0.81 | 99.6 |
| | $S_3$ | -569.4107 | -570.0864 | 0.79 | 160.8 |
| | $T_1$ | -569.5946 | -570.2393 | 0.82 | 64.9 |
| | $T_2$ | -569.5887 | -570.2333 | 0.82 | 68.6 |
| | $T_3$ | -569.4590 | -570.1210 | 0.80 | 139.1 |
| | $T_4$ | -569.4449 | -570.1113 | 0.80 | 145.2 |
| **Min $T_1$ A2** | $S_0$ | -569.6498 | -570.2870 | 0.82 | 34.9 |
| | $S_1$ | -569.5872 | -570.2328 | 0.82 | 68.9 |
| | $S_2$ | -569.4956 | -570.1649 | 0.80 | 111.6 |
| | $S_3$ | -569.4521 | -570.1168 | 0.80 | 141.8 |
| | $T_1$ | -569.5917 | -570.2371 | 0.82 | 66.3 |
| | $T_2$ | -569.5712 | -570.2149 | 0.82 | 80.2 |
| | $T_3$ | -569.4904 | -570.1582 | 0.80 | 115.8 |
| | $T_4$ | -569.4229 | -570.0944 | 0.80 | 155.8 |
| **Min $T_1$ A3** | $S_0$ | -569.6585 | -570.2942 | 0.82 | 30.4 |
| | $S_1$ | -569.5913 | -570.2365 | 0.82 | 66.6 |
| | $S_2$ | -569.5306 | -570.1859 | 0.81 | 98.4 |
| | $S_3$ | -569.4356 | -570.1128 | 0.77 | 144.3 |
| | $T_1$ | -569.5966 | -570.2420 | 0.82 | 63.2 |
| | $T_2$ | -569.5815 | -570.2251 | 0.82 | 73.8 |
| | $T_3$ | -569.4992 | -570.1589 | 0.81 | 115.3 |
| | $T_4$ | -569.4165 | -570.0898 | 0.79 | 158.7 |
| **Min $T_1$ B1** | $S_0$ | -569.6576 | -570.2927 | 0.82 | 31.4 |
| | $S_1$ | -569.5906 | -570.2343 | 0.82 | 68.0 |
| | $S_2$ | -569.5349 | -570.1888 | 0.81 | 96.6 |
| | $S_3$ | -569.4336 | -570.1093 | 0.77 | 146.5 |
| | $T_1$ | -569.5965 | -570.2399 | 0.82 | 64.5 |
| | $T_2$ | -569.5858 | -570.2288 | 0.82 | 71.5 |
| | $T_3$ | -569.4962 | -570.1580 | 0.80 | 115.9 |
| | $T_4$ | -569.4072 | -570.0752 | 0.80 | 167.8 |
| **Min $T_1$ B2** | $S_0$ | -569.6552 | -570.2916 | 0.82 | 32.1 |
| | $S_1$ | -569.5898 | -570.2340 | 0.82 | 68.2 |
| | $S_2$ | -569.5361 | -570.1885 | 0.81 | 96.7 |
| | $S_3$ | -569.4063 | -570.0792 | 0.77 | 165.4 |
| | $T_1$ | -569.5956 | -570.2405 | 0.82 | 64.1 |
| | $T_2$ | -569.5850 | -570.2297 | 0.82 | 70.9 |
| | $T_3$ | -569.4625 | -570.1214 | 0.81 | 138.9 |
| | $T_4$ | -569.4358 | -570.1020 | 0.80 | 151.1 |
| **Min $T_1$ B3** | $S_0$ | -569.6473 | -570.2841 | 0.82 | 36.8 |
| | $S_1$ | -569.5865 | -570.2321 | 0.82 | 69.4 |
| | $S_2$ | -569.4921 | -570.1634 | 0.80 | 112.5 |
| | $S_3$ | -569.4500 | -570.1048 | 0.81 | 149.3 |
| | $T_1$ | -569.5913 | -570.2365 | 0.82 | 66.7 |
| | $T_2$ | -569.5665 | -570.2086 | 0.82 | 84.1 |
| | $T_3$ | -569.4972 | -570.1660 | 0.80 | 110.9 |
| | $T_4$ | -569.4186 | -570.0920 | 0.79 | 157.3 |

# Chapter 14. General tools for constrained geometry optimizations

## 14.1. Introduction

Constrained geometry optimizations are essential tools in the investigation of potential energy surfaces (PES). Whereas the standard (i.e. unconstrained) optimizations of stationary points (e.g. equilibrium and transition structures) on the PES are considered trivial tasks, constrained geometry optimizations represent more complex numerical problems. For a survey of currently established methods see ref. 231. For certain applications as, for example, the location of a minimum on a hypersphere (e.g. used for mapping steepest descent paths)[232] or of an equilibrium structure in an intersection subspace between two or more PESs, these are numerically demanding,[233] and efficient implementations are, thus, very desirable.

Usually, constrained geometry optimizations are based on variations of the Lagrange multiplier method.[233-235] Here the space is extended form 3n-6(5) to 3n-6(5)+m, where n is the number of atoms and m is the number of constraints. For each constraint the Hessian of the Lagrangian will carry a negative eigenvalue. However, when locating a minimum energy crossing points (MECP) along PES intersection subspaces,[233,234] the method of the Lagrange multipliers is often impractical. The ultimate reason for the failure of this method are the difficulties in handling the Hessian. In fact:

1) the separation of the space into the constraint subspace and the disjoint subspace, in which the optimization is done, is defined implicitly by the eigenvectors of the Hessian of the Lagrangian, and
2) the so-called Broyden-Fletcher-Goldfarb-Shanno (BFGS)[236] Hessian update method cannot be exploited.

The first matter is under control in standard optimization with geometrical constraints, since here the second derivative of the constraint with respect to the internal coordinates can be computed without much effort. However, in the location of a MECP, the computation of second order derivative would be an unpractical and expensive procedure. Hence, constrained optimizations to locate MECP are performed with approximate Hessians in combination with Hessian update methods.

An alternative to the Lagrange multiplier method was proposed by Bearpark et al.[89] In this approach, the so-called "direct" approach, the subspace of the constraint is identified to first order and treated separately from the rest of the optimization. However, the minimization is still performed in the full space in combination with projection operators. The major advantage of the "direct" approach is that the definition of the subspace of the constraint is not implicitly defined by the Hessian of the Lagrangian but rather from the gradient of the constraints with respect to the nuclear displacements.

Recently Anglada and Bofill[237] demonstrated in an elegant paper the connection between the "direct" approach and that of the Lagrange multiplier approach. They demonstrate that the Lagrange multiplier method can, by a simple linear transformation, be recast into *one subspace of the constraint (of dimension m) and one subspace (of dimension 3n-6(5)-m) in which a*

*minimization is performed*. *The later is guaranteed to have a positive definite Hessian*. Hence, it combines the advantage of space subdivision, as suggested by the so-called direct approach, with a conventional minimization in combination with a BFGS Hessian update procedure. In the paper of Anglada and Bofill the method was implemented in the semiempirical program package AMPAC[238]. The method was assessed in combination with the AM1 Hamiltonian[239] using a reduced-restricted-quasi-Newton-Raphson method and explicit line-search techniques.

The combination of general geometrical constraints with optimizations in Cartesian internal coordinates is trivial.[240] A scheme for constrained optimizations in conjunction with curvilinear internal coordinates has been suggested by Baker et al.[241] However, this scheme requires that the geometrical constraints are included in the space of the redundant internal coordinates. It would be of advantage if the constraint could be excluded from this space since the constraint seldom qualifies to be view as a natural internal coordinate. However, both of these procedures have became more in demand over the last decade and the theory has accordingly developed.

In this Chapter the method of Anglada and Bofill will be explored, in combination with the Rational Function approach[242] and no line-search techniques. The method will be assessed at the state average CASSCF level of theory and in combination with force-constant weighted redundant internal coordinates as implemented in the MOLCAS 6.0 quantum chemistry program package.[243] Some further modifications of the approach will be suggested and it will be demonstrated how general constraints can be treated in combination with curvilinear internal coordinates without the explicit inclusion of the geometrical constraint in the subspace of the redundant internal coordinates. In particular, it will be presented *a scheme to optimize the crossing point*

*geometrically nearest to a given structure*, that in the future will be, hopefully, made automatic and more general.

## 14.2. Method

This section is subdivided into three part. The first part reviews and modifies the projected constrained optimization (PCO) method of Anglada and Bofill. This is followed by an explicit description of the presented implementation, in combination with a Rational Function optimization RFO and no linesearch. Finally, the last subsection describes the tools needed for combining arbitrary geometrical constraints with curvilinear internal coordinates.

### 14.2.1. The PCO Approach by Anglada and Bofill

The constrained geometry optimization using the Lagrange multiplier method is formulated as a minimization of the expression

$$\mathrm{L}(\mathrm{q},\lambda) = \mathrm{E}(q) - \lambda^{\mathrm{T}} r(q) \qquad (14\text{–}1)$$

where $E$ is the energy to be minimized with respect to the constraints r(**q**), and λ is the vector with the so-called Lagrange multipliers. A Taylor expansion to 2$^{nd}$ order of $L(\mathbf{q},\lambda)$ around $\mathbf{q}_0$ and $\lambda_0$ gives

$$L(q_0 + \Delta q, \lambda_0 + \Delta\lambda) = E(q_0) + \Delta q^T \frac{\partial E(q_0)}{\partial q} + \tfrac{1}{2}\Delta q^T W \Delta q - \lambda^T (r(q_0) + \frac{\partial r(q_0)}{\partial q}\Delta q) \quad (14\text{–}2)$$

Where W is defined as

$$W(q, \lambda_0) = \frac{\partial^2 E(q_0)}{\partial q^2} - \sum_{i=1,m} (\lambda_0)_i \frac{\partial^2 (r(q_0))_i}{\partial q^2} \quad (14\text{–}3)$$

This sets up the equation for the generalized elimination method.[231,244] One can note that the 2nd term of the RHS in Equation. 14-2 controls to first order the constraint. In the subspace which fulfill the constraint any displacement Δq must be such that

$$\frac{\partial r(q_0)}{\partial q}\Delta q = 0 \quad (14\text{–}4)$$

This defines a linear transformation which will to first order subdivide the original 3n-6(5) space into a m-dimensional space in which the constraints are fulfilled and a 3n-6(5)-m subspace in which a normal optimization is made. The unitary transformation matrix T contains two part and transform as

$$\Delta q = [T_c T_m]\begin{pmatrix} \Delta y \\ \Delta x \end{pmatrix} = T_c \Delta y + T_m \Delta x \quad (14\text{–}5)$$

where, y and x are the new parameters. y is of m dimensions and x of 3n-6(5)-m dimension. In particular one can note that at $\lambda_0$

$$\frac{\partial r(q_0)}{\partial q} T_c \neq 0 \qquad (14\text{–}6)$$

and

$$\frac{\partial r(q_0)}{\partial q} T_m = 0 \qquad (14\text{–}7)$$

These two equations are sufficient for the definition of T via a Gram-Schmidt procedure.[a]

One can proceed by introducing the transformation matrix into the Lagrangian expression (Equation. 14-2). The equation now splits into two parts (one of m and a second of 3n-6(5)m dimensions), one of which depends only on y,

$$\Delta y = -\left( \frac{\partial r(q_0)}{\partial q} T_c \right)^{-1} r(q_o) \qquad (14\text{–}8)$$

and a second part that depends on both x and y,

[a] By the way, note that Anglada and Bofill state that $\frac{\partial r(q_0)}{\partial q} T_c = \mathrm{I}$, that is obviously wrong.

$$Q(q_0+\Delta q,\lambda) = E(q_0) + \Delta y^T T_c^T \frac{\partial E(q_0)}{\partial q} + \tfrac{1}{2}\Delta y^T T_c^T W T_c \Delta y + \Delta x^T T_m^T \left( \frac{\partial E(q_0)}{\partial q} + W T_c \Delta y \right) + \tfrac{1}{2}\Delta x^T T_m^T W T_m \Delta x \qquad (14\text{–}9)$$

This equation is the projected energy expression, with $T_m^T W T_m$ being the reduced Hessian and $T_m^T \left( \frac{\partial E(q_0)}{\partial q} + W T_c \Delta y \right)$ is the reduced gradient. Solving Equation. 14-8 and substituting the result into Equation. 14-9 one minimizes *Q* with respect to Δx. The minimization of Equation. 14-9 can be done with any standard optimization technique. At convergence the solution to the Lagrangian in Equation. 14-1 is found.

Using the quasi-Newton condition applied to Equation. 14-1 one finds that the effective gradient to be used in an Hessian update procedure applied only to the molecular part of the Lagrangian Hessian is

$$h(q,\lambda) = \frac{\partial E(q)}{\partial q} - \frac{\partial r(q)}{\partial q}\lambda \qquad (14\text{–}10)$$

The update procedure is commenced by evaluating a series of $h(q,\lambda)$ for different values of q and a fixed value of λ. A suitable value of λ is the first order estimate of λ at convergence as given by

$$h(q_0,\lambda_0) = 0 \qquad (14\text{–}11)$$

To conclude the presentation of the PCO approach of Anglada and Bofill let us here summarize the major advantages of the presented method, compared to a optimization/maximization procedure applied to Equation. 14-1:

- the PCO approach have an explicit separation of the two subspaces, while an optimization/maximization indirectly separates the two subspaces by identifying the positive and negative eigen vectors of the Hessian of the Lagrangian,
- the presence of negative eigen values in the Hessian of the Lagrangian restricts the selection of Hessian update (variable metric) methods while the PCO approach allows the use of the BFGS update method to be applied to the reduced Hessian, and
- the technique by Bofill and Anglada does not explicitly require $\lambda$ to be determined.

In particular the first point is of importance since it allows to perform constrained optimization in cases where one can't or wouldn't like to compute explicit $2^{nd}$ derivatives of the constraints with respect to nuclear displacement. One such important case is in the search of a minimum energy cross point (MECP) on the search of a (conical) intersection.

### 14.2.2. An RFO Implementation without Line-search

This section will present an implementation of the PCO approach in combination with Rational Function optimization and a back-feed mechanism rather than a line-search.

For a given $q_0$ and a maximum step length of β, set $k=1$, $y_\beta=1$, $g_\beta=1$, $x_\beta=1$, $dy=\beta$, $g=\beta$ and $dx=\beta$.

(1) Compute $E(q_k)$, $\frac{\partial E(q_k)}{\partial q}$, an empirical estimate of $\frac{\partial^2 E(q_k)}{\partial q^2}$, $r(q_k)$, $\frac{\partial r(q_k)}{\partial q}$, and $\frac{\partial^2 r(q_k)}{\partial q^2}$.

(2) For $i=1,k$

Evaluate $T(q_i)$, $\Delta y(q_i)$, $\lambda(q_i)$, $x(q_i)$, $\Delta x(q_i)$ and the reduced gradient, $g_r(q_i)$.

If $dy < 0.75|\Delta y|$ or $|\Delta y| < 1.0\cdot 10^{-2}$

set $y_\beta = \min(2, y_\beta \times \sqrt{2})$

Else if $dy > 1.25|\Delta y|$ and $dy \geq 1.0\cdot 10 - 5$

set $y_\beta = \max(1/10, y_\beta / \sqrt{2})$

Set $dy = |\Delta y|$

and

If $i \neq k$

If $dx < |\Delta x|$ and $|\Delta x| < \beta$

set $x_\beta = \min(1, x\beta \times \sqrt{2})$

Else if $dx > 1.25|\Delta x|$ or $dx \geq \beta$

set $x_\beta = \max(1/5, x_\beta / \sqrt{2})$

Set $dx = |\Delta x|$

and

If $g < 0.75|g_r|$ and $g < \beta$

set $g_\beta = \min(1, g_\beta \times \sqrt{2})$

Else if $g > 1.25|g_r|$ or $g \geq \beta$

set $g_\beta = \max(1/5, g_\beta / \sqrt{2})$

Set $g = |g_r|$.

(3) For $i = 1, k$

Evaluate $h(q_i, \lambda_k)$ as expressed by Equation. 14-10.

(4) Compute W and update the BFGS procedure.

(5) Assemble the reduced Hessian according to Equation. 14-9.

(6) Minimize Q with respect to $\Delta x(q_k)$ with RFO in association with a step restriction of $\beta \times \max(y_\beta \times \min(x_\beta, g_\beta), \frac{1}{10})$.

(7) Evaluate $\Delta q(q_k)$ from $\Delta y(q_k)$ and $\Delta x(q_k)$.

(8) If not converged, set $k = k + 1$ and go to (1).

The design of this scheme has a major objective to give priority to the constraints condition over the overall minimization procedure. Once the constraints are fulfilled, the algorithm will protect this condition. The implemented method was tailored in order to achieve a better convergence on some test cases. Mainly, this refinement consisted in tuning the parameters relative to the components of the step length of the two sub-spaces.

### 14.2.3. Derivatives of the Constraints

Constrained geometry optimization require 1st and 2nd order derivatives of the constraints with respect to the coordinates. This is trivial for Cartesian coordinates. For curvilinear coordinates Baker et al[241] suggested to include the constraints in the definition of the redundant internal coordinate space, followed by a linear transformation after the generation of the non-redundant coordinates, such that the constraint equals on the non-redundant coordinates. This section presents the required derivatives for the case when the constraints not necessarily are explicitly expressed in the redundant space of internal coordinates.

Given

$$\frac{\partial}{\partial x} = \frac{\partial}{\partial q}\frac{\partial q}{\partial x} \tag{14–12}$$

The 1st order derivatives is trivially expressed as

$$\frac{\partial r}{\partial q} = \left(\frac{\partial q}{\partial x}\right)^{-1}\frac{\partial r}{\partial x} \tag{14–13}$$

And the 2nd derivative is expressed as

$$\frac{\partial^2 r}{\partial q^2} = \left(\frac{\partial q}{\partial x}\right)^{-1}\left[\frac{\partial^2 r}{\partial x^2} - \frac{\partial r}{\partial q}\frac{\partial^2 q}{\partial x^2}\right]\left(\frac{\partial q}{\partial x}\right)^{-1} \tag{14–14}$$

## 14.3. Results and Discussion

This section evaluates the efficiency of the method, with respect to single and multiple geometrical constraint optimizations, optimizations on hyperspheres applied to the mapping of Minimum Energy Paths MEPs (i.e. steepest descent paths, see Chapter 6), and location of MECP. A detailed analysis of the application of multiple constraints of different nature will be given.

### 14.3.1. Single Geometrical Constraint Optimization

As an example of a geometry optimization with a single geometrical constraint, one can study the energy profile of the rotation of ethene (see Figure 14–1). In this series of optimizations the $H_ACCH_C$ dihedral angle is fixed, i.e. the constraint is

$$r_1 = \phi_{H_ACCH_C} - \phi^0_{H_ACCH_C} \qquad (14\text{–}15)$$

On the average, the optimizations converge after 6 iterations for each selected angle.

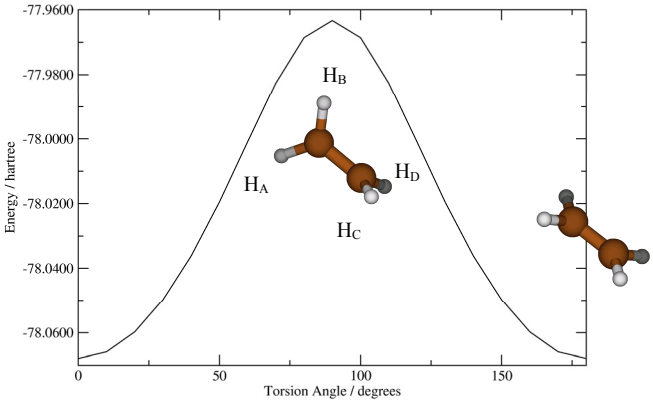


Figure 14–1: $C_2H_4$ hindered internal rotation

### 14.3.2. Multiple Geometrical Constraints Optimizations

The energy surface of the triplet 1,2-dioxoethane around the biradical minimum as a function of the OO bond distance and the OCCO dihedral angle is presented in this section, as an example of geometry optimization with multiple geometrical constraints (see Figure 14–2)., In this case the constraints are

$$r_1 = r_{OO} - r_{OO}^0 \tag{14–16}$$

and

$$r_2 = \phi_{OCCO} - \phi_{OCCO}^0 \tag{14–17}$$

The optimizations typically converge after 5 iterations for each selected pair of constraints.

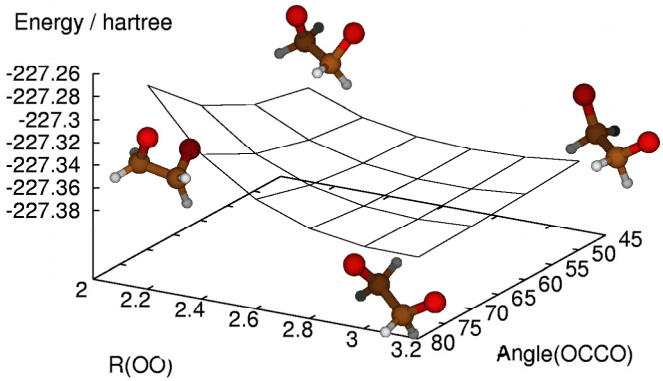


Figure 14–2: The potential energy surface of triplet 1,2-dioxetane as a function of the OO bond distance (Angstrom) and the OCCO dihedral angle (degrees).

### 14.3.3. Minimum Energy Path Optimizations

Minimum energy path (MEP) can be located by minimizing the energy on an hyperspheric cross-section of the PES with a fixed radius, and with the origin placed at some reference structure, usually chosen to be the optimised structure of a previous step. If one starts from a TS a full reaction path can be constructed by following the forward and reverse direction defined by the transition vector. If mass-weighted coordinates R(q) are used, such path yields the Intrinsic Reaction Coordinate (IRC) (see Section 4.3):

$$R(q) = \left(\sqrt{m_1} r_1(q), \sqrt{m_2} r_2(q), ..., \sqrt{m_n} r_n(q)\right) \qquad (14\text{–}18)$$

For this purpose the constraint is defined as

$$r_1 = \frac{\left(\sqrt{R(q) - R(q_{ref})}\right)^2 - R}{\sqrt{M_{tot}}} \qquad (14\text{–}19)$$

where R is the radius of the hypersphere and $M_{tot}$ is the total mass of the system.

As an example, this section analyzes 1,2-dioxoethane (see Figure 14–3) as it is dropped on the triplet state surface at a geometry close to the singlet transition state between the cyclic and biradical structure. The individual optimizations typically takes 7 iterations.

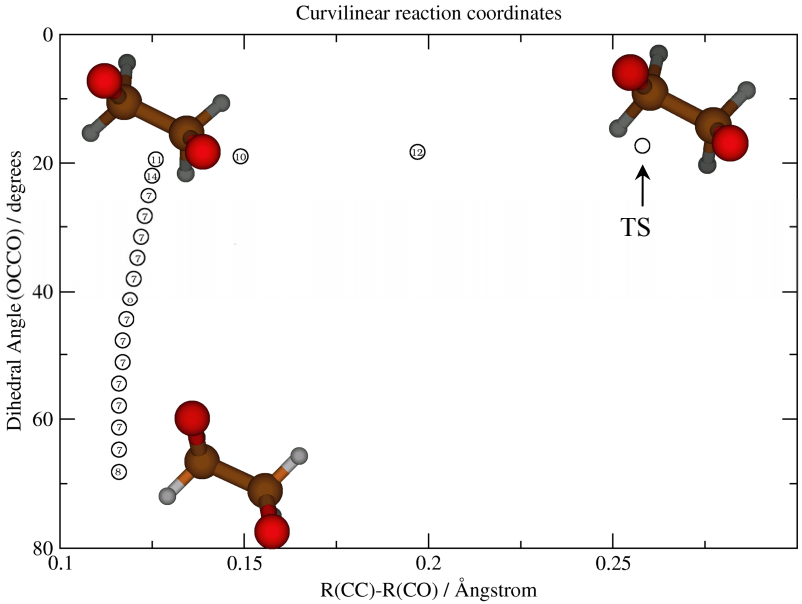


Figure 14–3: The minimum energy path of 1,2-dioxoethane on the triplet state surface starting at a geometry close to the singlet transition state.

### 14.3.4. Minimum Energy Cross Point Optimizations

A MECP is located by finding the lowest energy of the excited state (e.g. $E_1$) at which it is degenerate with a lower state (e.g. $E_0$). The constraint is the energy difference between the two states:

$$r = E_1 - E_0 \tag{14–20}$$

This section provides the results of the search for an intersection between the $^3$A and $^1$A state of *N*-methylthioacetamide.

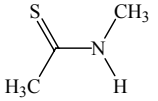


*N*-methylthioacetamide

The progression of the excited state energy ($E_1$) and of the energy difference ($E_1$-$E_0$), as a function of the number of iteration (Figure 14–4), display a fast convergence (in about five iterations, both energy difference and excited state energy are nearly at the final value). NMTAA was chosen as a test molecule for calculating MECP because, as reported in Section 13.4.2, other methods failed to obtain fully optimized singlet/triplet crossings of this molecule.

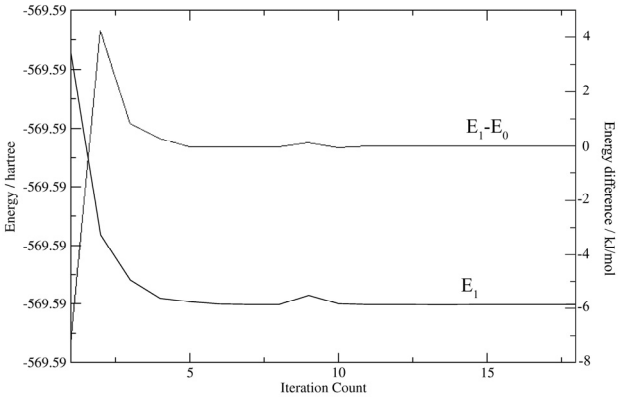


Figure 14–4: The excited triplet state energy of *N*-methylthioacetamide (indicated as $E_1$, see text) and the energy difference (indicated as $E_1$-$E_0$, see text) as a function of the iteration count during the MECP optimization.

### 14.3.5. Multiple Heterogeneous Constraints: MECP on a Hypersphere Optimizations

*The ultimate target of the present test is to find the crossing point geometrically closest to a given structure*. In order to achieve this target, energy difference between states of different spin multiplicity and the value of the geometrical distance from a given structure were used as constraints for a series of computations. Acrolein was chosen as test molecule, being a simple unsaturated carbonyl compound, with a considerable experimental and theoretical interest.[245,246] In this context, the used reference structure corresponds to the optimized planar minimum of the fundamental triplet state, that has got a $^3$n-π* nature. Thus, the main target would be to establish the structure and energy of the crossing point closest to the reference. All calculations were performed at the CASSCF level of theory with a minimum (6 electrons in 5 orbitals) active space comprising the π orbitals and one of the oxygen lone pairs, using the 6-31g* basis set.

First, an optimization of the minimum energy crossing point (MECP)[233] was performed, following the method described in section 14.3.4. The optimization yielded a structure located 7 kcal mol$^{-1}$ below the reference, that shows a twist of 93.3° degrees around the C=C bond, a lengthening of C=C and C-C bonds and shortening of the C=O bond, with respect to the reference structure. Moreover, such MECP connects the $^3$π-π* potential energy surface to that of the singlet ground state, and it is not related to the $^3$n-π* state.

The $T_1/S_0$ crossing point nearest (NCP) to the $T_1$ planar minimum is located by performing a series of minimizations in presence of two constraints. The

correspond to the constraints applied in previous Sections 14.3.3 and 14.3.4. As seen in these sections, the constraints can be defined as:

$$r_1 = E_1 - E_0 \tag{14–21}$$

$$r_2 = \frac{\left(\sqrt{R(q) - R(q_{ref})}\right)^2 - R}{\sqrt{M_{tot}}} \tag{14–22}$$

Using the same formalism of the first constraint, Equation. 14-22 can be expressed also as:

$$r_2 = R_1 - R_0\,, \tag{14–23}$$

assuming $R_1$ as the geometrical distance of a structure from the reference one, and $R_0$ as the radius of the hypersphere. The scope of the optimization is that of minimizing $E_1$ while keeping the value of both $r_1$ and $r_2$ equal to zero. One of such optimizations is analyzed in Figure 14–5. As found for NMTAA (see Figure 14–4), about 5 iterations were sufficient to achieve near convergence.

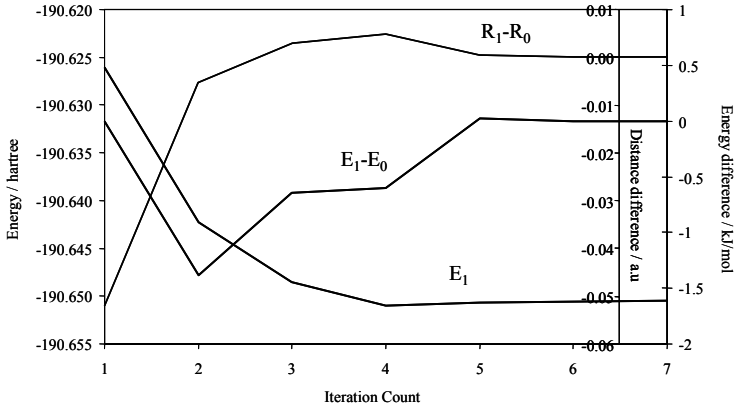


Figure 14–5: Energy of the $^3$n-π* state (indicated as $E_1$, see text), energy difference (indicated as $E_1$-$E_0$, see text) and distance difference from the constrained value as a function of iteration count during the optimization of the point of the $^3$n-π*/$S_0$ seam at 0.35 a.u. from the $T_1$ planar minimum (see Figure 14–6)

In order to find the NCP point, the minimization of $R_0$ was performed "manually", as explained below. *In the future, an algorithm to perform a simultaneous minimization of $E_1$ and $R_0$ will be implemented, to provide a tool to locate, in an unbiased way, the geometrically nearest and lowest energy crossing point to a given structure.*

In other words, given the n-1 dimensional hyperspherical cross section of the PES with a given radius $R_0$, and the n-1 dimensional singlet/triplet crossing space (where n is the number of degrees of freedom), the goal of the search is a structure belonging to the intersection of the two spaces and showing the lowest energy possible. The first optimization was performed with a radius

smaller than the 0.462 a.u. distance of MECP. Then, iteratively, once an optimized geometry with a given distance from the $T_1$ planar minimum was obtained, its structure was used as starting geometry for another calculation with a shorter radius. The procedures was iterated until it was not possible to achieve convergence anymore. In other words, the hyperspherical cross section did not intersect anymore the singlet/triplet crossing space. *The final structure was located 0.228 a.u. far and 108 kcal mol$^{-1}$ higher in energy with respect to the planar minimum, with the geometry parameters reported in Figure 14–6.* As desired, NCP is a $^3$n-$\pi^*$/$S_0$ crossing.

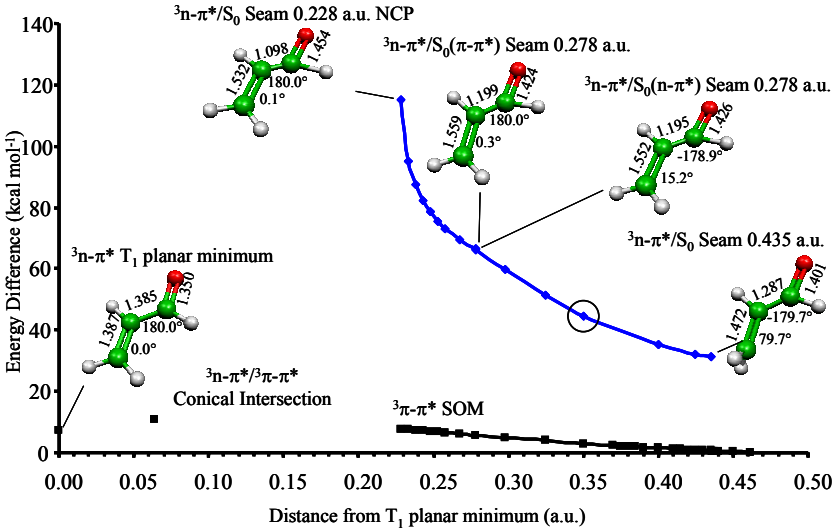


Figure 14–6: Acrolein, $^3$n-π* $T_1$ planar minimum, $^3$n-π*/$S_0$ NCP, $^3$n-π*/$^3$π-π* conical intersection, $^3$n-π*/$S_0$ seam (full diamonds, blue line), $^3$π-π* SOM (series of minima, full squares, black line). All geometrical parameters are in Å and degrees. The optimization of the circled point of the $^3$n-π*/$S_0$ seam at 0.35 a.u. from the $T_1$ planar minimum is the one analysed in Figure 14–5.

The location of the NCP to a given structure is very important when considering a photochemical process. In fact, it can give an idea of the accessibility of a certain crossing seam from a previously optimized minimum or MEP point on the excited state.

### 14.3.6. Mapping the intersection space: $^3$n-π*/$S_0$ seam

The methodology used in Section 14.3.5 can also be used to locate an approximate steepest descent path along the n-1 dimensional $^3$n-π*/$S_0$ intersection space.

Starting from NCP, a series of two constraints (energy difference/hypersphere) optimizations were performed, using the NCP structure as guess geometry, the planar minimum as reference geometry (i.e. the centre of the hypersphere), and setting a hypersphere radius longer than 0.228 a.u. The first optimized structure was then used as starting geometry for another optimization at longer radius and maintaining the planar minimum as reference geometry, in an iterative way. The $^3$n-π*/$S_0$ crossing seam reported in Figure 14–6 was build in this way (blue line).

At the beginning of the seam, the so generated optimized molecular structures are planar, showing only stretching distortions: C=C and C=O lengthening and C-C shortening, with respect to the $T_1$ planar minimum. Around 0.278 a.u. twisting around C=C begins, along with inversion of the stretching movements. Actually, two different structures where found at 0.278 a.u., with nearly degenerate energies. A change in the $S_0$ wave function, from a partial character of π-π* to a partial character of n-π*, is likely at the base of this fact. It could be imagined that the $^1$n-π*/$^1$π-π* seam crosses nearby the located singlet/triplet seam. The $^3$n-π*/$S_0$ seam ends (tentatively) at 0.435 a.u., because at longer distances the optimization switched to a $^3$π-π*/$S_0$ seam, that is lower in energy.

### 14.3.7. Mapping the intersection space: $^3\pi$-$\pi^*/S_0$ seam

The existence of crossing point with $^3\pi$-$\pi^*/S_0$ character (i.e. the MECP documented in Section 14.3.5) located lower in energy than any point of the $^3$n-$\pi^*/S_0$ seam documented in Section 14.3.6 suggests that certain low-energy region of $T_1$ must be dominated by a $\pi$-$\pi^*$ character. This is confirmed by relaxation of the $^3$n-$\pi^*/S_0$ seam point on $T_1$. In fact, a series of minima (SOM) was built performing a $T_1$ minimization over the same hyperspheres (same radius and reference geometry) of the seam (i.e. using the same procedure seen in Section 14.3.4). The resulting points are shown in Figure 14–6 with a black line.

The so obtained $T_1$ SOM represents a sort of bottom of the valley in correspondence of each point along the seam. Remarkably, it was found (via orbital occupancy analysis) that the $T_1$ SOM has a $^3\pi$-$\pi^*$ nature.

The low energy region of the $T_1$ surface showing a $^3\pi$-$\pi^*$ character and regions showing a $^3$n-$\pi^*$ character (as the $^3$n-$\pi^*$ planar minimum in Figure 14–6)must be somehow connected. Indeed, Figure 14–6 also reports the energy of a previously located $^3$n-$\pi^*/^3\pi$-$\pi^*$ conical intersection[246] that surely provides a point of link between these two $T_1$ regions.

The existence of a low lying $^3\pi$-$\pi^*$ region implies the possible existence of an extensive low lying $^3\pi$-$\pi^*/S_0$ seam. The procedure to compute the $^3\pi$-$\pi^*/S_0$ seam was the same as that used to locate NCP. In fact, it was located starting from the structure of MECP and performing iterative two constraints (singlet/triplet energy difference and hyperspherical cross section) minimizations of $E_1$. The seam is divided into two branches, depending if shortening or lengthening of the radius $R_0$ was applied at each step. This

seam is reported in Figure 14–7. The seam branch on the left side of Figure 14–7 (red line) is mainly characterized by the torsion around C=C bond, along with a C=C and C-C lengthening and C=O shortening. Also this seam is reported along with the $T_1$ SOM documented above. As can be seen, between 0.4 a.u. and the MECP the two curves are less than 10 kcal $mol^{-1}$ distant.

The seam branch on the right side of Figure 14–7 (green line) is the extension of the previous one, being still in the $^3\pi$-$\pi^*/S_0$ crossing subspace. The seam is the furtherance of the preceding one also with respect to the geometrical distortions. In fact, bond stretching and C=C torsion continue. In addiction to these distortions, there is also a torsion around the C-C bond, which leads to quite distorted structures. Notice the SOM curve and the right branch go along nearly in parallel and close to each other, being the energy difference between them never more than 1.5 kcal $mol^{-1}$. The point of the SOM at 0.490 a.u. from the $T_1$ planar minimum has the lowest energy of all the computed structures. The energies of all structures reported in this section were calculated as difference with respect to that of this structure.

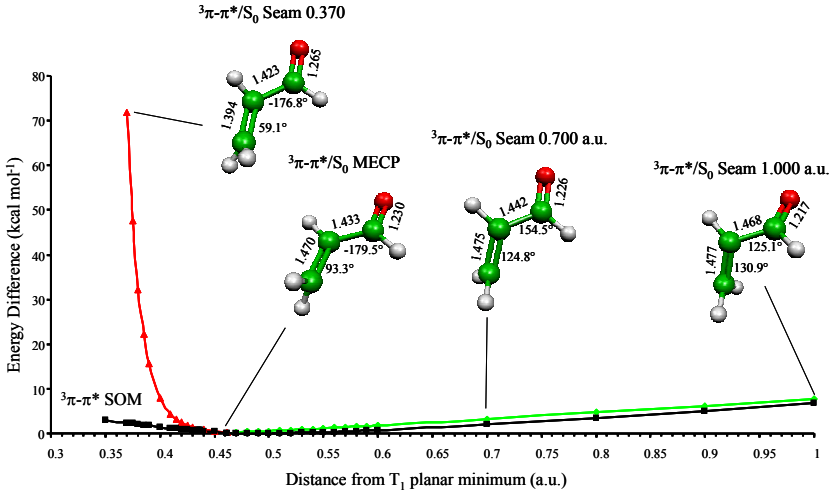


Figure 14–7: Acrolein, $^3\pi$-$\pi^*$/$S_0$ seam (full triangles, red line plus full diamonds, green line) and $^3\pi$-$\pi^*$ SOM. All geometrical parameters are in Å and degrees.

Energy difference shouldn't be the only thing to look at when comparing seams and minima. In fact, geometrical differences provide information on which vibrational mode should be populated to reach the seam from the $T_1$ valley. Thus, geometrical distances were estimated between points of the computed seams and SOMs at the same distance from the $T_1$ planar minimum, even if SOM doesn't rigorously correspond to a MEP. The results are summarized in Figure 14–8. The seams, as well as the SOM, follow the same colouring/symbol as in Figure 14–6 and Figure 14–7. The distance from the $T_1$ planar minimum is reported on the X Axis; the distance of the seam's point from the corresponding SOM's point is given on the Y Axis. The energy difference is on Z Axis. The projection on the XY plane is also reported. As can be seen, being close in energy doesn't imply being close

geometrically. Likely, only a small portion of the seam around the MECP could be vibronically accessible at room temperature from the $T_1$ state. A quantification of this amount, along with quantistic effects contribution treatment, would require a more rigorous and expensive procedure, and is out of the scope of this thesis.

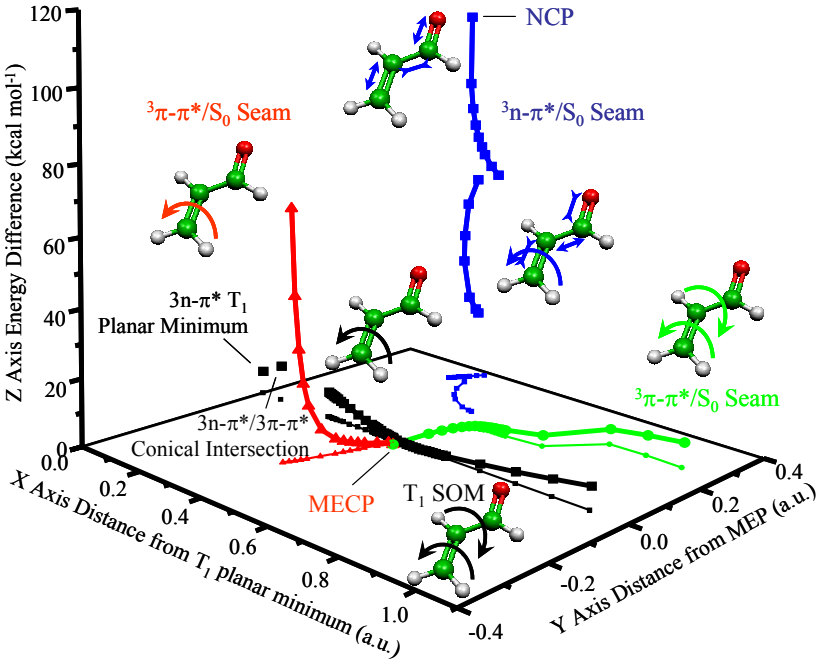


Figure 14–8: Acrolein, general view of the calculated seams, with relative distance from the corresponding points of the SOM. Arrows on the molecular structures represent the main movement characterizing each branch of the seams or the SOM.

## 14.4. Conclusions

A modified algorithm based on the approach of Anglada and Bofill has been implemented and tested. The results indicate that such implementation can be used with success in different cases of constrained geometry optimization. It has been shown that geometry optimizations subject to both geometrical and energy constraints are efficient. Most remarkably, it has been shown that geometry optimization in the presence of multiple and heterogeneous constraints (i.e. simultaneous geometrical and energy constraints) is also very efficient, This last features allows for the mapping of very different seams of intersections relating electronic states of different nature with the ground state.

# Chapter 15. Final Remarks and Future Perspectives

As stressed in the Introduction Chapter, the search for light-driven molecular rotors calls for a detailed comprehension of the mechanism of the photoisomerization process, in such a way to assist the design of novel functional materials. In this respect, Chapter 10 and Chapter 11 provide some hints on the (structural) factors responsible for a speed-up of the photoisomerization of PSBs. In fact, the provided data help to unveil the nature of the rhodopsin protein "catalysis" of photoisomerization. In particular, some factors able to regulate the rate of the isomerization for the retinal chromophores have been established.

The first factor concerns the shape of the potential energy surface in proximity of the Franck-Condon zone, or, in other words, the shape of the excited state surface in the surrounding of the structure of the equilibrium geometry of the fundamental state. It has been demonstrated that the presence of a long energy plateau along the MEP, located immediately after the FC region, is related to a longer isomerization time. Thus, an energy plateau of reduced length let the retinal chromophore to isomerise rapidly. This is due to the fact that, once electronically excited, the wave packet can lose coherence. In other words, due to the flat PES, the chromophore will oscillate in various directions, before turning into the slope that, in the end, will take it to the photochemical funnel. *These oscillations are responsible for the longer time spent by the chromophore to complete the partial isomerization on the*

*excited state*. On the other hand, if the PES shows a reduced energy plateau, the wave packet will have less possibility to lose coherence. In this case, the chromophore will oscillate less and will move faster towards the photochemical funnel. This behaviour has been observed in Chapter 10 when comparing retinal chromophores with 3 and 5 double bonds (Figure 10–1) and the chromophore locked by an eight member ring (Figure 10–3).

The second important factor related to the isomerization speed is represented by the coupling between the stretching modes, that characterise the evolution from the FC point, and the torsional modes, defining the isomerization itself. If these two modes are weakly coupled, the passage from the first to the second is slow. Moreover, during this passage, it could happen that the chromophore has time to explore different paths, possibly entering different competing isomerizations paths. See, for example, Section 9.3. If the aim is the construction of a molecular rotor, the isomerization has to be diastereospecific and unidirectional, and alternative paths are unwanted. In other words, when the chromophore is excited by a photon, it has to isomerise about a specific bond and only in the clockwise or counter clockwise direction. In Chapter 10 and Chapter 11 it has been demonstrated that a certain degree of helicity is needed to enhance the coupling of the two modes. This makes possible for the isomerization to begin just after electronic excitation, and concurrently with stretching motion. Figure 10–2 report this behaviour when the helicity is imposed as an external environmental constraint (intermolecular), while Figure 11–3 shows the same conduct when the constraint is due to the presence of a ring (intramolecular).

In the future, it will be possible to use the strategy that has been developed to analyse and explain the catalysis of the eight member ring lock (see Scheme 11–3 and the relative text in Section 11.4.2) to model novel locked systems. The aim is to maintain the same characteristics of efficiency of the eight member ring, with the addiction of the possibility to accomplish a complete isomerization. In fact, a quasi complete cis-trans isomerization will contrast the return to the starting material via a thermal reaction. In this case, a back isomerization (trans-cis) will require a second photochemical event. If the two isomerizations (cis-trans and trans-cis) occur after irradiating with photons of two different wavelength, the designed system would constitute a (very desirable) two colours switch. In other words, this molecule could exist in two different states, that could be easily interchanged between one another.

A ring lock will never allow the construction of a rotor, since is not possible to do a complete cycle without breaking the ring itself. Five member rings could find an usage as locks for unwanted isomerizations, leaving the possibility for only one double bond to isomerise. In this way, diastereospecificity will be achieved. A further intramolecular constraint would then be needed to obtain unidirectionality. Possibly, steric hindrance given by the substituent of stereogenic centres in the vicinity of the isomerising double bond could play the trick. A study towards this direction is reported in ref. 247.

The analysis of the behaviours of the *N*-methylthioacetamide molecule (Chapter 13) showed that this molecule could be a good potential rotor (even if some further modelling is needed). To turn this molecule into a stand alone rotor some structural changes are needed, to make the photoisomerization

unidirectional. If one considers NMTAA as a rotor inside an oligopeptide, the shape of the PES along the C-N torsional coordinate has to be "tilted" to provide some driving force for the isomerization in only one direction (compare the shape presented in Figure 13–7). In this case, some structural details will have to be added, but this would be to the detriment of the quasi non invasive nature of the NMTAA unit. Further studies will show if the NMTAA unit is capable, as it is, to prompt a change into a peptide chain conformation through its photoisomerization.

Among all the modelling projects presented above, it's likely that the tools developed in Chapter 14 will be of growing importance in the future. In fact, they will allow the mapping of both the minimum energy paths and the crossing seams nearest to the calculated path, providing a more complete view of the photoreactive event.

The *in vacuo* models investigated in this thesis will provide a reference point for the investigation of similar chromophores inserted into a specific environment. Few studies have already been presented, and more will come, that explore the behaviours of retinal chromophores into their wild environment, the protein cavity, through a QM/MM scheme,[248] or inserted into an oligopeptide.[249] All this aspects contribute to define the so-called *computational photobiology*,[250] in the sense that the computational tools nowadays available permit to study a light harvesting system as a bare molecule, or as a chromophore embedded in a protein cavity.

When considering all the above mentioned arguments, one can see how the complete modelling of an efficient and useful molecular rotor now looks closer.

# Appendix The Theoretical Background

*Ab initio* molecular orbital theory is concerned with predicting the properties of atomic and molecular systems. It is based upon the fundamental laws of quantum mechanics and uses a variety of mathematical transformation and approximation techniques to solve the fundamental equations. This appendix provides an overview of the theory underlying *ab initio* electronic structure methods (see refs. 77, 251).

## A.1. The Schrödinger Equation

Quantum mechanics explains how microscopic entities like electrons have both particle-like and wave-like characteristics. The Schrödinger equation[252] describes the wavefunction of a collection of particles like a molecule:

$$\left(-\frac{\hbar^2}{8\pi^2}\sum_i \frac{1}{m_i}\nabla_i^2 + V(R,r,t)\right)\Psi(R,r,t) = \frac{ih}{2\pi}\frac{\partial\Psi(R,r,t)}{\partial t} \qquad \text{(A-1)}$$

In this equation, $\Psi$ is the wavefunction, $V$ is the potential field in which the particles are moving, **R** and **r** denote, respectively, the relative positions of the nuclei and of the electrons within the molecule, $h$ is the Planck constant, and the summation is over all particles $i$ (nuclei + electrons) where $m_i$ is the mass of particle $i$. The differential operator on the left side of the equation is known as *"del-squared"*. The operator *"del"* is equivalent to partial differentiation with respect to $x_i$, $y_i$ and $z_i$ components of particle-$i$ position:

$$\nabla_i = \frac{\partial}{\partial x_i}\mathbf{i} + \frac{\partial}{\partial y_i}\mathbf{j} + \frac{\partial}{\partial z_i}\mathbf{k} \qquad \text{(A-2)}$$

The energy and many properties of the system can be obtained by solving the Schrödinger equation for $\Psi$, subject to the appropriate boundary conditions. Many different wavefunctions are solutions to it, corresponding to different stationary states of the system. If $V$ is not a function of time, the Schrödinger equation can be simplified using the mathematical technique known as separation of variables. One will obtain two equations, one depending on the position of the particles independent of time, the other function of time alone. The case when the time dependence treatment is needed is reported in Chapter 3. Otherwise, with regards to the calculation performed for this thesis, this separation is valid, and one can focus entirely on the more familiar time-independent Schrödinger equation:

$$\hat{H}\Psi(R,r) = E\Psi(R,r) \qquad \text{(A-3)}$$

where $E$ is the energy of the many particles system and $\hat{H}$ is the Hamiltonian operator. The various solutions to this equation correspond to different stationary states of the molecule. The one with the lowest energy is called the ground state. This equation is a non-relativistic description of the system which is not valid when the velocities of the particles approach the speed of light. Thus it does not give an accurate description of the core electrons in heavy nuclei (such as transition metals). Anyway, for the systems presented in this thesis relativistic effects are negligible.

The Hamiltonian *H*, like the energy in classical mechanics, is the sum of kinetic and potential parts:

$$\hat{H} = \hat{T} + \hat{V} \tag{A-4}$$

The kinetic energy operator $\hat{T}$ is a summation of $\nabla^2$ over all the particles *i* (nuclei + electrons) in the molecule:

$$\hat{T} = -\frac{\hbar^2}{8\pi^2}\sum_i \frac{1}{m_i}\nabla_i^2 \tag{A-5}$$

while the potential energy operator *V* represent the Coulomb interaction between each pair of charged entities (treating each atomic nucleus as a single charged mass):

$$\hat{V} = \frac{1}{4\pi\varepsilon_0}\sum_j \sum_{k<j} \frac{e_j e_k}{r_{jk}} \tag{A-6}$$

where $r_{jk}$ is the distance between two distinct pair of particles (*j*, *k*), and $e_j$ and $e_k$ are their charges. For an electron the charge is *-e* while for a nucleus the charge is *Ze*, where *Z* is the atomic number for the atom. Thus:

$$\hat{V} = \frac{1}{4\pi\varepsilon_0}\left( -\sum_i^{electrons}\sum_l^{nuclei} \frac{Z_l e^2}{r_{il}} + \sum_i^{electrons}\sum_j \frac{e^2}{r_{ij}} + \sum_l^{nuclei}\sum_{j<l} \frac{Z_l Z_j e^2}{r_{ij}} \right) \tag{A-7}$$

The first term corresponds to electron-nuclear attraction, the second to electron-electron repulsion and the third to nuclear-nuclear repulsion.

## A.2. The Born-Oppenheimer and Adiabatic Approximations

These are the first of several approximations used to simplify the solution of the Schrödinger equation. They simplify the general molecular problem by *separating nuclear and electronic motions*. This is possible since the nuclear masses are much greater than those of the electrons, and, therefore, nuclei move much more slowly. As a consequence, the electrons react essentially instantaneously to changes in nuclear positions. This makes it a reasonable approximation to suppose that the *electron distribution depends only on the instantaneous positions of the nuclei* and not on their velocities. In other words, the nuclei look fixed to the electrons, and the quantum-mechanical problem of electron motion in the field of fixed nuclei may first be solved, leading to an effective electronic energy $E^{\text{eff}}(\mathbf{R})$, which depends on all of the relative nuclear coordinates (**R**) and describes the potential energy surface (PES) for the system. (This effective energy is then used as a potential energy for the subsequent study of the nuclear motion). This approximation is called *Born-Oppenheimer approximation*[253] and, in conjunction with the *adiabatic approximation* (by which *one can neglect the coupling terms between different electronic functions*, i.e. different electronic states), allows the two parts of the problem to be solved independently. For this reason the potential energy surface described by $E^{\text{eff}}(\mathbf{R})$ is also called adiabatic surface (because its existence depends on the validity of the adiabatic approximation).

Quantitatively, the Born-Oppenheimer approximation may be formulated by writing down the Schrödinger equation for electrons in the field of fixed nuclei (by neglecting the kinetic energy term for the nuclei):

$$\hat{H}^{elec}\Psi^{elec}(\mathbf{R},\mathbf{r}) = E^{eff}(\mathbf{R})\Psi^{elec}(\mathbf{R},\mathbf{r}) \qquad \text{(A-8)}$$

where $\Psi^{elec}$ is the electronic wavefunction which depends on the electronic (**r**) and nuclear (**R**) coordinates. $\hat{H}^{elec}$ is the electronic Hamiltonian:

$$\hat{H}^{elec} = \hat{T}^{elec} + \hat{V} \qquad \text{(A-9)}$$

where $\hat{T}^{elec}$ is the electronic kinetic energy (the kinetic energy term for the nuclei has been neglected):

$$\hat{T}^{elec} = -\frac{\hbar^2}{8\pi^2 m_e}\sum_{i}^{elec}\nabla_i^2 \qquad \text{(A-10)}$$

and $\hat{V}$ is the Coulomb potential energy defined above.
Accordingly, $E^{\text{eff}}$(**R**) is also used as the effective potential for the nuclear Hamiltonian:

$$\hat{H}^{nucl} = \hat{T}^{nucl} + E^{eff}(\mathbf{R}) \qquad \text{(A-11)}$$

where:

$$\hat{T}^{nucl} = -\frac{\hbar^2}{8\pi^2}\sum_{j}^{nucl}\frac{1}{m_j}\nabla_j^2 \qquad \text{(A-12)}$$

This Hamiltonian is used in the Schrödinger equation for the nuclear motion, describing the vibrational, rotational and translational states of the nuclei. Solving the nuclear Schrödinger equation (at least approximately) is necessary for predicting the vibrational spectra of molecules.

There are some situations in which the Born-Oppenheimer approximation is not valid; this means that the separability of nuclear and electron motions fails and the total wavefunction is no more well approximated by a simple product of an electronic eigenfunction with a vibrational wavefunction (the eigenfunction of the nuclear part of the Schrödinger equation). In this case non-adiabatic effects are important and the meaning of classical chemical structures becomes less clear. In general one can suppose Born-Oppenheimer approximation to be valid; anyway in the vicinity of surface crossings (at degenerate or nearly degenerate states) this approximation fails and molecular motion is described not only by the energy surface of the state but also by the almost degenerate one with its own vibrational motions. *In other words, even if one can always calculate (by solving the electronic part of the Schrödinger equation) the potential energy surfaces for the states, one need also to estimate non-adiabatic coupling effects (such as surface hopping probability) to have a correct description of the molecular motion.*

The main task of theoretical studies of electronic structures is to solve, at least approximately, the Schrödinger equation for the electronic wavefunction, and hence find the effective nuclear potential function $E^{\text{eff}}(\mathbf{R})$. The potential surface $E^{\text{eff}}(\mathbf{R})$ is fundamental to the quantitative description of chemical structures and reactivity. When explored in function of **R**, it will

generally have a number of points with important chemical meaning (as seen in Chapter 4 - Chapter 6).

It has been shown how the wavefunction $\Psi$ depends on the relative coordinates of all particles, **R** and **r**. The square of the wavefunction, $\Psi^2$ (or $|\Psi|^2$ if $\Psi$ is complex), is interpreted as a measure of the probability density for the particles it describes. Therefore it is required that $\Psi$ *be normalised*: if one integrates over all space, the probability should be unity (the probability of finding all the particles anywhere in space is unity!). Secondly, $\Psi$ *must also be antisymmetric*, meaning that it must change sign when two identical particles (such as electrons) are interchanged. For an electronic wavefunction, antisymmetry is a physical requirements following from the fact that the electrons are fermions (i.e., particle that have the properties of antisymmetry and half-integral spin quantum number). More specifically, this requirement means that any valid wavefunction must satisfy the following condition:

$$\Psi\ (\mathbf{r}_1,...,\mathbf{r}_i,\ ...,\mathbf{r}_j,...,\mathbf{r}_n) = -\ \Psi\ (\mathbf{r}_1,...,\mathbf{r}_j,\ ...,\mathbf{r}_i,...,\mathbf{r}_n) \qquad \text{(A-13)}$$

## A.3. The Variational Principle

The Variational Principle says that any given wavefunction, approximation of the exact one, when inserted in the Schrödinger equation, will give as result a value for $E^{\text{eff}}(\mathbf{R})$ higher (i.e. an upper bond) or equal to the "real" one. Equality is achieved only when the wavefunction is exact. Given an approximate wavefunction, depending on same parameters, it is possible to calculate the energy as expecting value of the Hamiltonian operator, on the base of the following formula.

$$E^{eff} = \frac{\langle \Psi | \hat{H}^{elec} | \Psi \rangle}{\langle \Psi | \Psi \rangle} \qquad \text{(A-14)}$$

By minimizing the energy so expressed, in function of the chosen parameters, one obtain the best approximation for the wavefunction.

For this reason, next section will discuss possible ways of choosing approximate wavefunctions.

## A.4. Theoretical Models: Ab Initio Computational Approach

An exact solution to the Schrödinger equation is not possible for any but the most trivial systems. However, a number of simplifying assumptions and procedures do make an approximate solution possible for a large range of molecules. Such an approach defines a theoretical model: it is a theory (a set of reasonable assumptions and approximations) within which all structures, energies, and other physical properties can be explored once the mathematical procedure has been implemented. A theoretical-model chemistry results. If comparisons of computational results with the available experimental evidences prove favourable, the model acquires some predictive value in situations where experimental data are unavailable. In this section it will be described the theoretical models used to produce the results presented in the thesis.

A theoretical model should posses a number of important characteristics. First, it should be unique and well defined. The procedure to obtain an energy and a wavefunction as an approximate solution of the Schrödinger equation should be completely specified in terms of nuclear positions and the number

and spins of electrons in the molecule. A second desirable feature is *continuity*: all potential surfaces should be continuous with respect to nuclear displacements. A theoretical model should also be unbiased. No appeal to chemical intuition should be made in setting up the details of the calculations (a theory can only be used for the analysis of such concepts as bonding if presuppositions have not been built into its formulation). Another important requirement for a satisfactory theoretical model is size-consistency: relative errors involved in calculations should increase more or less in proportion to the size of the molecule. This is particularly important if the model is to be used in a comparative manner, relating properties of molecules of different sizes. While it is generally not possible to satisfy this condition fully, it is often possible to construct models that are size-consistent for infinitely separated systems. This means that applications of the model to a system of several molecules at infinite separation will yield properties that equal the sum of these same properties for the individual molecules.
It is also desirable that a theoretical model be variational, that is, yield a total energy that is an upper bound to that which would result from exact solution of the full Schrödinger equation.

### A.4.1. The Molecular Orbital Model

The first approximation that will be considered comes from the interpretation of $|\Psi|^2$ as a probability density for the electrons within the system. *Molecular orbital (MO) theory* is an approach to molecular quantum mechanics which uses *one-electron functions* (or orbitals) to approximate the full wavefunction $\Psi$ (the theoretical models discussed in this section are all based on this MO model). This approximate treatment of electron distribution

and motion assigns individual electrons to one-electron functions termed *spin-orbitals*. These comprise a product of a spatial function, termed molecular orbital, $\phi_1(x,y,z)$, $\phi_2(x,y,z)$, $\phi_3(x,y,z)$, ..., and either $\alpha$ or $\beta$ spin function (describing the spin component of the electron). The spin-orbitals are allowed complete freedom to spread throughout the molecule, their exact form being determined *variationally* to minimise the total energy. For simplification reasons, molecular orbitals are chosen to be orthogonal to each other and normalised (normalisation correspond to the physical requirement that the probability of finding the electron anywhere in space is unity):

$$\begin{aligned} \int \phi_i^* \phi_i d\tau &= 1 \\ \int \phi_i^* \phi_i d\tau &= 0, i \neq j \end{aligned} \qquad \text{(A-15)}$$

In the simplest version of the theory, as in the *restricted Hartree-Fock (RHF) method*, a single assignment of electrons to orbitals is made (this single assignment defines the so-called electron configuration). These orbitals are then combined together to form a suitable many-electron wavefunction $\Psi$ which is the simplest MO approximation to the Schrödinger equation.

The simplest possible way of making $\Psi$ for the description of an n-electron molecular system would be in the form of a simple product of spin orbitals (the so called Hartree product). However, such a wavefunction is not acceptable, as it does not have the property of antisymmetry. To ensure antisymmetry, the spin orbitals may be arranged in a *determinantal wavefunction* (often referred to as *Slater determinant*). For a molecule with n (even) electrons doubly occupying n/2 molecular orbitals $\phi_i$ (orthogonal and normalised), the many-electron wavefunction is:

$$\Psi = (n!)^{-1/2} \begin{vmatrix} \phi_1(1)\alpha(1) & \phi_1(1)\beta(1) & \phi_2(1)\alpha(1) & \ldots & \phi_{n/2}(1)\beta(1) \\ \phi_1(2)\alpha(2) & \phi_1(2)\beta(2) & \phi_2(2)\alpha(2) & \ldots & \phi_{n/2}(2)\beta(2) \\ \ldots & \ldots & \ldots & \ldots & \ldots \\ \phi_1(n)\alpha(n) & \phi_1(n)\beta(n) & \phi_2(n)\alpha(n) & \ldots & \phi_{n/2}(n)\beta(n) \end{vmatrix} \quad \text{(A-16)}$$

where the initial factor is necessary for normalisation.

The determinantal wavefunction does have the property of antisymmetry. Swapping two electrons correspond to interchanging two rows of the determinant, which will have the effect of changing its sign. Moreover, it is not possible for a molecular orbital $\phi_i$, to be occupied by two electrons of the same spin. This is the Pauli exclusion principle,[254] which follows because the determinantal wavefunction vanishes if two columns are identical. Hence orbitals may be classified as doubly occupied, singly occupied or empty. Since each orbital $\phi_i$ is later associated with an energy, this assignation of electrons is usually referred to as an electron configuration and is often represented by an electron configuration diagram such as shown below.

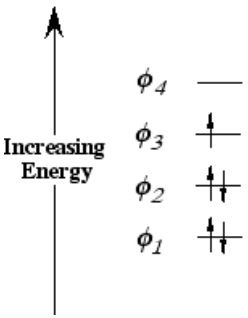

Most molecules have an even number of electrons and their ground states may be represented by closed-shell wavefunction with orbitals either doubly occupied or empty. This is the case of one of the most commonly used methods: the RHF method. Here the many-electron wavefunction $\Psi$ is represented by a single electron configuration corresponding to a single closed-shell type Slater determinant (see, as example, the *single-determinant wavefunction* written above), where $\alpha$ and $\beta$ coupled electrons are constrained to move in the same space (their spatial functions, *i.e.* molecular orbitals $\phi_i$, are identical).

### A.4.2. Basis Sets: The LCAO Approximation

A further approximation involves expressing the molecular orbitals $\phi_i$ as linear combination of a pre-defined finite set of N one-electron functions known as basis functions.

$$\phi_i = \sum_{\mu=1}^{N} c_{\mu i} \chi_\mu \qquad \text{(A-17)}$$

where the coefficients $c_{\mu i}$ are known as the molecular orbital expansion coefficients.

The basis functions (also chosen to be normalised) constitute the basis set. These basis functions (which are defined in the specification of the model) are usually centred on the atomic nuclei and so bear some resemblance to atomic orbitals. If the basis functions are the atomic orbitals for the atoms making up the molecule, the previous equation is often described as the

*linear combination of atomic orbitals (LCAO) approximation*, and is frequently used in qualitative descriptions of electronic structure. However, the actual mathematical treatment is more general than this, and any set of appropriately defined functions may be used.

To provide a basis set that is well defined for any nuclear configuration and therefore useful for theoretical model, it is convenient to define a particular set of basis functions associated with each nucleus, depending only on the charge on that nucleus. Such functions may have the symmetry properties of atomic orbitals, and may be classified as *s, p, d, f,...* types according to their angular properties. Two types of basis functions have received widespread use: Slater-type functions[255] and gaussian-type functions.[256] The former provide a reasonable representations to atomic orbitals but are not well suited to numerical work, and their use in practical molecular orbital computations has been limited. The latter are less satisfactory as representation of atomic orbitals (particularly because they do not have a cusp at the origin), nevertheless they have the important advantage that all integrals in the computations can be evaluated explicitly (analytically) without recourse to numerical integration.

Actually, linear combination of gaussian functions are used to define the basis functions (for example an *s*-type basis function $\chi_\mu$ can be expanded in terms of *s*-type gaussians $g_s$):

$$\chi_\mu = \sum_s d_{\mu s} g_s \qquad \text{(A-18)}$$

where the *d* coefficients (called contraction coefficients) are fixed constants within a given basis set. Basis functions of this type are called contracted

gaussians, the individual *g* being termed primitive gaussians. All of the construction result in the following expansion for molecular orbitals:

$$\phi_i = \sum_{\mu=1}^{N} c_{\mu i} \sum_{m} d_{\mu m} g_m \qquad \text{(A-19)}$$

where *m* represents the generic angular type (*s, p, d, f,...*).

Given the basis set, the unknown coefficients $c_{\mu i}$ are determined so that the total electronic energy calculated from the many-electron wavefunction is minimized and, according to the variational theorem, is as close as possible (an upper bound) to the energy corresponding to the exact solution of the Schrödinger equation. *The Self Consistent Field (SCF) procedure is the iterative methods through which expansion coefficients* $c_{\mu i}$ *are optimized to gain the minimum value of the energy* (a threshold in the energy gap between consecutive iterations is chosen, under which the procedure is considered "*convergent*"). *This energy and the corresponding wavefunction represent the best that can be done within the chosen approximation*, that is, the best given the constrains imposed by: (a) the use of a limited (not infinite) basis set, and (b) the constraint in the wavefunction extension (for the RHF methods being the use of a single-determinant wavefunction).

### A.4.3. Post-SCF and Dynamic Correlation Methods: CAS-SCF, CIS and CAS-PT2

The main deficiency in HF theory stands in its single-determinant wavefunction. Even with a large and completely flexible basis set, the full

solution of the Schrödinger equation cannot be expressed in terms of a single electron configuration. Moreover a chemical system undergoing bond-breaking/bond-forming processes (and in general transition states) cannot be expressed by a single-determinant wavefunction, and single-excitation states (as the spectroscopic excited state in polyenes) are open-shell electron configurations (not closed-shell as in the RHF methods). To correct for such a deficiency, it is necessary to use wavefunctions that go beyond the HF level, i.e. that represent more than a single electron configuration. This is done in post-SCF methods.

If $\Psi_0$ is the HF many-electron wavefunction, the extended approximate form for the more accurate wavefunction $\Psi$ is

$$\Psi = a_0 \Psi_0 + a_1 \Psi_1 + a_2 \Psi_2 + a_3 \Psi_3 + ... \qquad \text{(A-20)}$$

Here $\Psi_1$, $\Psi_2$, $\Psi_3$, ... are wavefunctions (Slater determinants) corresponding to other electron configurations, and the linear coefficients $a_0$, $a_1$, $a_2$, $a_3$, ..., are to be determined (optimised through a variational SCF procedure) together with the expansion coefficients defining molecular orbitals, in order to get the minimum energy value. Inclusion of wavefunctions for all possible alternative configurations (within the framework of a given basis set) is term full configuration interaction (full-CI). It represents the best that can be done using that basis set. Practical methods seek to limit the number of configurations or to approximate the effect which their inclusion has on the total wavefunction.

### A.4.3.1. The CASSCF Method

In the CASSCF method[80] all the electron configurations arising within a chosen active space of orbitals (a set of chemically-important orbitals which

is chosen depending on the chemical process one is interested in) are considered into the multiconfigurational expansion for $\Psi$. Thus the orbital space is divided into three subsets: a core space (with all doubly occupied orbitals), a valence or active space (where all possible configurations are considered in) and a virtual space (with all empty orbitals).

#### A.4.3.2. The CIS Method

In the CIS method[74] only single-excitation-type Slater determinants are added into the expansion for $\Psi$. Moreover the molecular orbitals are determined through a RHF computation on the system. This method allows one to correctly describe only single-excitation electronic states (as it is the case for the spectroscopic ionic states of polyenes) at a lower computational effort than with CASSCF.

#### A.4.3.3. Perturbation Theory Methods

CASSCF is certainly a suitable method for mapping the potential energy surfaces both in the ground and in the excited states, and it gives accurate descriptions of chemical reactivity problems. Nevertheless to have the correct energetics in chemical and photochemical problems, contributions due to dynamic electron correlation have to be considered. These depend on the *inadequacy of CASSCF to describe the instantaneous interelectronic repulsion* due to the $1/r_{ij}$ terms in the Hamiltonian (*dynamic correlation effects*). The correction due to this term is necessary to have correct (comparable to experimental data) energy gaps and activation barriers. Second order perturbation theory methods (see below) compute these contributions perturbatively.[257] Multireference-CI methods compute the same correction variationally. The CASSCF wavefunction is perturbed by adding more terms to the multiconfigurational expansion of $\Psi$, including also Slater determinants of core-virtual excitation type, valence-virtual excitation type,

and so on. The energetic effect due to this perturbation is then computed and added to the energy (to gain a second order corrected value) and to the wavefunction (to gain a first order corrected function). To take in account these effects, in this thesis the CASPT2[85] method has been widely used. It computes dynamic correlation contribution by adding perturbatively all possible configurations to CASSCF wavefunctions.
Next two paragraphs will discuss the two methods (CASSCF and CASPT2) that have been extensively used in this thesis.

## A.5. The CASSCF method

In recent years the CASSCF method has been extensively used for mapping excited state potential energy surfaces of organic compounds.[20] This *ab initio* quantum chemical method also provides the "natural" basis for the accurate evaluation of the excited state energetics. In fact, vertical and 0-0 excitation energies and ground and excited state energy barriers can be evaluated with just few kcal mol-1 error by employing multireference methods which include the evaluation of the dynamic correlation energy. These methods, which require the multireference CASSCF wavefunction as the starting point, are the multireference configuration interaction method (MR-CI[83]) and multireference perturbation theory methods (e.g. MRMP2,[84] CASPT2[85]). In the following, a conceptual introduction to the CASSCF method is given.

$$\phi_{MO_i} = c_1\phi_{AO_1} + c_2\phi_{AO_2} + \ldots + c_i\phi_{AO_i} + \ldots + c_n\phi_{AO_n}$$

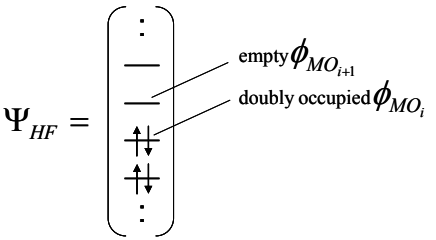


$D_i$

Scheme A-7

The CASSCF method is, essentially, a combination of the standard *ab initio* Hartree-Fock (HF) and Configuration Interaction (CI) methods. In the HF method, the wavefunction used to describe the electronic structure of the molecule is a single reference wavefunction $\psi_{HF}$. This means that it is constructed using a single Slater determinant ($D_i$). The "structure" of a Slater determinant is illustrated in Scheme A-7. Each molecular orbital $\phi_{MOi}$ is constructed as a linear combination of atomic orbitals ($\phi_{AOi}$) using a suitable atomic basis set. The shape of each orbital is "optimised" in a variational process by changing the values of the orbital coefficients $c_1$, $c_2$, ..., $c_i$, ...,$c_n$ (n is the number of atomic orbitals) so that to get the lowest possible value for the energy. A wavefunction of this type is certainly capable of describing the electronic configuration of systems where all the molecular orbitals are doubly occupied. These are the so-called closed-shell systems. Thus the HF method is usually applied to the investigation of the equilibrium structure of ground state species and to the study of ground state conformational problems. However this method cannot be applied to chemical processes

which involve singly or partially occupied orbitals. These chemical processes correspond to ground state reactions involving radical pairs of diradical intermediates or excited state processes where a diradical character develops after photoexcitation. To deal with these problems one may try to use the configuration interaction (CI) method.

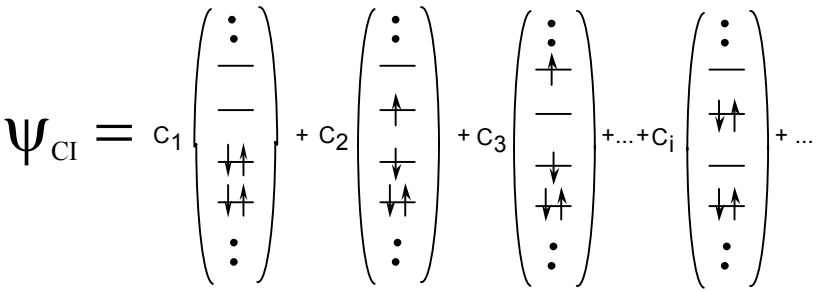


Scheme A-8

In this method, the molecular orbitals produced by a HF computation are employed to generate a multireference wavefunction. As shown in Scheme A-8 above, the **CI** wavefunction is defined as a linear combination of Slater determinants describing different electronic configurations, including both closed shell and diradical configurations. Most important each configuration corresponds to a different electronic excitation of the reference closed-shell electronic configuration. The coefficients $C_1$, $C_2$, ...,$C_i$,..., ...$C_m$ (where m is the number of Slater determinants) are determined by computing the eigenvectors of a (m x m) **CI** Hamiltonian matrix, whose matrix elements have the form $<D_i|H|D_j>$, where $D_i$ is a Slater determinant and H is the Hamiltonian operator of the molecule under investigation. The eigenvalues of the **CI** Hamiltonian provide the potential energies associated to the ground

state and m-1 different excited states. Each eigenvector describes the corresponding electronic structure of these states. However, in order to get accurate results with the **CI** method, the wavefunction must contain an extremely large number of Slater determinants, which makes the calculation often very difficult if not impossible.

In order to solve this problem, one can think of using a wavefunction containing a limited number of Slater determinants (i.e. a so called truncated **CI** wavefunction). but rather than "optimise" only the coefficient of the **CI** wavefunction $C_1$, $C_2$, ...,$C_i$,..., $C_m$, one optimises simultaneously these coefficients and the atomic orbital coefficients $c_1$, $c_2$, ..., $c_i$,..., $c_n$ of the molecular orbitals used to construct the Slater determinants. Thus one has n+m variational coefficients. This type of wavefunction defines the multireference-self-consistent-field (MCSCF) method. Thus the MCSCF wavefunction is a **CI** wavefunction which contains only a very limited number of Slater determinants which describe only a limited number of electronic excitations. *The choice of the subset of the electronic excitations that must be used to build the MCSCF wavefunction is critical.* In order to define this subset, the molecular orbitals are grouped in three different sets: the core orbitals, the valence orbitals and the virtual orbitals. The core orbitals are the orbitals that remain always doubly occupied in the entire MCSCF Slater determinant set. The virtual orbitals are the orbitals that remain always empty. Finally the valence orbitals (or active orbitals) are the orbitals that change occupancy. The electrons filling the valence orbital set are the valence electrons (or active electrons). One variety of the MCSCF method is the CASSCF method. *This method is defined by a wavefunction whose Slater determinants describe <u>all</u> possible electronic excitations within*

*the chosen set of the active electrons and orbitals. Thus CAS stands for complete-active-space*.

The choice of the orbitals that must be included in the valence space is a function of the molecular system and, most importantly, of the type of chemical or physical process that one must investigate. For instance if one is interested in the behaviour of an excited state of a chromophore containing a π-system, the valence orbitals must contain the orbitals involved in the photoexcitation process. Similarly if one wants to investigate a chemical reaction then all the orbitals taking part in the bond-breaking and bond-forming process must be enclosed in the valence space. A simple example of CASSCF wavefunction can be described for the very basic π system: the ethylene molecule. By selecting the two π and π* orbitals as the active orbitals and the two π electrons as the active electrons one can construct a CASSCF wavefunction containing four different Slater determinants (see Scheme A-9).


ETHYLENE ACTIVE MOLECULAR ORBITALS

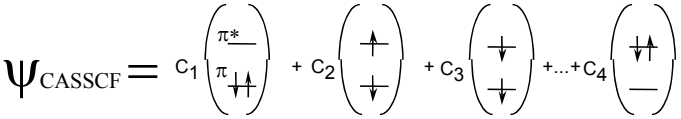


Scheme A-9

The determinant corresponding to the electronic configuration with the doubly occupied π orbital ($C_1$ coefficient) describes a closed-shell system while the others describe all the configurations which can be generated by moving one or both the electrons to the higher energy orbital. For the equilibrium geometry of ethylene in its ground state the configuration which dominates the wavefunction (i.e. the configuration with the largest weight) is expected to be the closed-shell configuration. In fact, this configuration describes the π bonding in an MO treatment. Nevertheless, if the ethylene molecule is highly twisted, such as along the reaction path describing a Z/E isomerization, then other configurations start to acquire a relevant contribution. For instance near a 90° rotation the $C_1$ and $C_4$ coefficients ($C_4$ is the coefficient of a doubly excited configuration) have similar magnitude since the molecule will posses a pair of quasi degenerate orbitals. Of course the weights of the configurations are expected to change when the molecule

is promoted to an excited state via absorption of a photon. In this case the configurations which will be representative of the singlet excited state will be the singly excited configuration $C_2$ (rather then the doubly excited configuration $C_4$). On the other hand the configuration corresponding to coefficient $C_3$ is the triplet state configuration and does not mix (by symmetry) with the other singlet configurations.

Once the CASSCF wavefunction has been constructed by choosing the proper set of orbitals and electrons the energy of the molecule can be computed as an eigenvalue of the **CI** matrix of (m x m) dimensions constructed using simultaneously optimised orbitals. Thus, there will be m eigenvalues and m corresponding eigenvectors of the **CI** matrix. The lowest eigenvalue provides a value for the ground state energy while the others will be excited state energies. The corresponding eigenvector gives a description of the electronic structure of the state. One of the advantages of the CASSCF method is that for each state of interest (ground or excited) one gets the best set of orbitals thus improving the description with respect to a simple **CI** treatment. The success of the CASSCF method for excited state potential energy surface mapping is due to two specific features. The first is that the method is accurate enough to be able to model the correct shape of the energy surface and the position (i.e. the molecular structure) of the energy minima, transition states and reaction coordinates. The second is that the first and second derivatives of the potential energy (i.e. the gradient vector and Hessian matrix respectively) can be computed analytically. This very important technical feature allows the use of different powerful computational tools for the exploration and mapping of the energy surface.

The CASSCF energetics is usually not enough accurate to reproduce excitation energies and reaction barriers with chemical accuracy. For this reason one need to go beyond the CASSCF method. Indeed the CASSCF wavefunction needs to be further improved since it cannot describe satisfactorily the "dynamic correlation" effects. This term indicates the description of the instantaneous mutual repulsion of two electrons with opposite spins. Methods which provide a wavefunction capable of describing the dynamic correlation are the MR-CI and multireference-MP2 methods. On the other hand these methods are computationally very expensive. For this reason a common strategy is that of evaluating the reaction coordinate at the CASSCF level of theory and then correct the energy profile by computing a few relevant point using one of the “correlated” methods. Recently the multireference-MP2 method has been extensively employed to evaluate the excitation energies and reaction barriers of medium size organic molecules. In this method the dynamic correlation is "added" to the CASSCF wavefunction, that acts as the zeroth order wavefunction, using the perturbation theory. In practice, the basic CASSCF wavefunction is enriched by adding to the set of Slater determinants enclosed in the CAS, other Slater determinants representing single and double excitations from the set of the core orbitals to the virtual orbitals, from that of the core to that of the valence and from the valence to the virtual. In this thesis the CASPT2[85] multireference-MP2 methods have been used.

Very recently, a method for computing second-order multiconfigurational perturbation theory energy gradients numerically has been implemented and applied to a range of organic chromophores, including 1,3 butadiene, acrolein and two protonated Schiff bases.[193]

## A.6. Use of Perturbation Theory

As already said above, CASSCF is able to recover only a small fraction of the total correlation energy, the so-called dynamic electron correlation energy is not accounted for. The electrons in both the Hartree Fock wavefunctions and the core electrons of the MCSCF wavefunction only "feel" a repulsive electrostatic potential resulting from the averaged effect of the rest of the electrons. There is, however, an instantaneous electron repulsion, as a consequence of which two electrons can not get too close to each other; this Conical intersections classified according to re. This term is quite important when comparing energies from different parts of potential energy surfaces, since its magnitude can be quite different depending on the electronic distribution.

A full-CI treatment would fully recover this correlation energy. Due to the impossibility of this approach in most molecular systems, various tools have been developed to approximate these effects. One of the most widely used because of its relative simplicity is the second order Møller-Plesset method, MP2. It is based on a more general Rayleigh-Schrödinger perturbation theory, which has been widely used in different branches of science.

### A.6.1. Rayleigh-Schrödinger Perturbation Theory

General Perturbation theory is based on the partition of the exact Hamiltonian in two parts. The first one is represented by the part of the Hamiltonian for which an exact solution can be obtained: the zeroth-order Hamiltonian, $H^0$. The remaining part is chosen as the term that prevents an easy solution to the

problem: the perturbation $V$, which is multiplied by an ordering parameter λ, later set equal to unity. The two parts make up the total Hamiltonian:

$$H = H_0 + \lambda V \tag{A-21}$$

Rayleigh-Schrödinger perturbation theory expands the eigenvalues and eigenfunctions of the Schrödinger equation in a power series of $\lambda$. The eigenvalue problem can be expressed as:

$$\begin{aligned}&\left(H_0 + \lambda V\right)\left(\left|\Psi^{(0)}\right\rangle + \lambda\left|\Psi^{(1)}\right\rangle + \lambda^2\left|\Psi^{(2)}\right\rangle + \ldots\right) = \\ &\left(E^{(0)} + \lambda E^{(1)} + \lambda^2 E^{(2)} + \ldots\right)\left(\left|\Psi^{(0)}\right\rangle + \lambda\left|\Psi^{(1)}\right\rangle + \lambda^2\left|\Psi^{(2)}\right\rangle + \ldots\right)\end{aligned} \tag{A-22}$$

$\psi^{(0)}$ and $E^{(0)}$ hence represent the known solutions of the zeroth-order Hamiltonian of a system. Taking intermediate normalisation (i.e. setting $\left\langle\Psi^{(0)}\middle|\Psi^{(0)}\right\rangle = 1$ and $\left\langle\Psi^{(0)}\middle|\Psi^{(n)}\right\rangle = 0$ ), equating coefficients on $\lambda$ and multiplying by $\left\langle\Psi^{(0)}\right|$, the following expressions for the different energy orders are obtained:

$$E^{(0)} = \left\langle\Psi^{(0)}\middle|H_0\middle|\Psi^{(0)}\right\rangle \tag{A-23}$$

$$E^{(1)} = \left\langle\Psi^{(0)}\middle|V\middle|\Psi^{(0)}\right\rangle \tag{A-24}$$

$$E^{(2)} = \left\langle\Psi^{(0)}\middle|V\middle|\Psi^{(1)}\right\rangle \tag{A-25}$$

An expression for the first order wavefunction can also be obtained equating coefficients in Equation A-22

$$\left(E^{(0)} - H_0\right)\left|\Psi^{(1)}\right\rangle = \left(V - E^{(1)}\right)\left|\Psi^{(0)}\right\rangle = \left(V - \left\langle\Psi^{(0)}\middle|V\middle|\Psi^{(0)}\right\rangle\right)\left|\Psi^{(0)}\right\rangle \qquad \text{(A-26)}$$

where the expression for $E^{(1)}$ in Equation A-24 was used. This last equation constitutes an inhomogeneous differential equation. The solution for the second order energy arises from expanding the first order wavefunction in terms of a complete set of eigenfunctions of the zeroth-order Hamiltonian:

$$\left|\Psi_i^{(1)}\right\rangle = \sum_n c_n^{(1)}\left|n\right\rangle = \sum_n \left|n\right\rangle\left\langle n\middle|\Psi_i^{(1)}\right\rangle \qquad \text{(A-27)}$$

with $n$ running for all eigenfunctions of $H_0$ except for $\psi^0$. If Equation A-27 is multiplied by $\langle n|$, the following expression is obtained:

$$\left(E^0 - E_n^0\right)\left\langle n\middle|\Psi^{(1)}\right\rangle = \left\langle n\middle|V\middle|\Psi^{(0)}\right\rangle \qquad \text{(A-28)}$$

This last expression can be used in Equation A-27 and substituting the resulting $\psi^{(1)}$ in Equation A-25 the second order energy is given by:

$$E_0^{(2)} = \sum_n \frac{\left|\langle 0|V|n\rangle\right|^2}{E_0^{(0)} - E_n^{(0)}} \qquad \text{(A-29)}$$

The expression for the second order energy is hence given by a summation over the complete set of eigenfunctions of the zeroth-order Hamiltonian. It contains an integral involving these eigenfunctions and the perturbation term, divided by the difference between the corresponding eigenvalues. The efficiency and accuracy of an MP2 calculation will therefore be very much influenced by the choice of zeroth-order Hamiltonian.

### A.6.2. Second order Møller-Plesset perturbation theory

Second order Møller-Plesset (MP2) perturbation theory (also referred to as many-body perturbation theory, MBPT) defines the zeroth-order Hamiltonian as the Hartree-Fock Hamiltonian. One can distinguish RMP2 from UMP2, depending on whether an RHF or UHF Hamiltonian is used. Since the equations presented in the development of Hartree-Fock were the RHF ones, the RMP2 equations will be derived here.

The Rayleigh-Schrödinger perturbation term, $V$, is defined as the difference between the total and the zeroth-order Hamiltonian. In this case, it is given by the difference between the electron-electron repulsion term and the Fock operator:

$$V = \sum_{i<j} r_{ij}^{-1} - V^{HF} = \sum_{i<j} r_{ij}^{-1} - \sum_{i} v^{RHF}(i) \qquad \text{(A-30)}$$

where the fact that $V^{HF}$ is a mono-electronic operator has been exploited, and $i$ and $j$ run over the total number of electrons. The Rayleigh-Schrödinger solution for the second order perturbation energy is given by Equation A-29. A complete set of eigenfunctions expanding the solutions of the Hartree-Fock

Hamiltonian is required. This is given by the different Configuration State Functions (CSF's) formed using all the resulting orbitals of the Hartree-Fock calculation. These configurations can be expressed as replacements of the occupations of the electrons from the ground state configuration. $\Psi_a^r, \Psi_{ab}^{rs}, \Psi_{abc}^{rst}$ represent single, double and triple replacements from the ground state configurations. This notation becomes useful since not all the CSF's are required for the computation of the second order perturbation energy. It can be proved that

$$\left\langle \Psi_0 \middle| V \middle| \Psi_a^r \right\rangle = \left\langle \Psi_0 \middle| H - H_0 \middle| \Psi_a^r \right\rangle = \left\langle \Psi_0 \middle| H \middle| \Psi_a^r \right\rangle - f_{ar} = 0 \qquad \text{(A-31)}$$

$f_{ar}$ vanishes since the functions are eigenvalues of the Fock operator and the Brillouin theorem determines that the first term is also zero. The terms involving configurations differing by more than 3 occupied spin-orbitals with the Hartree-Fock ground state configuration also vanish due to the two-particle nature of the perturbation. Hence Equation A-29 only involves the interaction of the Hartree-Fock ground state configuration with double replacement states. The final expression for the second order perturbation energy becomes

$$E_0^{(2)} = \sum_{a<b,r<s} \frac{\left|\langle ab|rs\rangle\right|^2}{\varepsilon_a + \varepsilon_b - \varepsilon_r - \varepsilon_s} \qquad \text{(A-32)}$$

which represents a general expression where the summations run over all the various spin-orbitals and the denominators contain the difference between the orbital energy of the ground state occupied orbitals and the virtual ones.

### A.6.3. The CASPT2 method

In the early 80's, Roos and coworkers[258] developed an implementation of a second-order of Rayleigh-Schrödinger perturbation theory using a CASSCF wavefunction as the zeroth-order reference. The first order interacting space was however restricted to external double excitations with respect to the zeroth-order wavefunction. This did not constitute the full first order interacting space since internal and semi-internal excitations were discarded in order to avoid the computation of some three and four-particle density matrices. This approximation was not fully successful since test applications were not very encouraging. The development of new methods to compute N-particle density matrices made it possible to develop the CASPT2,[259] which included the full first order interacting space.

CASPT2 hence constitutes a full generalised application of Rayleigh-Schrödinger perturbation theory for the case of Multi-Reference wavefunctions in the same way that Møller-Plesset theory does for single reference Hartree-Fock wavefunctions. Considering that the MCSCF Hamiltonian is diagonalised to obtain the zeroth-order wavefunctions which is used to apply the perturbation, the method can be classified as having a *diagonalise then perturb* approach. The crucial step in developing such a theory consists on defining a zeroth-order Hamiltonian which would ensure a rapidly converging perturbation expansion and a computationally efficient method. As shown below, for CASPT2 this is done defining a structured

operator consisting of summations of space projected sums of one-particle operators.

CASPT2 formulation is greatly facilitated by the use of second quantisation.[260] Within the formulation of Rayleigh-Schrödinger perturbation theory, an approximate solution of the Schrödinger equation can be found by expanding the first order wavefunction into a set of configurations. The entire configuration space can be divided into four subspaces:

$V_0$: The one-dimensional space spanned by $|0\rangle$ the zeroth-order wavefunction.

$V_K$: Space spanned by the orthogonal complement to $|0\rangle$.

$V_{SD}$: Space spanned by all single and double replacement states generated from $|0\rangle$.

$V_{TQ}$: Space spanned by all higher excitations not included in the previous spaces.

The replacement states arise from applying the spin-averaged excitation operators, $\hat{E}_{rs}$, to the first order wavefunction.

$$\hat{E}_{rs} = s^{\dagger} r + \bar{s}^{\dagger} \bar{r} \qquad \text{(A-33)}$$

The functions from $V_k$ and $V_{TQ}$ do not interact with the reference state through the total Hamiltonian. Hence, to be able to assimilate the first order wavefunction to the space spanned by $V_{SD}$, the zeroth-order Hamiltonian is defined as:

$$\hat{H}_0 = \hat{P}_0 F \hat{P}_0 + \hat{P}_K F \hat{P}_K + \hat{P}_{SD} F \hat{P}_{SD} + \hat{P}_{TQ} F \hat{P}_{TQ} \qquad \text{(A-34)}$$

where the operators $P_x$ represent the projectors into the space $V_x$ and the operator $F$ is a one-particle operator. The choice for this latter operator is somewhat arbitrary, but it should reproduce the results of a closed-shell second-order result when the number of active orbitals is zero. An operator $F_{qp\sigma}$ can be defined as:

$$\hat{F}_{pq\sigma} = \hat{a}_{p\sigma}\left[\hat{H}, \hat{a}^*_{q\sigma}\right] - \hat{a}^*_{p\sigma}\left[\hat{a}_{q\sigma}\right] \qquad \text{(A-35)}$$

And its expectation values are given by:

$$f_{pq} = \tfrac{1}{2}\sum_{\sigma} \langle 0 | \hat{F}_{pq\sigma} | 0 \rangle \qquad \text{(A-36)}$$

The resulting diagonal terms correspond to energy differences. When the index refers to inactive orbitals, this energy difference is between the system, represented by $|0\rangle$, and its positive ion. For secondary orbitals it is between the negative ion and $|0\rangle$, and for active orbitals the energy difference represents an intermediate situation. These expectation values are used to define the Hartree-Fock for the closed-shell case since this operator can be expressed as:

$$\hat{F}_{H-F} = \sum_{pq} f_{pq} \hat{E}_{pq} \qquad \text{(A-37)}$$

For an MCSCF wavefunction, the matrix elements $\boldsymbol{f_{qp}}$ are zero for $p$ and $q$ representing core and virtual orbitals. A new set of orbitals can be defined after diagonalising the three blocks of $\boldsymbol{f}$ corresponding to the core-core, valence-valence and virtual-virtual orbital sub-spaces, in the same manner than the canonical orbitals are found in the single-determinant case. The resulting matrix, $\boldsymbol{f'}$, is diagonal but for the core/valence and valence/virtual blocks. A general Fock-type operator $F_N$ is defined as

$$\hat{F}_N = \left\{\hat{F}_D\right\} + \left\{\hat{F}_T\right\} = \left\{\sum_{it}\left[f'_{it}\hat{E}_{it} + f'_{ti}\hat{E}_{ti}\right] + \sum_{at}\left[f'_{at}\hat{E}_{at} + f'_{ta}\hat{E}_{ta}\right]\right\} \qquad \text{(A-38)}$$

were the indices $i$, $t$, $a$ and $p$ run over the inactive, active, secondary and the entire orbital subspace respectively and $\varepsilon_p$ represent the diagonal elements of the matrix $\boldsymbol{f'}$. Two different implementations of CASPT2 were initially developed. In the first one, the operator $F_N$ contained only the diagonal elements $F_D$ while in the second one it was expanded to contain also $F_T$ .
The system of linear equations derived by Rayleigh-Schrödinger perturbation theory in Equation A-27 can also be expressed as:

$$\sum_{j=1}^{M} c_j \left\langle i\middle|\hat{H}_0 - E_0\middle|j\right\rangle = -\left\langle i\middle|\hat{H}\middle|0\right\rangle, i = 1,\ldots,M \qquad \text{(A-39)}$$

where $c_j$'s are the coefficients in the expansion of $\Psi^{(1)}$ with the configurations of $V_{SD}$ ($\left|i\right\rangle$ and $\left|j\right\rangle$), and M represents the replacement states. Considering that the wavefunctions generated by the excitation operators may contain

linear dependencies, M ≥ dim $V_{SD}$, a matrix equation can be derived from Equation A-35 constructing the matrix **F**, which contains the representation of the operator $F_N$ in the sub-space $V_{SD}$:

$$\left[F_N - E_0 S\right]C = -V \tag{A-40}$$

where the following definitions have been used:

$$\left(F_N\right)_{ij} = \left\langle i\middle|\hat{F}_N\middle|j\right\rangle, \left(S\right)_{ij} = \left\langle i\middle|j\right\rangle, \left(V\right)_{ij} = \left\langle i\middle|\hat{H}\middle|0\right\rangle \tag{A-41}$$

The structure of the matrix $\mathbf{F_N}$ depends on the operator $F_N$ chosen. For the case where only the diagonal elements are included, the resulting matrix is block diagonal. The resulting eight diagonal blocks correspond to a set of various sub-spaces of $V_{SD}$. They are grouped into internal, semi-internal and external when they include none, one and two virtual orbitals respectively. Each of the sub-spaces is generated by:

*Internal:* $V_a$: $\hat{E}_{ti}\hat{E}_{uv}|0\rangle$

$V_b$: $\hat{E}_{ti}\hat{E}_{uj}|0\rangle$

*Semi-internal:* $V_c$: $\hat{E}_{at}\hat{E}_{uv}|0\rangle$

$V_d$: $\hat{E}_{ai}\hat{E}_{tu}|0\rangle$, $\hat{E}_{ti}\hat{E}_{au}|0\rangle$, $\hat{E}_{\chi a}\hat{E}_{u\eta}|0\rangle$

$V_e$: $\hat{E}_{ti}\hat{E}_{aj}|0\rangle$

*External:* $V_f$: $\hat{E}_{at}\hat{E}_{bu}|0\rangle$

$V_g$: $\hat{E}_{ai}\hat{E}_{bt}|0\rangle$

$V_h$: $\hat{E}_{ai}\hat{E}_{bj}|0\rangle$

where the indices $(i,j)$, $(t,u,v)$ and $(a,b)$ refer to inactive, active and secondary orbitals respectively. When the off-diagonal elements are included in $F_N$, the resulting matrix contains additional sparse blocks. A more accurate result is obtained in this latter case but at the expense of a significant computational effort.

The first order wavefunction is expanded into the various configurations of $V_{SD}$ with coefficients obtained by solving Equation A-38. In order to obtain these coefficients, required for the computation of the second order perturbation energy, a diagonalisation of $[\mathbf{F_N}\text{-}E_0\mathbf{S}]$ needs to be performed in two steps. First, the overlap matrix **S** is diagonalised. In case of linear dependencies of the functions used to expand $V_{SD}$, some of the resulting diagonal elements would result in values close to zero. In such cases, the corresponding eigenvectors are discarded and a matrix of a smaller dimension is obtained:

$$\Lambda s = U^{\dagger} \mathrm{SU} \tag{A-42}$$

With this transformation, the first order interacting space can be expressed as

$$\left[\widetilde{F}_D - E_0 1\right]\widetilde{C} = -\widetilde{V} \tag{A-43}$$

where the following definitions have been used:

$$\widetilde{F}_D = U\Lambda_s^{-1/2} F_D U\Lambda_s^{-1/2},\ U\Lambda_s^{-1/2}\widetilde{C} = C \text{ and } \widetilde{V} = U\Lambda_s^{-1/2} V \tag{A-44}$$

The following step consists on diagonalising the Fock matrix, which after the transformation retains its block structure. The diagonal matrix $\mathbf{\Lambda}_{\mathrm{D}}$ is related to $\mathbf{F}_{\mathrm{D}}$ by

$$\Lambda_D = W^{\dagger} \widetilde{F}_D W \tag{A-45}$$

and the final form for the interacting space is given by

$$\left[\Lambda_D - E_0 1\right]\widetilde{\widetilde{C}} = -\widetilde{\widetilde{V}} \Rightarrow \widetilde{\widetilde{C}} = -\left[\Lambda_D - E_0 1\right]^{-1}\widetilde{\widetilde{V}} \tag{A-46}$$

where

$$U\Lambda_S^{-1/2} W\widetilde{\widetilde{C}} = C \text{ and } \widetilde{\widetilde{V}} = \left[U\Lambda_S^{-1/2} W\right]^{\dagger} \mathrm{V} \tag{A-47}$$

Using the expression for the coefficients of the first order wavefunction, given by Equation A-43, the second order perturbation energy can be obtained following Equation A-29, as obtained by Rayleigh-Schrödinger perturbation theory:

$$E_2 = \left\langle 0 \middle| \hat{H} \middle| \Psi^{(1)} \right\rangle = V^{\dagger} C = -\tilde{\tilde{V}}^{\dagger} \left[ \Lambda_D - E_0 1 \right]^{-1} \tilde{\tilde{V}} \qquad \text{(A-48)}$$

This last expression has an easy solution and results in a summation of terms expanding the linear independent functions contained in $V_{SD}$. Each term consist of a multiplication of matrix elements that contain the interaction of the reference function with $V_{SD}$ divided by a scalar representing an energy difference between the functions in $V_{SD}$ and the reference function.

### A.6.4. The MS-CASPT2 method

The CASPT2 method can be inadequate at avoided crossing. In such instances, the CASSCF wave function is not a good reference state for the perturbation calculation, and strong mixing occurs between the reference state and one or more secondary-space CASSCF states, orthogonal to the reference state. Unfortunately, CASPT2 cannot account for this mixing. The CASPT2 method can also run into problems when valence-Rydberg mixing occurs at the CASSCF level. As in avoided crossings, in such instances the CASSCF wave function is not a good zeroth-order description for either the valence or Rydberg states. A natural remedy to this prob1em, and also applicable to avoided crossing regions, is to use multistate CASPT2 (MS-CASPT2). MS-CASPT2 uses a multi-dimensional reference space that is

spanned by two or more state-average CASSCF states. An effective Hamiltonian $H^{eff}$ is computed perturbatively and diagonalized within the reference space, permitting the CASSCF states to interact via $H^{eff}$.

The formalism of this method is out of the needs of this thesis, and can be found in ref. 192. Simplifying, it can be said that the multireference $H^{eff}$ is based on a linear combination of single states operators. Therefore, the diagonal elements of the second order $H^{eff}$ are given by the single reference CASPT2 energies, while the off-diagonal are just combination of the reference states.

# Bibliography


(1) Feynman, R. P. In *Engineering and Science*, **1960**; Vol. February.

(2) Taniguchi, N. In *Proc. Intl. Conf. Prod. Eng. Tokyo, Part II*; Japan Society of Precision Engineering, **1974**.

(3) Drexler, K. E. *Engines of Creation The coming Era of Nanotechnology*; Anchor Books: New York, **1986**.

(4) Drexler, K. E. *Nanosystems: Molecular Machinery, Manufacturing, and Computation*; John Wiley & Sons, Inc.: New York, **1992**.

(5) *Wikipedia, the free encyclopedia* http://en.wikipedia.org/wiki/Main_Page

(6) *Istituto e Museo di Storia della Scienza* http://www.imss.fi.it

(7) Sinicropi, A.; Pischel, U.; Basosi, R.; Nau, W. M.; Olivucci, M. *Angew. Chem. Int. Ed.* **2000**, *39*, 4582-4586; Sinicropi, A.; Nau, W. M.; Olivucci, M. *Photochemical & Photobiological Sciences* **2002**, *1*, 537-546.

(8) Sinicropi, A.; Pogni, R.; Basosi, R.; Robb, M. A.; Gramlich, G.; Nau, W. M.; Olivucci, M. *Angew. Chem. Int. Ed.* **2001**, *40*, 4185-4189.

(9) Ismail, N.; Blancafort, L.; Olivucci, M.; Kohler, B.; Robb, M. A. *J. Am. Chem. Soc.* **2002**, *124*, 6818.

(10) Garavelli, M.; Page, C. S.; Celani, P.; Olivucci, M.; Schmid, W. E.; Trushin, S. A.; Fuss., W. *J. Phys. Chem. A* **2001**, *105*, 4458-4469.

(11) Badjic, J. D.; Balzani, V.; Credi, A.; Silvi, S.; Stoddart, J. F. *Science* **2004**, *303*, 1845-1849.

(12) Koumura, N.; Zijlstra, R. W. J.; Van Delden, R. A.; Harada, N.; Feringa, B. L. *Nature (London)* **1999**, *401*, 152-155.

(13) Astumian, R. D. In *Scientific American*, **2001**; Vol. July, pp 56-64.

(14) Hong, F. T. In *CRC Handbook of Organic Photochemistry and Photobiology*; Second Edition ed.; Horspool, W., Lenci, F., Eds.; CRC Press: Boca Raton FL, **2004**, p 134.

(15) El-Sayed, M. A. *Acc. Chem. Res.* **1992**, *25*, 279-286.

(16) Cordy, M. *The Miracle Strain*; Bantam Press, **1997**.

(17) Libertino, S.; Fichera, M.; D'arrigo, G.; La Mantia, A.; Ricceri, D. *Synthetic Metals* **2003**, *138*, 71-74; Libertino, S.; Fichera, M.; La Mantia, A.; Ricceri, D. *Synthetic Metals* **2003**, *138*, 141-144.

(18) Hampp, N. *Chem. Rev.* **2000**, *100*, 1755-1776; Birge, R. R. *Ann. Rev. Phys. Chem.* **1990**, *41*, 683-733; Rothschild, K. J.; Gite, S.;

Mamaev, S.; Olejnik, J. In *CRC Handbook of Organic Photochemistry and Photobiology*; Second Edition ed.; Horspool, W., Lenci, F., Eds.; CRC Press: Boca Raton FL, **2004**, p 133; Hampp, N. A. *Appl. Microbiol. Biotechol* **2000**, *53*, 633-639.

(19) Klessinger, M. *Ang. Chem. Int. Ed.* **1995**, *34*, 549-551.

(20) Bernardi, F.; Olivucci, M.; Robb, M. A. *Chem. Soc. Rev.* **1996**, *25*, 321-328.

(21) Robb, M. A.; Garavelli, M.; Olivucci, M.; Bernardi, F. In *Reviews in Computational Chemistry*; Lipkowitz, K. B., D. B. Boyd, Ed.; Wiley-VCH: John Wiley and Sons Inc.: New York, **2000**; Vol. 15, pp 87-146.

(22) Anglada, J. M.; Bofill, J. M. *J. Comp. Chem.* **1997**, *18*, 992-1003.

(23) Kandori, H.; Shichida, Y.; Yoshizawa, T. *Biochemistry (Moscow)* **2001**, *66*, 1197-1209.

(24) Mathies, R. A.; Lugtenburg, J. In *Handbook of Biological Physics*; Stavenga, D. G., W. J. de Grip, E.N. Pugh, Ed.; Elsevier Science B. V., **2000**; Vol. 3; Needleman, R. In *CRC Handbook of Organic Photochemistry and Photobiology*; Horspool, W. M., P.-S. Song, Ed.; CRC Press: Boca Raton, FL, **1995**; Yoshizawa, T.; Kuwata, O. In *CRC Handbook of Organic Photochemistry and Photobiology*; Horspool, W. M., P.-S. Song, Ed.; CRC Press: Boca Raton, FL, **1995**; Menon, S. T.; Han, M.; Sakmar, T. P. *Physiol. Rev.* **2001**, *81*, 1659-1688.

(25) Ottolenghi, M.; Sheves, M. *Isr. J. Chem.* **1995**, *35*, 193-513.

(26) Shichida, Y.; Yoshizawa, T. In *CRC Handbook of Organic Photochemistry and Photobiology*; Second Edition ed.; Horspool, W., Lenci, F., Eds.; CRC Press: Boca Raton FL, **2004**, p 125.

(27) Wald, G.; Nobel Lecture, **1967**.

(28) Wald, G. *Science* **1968**, *162*, 230-239.

(29) Hecht, S.; Shaler, S.; Pirenne, M. H. *J. Gen. Physiol* **1942**, *25*, 819.

(30) Langley, S. P. *Phil Mag* **1889**, *27*, 1.

(31) Jung, K.-H.; Spudich, J. L. In *CRC Handbook of Organic Photochemistry and Photobiology*; Second Edition ed.; Horspool, W., Lenci, F., Eds.; CRC Press: Boca Raton FL, **2004**, p 124.

(32) Oesterhelt, D.; Stoeckenius, W. *Nature (London), New Biol.* **1971**, *233*, 149-152.

(33) Venter, J. C.; Remington, K.; Heidelberg, J. F.; Halpern, A. L.; Rusch, D.; Eisen, J. A.; Wu, D.; Paulsen, I.; Nelson, K. E.; Nelson, W.; Fouts, D. E.; Levy, S.; Knap, A. H.; Lomas, M. W.; Nealson, K.; White, O.; Peterson, J.; Hoffman, J.; Parsons, R.; Baden-Tillson,

H.; Pfannoch, C.; Rogers, Y.-H.; Smith, H. O. *Science* **2004**, *304*, 66-74.
(34) Bennet, N.; Michel-Villaz, M.; Kuhn, H. *Eur. J. Biochem.* **1982**, *127*, 97; Emeis, D.; Kuhn, H.; Reichert, J.; Hofmann, K. P. *FEBS Lett.* **1982**, *143*, 29.
(35) Fukada, Y.; Yoshizawa, T. *Biochim. Biophys. Acta* **1981**, *675*, 195.
(36) Yau, K. W. *Invest. Ophtalmol. Vis. Sci.* **1994**, *35*, 9.
(37) Baylor, D. *Proc. Natl. Acad. Sci. USA* **1996**, *93*, 560.
(38) Gether, U.; Kobilka, B. K. *J. Biol. Chem.* **1998**, *273*, 979.
(39) Han, M.; Lou, J.; Nakanishi, K.; Sakamar, T. P.; Smith, S. O. *J. Biol. Chem.* **1997**, *272*, 23081-23085; Robinson, P. R.; Cohen, G. B.; Zhukovsky, E. A.; Oprian, D. D. *Neuron* **1992**, *9*, 719.
(40) Baldwin, J. M.; Schertler, G. F.; Unger, V. M. *J. Mol. Biol.* **1997**, *272*, 144.
(41) Okada, T.; Le Trong, I.; Fox, B. A.; Behnke, C. A.; Stenkamp, R. E.; Palczewski, K. *J. Struct. Biol.* **2000**, *130*, 73.
(42) Palczewski, K.; Kumasaka, T.; Hori, T.; Behnke, C. A.; Motoshima, H.; Fox, B. A.; Le Trong, I.; Teller, D. C.; Okada, T.; Stenkamp, R. E.; Yamamoto, M.; Miyano, M. *Science* **2000**, *289*, 739.
(43) Teller, D. C.; Okada, T.; Behnke, C.; Palczewski, K.; Stenkamp, R. E. *Biochemistry* **2001**, *40*, 7761-7772.
(44) Fishkin, N.; Berova, N.; Nakanishi, K. *Chemical Record* **2004**, *4*, 120-135.
(45) Hargrave, P. A.; Mcdowell, J. H.; Curtis, D. R.; Wang, J. K.; Juszczak, E.; Fong, S. L.; Rao, J. K.; Argos, P. *Biophys. Struct. Mech.* **1983**, *9*, 235; Bownds, D. *Nature (London)* **1967**, *216*, 1178; Ovchinnikov, Y. A.; Abdulaev, N. G.; Feigina, M.; Artamonov, I. D.; Bogachuk, A. S. *Bioorg. Khim.* **1983**, *9*, 1331.
(46) Nathans, J. *Biochemistry* **1990**, *29*, 9746.
(47) Okada, T.; Fujiyoshi, Y.; Silow, M.; Navarro, J.; Landau, E. M.; Shichida, Y. *Proc. Natl. Acad. Sci. USA* **2002**, *99*, 5982.
(48) Yoshizawa, T.; Wald, G. *Nature (London)* **1963**, *197*, 1279.
(49) Shichida, Y.; Matuoka, S.; Yoshizawa, T. *Photochem. Photobiol.* **1984**, *7*, 221.
(50) Schoenlein, R. W.; Peteanu, L. A.; Mathies, R. A.; Shank, C. V. *Science* **1991**, *254*, 412-415.
(51) Tachibanaki, S.; Imai, H.; Mizukami, T.; Okada, T.; Imamoto, Y.; Matsuda, T.; Fukada, Y.; Terakita, A.; Shichida, Y. *Biochemistry* **1997**, *36*, 14173-14180; Hug, S. J.; Lewis, J. W.; Einterz, C. M.;

Thorgeirsson, T. E.; Kliger, D. S. *Biochemistry* **1990**, *29*, 1475; Pan, D.; Mathies, R. A. *Biochemistry* **2001**, *40*, 7929-7936.
(52) Kim, J. E.; Mccamant, D. W.; Zhu, L.; Mathies, R. A. *J. Phys. Chem. B* **2001**, *105*, 1240-1249.
(53) Oseroff, A. R.; Callender, R. H. *Biochemistry* **1974**, *13*, 4243.
(54) Borhan, B.; Souto, M. L.; Imai, H.; Shichida, Y.; Nakanishi, K. *Science* **2000**, *288*, 2209.
(55) Furutani, Y.; Kandori, H.; Shichida, Y. *Biochemistry* **2003**, *42*, 8494-8500.
(56) Stoeckenius, W.; Lozier, R. H.; Bogomolni, R. *Biochem. Biophys. Acta* **1979**, *505*, 215-278.
(57) Ibawe, N.; Kuma, K.-I.; Hasegawa, M.; Osawa, S.; Migata, T. *Proc. Natl. Acad. Sci. USA* **1989**, *86*, 9355-9359; Madigan, M. T.; Martinko, J. M.; Parker, J. B. *Biology of Microorganisms*; 8th ed.; Prentice Hall: New York, **1997**.
(58) *Great Salt Lake Bacteria* http://people.westminstercollege.edu/faculty/tharrison/gslfood/studentpages/Bacteria.html
(59) *Why Owens Lake is Red (DesertUSA)* http://www.desertusa.com/mag98/april/owens/owenslake.html
(60) *Fotorecettori e Recettori Olfattivi* http://www.biologia.uniba.it/fisiologia/corcelli/it/home.htm
(61) Dencher, N. A.; Heyn, M. P. *FEBS Lett.* **1979**, *108*, 307-310; Dencher, N. A.; Heyn, M. P. *Methods Enzymol.* **1982**, *88*, 5-10; Wang, J.; Link, S.; Heyes, C.; El-Sayed, M. A. *Biophys. J.* **2002**, *83*, 1557-1566.
(62) Shen, Y.; Safinya, C. R.; Liang, K. S.; Ruppert, A. F.; Rothschild, K. J. *Nature (London)* **1993**, *366*, 48-50; Lukashev, E. P.; Robertson, B. *Bioelectrochem. Bioenerg.* **1995**, *37*, 157-160.
(63) Lanyi, J.; Luecke, H. *Current Opinion in Struct. Biol.* **2001**, *11*, 415-419; Lanyi, J.; Varo, G. *Isr. J. Chem.* **1995**, *35*, 157-160.
(64) Rammelsberg, R.; Huhn, G.; Luebben, M.; Gerwert, K. *Biochemistry* **1998**, *37*, 5001-5009; Zscherp, C.; Schlesinger, R.; Heberl, J. *Biochem. Biophys. Res. Commun.* **2001**, *283*, 57-63.
(65) Dirac, P. A. M. *Proc. Roy. Soc. (London) A* **1928**, *117*, 610-624; Dirac, P. A. M. *Proc. Roy. Soc. (London) A* **1928**, *118*, 351-361; Dirac, P. A. M. *Principles of Quantum Mechanics*; 4th ed.; Oxford University Press, **1982**.

(66) Dirac, P. A. M. *Proc. Roy. Soc. (London) A* **1927**, *117*, 243-265; Fermi, E. *Nuclear Physics, Revised Edition*; University of Chicago Press, **1950**.

(67) Reid, G. D.; Wynne, K. In *Encyclopedia of Analytical Chemistry*; Meyers, R. A., Ed.; John Wiley & Sons Ltd: Chichester, **2000**, pp 13644-13670; Reid, G. D.; Wynne, K. In *Handbook of Laser Technology and Applications*; Webb, C. E., Jones, J. D. C., Eds.; Institute of Physics Press, **2003**; Vol. III D6.3, p 2507.

(68) Zewail, A. H. *The Chemical Bond. Structure and Dynamics*; Academic Press: Boston, **1992**.

(69) Grimberg, B. I.; Lozovoy, V. V.; Dantus, M.; Mukamel, S. *J. Phys. Chem. A* **2002**, *106*, 697-718; Mukamel, S. *Annu. Rev. Phys. Chem.* **1990**, *41*, 647-681; Pollard, W. T.; Mathies, R. A. *Annu. Rev. Phys. Chem.* **1992**, *43*; Kosloff, R. *J. Phys. Chem.* **1988**, *92*, 2087-2100; Heller, E. J. *Acc. Chem. Res.* **1981**, *14*, 368-375; Stock, G.; Domcke, W. In *Conical Intresections Electronic Structure, Dynamics and Spectroscopy*; Domcke, W., Yarkony, D. R., Köppel, H., Eds.; World Scientific: Singapore, **2004**; Domcke, W.; Stock, G. In *Advances in Chemical Physics*; Prigogine, I., Rice, S. A., Eds.; Wiley US, **1997**; Vol. 100.

(70) Zewail, A. H.; Nobel Lecture, **1999**.

(71) *Masters of Photography: Eadweard Muybridge* http://www.masters-of-photography.com/M/muybridge/muybridge_galloping_horse_full.html

(72) *MATRIX* http://whatisthematrix.warnerbros.com/cmp/sfx-bullet_stills.html

(73) Mckee, M. L.; Page, M. In *Reviews in Computational Chemistry*; Lipkowitz, K. B., D. B. Boyd, Ed.; VCH Publishers, **1993**; Vol. 4, pp 35-65.

(74) Foresman, J. B.; Head-Gordon, M.; Pople, J. A.; Frisch, A. *J. Phys. Chem.* **1992**, *96*, 135 and references therein.

(75) Truhlar, D. G.; Steckler, R.; Gordon, M. S. *Chem. Rev.* **1987**, *1*, 217; Truhlar, D. G.; Gordon, M. S. *Science* **1990**, *249*, 491.

(76) Leach, A. R. *Molecular Modelling*; Longman: Singapore, **1996**; Kendall, R. A.; Harrison, R. J.; Littlefield, R. J.; Guest, M. F. In *Review in Computational Chemistry*; Lipkowiz, K. B., Boyd, D. B., Eds.; Wiley-VCH: New York, **1995**; Vol. 6, pp 209-301.

(77) Foresman, J. B.; Frisch, A. *Exploring Chemistry with Electronic Structure Methods*; Gaussian, Inc.: Pittsburgh, **1996**; Vol. Chapter 3 and references therein.
(78) Klessinger, M.; Michl, J. *Excited States and Photochemistry of Organic Molecules*; VCH: New York, **1995** and references therein.
(79) Bartlett, R. J.; Stanton, J. F. In *Review in Computational Chemistry*; Lipkowiz, K. B., Boyd, D. B., Eds.; Wiley-VCH: New York, **1997**; Vol. 5, pp 65-169.
(80) Roos, B. O. In *Adv. Chem. Phys. (Ab initio Methods in Quantum Chemistry-II)*; Lawley, K. P., Ed.; Wiley: New York, **1987**; Vol. 69, pp 399-446.
(81) Szabo, A.; Ostlund, N. S. *Modern Quantum Chemistry: Introduction to Advanced Electronic Structure Theory*; Dover Publications, Inc.: Mineola, **1996**.
(82) Trulson, M. O.; Mathies, R. A. *J. Phys. Chem.* **1990**, *94*, 5741.
(83) Kozlowski, P. M.; Dupuis, M.; Davidson, E. R. *J. Am. Chem. Soc.* **1995**, *117*, 774-778.
(84) Mcdouall, J. J.; Peasley, K.; Robb, M. A. *Chem. Phys. Lett.* **1988**, *148*, 183.
(85) Andersson, K.; Malmqvist, P.-Å.; Roos, B. O. *J. Chem. Phys.* **1992**, *96*, 1218.
(86) Schlick, T. In *Review in Computational Chemistry*; Lipkowiz, K. B., Boyd, D. B., Eds.; Wiley-VCH: New York, **1993**; Vol. III, pp 1-71; Schlegel, H. B. In *Ab initio Methods in Quantum Chemistry-I*; Lawley, K. P., Ed.; John Wiley & Sons, Ltd.: New York, **1987**; Vol. 67, pp 249-286 and references therein.
(87) Gonzales, C.; Schlegel, H. B. *J. Phys. Chem.* **1990**, *94*, 5523.
(88) Ragazos, I. N.; Robb, M. A.; Bernardi, F.; Olivucci, M. *Chem. Phys. Lett.* **1992**, *197*, 217.
(89) Bearpark, M. J.; Robb, M. A.; Schlegel, H. B. *Chem. Phys. Lett.* **1994**, *223*, 269.
(90) Van Der Lugt, W. T. A. M.; Oosteroff, L. J. *J. Am. Chem. Soc.* **1969**, *91*, 6042.
(91) Bernardi, F.; Bottoni, A.; Olivucci, M.; Robb, M. A.; Venturini, A. *J. Am. Chem. Soc.* **1993**, *115*, 3322-3323.
(92) Pullen, S.; Ii, L. A. W.; Donovan, B.; Sension, R. J. *Chem. Phys. Lett.* **1995**, *242*, 415.
(93) Reid, P. J.; Doig, S. J.; Wickham, S. D.; Mathies, R. A. *J. Am. Chem. Soc.* **1993**, *115*, 4754 and references therein.
(94) Cyr, D. R.; Hayden, C. C. *J. Chem. Phys.* **1996**, *104*, 771.

(95) Kandori, H.; Katsuta, Y.; Ito, M.; Sasabe, H. *J. Am. Chem. Soc.* **1995**, *117*, 2669-2670.
(96) Nakanishi, K.; Chen, A.-H.; Derguini, F.; Franklin, P.; Hu, S.; Wang, J. *Pure & Appl. Chem.* **1994**, *66*, 981-988.
(97) Zimmerman, H. E. *J. Am. Chem. Soc.* **1966**, *88*, 1566.
(98) Michl, J. *Top. Curr. Chem.* **1974**, *46*, 1.
(99) Michl, J. *J. Mol. Photochem.* **1972**, *243,257*.
(100) Salem, L. *J. Am. Chem. Soc.* **1974**, *96*, 3486-3501.
(101) Teller, E. *J. Phys. Chem.* **1937**, *41*, 109.
(102) Gerhartz, W.; Poshusta, R. D.; Michl, J. *J. Am. Chem. Soc.* **1977**, *99*, 4263; Gerhartz, W.; Poshusta, R. D.; Michl, J. *J. Am. Chem. Soc.* **1976**, *98*, 6427.
(103) Dauben, W. G.; Salem, L.; Turro, N. J. *Acc. Chem. Res.* **1975**, *8*, 41.
(104) Bonacic-Koutecky, V.; Michl, J. *Teor. Chim. Acta* **1985**, *68*, 45.
(105) Salem, L.; Rowland, C. *Angew. Chem. Int. Ed.* **1972**, *11*, 92; Borden, W. T. *Diradicals*; Wiley: New York, **1982**.
(106) Michl, J.; Bonacic-Koutecky, V. *Tetrahedron* **1988**, *44*, 7559; Bonacic-Koutecky, V.; Schoffel, K. J.; Michl, J. *Theor. Chim. Acta* **1987**, *72*, 459-474.
(107) Michl, J.; Bonacic-Koutecky, V. *Electronic Aspects of Organic Photochemistry*; Wiley: New York, **1990**.
(108) Yarkony, D. R. *Rev. Mod. Phys.* **1996**, *68*, 985 and references therein; Yarkony, D. R. *J. Chem. Phys.* **1990**, *92*, 2457.
(109) Atchity, G. J.; Xantheas, S. S.; Ruedenberg, K. *J. Chem. Phys.* **1991**, *95*, 1862-1876 and references therein.
(110) Grimbert, D.; Segal, G.; Devaquet, A. *J. Am. Chem. Soc.* **1975**, *97*, 6629.
(111) Bernardi, F.; De, S.; Olivucci, M.; Robb, M. A. *J. Am. Chem. Soc.* **1990**, *112*, 1737-1744.
(112) Palmer, I. J.; Ragazos, I. N.; Bernardi, F.; Olivucci, M.; Robb, M. A. *J. Am. Chem. Soc.* **1993**, *115*, 673-682.
(113) Celani, P.; Ottani, S.; Olivucci, M.; Bernardi, F.; Robb, M. A. *J. Am. Chem. Soc.* **1994**, *116*, 10141-10151.
(114) Palmer, I. J.; Ragazos, I. N.; Bernardi, F.; Olivucci, M.; Robb, M. A. *J. Am. Chem. Soc.* **1994**, *116*, 2121-2132.
(115) Reguero, M.; Olivucci, M.; Bernardi, F.; Robb, M. A. *J. Am. Chem. Soc.* **1994**, *116*, 2103-2114 and references therein.
(116) Yamamoto, N.; Bernardi, F.; Bottoni, A.; Olivucci, M.; Robb, M. A.; Wilsey, S. *J. Am. Chem. Soc.* **1994**, *116*, 2064-2074 and

references therein; Wilsey, S.; Bearpark, M. J.; Bernardi, F.; Olivucci, M.; Robb, M. A. *J. Am. Chem. Soc.* **1996**, *118*, 4469-4479.
(117) Celani, P.; Bernardi, F.; Olivucci, M.; Robb, M. A. *J. Chem. Phys.* **1995**, *102*, 5733-5742.
(118) Wilsey, S.; Bearpark, M. J.; Bernardi, F.; Olivucci, M.; Robb, M. A. *J. Am. Chem. Soc.* **1996**, *118*, 176-184.
(119) Bearpark, M. J.; Bernardi, F.; Clifford, S.; Olivucci, M.; Robb, M. A.; Smith, B. R.; Vreven, T. *J. Am. Chem. Soc.* **1996**, *118*, 169-175.
(120) Celani, P.; Garavelli, M.; Ottani, S.; Bernardi, F.; Robb, M. A.; Olivucci, M. *J. Am. Chem. Soc.* **1995**, *117*, 11584-11585.
(121) Desouter-Lecomte, M.; Lorquet, J. C. *J. Chem. Phys.* **1979**, *71*, 4391.
(122) Teller, E. *Israel J. Chem* **1969**, *7*, 227.
(123) Herzberg, G.; Longuet-Higgins, H. C. *Discuss. Faraday. Soc.* **1963**, *35*, 77.
(124) Olivucci, M. *Superfici Adiabatiche e Diabatiche nel trattamento della Reattività Chimica*, Ph. D. Thesis; University of Bologna: Bologna, **1988**
(125) Bernardi, F.; Olivucci, M.; Robb, M. A. *Israel J. Chem.* **1993**, *33*, 265-276.
(126) Fuss, W.; Kompa, K. L.; Lochbrunner, S.; Müller, A. M. *Chem. Phys.* **1998**, *232*, 174; Trushin, S. A.; Fuss, W.; Schmid, W. E. *Chem. Phys.* **2000**, *259*, 313; Diau, E. W. G.; De Feyter, S.; Zewail, A. H. *J. Chem. Phys.* **1999**, *110*, 9785; Chachisvilis, M.; Zewail, A. H. *J. Phys. Chem. A* **1999**, *103*, 7408.
(127) Zhong, D.; Diau, E. W. G.; Bernhardt, T. M.; De Feyter, S.; Roberts, J. D.; Zewail, A. H. *Chem. Phys. Lett.* **1998**, *298*, 129; Metsdagh, J. M.; Visicot, J. P.; Elhanine, M.; Soep, B. *J. Chem. Phys.* **2000**, *113*, 237.
(128) Zewail, A. H. *J. Phys. Chem.* **1996**, *100*, 12701.
(129) Leigh, W. J.; Postigo, A. *J. Chem. Comm.* **1993**, *24*, 1836.
(130) Migani, A.; Olivucci, M. In *"Conical Intersections: Electronic Structure, Dynamics and Spectroscopy"*; Domcke, W., Yarkony, D. R., Köppel, H., Eds.; World Scientific: Singapore, **2004**.
(131) Smith, B. R.; Bearpark, M. J.; Robb, M. A.; Bernardi, F.; Olivucci, M. *Chem. Phys. Lett.* **1995**, *242*, 27.
(132) Palmer, I. J.; Olivucci, M.; Bernardi, F.; Robb, M. A. *J. Org. Chem.* **1992**, *57*, 5081-5087.
(133) Garavelli, M.; Celani, P.; Bernardi, F.; Robb, M. A.; Olivucci, M. *J. Am. Chem. Soc.* **1997**, *119*, 6891-6901.

(134) Nau, W. M.; Greiner, G.; Rau, H.; Olivucci, M.; Robb, M. A. *Ber. Bunsenges. Phys. Chem.* **1998**, *102*, 486-492.
(135) Flükiger, P.; Lüthi, H. P.; Portmann, S.; Weber, J. *MOLEKEL 4.3*, Swiss Center for Scientific Computing, Manno (Switzerland), **2002**
(136) Garavelli, M.; Bernardi, F.; Olivucci, M.; Vreven, T.; Klein, S.; Celani, P.; Robb, M. A. *Faraday Discuss.* **1998**, *110*, 51.
(137) De Vico, L.; Page, C. S.; Garavelli, M.; Bernardi, F.; Basosi, R.; Olivucci, M. *J. Am. Chem. Soc.* **2002**, *124*, 4124-4134.
(138) Vreven, T.; Bernardi, F.; Garavelli, M.; Olivucci, M.; Robb, M. A.; Schlegel, H. B. *J. Am. Chem. Soc.* **1997**, *119*, 12687.
(139) Gonzalez-Luque, R.; Garavelli, M.; Bernardi, F.; Merchan, M.; Robb, M. A.; Olivucci, M. *Proc. Natl. Acad. Sci. USA* **2000**, *97*, 9379-9384.
(140) Zhong, Q.; Ruhman, S.; Ottolenghi, M.; Sheves, M.; Friedman, N.; Atkinson, G. H.; Delaney, J. K. *J. Am. Chem. Soc.* **1996**, *118*, 12828-12829.
(141) Kakitani, T.; Akiyama, R.; Hatano, Y.; Imamoto, Y.; Shichida, Y.; Verdegem, P.; Lugtenburg, J. *J. Phys. Chem. B* **1998**, *102*, 1334-1339.
(142) Haran, G.; Morlino, E. A.; Matthes, J.; Callander, R. H.; Hochstrassen, R. M. *J. Phys. Chem. A* **1999**, *103*, 2202-2207.
(143) Garavelli, M.; Bernardi, F.; Celani, P.; Robb, M. A.; Olivucci, M. *J. Photochem. Photobiol. A: Chem.* **1998**, *114*, 109-116.
(144) Olivucci, M.; Robb, M. A.; Bernardi, F. In *Conformational Analysis of Molecules in Excited States*; Waluk, J., Ed.; Wiley-VCH: John Wiley and Sons Inc.: New York, **2000**, pp 297-366.
(145) Bernardi, F.; Olivucci, M.; Michl, J.; Robb, M. A. *The Spectrum* **1996**, *9*, 1-6.
(146) Yamamoto, N.; Olivucci, M.; Celani, P.; Bernardi, F.; Robb, M. A. *J. Am. Chem. Soc.* **1998**, *120*, 2391-2407.
(147) Garavelli, M.; Celani, P.; Yamamoto, N.; Bernardi, F.; Robb, M. A.; Olivucci, M. *J. Am. Chem. Soc.* **1996**, *118*, 11656-11657.
(148) Mead, C. A.; Truhlar, D. G. *J. Chem. Phys.* **1979**, *70*, 2284-2296.
(149) Garavelli, M.; Vreven, T.; Celani, P.; Bernardi, F.; Robb, M. A.; Olivucci, M. *J. Am. Chem. Soc.* **1998**, *120*, 1285-1288.
(150) Garavelli, M.; Celani, P.; Fato, M.; Bearpark, M. J.; Smith, B. R.; Olivucci, M.; Robb, M. A. *J. Phys. Chem. A* **1997**, *101*, 2023-2032.
(151) Friedrich, L. E.; Schuster, G. B. *J. Am. Chem. Soc.* **1969**, *91*, 7204-7205.
(152) Friedrich, L. E.; Schuster, G. B. *J. Am. Chem. Soc.* **1972**, *94*, 1193.

(153) Becker, R. S.; Inuzuka, K.; King, J. *J. Chem. Phys.* **1970**, *52*, 5164.
(154) Celani, P.; Robb, M. A.; Garavelli, M.; Bernardi, F.; Olivucci, M. *Chem. Phys. Lett.* **1995**, *243*, 1.
(155) Garavelli, M.; Negri, F.; Olivucci, M. *J. Am. Chem. Soc.* **1999**, *121*, 1023-1029.
(156) Olivucci, M.; Bernardi, F.; Ottani, S.; Robb, M. A. *J. Am. Chem. Soc.* **1994**, *116*, 2034-2048.
(157) Olivucci, M.; Ragazos, I. N.; Bernardi, F.; Robb, M. A. *J. Am. Chem. Soc.* **1993**, *115*, 3710-3721.
(158) Heller, H. G.; Elliot, C. C.; Koh, K.; Al-Shihry, S.; Whittall, J. In *Photochemistry and Polymeric Systems*; Kelly, J. M., McArdle, C. B., Maunder, M. J. d. F., Eds.; Royal Society of Chemistry: London, **1993**, pp 156-168.
(159) Jacobs, H. J. C.; Havinga, E. In *Advances in Photochemistry*; Pitts Jr, J. N., Hammond, G. S., Gollnick, K., Eds.; John Wiley & Sons: New York, **1979**; Vol. 11, pp 305-373; Dauben, W. G.; Mcinnis, E. L.; Mincho, D. M. *Photochemical rearrangements in trienes*; Academic Press: London, **1980**; Vol. 3.
(160) Jacobs, H. J. C. *Pure and Applied Chemistry* **1995**, *67*, 63; Brouwer, A. M.; Cornelisse, J.; Jacobs, H. J. C. *J. Photochem. Photobiol. A: Chem.* **1988**, *42*, 117; Brouwer, A. M.; Cornelisse, J.; Jacobs, H. J. C. *J. Photochem. Photobiol. A: Chem.* **1988**, *42*, 313.
(161) Matuszewski, B.; Burgstahler, A. W.; Givens, R. S. *J. Am. Chem. Soc.* **1982**, *104*, 6875; Dauben, W. G.; Rabinowitz, J.; Vietmeyer, N. D.; Wendschuh, P. H. *J. Am. Chem. Soc.* **1972**, *94*, 4285.
(162) Sinicropi, A. *The Mechanism of Light Energy Wastage and Exploitation in* $^1n,\pi^*$ *Chromophores.*, Ph. D. Thesis; University of Siena: Siena, **2002**
(163) Meyer, H.-D.; Manthe, U.; Cederbaum, L. S. *Chem. Phys. Lett.* **1990**, *165*, 73; Beck, M. H.; Jäckle, A.; Worth, G. A.; Meyer, H.-D. *Phys. Rep.* **2000**, *324*, 1.
(164) Leforestier, C. *J. Chem. Phys.* **1978**, *68*, 4406; Wang, I.; Karplus, M. *J. Am. Chem. Soc.* **1973**, *95*, 8160; Warshel, A.; Karplus, M. *Chem. Phys. Lett.* **1975**, *32*, 11.
(165) Littlejohn, R. *Phys. Rep.* **1986**, *138*, 193; Hermann, H. F. *Ann. Rev. Phys. Chem.* **1994**, *45*, 83; Sepulveda, M. A.; Grossmann, F. *Adv. Chem. Phys.* **1996**, *96*, 191.
(166) Helgaker, T.; Uggerud, E.; Jensen, H. *Chem. Phys. Lett.* **1990**, *173*, 145.
(167) Chen, W.; Hase, W.; Schlegel, H. *Chem. Phys. Lett.* **1994**, *228*, 446.

(168) Sloane, C. S.; Hase, W. L. *J. Chem. Phys.* **1977**, *66*, 1523; Chapman, S.; Bunker, D. L. *J. Chem. Phys.* **1975**, *62*, 2890.
(169) Martínez, T. J.; Ben-Nun, M.; Levine, R. D. *J. Phys. Chem.* **1996**, *100*, 7884.
(170) Tully, J. C.; Preston, R. K. *J. Chem. Phys.* **1971**, *55*, 562.
(171) Blais, N. C.; Truhlar, D. G.; Mead, C. A. *J. Chem. Phys.* **1988**, *89*, 6204.
(172) Amarouche, M.; Gadea, F. X.; Durup, J. *Chemical Physics* **1989**, *130*, 145.
(173) Sanchez-Galvez, A.; Hunt, P.; Robb, M. A.; Olivucci, M.; Vreven, T.; Schlegel, H. B. *J. Am. Chem. Soc.* **2000**, *122*, 2911-2924.
(174) Frisch, M. J.; Trucks, G. W.; Schlegel, H. B.; Scuseria, G. E.; Robb, M. A.; Cheeseman, J. R.; Zakrzewski, V. G.; Montgomery Jr., J. A.; Stratmann, R. E.; Burant, J. C.; Dapprich, S.; Millam, J. M.; Daniels, A. D.; Kudin, K. N.; Strain, M. C.; Farkas, O.; Tomasi, J.; Barone, V.; Cossi, M.; Cammi, R.; Mennucci, B.; Pomelli, C.; Adamo, C.; Clifford, S.; Ochterski, J.; Petersson, G. A.; Ayala, P. Y.; Cui, Q.; Morokuma, K.; Malick, D. K.; Rabuck, A. D.; Raghavachari, K.; Foresman, J. B.; Cioslowski, J.; Ortiz, J. V.; Baboul, A. G.; Stefanov, B. B.; Liu, G.; Liashenko, A.; Piskorz, P.; Komaromi, I.; Gomperts, R.; Martin, R. L.; Fox, D. J.; Keith, T.; Al-Laham, M. A.; Peng, C. Y.; Nanayakkara, A.; Gonzalez, C.; Challacombe, M.; Gill, P. M. W.; Johnson, B.; Chen, W.; Wong, M. W.; Andres, J. L.; Gonzalez, C.; Head-Gordon, M.; Replogle, E. S.; Pople, J. A. *Gaussian 98*, Revision A.7; Gaussian, Inc.: Pittsburgh PA, **1998**
(175) Andersson, K.; Blomberg, M. R. A.; Fülscher, M. P.; Karlstöm, G.; Lundh, R.; Malmqvist, P.-Å.; Neogrády, P.; Olsen, J.; Roos, B. O.; Sadlej, A. J.; Schütz, M.; Seijo, L.; Serrano-Andrés, L.; Siegbahn, P. E. M.; Widmark, P.-O. *MOLCAS*, Version 4.1; University of Lund: Lund, Sweden, **1997**
(176) Andersson, K.; Barysz, M.; Bernhardsson, A.; Blomberg, M. R. A.; Cooper, D. L.; Fülscher, M. P.; Graaf, C. D.; Hess, B. A.; Karlström, G.; Lindh, R.; Malmqvist, P.-Å.; Nakajima, T.; Neogrády, P.; Olsen, J.; Roos, B. O.; Schimmelpfennig, B.; Schütz, M.; Seijo, L.; Serrano-Andrés, L.; Siegbahn, P. E. M.; Stålring, J.; Thorsteinsson, T.; Veryazov, V.; Widmark, P.-O. *MOLCAS*, Version 5.4; Lund University, Sweden: **2002**
(177) Kim, J. E.; Pan, D.; Mathies, R. A. *Biochemistry* **2003**, *42*, 5169-5175.

(178) Ye, T.; Friedman, N.; Gat, Y.; H.Atkinson, G.; Sheves, M.; Ottolenghi, M.; Ruhman, S. *J. Phys. Chem. B* **1999**, *103*, 5122-5130.
(179) Ruhman, S.; Hou, B.; Friedman, N.; Ottolenghi, M.; Sheves, M. *J. Am. Chem. Soc.* **2002**, *124*, 8854-8858.
(180) Kim, J. E.; Tauber, M. J.; Mathies, R. A. *Biochemistry* **2001**, *40*, 13774-13778.
(181) Song, L.; El-Sayed, M. A.; Lanyi, J. K. *J. Phys. Chem.* **1996**, *100*, 10479-10481.
(182) Freedman, K. A.; Becker, R. S. *J. Am. Chem. Soc.* **1986**, *108*, 1245-1251.
(183) Lugonov, S. L.; Song, L.; El-Sayed, M. A. *J. Phys. Chem.* **1996**, *100*, 18586-18591.
(184) Kandori, H.; Matuoka, S.; Shichida, Y.; Yoshizawa, T.; Ito, M.; Tsukida, K.; Balogh-Nair, V.; Nakanishi, K. *Biochemistry* **1989**, *28*, 6460-6467.
(185) Hou, B.; Friedman, N.; Ruhman, S.; Sheves, M.; Ottolenghi, M. *J. Phys. Chem. B* **2001**, *105*, 7042-7048.
(186) Kandori, H.; Sasabe, H.; Nakanishi, K.; Yoshizawa, T.; Mizukami, T.; Shichida, Y. *J. Am. Chem. Soc.* **1996**, *118*, 1002-1005.
(187) Verdegem, P. J. E.; Bovee-Geurts, P. H. M.; De Grip, W. J.; Lugtenburg, J.; De Groot, H. J. M. *Biochemistry* **1999**, *38*, 11316-11324.
(188) Molnar, F.; Ben-Nun, M.; Martínez, T. J.; Schulten, K. *J. Mol. Struct.* **2000**, *506*, 169-178.
(189) Ben-Nun, M.; Molnar, F.; Shulten, K.; Martínez, T. J. *Proc. Natl. Acad. Sci. USA* **2002**, *99*, 1769-1773.
(190) Wang, Q.; Kochendoerfer, G. G.; Schoenlein, R. W.; Verdegem, P. J. E.; Lugtenburg, J.; Mathies, R. A.; Shank, C. V. *J. Phys. Chem.* **1996**, *100*, 17388-17394.
(191) Jang, G.-F.; Kuksa, V.; Filipek, S.; Bartl, F.; Ritter, E.; Gelb, M. H.; Hofmann, K. P.; K.Palczewski *J. Biol. Chem.* **2001**, *276*, 26148-26153.
(192) Finley, J.; Malmqvist, P.-Å.; Roos, B. O.; Serrano-Andrés, L. *Chem. Phys. Lett.* **1998**, *288*, 299-306.
(193) Page, C. S.; Olivucci, M. *J. Comput. Chem.* **2002**, *24*, 298-309.
(194) Sinicropi, A.; Migani, A.; De Vico, L.; Olivucci, M. *Photochem. Photobiol. Sci.* **2003**, *2*, 1250-1255.
(195) Migani, A.; Robb, M. A.; Olivucci, M. *J. Am. Chem. Soc.* **2003**, *125*, 2804.

(196) Warshel, A. *Nature (London)* **1976**, *260*, 679; Liu, R. S. H.; Asato, A. E. *Proc. Natl. Acad. Sci. USA* **1985**, *82*, 259.
(197) De Vico, L.; Garavelli, M.; Bernardi, F.; Olivucci, M. *J. Am. Chem. Soc.* **2005** in press.
(198) Mizukami, T.; Kandori, H.; Shichida, Y.; Chen, A.-H.; Derguini, F.; Caldwell, C. G.; Bigge, F.; Nakanishi, K.; Yoshizawa, T. *Proc. Natl. Acad. Sci. USA* **1993**, *90*, 4072-4076.
(199) Eliel, E. L.; Wilen, S. H. *Stereochemistry of organic compounds, cap. 9*; Wiley & Sons, **1994**.
(200) Zilberg, S.; Haas, Y. *Photochem. Photobiol. Sci.* **2003**, *2*, 1256-1263.
(201) Thomasson, W. A. *Unraveling the Mystery of Protein Folding* http://www.faseb.org/opar/protfold/protein.html
(202) Pauling, L.; Corey, R. B.; Branson, H. R. *Proc. Natl. Acad. Sci. USA* **1951**, *37*, 205-211.
(203) Anfinsen, C. B.; Redfield, R. R.; Choate, W. I.; Page, J.; Carroll, W. R. *J. Biol. Chem.* **1954**, *207*, 201-210.
(204) Alzheimer, A. *Zontralblatt fur Nervenkrankheiten* **1906**, *25*, 1134.
(205) Nielsen, E. B.; Schellman, J. A. *J. Phys. Chem.* **1967**, *71*, 2297.
(206) Frank, R.; Jacob, M.; Thunecke, F.; Fischer, G.; Schutkowski, M. *Angew. Chem. Int. Ed. Engl.* **2000**, *39*, 1120.
(207) Sifferlen, T.; Rueping, M.; Gademann, K.; Jaun, B.; Seebach, D. *Helv. Chim. Acta* **1999**, *82*, 2067.
(208) Zhao, J.; Wildemann, D.; Jacob, M.; Vargas, C.; Schiene-Fischer, C. *Chem. Commun.* **2003**, *22*, 2810-2811.
(209) Miwa, J. H.; Patel, A. K.; Vivatrat, N.; Popek, S. M.; Meyer, A. M. *Organic Letters* **2001**, *3*, 3373-3375.
(210) Miwa, J. H.; Pallivathucal, L.; Gowda, S.; Lee, K. E. *Organic Letters* **2002**, *4*, 4655-4657.
(211) Kumita, J. R.; Smart, O. S.; Woolley, G. A. *Proc. Natl. Acad. Sci. USA* **2000**, *97*, 3803; Renner, C.; Beherendt, R.; Spörlein, S.; Wachtveil, J.; Moroder, L. *Biopolymers* **2000**, *54*; Beherendt, R.; Renner, C.; Schenk, M.; Wang, F.; Wachtveitl, J.; Oesterhelt, D.; Moroder, L. *Angew. Chem. Int. Ed. Engl.* **1999**, *38*, 2771.
(212) Frank, R.; Jacob, M.; Thunecke, F.; Fischer, G.; Schutkowski, M. *J. Phys. Chem. A* **2000**, *104*, 7957.
(213) Kato, C.; Hamaguchi, H.; Tasumi, M. *J. Phys. Chem.* **1985**, *89*, 407.
(214) Harada, I.; Tasumi, M. *Chem. Phys. Lett.* **1980**, *70*, 279-282.
(215) Chen, X. G.; Asher, S. A.; Schweitzer-Stenner, R.; Mirkin, N. G.; Krimm, S. *J. Am. Chem. Soc.* **1995**, *117*, 2884.

(216) Li, Y.; Garrell, R. L.; Houk, K. N. *J. Am. Chem. Soc.* **1991**, *113*, 5895.
(217) Helbing, J.; Bregy, H.; Bredenbeck, J.; Pfister, R.; Hamm, P.; Huber, R.; Wachtveil, J.; De Vico, L.; Olivucci, M. *J. Am. Chem. Soc.* **2004**, *126*, 8823-8834.
(218) Thomsen, I.; Clausen, K.; Scheibye, S.; Lawesson, S.-O. *Org. Synth.* **1984**, *62*, 158.
(219) Bredenbeck, J.; Hamm, P. *Rev. Sci. Instrum.* **2003**, *74*, 3188.
(220) Hamm, P.; Kaindl, R. A.; Stenger, J. *Opt. Lett.* **2000**, *25*, 1798.
(221) Ataka, S.; Takeuchi, H.; Harada, I.; Tasumi, M. *J. Phys. Chem.* **1984**, *88*, 449.
(222) Alfano, J. C.; Walhout, P. K.; Kimura, Y.; Barbara, P. F. *J. Chem. Phys.* **1993**, *98*, 5996; Hart, E. J.; Boag, J. W. *J. Am. Chem. Soc.* **1962**, *84*, 4090-4095.
(223) Hamm, P.; Ohline, S. M. *J. Chem. Phys.* **1997**, *106*, 519.
(224) Sieler, G.; Schweitzer-Stenner, R. *J. Am. Chem. Soc.* **1997**, *119*, 1720.
(225) Walter, W.; Schaumann, E. *Chem. Ber.* **1971**, *104*, 3361.
(226) Gilbert, A.; Baggot, J. *Essential of Molecular Photochemistry*; Blackwell Scientific Publications: Oxford, **1991**; El-Sayed, M. A. *J. Chem. Phys.* **1964**, *41*, 2462.
(227) Adamo, C.; Barone, V. *Chem. Phys. Lett.* **2000**, *330*, 152-160.
(228) Markham, L. M.; Hudson, B. S. *J. Phys. Chem.* **1996**, *100*, 2731-2737.
(229) Asher, S. A.; Chi, Z.; Li, P. *Raman Spectrosc.* **1998**, *29*, 927.
(230) Larson, D. B.; Arnett, J. F.; Seliskar, C. J.; Mcglynn, S. P. *J. Am. Chem. Soc.* **1974**, *96*, 3370.
(231) Gill, P. E.; Murray, W. In *Numerical Methods for Constrained Optimization*; Gill, P. E., Murray, W., Eds.; Academic Press: London, **1974**.
(232) Gonzales, C.; Schlegel, H. B. *J. Chem. Phys.* **1991**, *95*, 5853; Fukui, K. *Acc. Chem. Res.* **1981**, *14*, 363.
(233) Koga, N.; Morokuma, K. *Chem. Phys. Lett.* **1985**, *119*, 371.
(234) Mana, M. R.; Yarkony, D. R. *J. Chem. Phys.* **1993**, *99*, 5251; Yarkony, D. R. *J. Chem. Phys.* **1993**, *97*, 4407.
(235) Farazdel, A.; Dupuis, M. *J. Comput. Chem.* **1991**, *12*, 276.
(236) Shanno, D. F. *Math. Comp.* **1970**, *24*, 647; Goldfarb, D. *Math. Comp.* **1970**, *24*, 23; Fletcher, R. *Comp. J.* **1970**, *13*, 317; Broyden, C. G. *J. Inst. Math. Appl.* **1970**, *6*, 222.
(237) Anglada, J. M.; Bofill, J. *J. Comput. Chem.* **1997**, *18*, 992.

(238) AMPAC program, local version, extended by D. Liotard, 1987
(239) Dewar, M. J. S.; Zoebisch, E. G.; Healy, E. F.; Stewart, J. J. P. *J. Am. Chem. Soc.* **1985**, *197*, 3902.
(240) Baker, J.; Bergon, D. *J. Comput. Chem.* **1993**, *14*, 1339; Baker, J. *J. Comput. Chem.* **1992**, *13*, 240; Baker, J. *J. Comput. Chem.* **1993**, *14*, 1085.
(241) Baker, J. *J. Comput. Chem.* **1997**, *18*, 1079.
(242) Banerjee, A.; Adams, N.; Simons, J.; Shepard, R. *J. Phys. Chem.* **1985**, *89*, 52.
(243) Andersson, K.; Barysz, M.; Bernhardsson, A.; Blomberg, M. R. A.; Carissan, Y.; Cooper, D. L.; Fülscher, M. P.; Gagliardi, L.; De Graaf, C.; Hess, B. A.; Hagberg, D.; Karlström, G.; Lindh, R.; Malmqvist, P.-Å.; Nakajima, T.; Neogrády, P.; Olsen, J.; Raab, J.; Roos, B. O.; Ryde, U.; Schimmelpfennig, B.; Schütz, M.; Seijo, L.; Serrano-Andrés, L.; Siegbahn, P. E. M.; Stålring, J.; Thorsteinsson, T.; Veryazov, V.; Widmark, P.-O. *MOLCAS*, Version 6.0; Lund University, Sweden: **2004**; Karlström, G.; Lindh, R.; Malmqvist, P.-Å.; Roos, B. O.; Ryde, U.; Veryazov, V.; Widmark, P.-O.; Cossi, M.; Schimmelpfennig, B.; Neogrady, P.; Seijo, L. *Computational Materials Science* **2003**, *28*, 222-239.
(244) Fletcher, R. *Practical Methods of Optimization*; Wiley: New York, **1981**.
(245) Schuster, D. I. In *The chemistry of enones*; Petai, S., Rappoport, Z., Eds.; John Wiley and Sons: Chichester, UK, **1989**; Vol. 2, pp 693-756; Schuster, D. I. In *Rearrangements in ground and exited states*; de Mayo, P., Ed.; Academic Press: London, **1980**; Vol. 3, pp 161-279.
(246) Reguero, M.; Olivucci, M.; Bernardi, F.; Robb, M. A. *J. Am. Chem. Soc.* **1994**, *116*, 2103-2114.
(247) Sampedro Ruiz, D.; Migani, A.; Pepi, A.; Busi, E.; Basosi, R.; Latterini, L.; Elisei, F.; Fusi, S.; Ponticelli, F.; Zanirato, V.; Olivucci, M. *J. Am. Chem. Soc.* **2004**, *126*, 9349-9359.
(248) Migani, A.; Sinicropi, A.; Ferré, N.; Cembran, A.; Garavelli, M.; Olivucci, M. *Faraday Discuss.* **2004**, *127*, 179-191; Ferré, N.; Olivucci, M. *J. Am. Chem. Soc.* **2003**, *125*, 6868-6869; Ferré, N.; Olivucci, M. *J. Mol. Struct. (Theochem)* **2003**, *632*, 71-82; Ferré, N.; Cembran, A.; Garavelli, M.; Olivucci, M. *Theor. Chim. Acc.* **2004**, *112*, 335-341; Andruniow, T.; Ferré, N.; Olivucci, M. *PNAS USA, in press* **2004**

(249) Andruniow, T.; Fantacci, S.; Angelis, F. D.; Olivucci, M. *paper in preparation* **2004**
(250) Sinicropi, A.; Andruniow, T.; De Vico, L.; Ferré, N.; Olivucci, M. *Pure & Appl. Chem.* **2005** in press.
(251) Hehre, W. J.; Radom, L.; Schleyer, P. V. R.; Pople, J. A. *Ab Initio Molecular Orbital Theory*; Wiley: New York, **1986** and references therein.
(252) Schrödinger, E. *Ann. Physik* **1926**, *79*, 361.
(253) Born, M.; Oppeheimer, J. R. *Ann. Physik* **1927**, *84*, 457.
(254) Pauli, W. *Z. Physik.* **1925**, *31*, 765.
(255) Slater, I. *J. Phys. Rev.* **1930**, *36*, 57.
(256) Boys, S. F. *Proc. Roy. Soc. (London) A* **1950**, *200*, 542-554.
(257) Møller, C.; Plesset, M. S. *Phys. Rev.* **1934**, *46*, 618.
(258) Roos, B. O.; Linse, P.; Siegbahn, P. E. M.; Blomberg, M. R. A. *Chem. Phys.* **1981**, *66*, 197.
(259) Andersson, K.; Malmqvist, P.-Å.; Ross, B. O.; Sadlej, A. J.; Wolisnki, K. *J. Phys. Chem.* **1990**, *94*, 5483.
(260) Helgaker, T.; Jørgensen, P.; Olsen, J. *Molecular Electronic-Structure Theory*; Wiley, **2000**.

# List of Publications

**De Vico, L.** "Cammini di Fotoisomerizzazione dei Cromofori delle Proteine Rodopsiniche", Tesi di Laurea, Università degli Studi di Siena, AA 2000/2001, Relatore Prof. Massimo Olivucci.

**De Vico, L.**; Page, C. S.; Garavelli, M.; Bernardi, F.; Basosi, R.; Olivucci, M. "Reaction Path Analysis of the 'Tunable' Photoisomerization Selectivity of Free and Locked Retinal Chromophores" *J. Am. Chem. Soc.* **2002**, *124*, 4124-4134.

Sinicropi, A.; Migani, A.; **De Vico, L.**; Olivucci, M. "Photoisomerization acceleration in retinal protonated Schiff-base models" *Photochem. Photobiol. Sci.* **2003**, *2*, 1250-1255.

Helbing, J.; Bregy, H.; Bredenbeck, J.; Pfister, R.; Hamm, P.; Huber, R.; Wachtveil, J.; **De Vico, L.**; Olivucci, M. "A Fast Photoswitch for Minimally Perturbed Peptides: Investigation of the trans→cis Photoisomerization of N-Methylthioacetamide" *J. Am. Chem. Soc.* **2004**, *126*, 8823-8834.

**De Vico, L.**; Garavelli, M.; Bernardi, F.; Olivucci, M. "Photoisomerization Mechanism of 11-cis-Locked Artificial Retinal Chromophores: Acceleration and Primary Photoproduct Assignment" *J. Am. Chem. Soc.* **2005**, *in press*.

Sinicropi, A.; Andruniow, T.; **De Vico, L.**; Ferré, N.; Olivucci, M. "Towards A Computational Photobiology" *Pure & Appl. Chem.* **2005**, *in press*.

**De Vico, L.**; Olivucci, M.; Lindh, R. “General tools for constrained geometry optimizations” paper in preparation.

# Presentations

## Poster Presentations

**Luca De Vico** and Massimo Olivucci. "Photoisomerization Paths of Free and Locked Retinal Chromophores"

- "**Postgraduate Winter School on Organic Reactivity WISOR XII**", Bressanone (Italy), 6-13 January 2003
- "**V Edizione del Congresso del Gruppo Interdivisionale di Chimica Computazionale: dal Calcolo della Struttura Elettronica alla Bioinformatica**", Siena (Italy), Certosa di Pontignano, 18-19 December 2003

**Luca De Vico**; Massimo Olivucci; Jan Helbing; Harald Bregy; Jens Bredenbeck; Rolf Pfister; Peter Hamm; Robert Huber; Josef Wachtveitl "A Fast Photoswitch for Minimally Perturbed Peptides: Investigation of the trans→cis Photoisomerization of N-Methylthioacetamide"

- "**XX IUPAC SYMPOSIUM ON PHOTOCHEMISTRY**", Granada (Spain), 17-22 July 2004
- "**μ Theochem, Modelling and Understanding in Theoretical Chemistry. A Conference in Honour of Professor Jacopo Tomasi**", Lucca (Italy), 1-4 August, 2004

# Oral Presentations

"Photoisomerization Paths of Free and Locked Retinal Chromophores"

- "**Convegno Nazionale di Fotochimica 2001**" organized by GIF – GIDF, Siena (Italy), Certosa di Pontignano, 19-20 December 2001
- **Riunione annuale delle Sezione Toscana delle Società Chimica Italiana**, Siena (Italy), 20 December 2002

"Structural Factors Affecting Excited State Potential Energy Surfaces of Artificial Retinal Chromophores"

- Seminar, Lund (Sweden), 24 April 2004